

Spatiotemporal stimulation strategies in neuroprostheses to improve locomotion after spinal cord injury

Thèse N° 9048

Présentée le 1^{er} février 2019

à la Faculté des sciences de la vie

Unité du Prof. Courtine

Programme doctoral en neurosciences

pour l'obtention du grade de Docteur ès Sciences

par

JÉRÔME GANDAR

Acceptée sur proposition du jury

Prof. S. Micera, président du jury

Prof. G. Courtine, directeur de thèse

Prof. A. Prochazka, rapporteur

Dr E. Neufeld, rapporteur

Prof. D. Ghezzi, rapporteur

2019

Thesis abstract

Spinal cord injury (SCI) disrupts communication within central nervous system and lead to range of neurological disorders including paralysis. Current rehabilitation strategies to restore locomotion are poorly effective in people with severe SCI. Epidural electrical stimulation (EES) showed promising results in animal models and humans to improve recovery. However, EES protocols have remained empirical, which has limited the efficacy of this paradigm. In this thesis, I report my contribution to the development of EES related software and hardware that were driven by the understanding of the mechanisms underlying EES. These neurotechnologies showed a remarkable efficacy to reestablish locomotion in animal models of leg paralysis.

EES protocols have primarily been delivered with continuous stimulations applied over the middle of the spinal cord, independently of current limb positions. However the natural activity of the spinal cord does not correspond to this limited monotone modulation. In the first part of this thesis, we developed spatiotemporal stimulation protocols that seek to reproduce the natural activity of the spinal cord during walking. Using computational models, we identified optimal electrode locations that target individual posterior roots. These simulations steered the design of spatially selective spinal implants. Control software triggered stimulation trains in real-time to engage extensor and flexor synergies according to limb positions. This spatiotemporal neuromodulation therapy enhanced locomotor performances in rats with severe SCI.

However, these spatiotemporal neuromodulation protocols were controlled via an external computer. The animal had no control over the occurrence of the stimulation. To remedy this limitation, we designed a brain-spine interface. We linked motor states decoded from leg motor cortex activity to spinal cord stimulation protocols to elicited the intended movements. We implemented this brain-spine interface in a nonhuman primate models of transient unilateral leg paralysis. All the animals immediately regained movements of the paralyzed leg.

There is often a mechanical mismatch between current stiff implants and the soft neural tissues of the host. The third part of this thesis is dedicated to the design and fabrication of soft neural implants that present the same elasticity as the dura mater. These implants maintain the ability to deliver electrochemical stimulation while being stretched. Such interfaces can be applied to multiple neuroprosthetic applications, including the restoration of locomotion in paralyzed rats.

In the last part of this thesis, I addressed the current limitations of spinal implant specificity. We found that EES activates the large afferent fibers within the dorsal roots and developed novel implants that take advantage of the known trajectories of the dorsal roots to increase the specificity of EES. First, we built a precise anatomical computational model of the lumbosacral roots. We then ran simulations that identified multipolar electrode configurations capable of steering the current specifically. These results drove the fabrication of soft neural implants that we inserted chronically in rat models of severe SCI. Experiments showed that multipolar EES increases the specificity of the stimulation compared to conventional protocols.

All the concepts developed and validated in my thesis are already applied or are steering applications in humans with SCI.

Keywords: Spinal cord injury, rehabilitation, neuroprosthesis, neuromodulation, locomotion, closed-loop control, computational modeling

Résumé de la thèse

La lésion de la moelle épinière (LME) perturbe la communication au sein du système nerveux central et entraîne divers troubles neurologiques, dont la paralysie. Les stratégies de réadaptation actuelles pour restaurer la locomotion sont peu efficaces chez les personnes atteintes de LME grave. La stimulation électrique périodurale (SEE) a montré des résultats prometteurs chez les modèles animaux et chez l'homme pour améliorer la récupération. Cependant, les protocoles SEE sont restés empiriques, ce qui a limité l'efficacité de ce paradigme. Dans cette thèse, je décris ma contribution au développement de logiciels et de matériels liés à l'SEE, qui reposaient sur la compréhension des mécanismes sous-jacents à l'SEE. Ces neurotechnologies ont montré une efficacité remarquable pour rétablir la locomotion dans les modèles animaux avec une paralysie des jambes.

Les protocoles SEE ont principalement été appliqués avec des stimulations continues positionnées au milieu de la moelle épinière, indépendamment de la position des membres actuels. Cependant, l'activité naturelle de la moelle épinière ne correspond pas à cette modulation monotone limitée. Dans la première partie de cette thèse, nous avons développé des protocoles de stimulation spatio-temporelle qui cherchent à reproduire l'activité naturelle de la moelle épinière pendant la marche. À l'aide de modèles informatiques, nous avons identifié les emplacements optimaux des électrodes qui ciblent les racines postérieures individuellement. Ces simulations ont permis de concevoir des implants épiduraux spatialement sélectifs. Le logiciel de contrôle déclenchait des trains de stimulation en temps réel pour recruter les synergies des extenseurs et les fléchisseurs en fonction de la position des membres. Cette thérapie spatio-temporelle de neuromodulation a amélioré les performances locomotrices chez des rats présentant une LME sévère.

Cependant, ces protocoles de neuromodulation spatio-temporels étaient contrôlés via un ordinateur externe. L'animal n'avait aucun contrôle sur la survenue de la stimulation. Pour remédier à cette limitation, nous avons conçu une interface cerveau-moelle épinière. Nous avons lié les états décodés de l'activité du cortex moteur de la jambe aux protocoles de stimulation de la moelle épinière afin d'obtenir les mouvements prévus. Nous avons implémenté cette interface cerveau-moelle dans un modèle de primates non-humain avec une paralysie unilatérale transitoire des jambes. Tous les animaux ont immédiatement repris les mouvements de la jambe paralysée.

Il existe souvent un décalage mécanique entre les implants rigides actuels et les tissus neuraux mous de l'hôte. La troisième partie de cette thèse est consacrée à la conception et à la fabrication d'implants neuronaux souples présentant la même élasticité que la dure-mère. Ces implants maintiennent la capacité de fournir une stimulation électrochimique tout en étant étirés. De telles interfaces peuvent être appliquées à de multiples neuroprothèses, y compris pour restaurer la locomotion chez des rats paralysés.

Dans la dernière partie de cette thèse, j'ai abordé les limitations actuelles de la spécificité des implants spinaux. Nous avons constaté que l'SEE active les grosses fibres afférentes dans la pourriture dorsale et a développé de nouveaux implants qui tirent parti des trajectoires connues des racines dorsales pour accroître la spécificité de la SEE. Tout d'abord, nous avons construit un modèle de calcul anatomique précis des racines lombo-sacrées. Nous avons ensuite effectué des simulations identifiant des configurations d'électrodes multipolaires capables de diriger le courant de manière spécifique. Ces résultats ont conduit à la fabrication d'implants neuraux mous que nous avons insérés de manière chronique dans les modèles de LME sévère chez le rat. Les expériences ont montré que l'SEE multipolaire augmentait la spécificité de la stimulation par rapport aux protocoles conventionnels. Tous les concepts développés et validés dans ma thèse sont déjà appliqués ou arrivent vers des applications chez l'homme avec une LME.

Mots clefs : lésion de la moelle épinière, réhabilitation, neuroprothèse, neuromodulation, locomotion, control en boucle fermée, modèle numérique

Acknowledgments

Firstly, I would like to acknowledge Prof. Grégoire Courtine to allowed me to be a member of his laboratory and accept the role of supervisor for my Phd thesis. All along, he gave me guidance to achieve my scientific work. His leadership drove me to bring out the best of my capacity and to reach top quality work. His unbending mind and the uncountable hours he dedicated to his objectives awarded him with great achievements. I will always be surprised, how within the time of my phd thesis the technology passed from rats to humans.

Next, I thank Marco Capogrosso who followed my scientific progress and advised me during my thesis. He was a mentor who supported me during challenging times. He gave me his time to help in the writing of publications. In additions to be an accomplished scientist, he is also a friends with whom I spent amazing evenings. I thank also Nikolaus Wenger and Eduardo Martin Moraud for supervising my work when I started in the laboratory and with whom I spent too much time in surgery room to implant multi-electrode array and to stay optimist even when nothing was working in recording room. I give special thanks to Laetitia Baud for the intensive training she gave to my rats and also all the administrative hidden jobs she did.

During my phd, I have been surrounded by amazing scientific lab team and all members deserve acknowledgments for the work they did for me. I especially thank Sophie for her scientific rigor, her precious advices and to have always trusted in me; Polina and Arnaud for their surgical skills and their patience when stimulators were not sending pulses; Quentin for his histological knowledges; the couple Mignardot for the stress release sessions at Cube or hiking in Alpes.

I met outstanding people outside the laboratory like Frederic who spent days to build crazy spinal implants and Ulrike who taught me CT-scan secrets. I thank all contributors to my works.

Finally, A huge thanks to my family for their supports and interests in my thesis. I greatly appreciate the support of my friends who kept me motivated and replenish my energy with their happiness during this great journey.

Contents

Thesis abstract	i
Résumé de la thèse	iii
Acknowledgments	v
1 Introduction	1
1.1 Overall impact of spinal cord injury	1
1.2 Rehabilitation state of the art	2
1.2.1 Failures of standard procedure	2
1.2.2 Possibilities of spontaneous locomotion recovery	2
1.2.3 Sensory feedback drive locomotion	3
1.2.4 Activity-dependent plasticity to bypass lesion	3
1.2.5 Neural reorganization limited for rehabilitation	4
1.3 Neuroprostheses may have solutions	5
1.3.1 Spinal neuromodulation to restore locomotion	5
1.4 Optimization with spatiotemporal neuromodulation	6
1.4.1 Spinal cord spatial selectivity	6
1.4.2 Spinal cord temporal structure	7
1.4.3 Computational models support strategy developments	7
1.5 Implants for a spatial selectivity	8
1.5.1 Rostro-caudal axis	8
1.5.2 Medio-lateral axis	8
1.5.3 MEA precursors for spinal cord	9
1.5.4 Polyimide: a microelectronic veteran	9
1.5.5 Polydimethylsiloxane (PDMS): a promising recruit	9
1.6 A real-time platform to control stimulations	10
1.6.1 Closed loop requirements	10
1.6.2 Existing platforms	11
1.7 Non-human primates for strategy validation	11
1.7.1 A brain-spinal interface to bridge a complete SCI	11
1.8 Multipolar stimulation strategy to increase specificity	12

2	Objectives	15
2.1	Aim 1: Spinal spatiotemporal neuromodulation according to the gait cycle.	16
2.2	Aim 2: Brain-spine interface in nonhuman primates	16
2.3	Aim 3: Development of spinal cord friendly implants.	17
2.4	Aim 4: From mono- to multi-polar stimulation strategies	17
3	Spatiotemporal neuromodulation therapies engaging muscle synergies to improve motor control after spinal cord injury	19
3.1	Abstract	20
3.2	Introduction	21
3.3	Results	22
3.3.1	Dynamics of hindlimb motoneuron activation during gait . . .	22
3.3.2	Electrode position to target extensor vs. flexor hotspots	23
3.3.3	Hardware: spatially selective spinal implants	24
3.3.4	Software: parameters adjusted through movement feedback .	26
3.3.5	Spatiotemporal neuromodulation after complete SCI	26
3.3.6	Gradual adjustment of extension vs. flexion movements	30
3.3.7	Spatiotemporal neuromodulation after clinically relevant SCI	30
3.4	Discussion	32
3.5	Online methods	36
3.5.1	Animal Models and surgical procedures	36
3.5.2	Multimodal recordings and data analysis	37
3.5.3	Anatomical and imaging procedures	40
3.5.4	Computational model	42
3.5.5	Acute electrophysiological experiments	43
3.5.6	Spinal implant design and fabrication	44
3.5.7	Long term functionality of spinal implants	45
3.5.8	Real-time monitoring platform and control policies	46
3.5.9	Behavioral recordings	47
3.5.10	Statistics analysis	49
3.6	Supplementary videos	50
3.6.1	Video 1: Tailored spinal implant to achieve spatial selectivity. .	50
3.6.2	Video 2: Spatiotemporal neuromodulation therapies after complete SCI.	50
3.6.3	Video 3: Spatiotemporal neuromodulation improves motor control after clinically relevant SCI.	50
3.7	Supplementary figures	51

4	A brain-spinal interface alleviating gait deficits after spinal cord injury in primates	65
4.1	Abstract	66
4.2	Introduction	67
4.3	Results	67
4.4	Discussion	72
4.5	Methods	75
4.5.1	Animal husbandry, surgical intervention and behavioral training	75
4.5.2	Experimental recordings	76
4.5.3	Data acquisition	77
4.5.4	Decoding of motor states from neural signals	78
4.5.5	Data processing and analysis	80
4.5.6	Anatomical procedures	82
4.5.7	Statistical procedures	83
4.6	Supplementary video	84
4.6.1	Video 1: Technical design and therapeutic effects of the brain–spinal interface.	84
4.7	Supplementary figures	85
5	Electronic dura mater for long-term multimodal neural interfaces	103
5.1	Abstract	104
5.2	Introduction	105
5.3	Results	105
5.4	Discussion	112
5.5	Materials and Methods	114
5.5.1	Soft e-dura materials and fabrication process	114
5.5.2	Description of the implants prepared for the biocompatibility study	116
5.5.3	Mechanical spinal cord model (fig. S5.9A)	117
5.5.4	In vitro electrochemical characterization of e-dura electrodes	118
5.5.5	In vivo Electrochemical Impedance Spectroscopy of e-dura electrodes (fig. 5.3E)	119
5.5.6	Scanning Electron Microscopy of e-dura electrodes (fig. S5.14)	119
5.5.7	Mechanical characterization of the platinum-silicone composite (fig. S5.3)	120
5.5.8	Tensile mechanical properties of rat spinal cord (Fig. 5.1B) . .	120
5.5.9	Animal groups and surgical procedures	120
5.5.10	Rehabilitation procedures after spinal cord injury	123
5.5.11	Histology and Morphology of explanted spinal cord	123
5.5.12	μ -Computed Tomography	124

5.5.13	Recordings and analysis of muscle activity and whole-body kinematics (Fig. 5.2, 5.4, S5.6, S5.17, S5.18)	125
5.5.14	Acute recordings of electrocorticograms in mice (Fig. 5.4A) . .	126
5.5.15	Long-term in vivo recordings of electrocorticograms in freely behaving rats (Fig. 5.4B, S5.15)	126
5.5.16	Chronic recordings of electrospinograms (Fig. 5.4C, S5.16) . .	127
5.5.17	Electrochemical stimulation of the spinal cord (Fig. 5.4E, S5.17)	127
5.5.18	Statistical analysis	128
5.6	Supplementary text	128
5.6.1	Deformation analysis of the spinal cord - implant model (fig. S5.10)	128
5.7	Supplementary videos	131
5.7.1	Movie S1: Electronic dura mater.	131
5.7.2	Movie S2: e-dura bio-integration.	131
5.7.3	Movie S3: e-dura applications.	131
5.8	Supplementary figures	132
6	Model-driven optimization of multipolar electrical stimulation of the lumbo-sacral posterior roots using transversal epidural implant	151
6.1	Abstract	152
6.2	Introduction	153
6.3	Results	154
6.3.1	Precise rat spinal cord anatomy	154
6.3.2	Modelization of belt strategy	154
6.3.3	Transversal spinal implants	156
6.3.4	Transversal spinal implant selectivity	156
6.3.5	Multipolar combination selection	157
6.3.6	Multipolar experimental validation	159
6.3.7	Multipolar stimulation combined with spatiotemporal neuro-modulation	161
6.4	Discussion	162
6.4.1	Lateral spinal cord recruitments led to novative spinal implant design	163
6.4.2	Multipolarity increased specificity	163
6.4.3	Paradigm compatibility: spatiotemporal multipolar protocols for long term rehabilitation	164
6.5	Conclusion	164
6.6	Methods	165
6.6.1	MicroComputed tomography (μ CT scan)	165
6.6.2	MRI	165

Contents

6.6.3	Computer Model	165
6.6.4	3D Geometry	165
6.6.5	Physics	166
6.6.6	Biophysical Model	167
6.6.7	Genetic Algorithm	167
6.6.8	Selectivity	167
6.6.9	Spinal implant fabrication	168
6.6.10	Surgical procedures	169
6.6.11	Motor-evoked potential recruitments	170
6.6.12	Rehabilitation procedures after spinal cord injury	170
6.6.13	Kinematics, kinetics and muscle activity recording	171
6.6.14	Closed-loop platform	171
6.6.15	Behavioral condition	171
6.6.16	Biocompatibility	172
6.6.17	Principal Component Analysis	172
6.6.18	Statistics	173
6.7	Supplementary figures	174
7	Discussion & Outlook	179
7.1	Spatiotemporal neuromodulation enhances locomotion	179
7.1.1	Spatiotemporal natural modulation	180
7.1.2	Key areas to control spinal cord	180
7.1.3	Selective movements	180
7.1.4	Superiority of spatiotemporal neuromodulation	181
7.1.5	Spatiotemporal neuromodulation for rehabilitation	181
7.1.6	Spatiotemporal features conserved through species	181
7.2	Closed loop platform for temporal regulation	182
7.2.1	Motion tracking for feedback	182
7.2.2	The Brain to control legs	183
7.2.3	Software modularity	183
7.3	Biocompatibility enhanced with soft spinal implant	184
7.3.1	No physical constraints	184
7.3.2	No foreign body reactions	184
7.3.3	Microfluidic advantages	184
7.3.4	Usable for spinal neuromodulation	185
7.4	Multipolar strategies to fine tune stimulations	185
7.4.1	Multipolarity to increase specificity	185
7.4.2	Personalized stimulation	186
7.5	Ready for clinical trials	186
7.5.1	Spatiotemporal stimulations for patients	186

7.5.2	Soft implants in validation	186
7.5.3	Promising future	187
List of figures		188
List of supplementary figures		188
Publication and contributions		191
List of Abbreviation		193
Bibliography		211
Curriculum Vitae		213

Introduction

1.1 Overall impact of spinal cord injury

The World Health Organization estimated in its last report about spinal cord injury (SCI) that up to 500'000 additional people are affected each year [1]. The origin of this trauma mainly comes from 3 cases: car crashes, falls and forms of violence. This prevalence only increased during previous years, mostly linked with rising average age, and so falling risk, of the world population.

Consequences following the incident depend on the level of SCI along the rostro-caudal axis of the spinal cord, but also on the extent in coronal plan. Lesions at cervical spinal segment affect around 58% of the victims and usually lead to tetraplegia [2]. The rest of patients suffers from lower lesions (e.g thoracic), leading to different degrees of paraplegia. The most striking consequence is locomotor impairment, which seriously diminishes the patients autonomy. Alongside affecting locomotion capabilities, SCI leads to a wider rang of disabilities. Indeed, the injury also impacts other systems such as reproduction, bladder expression and thermal regulation, which all impact life quality.

The two main categories for lesion classification are "complete" or "incomplete". The latter group represents a much larger case proportion with almost 68% (47% tetraplegia and 21% paraplegia) of occurrence against 32% (respectively 12 and 20 %). In order to describe SCI with more precision, the American Spinal Injury Association (ASIA) created a scale to differentiate patients and the complications beget by the injury. Victims are divided in 4 categories based on clinical assessment of locomotor and sensory systems. The ASIA rating focuses only on sensory-motor aspect of SCI and does not account for other debilitating conditions engendered by a SCI.

- ASIA-A : The most severe case, where the patient suffers an extended spinal cord lesion, there is no remaining motor control and sensation informations below the level of injury.
- ASIA-B : This case remains a severe lesion that leads to a complete motor paraly-

sis, but allows some residual sensory feedbacks.

- ASIA-C : With a moderate injury, the subject has sensations and shows some limited motor capabilities. Main muscles below the trauma have a significantly reduce efficiency, graded 3/5 or less by clinician (based on voluntary control, global range of motion and capacity of resistance against gravity).
- ASIA-D : The lowest grade concerns a small lesion, where the patient has incomplete motor deficit, which leads to a reduced muscle activity graded between 3/5 or higher for key muscles below the injury.

These disabling conditions have cost for both the patient and the society. During the first year after injury, a moderate case (ASIA-D) costs can rise to more than 300'000 US\$ and a severe tetraplegia (ASIA-A) can lead to expenses higher than 2.5 millions \$ over a lifetime [2].

1.2 Rehabilitation state of the art

1.2.1 Failures of standard procedure

Currently, there is no cure for victims of severe SCI and the majority of people remain in a disabled state for the rest of their life. The only procedures offered today are divided in two phases. An immediate action is to proceed to a surgery to clean the injury area from any bone debris or foreign bodies to avoid any further complication as spinal cord compression or pain sensations. A second step includes an extensive neurological rehabilitation procedure after recovery from surgery and stabilization of the spinal cord shock [3].

Rehabilitation strategies are not the same for patients with complete or incomplete lesion. In the first case, the goal is mainly oriented to reduce side effects of functional disability and teach patients how to use assistive devices in order to become more independent. In the second case, for patients with incomplete SCI, a wider range of rehabilitation procedures exist, as physical training and electrical stimulation [4].

1.2.2 Possibilities of spontaneous locomotion recovery

Despite the absence of a proven clinical solution, few patients (<1%) show substantial signs of recovery [2]. These observations emphasize the existence of one or more natural mechanisms to repair this type of lesion. However, the variability between

patients, the state of their lesion and eventual recovery makes it extremely difficult to build any prognosis for the victims. Nevertheless, it appears that subjects suffering from an incomplete lesion of the spinal cord are more likely to recover more motor functions [5], and patients showed a largest recovery rate of locomotion during the three first months following the incident and their recovery reaches a plateau after 12 months. The remaining connections therefore play a role in recovery, and there is a temporal window, where the body is more prone to repair itself. The involvement of the remaining neuronal circuits has also been shown by other studies that classified the extent of recovery between ASIA-A and -B [4]. The 2nd class with patients who still have sensory feedback counted more people that recovered some motor function spontaneously. Those observations lead to conclude that the more residual functions remained active the more recovery occurs. This reflects the importance of sensory feedback loops in recovery mechanisms after an disruption of the spinal cord.

1.2.3 Sensory feedback drive locomotion

Over the last century, multiple evidences highlighted the leading role of sensory feedback circuits to control locomotion. Pioneers such as Sherrington observed that a cat with a complete spinal cord transection at thoracic level could exhibit leg flexion and coordinated stepping with appropriate proprioceptive feedback [6]. Despite the obvious missing input from the cortex, the cat was moving legs in response to the mechanic backward movement imposed by a treadmill, like a sequence of reflexes that drove locomotion. The spinal circuits has the capacity to integrate multiple sensory informations overtime and to provide a motor reaction in response. While this loop could be compare to a basic H-reflex following a pressure on the knee, in fact this circuit is actually more complex. Indeed, later studies highlight the impressive capacity of this reflex to adapt locomotion to various external sensory feedback [7].

These experiments underline the importance of sensory feedback loops for walking, and also that those neural networks remain active even when deprived from motor cortex input. Therefore, these circuits became the center of interest for the rehabilitation protocols which imply to keep those reflex loops active despite the missing supraspinal connection for potential spontaneous recovery. The concept behind this rehabilitation is also known as activity-dependent plasticity.

1.2.4 Activity-dependent plasticity to bypass lesion

Activity-dependent plasticity is a characteristic of the central nervous system to re-organize itself. Unused connexion tend to disappear, while the most active fibers

are reinforced and will increase the number of new connections they form. In order to overcome a lost path, the body cannot repair the connection by growing new fiber by itself, so it tries generating new connectome to bypass the gap. Dead fibers will be abandoned while remaining paths will be recycled for the most demanding connexions [8].

This plasticity applied to the spinal cord was demonstrated in the 80s with several cat experiments [9] [10]. After a complete spinal cord interruption, cats were repeatedly trained to walk on a treadmill with assistive body weight devices during an extensive period of time. After the training, cats could progressively carry more load until a recovery of full body weight support[9]. The task was learned by the spinal cord and reinforced over time by training. Additional tasks were taught with similar protocols such as standing [10] or trunk balance regulation [11]. The spinal cord was no longer seen as a simple relay between brain and muscles, but rather as a rank of complex neural networks capable of plasticity. However, repeated task efficiency is limited to practiced activity and barely affected non-trained tasks.

1.2.5 Neural reorganization limited for rehabilitation

Observations made on cats have been adapted and applied to patients with an incomplete SCI. Subjects were positioned in heavy machines for body weight support and trained on treadmills [12]. After extensive rehabilitation sessions, they performed more steps and with a better quality. However, even in patients who recovered some walking skill, their volitional muscle activity was still minimal. Those results led to protocols for rehabilitation with patient who still have sensory residual feedback. Even if some improvements are recorded, the success of such training is limited and highly dependent on the patient situation [13]. This strategy remains the main concept to rehabilitation therapy used today to help patient with a incomplete SCI, since no protocol has shown better performance.

Despite, all those steps forward in the rehabilitation process, only few patients show progress and can benefit from an efficient therapy. Many of them suffering a complete spinal cord lesion or with limited proprioception feedback will see their chance considerably reduced to recover anything [14]. However, scanner imagery reveals that a majority of ASIA-A patient suffering a complete motor paralysis have a portion of spinal cord white matter maintained across the lesion level [15]. This observation has important therapeutic implications and could be used to drive neural plasticity in patients devoid of residual function by artificially active sensory feedback loops below the lesion.

1.3 Neuroprostheses may have solutions

A neuroprosthesis defines any device that interact with the neural system at motor, sensory or cognitive level to palliate a deficit from an injury [16] or disease [17] [18]. Cochlear implants restoring hearing in deaf people is a well known example. An arsenal of new neural technologies pop up based on novel methods to record and modulate neural activity using electricity, chemical compounds and/or light sensitivity. They are opening new paths for therapeutic treatments [19], that deserve to be explored and tested.

1.3.1 Spinal neuromodulation to restore locomotion

In the majority of SCIs, the lesion disrupts connections between motor neurones and brain, while the neuronal networks coordinating leg movements are located below the level of injury [7] [20] [21] [22]. Due to a major interruption of supraspinal signals, these neuronal networks are in a non-functional state [23]. Despite the residual connections and the preservation of locomotor circuits, a majority of spinal cord injured patients remain bound to a wheelchair for the rest of their lives, and many of the less severe cases continue to suffer from significant locomotor impairments. In order to promote activity-dependent plasticity observed in patients with residual function, a number of neuroprosthetic interventions exploiting electrical and chemical neuromodulation therapies have been designed to restore locomotion [19] [23].

Epidural electrical stimulation (EES) is promising therapy

Experimentally, epidural electrical stimulation of lumbosacral and thoracic segments has enabled improvement of motor control in animal models and humans with SCI [24] [21] [25] [26]. In combination with monoaminergic drugs, the application of EES on the dorsal aspect of lumbosacral segments instantly promotes motor permissive states in paralyzed rats even with a complete SCI [27]. Electrochemical stimulations transform lumbosacral circuits from non-functional to functional states, enabling the spinal cord to utilize sensory input as a source of control to coordinate movement. Under continuous EES, the isolated lumbosacral circuitry of rodents is capable of coordinating a wide range of motor behaviors including standing and walking at different speeds and in various directions [7]. Similar results have been obtained in humans with complete motor paraplegia (ASIA-A/B) [21] [28] [29].

Empirical driven protocols

The neurotechnology and neuromodulation protocols for spinal cord are at the early stages of development [30]. Experimental and clinical studies employed wire electrodes [27] or electrode arrays designed for pain treatment [21]. Empirical knowledge and visual observations have guided electrode positioning, the selection of active site configurations, and stimulation parameters. Pulse width, amplitude and frequency of electric pulse train were manually adjusted and kept constant over trials [31]. The general strategy was to stimulate loosely the dorsal aspect of the lumbar spinal segments to engage proprioceptive feedback afferent fibers. The objective was to activate through these pathways the central pattern generator networks and increase the global excitability of local neural circuits to enable sensory feedback to drive motor functions [32]. However, extensive mappings revealed that each electrode location, electrode configuration, and stimulation parameter modulated specific aspects of standing and stepping [7] [33] [34]. In addition, preliminary evaluations have suggested that non-regular temporal patterns [18] [35] and closed-loop [36] [37] adjustment of stimulation parameters augmented the therapeutic impact of neuromodulation therapies. This intensive and empirical labor approach slowed development to elaborate efficient EES protocols. This sub-optimal method has reduced the massive number of useful stimulation protocols to simple monopolar paradigms, with continuous neuromodulation. Despite encouraging results, this framework is disclaimed as inappropriate to mediate maximum therapeutic effects.

1.4 Optimization with spatiotemporal neuromodulation

This continuous neuromodulation paradigm encompassed two major limitations to efficiently promote EES strategies to clinical application.

1.4.1 Spinal cord spatial selectivity

The first missing component is the spatial selectivity. Stimulations are restricted to mid line spinal cord area that were selected by empirical mapping experiment. However, computer simulations and some experiments reported a spatial diversity of motor capability. Each muscle involved in the production of lower-limb movement has its motoneurons spatially distributed inside the spinal cord [38] [39]. Applying stimulations with a better accuracy during the rehabilitation could promote some specific locomotor functions and enhance the final recovery.

1.4.2 Spinal cord temporal structure

The second missing aspect is the temporal structure inside stimulation protocols. Currently, it is restricted to constant patterns of stimulation without modulations during gait cycles, unconcerned by the current state of legs. Yet each muscle has its own precise temporal sequences [40] [41] and current continuous stimulations only facilitate sensory feedback drive instead of reinforcing it with an appropriate timing. The spinal cord network activity is a dynamic structure and reducing it to a mono pattern of activation is missing a complete dimension of opportunities.

1.4.3 Computational models support strategy developments

Computational modeling helped understanding complex neural network and was involved in the development of neuromodulation strategies [42] [43] [44] [45]. Simulations represented a useful technique to analyze voltage field propagation, to create a virtual environment and to vet new inventions. In case of deep brain stimulation, many parameters of modulation have been characterized first using computational modeling before reaching clinical testing, as current steering, pulse waveform, temporal pattern and electrode layout [17].

hybrid Finit-Element-Model (FEM) reveals dorsal root activation

EES numeric simulations integrated existing models for electrical field gradient. In addition, they required a set of biophysique equations linked to neuron depolarization characterization and action potential propagations [46]. This approach is compelling to delelop spinal cord stimulation protocols since activated structures can be located far from the stimulation active site. These hybrid FEM-biophysical models suggest interaction of EES with afferent fibers coming from muscle spindles to drive alternate stepping pattern after an interruption of the corticospinal track, which are confirmed by experimental observations. They located activation directly in dorsal root afferent fibers, instead of inside the spinal cord itself. Observations hardly discriminable with empiric methods, but impact drastically stimulation protocol designs

Computational optimization

Computational modeling became mandatory with the availability of high-density electrode array [47], where any empirical testing methods are futile compared to the near-infinite stimulation combinations. A virtual space can be used to optimize any parameters of stimulation and extract preferential pattern for desired functional out-

come [46]. Once in a virtual world, tools like genetic algorithms and machine learning become available and helpful for the design of new generation multi-electrode array (MEA).

1.5 Implants for a spatial selectivity

The 3D organization of spinal cord has been underestimated by considering it solely as a relay between the cortex and motoneuron pools. In fact, the spine has a complex structure with interesting spatial distribution and an extended connectome capable of reacting specifically to various external sensory feedback or electric pulses [48].

1.5.1 Rostro-caudal axis

A wide range of stimulus locations along the rostro-caudal axis of the spinal cord from T12 to S1 spinal segments have been tested over time. Some stimulations in the upper part as L2 evoked facilitation for hind limb flexion and leg coordination. Stimulations located around S1 were more involved in lower limb extension, as well as standing and weight bearing.

Such observations indicated a defined somatotopy in the lumbar enlargement. The exploitation of the spatial and specific organization of those segments could potentially be achieved using multielectrode stimulation protocols. Combination of L2 and S1 electrode provide a first multi-segment stimulation approach to analyze effect on stepping [49], and result in surprising a chronic frame work to restore locomotion in rats after a SCI [7]. Already with the addition of one electrode, effect on rehabilitation is noticed, which encourages theories involving MEA and the development of new implants.

1.5.2 Medio-lateral axis

On the other hand, exploration of medio-lateral axis was left behind and poorly characterized. This was probably due to neurotechnological leak regarding available devices to properly record and stimulate at this location, and that can be safely implanted for long term neuro-rehabilitation protocols. To achieve this aim, it is necessary to use a MEA technologies, which are already broadly used for neuroposthetic applications, such as cochlear implants [19]. They offer the possibility to set a large number of electrode in a restricted area and are easily sealed to ensure a proper stability over time. However, the spine is a complex area with heavy constraints that standard MEA

does not respect yet [50] [51].

1.5.3 MEA precursors for spinal cord

Nevertheless, technological progress leads to promising innovations and recent experiment exhibited new MEA implantable in the epidural space. Despite the bulkiness and current software underoptimization, the implant was able to stimulate precisely and punctually large aspect of the dorsal spinal cord [47]. Localized stimulation activated specific group of muscles and support the theory that thorough stimulations could help to recover more motor function after a SCI.

The next sections present two materials usable to build MEA: polyimide and Polydimethylsiloxane (PDMS).

1.5.4 Polyimide: a microelectronic veteran

Polyimide is a polymer present in industry since more than half a century and used for medical purpose for more than 20 years. This compound was mainly used for its stability property against temperature and acids. In the electronic industry, it is used for its flexibility and insulation capacities, combined with lithography techniques, it allows to build flexible electronic devices. By replacing the copper originally used as conductor by gold, the composites based on polyimide revealed a capability to integrate living bodies without rejection. Therefore, they became basic components for the fabrication of multiple neuroposthetic devices [52].

Today, polyimide implants are commercialized and available with various shapes and designs. They evolved overtime into robust solutions to record and stimulate neural circuits [53]. However, their flexibility allows them to bend only in one dimension. That is why, those implants are often elongated and applied only on surface with a small curvature angle. This limitation prevents the use of implant based on polyimide in multiple areas of the nervous system. In the case of spinal cord, flexible materials are usable, but in a restricted manner. They are limited to the middle portion of the spinal cord dorsal aspect to avoid any damage on side linked to mechanical stress.

1.5.5 Polydimethylsiloxane (PDMS): a promising recruit

A common limitation that restricts a long-term bio-integration is the important biomechanical mismatch between the neural tissue viscoelasticity and the implant stiffness. Elasticity and shear moduli of neural tissue are below 1500 kPa and non-linear to

endure body dynamic various constraints. In opposition, most MEA are made with materials that possess an elastic modulus in the range of GPa. Even if, in our perspective, they seem soft, they are rigid compare to neural tissue. As a result, their surgical insertion and each micro movement over time will trigger acute and long-term biocompatibility reaction.

PDMS is a material made of silicone polymers, with a shear modulus comparable to tissues, known for being inert face to biocompatibility issues and already applied in many medical applications, such as microfluidic channel. The use of PDMS allows to build implants with lithography, which results in structures that could reach nanometer size precision. Even though this material properties are known for a long time, it is only recently that stretchable conductive tracks were reliably embedded inside [54]. This innovation opened the opportunity to a new kind of implant that will be flexible and stretchable. The technology has demonstrated promising results in-vitro, and previous PDMS bio-integration are encouraging up coming steps [55]. The new technique still has to prove its capacity to reliably survive and deliver stimulation in-vivo for a long-term biointegration.

1.6 A real-time platform to control stimulations

To abrogate continuous neuromodulation, the framework has to involve a closed-loop paradigm to adjust stimulation in real time. The healthy body has continuously proprioceptive afferent fibers that provide feedback on limb position and movement to adjust the leg trajectories in real time. One of the first neuroprosthetic devices that integrate real-time feedback comes from developments in the field of epilepsy. The device tracked cortical activity and detected aberrant signals in real-time, in response to which stimulation was delivered to prevent a crisis [37]. This strategy managed to reduce abnormal cortical activity and immediately interrupted behavioral seizures.

1.6.1 Closed loop requirements

Those closed-loop systems need three components to work:

1. An input; which can be a neural signal, but can be also physic or physiologic signals.
2. An algorithm; which will analyze the signal as fast as required. Here, the notion of real-time depends on the speed of analysis versus the occurrence of upgrade that can be daily or every millisecond.

3. An output; any kind of simulation or anything that will interact with the subject, electric or optic stimulations, mechanical actuation.

1.6.2 Existing platforms

In rodents SCI, such platform developments are at the early stage [56], but already exhibit their utility. Based on kinematic information of the foot trajectory, stimulation parameters of EES can be adjusted for each individual gait cycle to adapt the step height and pass obstacle as stairs [56]. Such algorithm had a resolution at gait cycle level, around a second, but a step could be decomposed with much smaller sub-phases in function of each muscle activity, which are lower than 100 millisecond. Such improvement could optimize the capability of alternating antagonist muscle and reduce the co-activation as suggested by computation model [46].

1.7 Non-human primates for strategy validation

Scientific progress led to the design of interventions that mediate striking functional recovery after neuromotor disorders in rodent models. However, the final goal is to bring the development toward clinical validations in humans. This requires passing through the non-human primate (NHP) models as they represent the closest model to humans regarding many aspects such as body size, physiology, neuroanatomy and inflammatory responses after a SCI. In order to validate rodent works, before clinical trials, NHP model ensures the safety and therapeutic efficiency [57] [58].

If some aspects are conserved through evolution, there are also crucial differences in the anatomical and functional organization of the motor systems and behaviors among rodents and primates [59] [57] [60]. These nontrivial discrepancies may partly explain the limited success of translational medicine in neuromotor disorders. For this reason, NHP research provides a unique and needed solution to properly translate the technology. However, behind the necessity rise important constraints as ethic, high cost or expertise which prevent this step for many researches [57].

1.7.1 A brain-spinal interface to bridge a complete SCI

EES can restore locomotion even in rodents suffering a complete spinal cord lesion [7]. However, natural volitional control restoration was achieved only when spared tissue was present at lesion site [31]. In case of complete SCI, an artificial technique, involving reading the intention of movement in the cortex and delivering appropriate

spinal cord stimulation, can bypass the lesion site. Brain-computer interface (BCI) technologies allow to link intended motor states to any task or movement intention [61] [62]. The most frequent applications of BCI is to connect a patient to a robotic arm. The subject trains a classifier that will recognize firing neuron patterns and decide to which task they are correlated. Such interventions are already approved for research application in humans.

NHP brain more suitable

Such results fused with EES technology create a brain spinal interface (BSI) and could bypass any gap left by a severe injury. For this achievement, NHP model is more suitable than rodent because its cortical activity is similar to humans while walking. In addition, premotor cortex of NHP has already been involved to detect walking intention [63]. NHP were implanted with an array in premotor cortex area that control limb movements. After training sessions, NHP could guide a virtual limb toward targets displayed on screens with success.

Fusion of technologies required

The fusion of EES and BCI technologies will not be enough. BCI experiments are often restricting movements because of wires or experimental setup and a rehabilitation study cannot tolerate it. To get rid of cables, engineers developed a fully wireless device to record and transmit electrophysiological signals from NHP to external computer [64]. They extracted similar data, but allowed the subject to freely behave in the environment. Such piece of technology merges with BCI and EES could provide the first brain-spinal interface to restore leg voluntary control after a complete spinal cord lesion.

1.8 Multipolar stimulation strategy to increase specificity

So far, stimulation paradigms were implemented using monopolar stimuli, involving only one electrode or contact at the time or far from each other which was similar to two times monopolar stimulations [31] [47]. Interaction between electrodes or multiple electric fields is a known effect and usually avoided because generating unpredictable behavior. With the help of numeric models, the electric field generated by each electrode independently or in interaction with their close neighbors can be predicted. Those predictions could involve anodic and cathodic polarities to active or shield subspecific areas. A multipolar neuromodulation strategy could revolve

1.8. Multipolar stimulation strategy to increase specificity

stimulation protocol by looking for electrode crosstalk instead of avoiding them.

A residual multipolar electric field can take an almost infinite number of shapes and each of them can either activate or shield a different area in function of their polarity. Each active site combination creates a virtual electrode with their coupled electrical field. With a protocol based on multipolar stimulation, spatial specificity could be highly enhanced without increasing the real number of electrode.

Adaptation is the key of success

Laboratory experiments tend to reduce the variability of models to report an effect. Indeed, the rodents used are of specific age, size and weight with the same genetic background and imposed locomotion. Patients all have their own characteristics and therefore have a huge variance. An adaptation of the implant is possible, but a personalization of stimulation protocol via multipolar combinations offers more versatility. This approach can be adapted at any time of the rehabilitation and according to the needs of any patient.

Objectives

Hindlimb paralysis resulting from a spinal cord injury remains an unsolved condition and our research targets neuroprosthetic rehabilitation strategies to restore locomotion. Continuous monopolar epidural stimulations on the spinal cord were used for decades and have undoubtedly led to great results, such as restoration of voluntary motor control in rats [31].

However, standard rehabilitation procedures ignored patients suffering from complete spinal cord. They struggled with protocols, which are based on intensive empirical trials. This inefficient approach has reduced the enormous number of useful stimulation protocols to simple continuous monopolar paradigms, while the spinal cord activity is a complex dynamic system. Additionally, such development was slowed by unadapted spinal devices and require innovative technologies to design tailored spinal implants.

Here, we proposed a spatiotemporal stimulation protocol to reproduce natural spinal cord activity. Then, we replicate this work in NHP model with the addition of brain implants to bypass any kind of lesion. We investigate new spinal implants to ensure a reliable long-term biocompatibility. Finally, we integrated multipolar stimulations into our protocol to restore locomotion after a SCI.

2.1 Aim 1: Spinal spatiotemporal neuromodulation according to the gait cycle.

The first aim was to develop an implant and a strategy to reproduce the natural spinal cord activity during locomotion in rats, according to space and time. We exploited the natural somatotopy of existing motoneuron pools in the spinal cord to design polyimide implants with multiple active sites that fitted the dorsal aspect of the spinal cord. The temporal structure was defined from muscle synergies recorded in intact rats. Then, we combined a motion tracking system with high-speed stimulator devices to create a close-loop platform in order to issue epidural electrical stimulations at the correct location in real-time according to tracked movements. Completely paralyzed rats were used in a first part to test the platform, characterize temporal and spatial components. In a second part, a clinically relevant model of lesion was applied to validate rehabilitation advantages. This work and results are presented in the first part "Spatiotemporal neuromodulation therapies engaging muscle synergies to improve motor control after spinal cord injury", an adaptation of the manuscript published in Nature Medicine.

2.2 Aim 2: Brain-spine interface in nonhuman primates

The next aim was to create a bridge between the brain and dormant neural circuits below a SCI. NHP were involved because their brains are more suitable to perform such neural recordings. We combined a multielectrode array to record brain activity, wireless modules for communications and a pulse generator to stimulate spinal cord. Only clinically approved devices were used for this setup to prove a translational feasibility with existing tools and facilitate the validation for clinical trials. We wanted to reproduce results found in rat as left-right and flexion-extension selectivity with EES, and provide a spatiotemporal neuromodulation triggered by the brain activity to facilitate recovery after a SCI. Details of this work and results are developed in the second part "A brain-spine interface alleviating gait deficits after spinal cord injury in primates", an adaptation of the manuscript published in Nature.

2.3 Aim 3: Development of spinal cord friendly implants.

In the next chapter, we aimed at the development of a new spinal implant type. An important source of device failures in neuroprosthetic is related to the mismatch between implant stiffness and neural tissue softness. We exploited PDMS properties to build an implant, which embedded micro-cracks gold lines to conduct electricity and integrated a microfluidic channel. Every components inside the implant are made to allow flexibility and stretchability. Its shear modulus is magnitude closer to neural tissue compare to conventional implants. We implanted our implant for a long-term biocompatibility study to confirm such properties help to smooth integration. Then, we applied this technology to a wide range of applications to show the versatility that it could offer. Finally, we wanted to test the micro-channel to drug delivery in the framework of spinal cord rehabilitation after a SCI with EES and monoaminergic agents injected intrathecally. We highlighted results of this studies in the third part : "Electronic dura mater for long-term multimodal neural interfaces", an adaptation of the manuscript published in Science.

2.4 Aim 4: From mono- to multi-polar stimulation strategies

The final objective was to integrate multipolar strategies to increase specificity of epidural electric stimulation. First, we used a computational model of a rat spinal cord to simulate electric fields of many electrodes with various polarities and select most selective patterns. Then, we developed a new shape of epidural implants based on PDMS technology for rats that fit computational predictions. We tested simulations with in-vivo experiments. Finally, we implanted transversal spinal implants in rats with a severe SCI. Implant were controlled with a closed-loop real-time platform stimulating according to the leg movement. This study is reported in the last part "Model-driven optimization of multipolar electrical stimulation of the lumbosacral posterior roots using transversal epidural implant", a manuscript in preparation for a future publication.

Spatiotemporal neuromodulation therapies engaging muscle synergies to improve motor control after spinal cord injury

Nikolaus Wenger^{1,2,*}, Eduardo Martin Moraud^{3,*}, Jerome Gandar^{1,*}, Pavel Musienko^{1,4,5,&}, Marco Capogrosso^{3,6,&}, Laetitia Baud¹, Camille G. Legoff¹, Quentin Barraud¹, Natalia Pavlova^{1,4}, Nadia Dominici^{1,7}, Ivan R. Minev⁸, Leonie Asboth¹, Arthur Hirsch⁸, Simone Duis¹, Julie Kreider¹, Andrea Mortera², Oliver Haverbeck⁹, Silvio Kraus⁷, Felix Schmitz¹⁰, Jack DiGiovanna³, Rubia van den Brand¹, Jocelyne Bloch¹¹, Peter Detemple¹⁰, Stéphanie P. Lacour⁸, Erwan Bézard^{12,13,14}, Silvestro Micera^{3,6} and Grégoire Courtine^{1,11}

Nature Medicine, 2016

1. International Paraplegic Foundation Chair in Spinal Cord Repair, Center for Neuroprosthetics and Brain Mind Institute, School of Life Sciences, Swiss Federal Institute of Technology (EPFL), Lausanne, Switzerland.
2. Departments of Neurology and Experimental Neurology, Center for Stroke Research Berlin, and Excellence Cluster NeuroCure, Charité-Universitätsmedizin Berlin, Berlin, Germany
3. Bertarelli Foundation Chair in Translational Neuroengineering, Center for Neuroprosthetics and Institute of Bioengineering, School of Bioengineering, EPFL, Lausanne, Switzerland.
4. Motor Physiology Laboratory, Pavlov Institute of Physiology, St. Petersburg, Russia.
5. Institute of Translational Biomedicine, St Petersburg State University, St Petersburg 199034, Russia
6. The BioRobotics Institute, Scuola Superiore Sant'Anna, Pisa, Italy.
7. MOVE Research Institute Amsterdam, Faculty of Human Movement Sciences, VU University Amsterdam, Amsterdam, The Netherlands
8. Bertarelli Foundation Chair in Neuroprosthetic Technology, Center for Neuroprosthetics and Institute of Bioengineering, EPFL, Lausanne, Switzerland.
9. Micromotive GmbH, Mainz, Germany.
10. Fraunhofer ICT-IMM, Mainz, Germany.
11. Centre Hospitalier Universitaire Vaudois (CHUV), Lausanne, Switzerland.
12. Motac Neuroscience Inc., Beijing, China.
13. University of Bordeaux, Institut des Maladies Neurodégénératives, UMR 5293, Bordeaux, France
14. CNRS, Institut des Maladies Neurodégénératives, UMR 5293, Bordeaux, France

*,& equal contributions

3.1 Abstract

Electrical neuromodulation of lumbar segments improves motor control after spinal cord injury in animal models and humans. However, the physiological principles underlying the effect of this intervention remain poorly understood, which has limited this therapeutic approach to continuous stimulation applied to restricted spinal cord locations. Here, we developed novel stimulation protocols that reproduce the natural dynamics of motoneuron activation during locomotion. For this, we computed the spatiotemporal activation pattern of muscle synergies during locomotion in healthy rats. Computer simulations identified optimal electrode locations to target each synergy through the recruitment of proprioceptive feedback circuits. This framework steered the design of spatially selective spinal implants and real-time control software that modulate extensor versus flexor synergies with precise temporal resolution. Spatiotemporal neuromodulation therapies improved gait quality, weight-bearing capacities, endurance and skilled locomotion in multiple rodent models of spinal cord injury. These new concepts are directly translatable to strategies to improve motor control in humans.

Publication contributions

I planned, coordinated and performed all experiments involving injured rats. I developed the software used to trigger stimulations via the real-time control platform. I assisted to surgeries, participated to rat rehabilitation process and recordings of the behavioral testing. I performed analysis related to spatial, temporal and spatiotemporal stimulations. I supervised the creation of all figures and prepared figures concerning my analyzed data. I was involved in the writing process of the manuscript.

3.2 Introduction

Spinal cord injury (SCI) disrupts the communication between supraspinal centers and spinal circuits, which leads to a range of motor disabilities. Neuromodulation strategies provide access to surviving circuits and pathways to alleviate these deficits [19] [65]. In particular, electrical and chemical neuromodulation of the lumbar spinal cord has mediated significant improvement of lower-limb motor control in animal models [66] [7] [31] [67] [56] and humans [67] [68] [69] [70] [71] with SCI.

Computer simulations [46] [43] [44] and experimental studies [56] [72] [49] [73] have provided evidence that electrical neuromodulation applied to the dorsal aspect of lumbar segments primarily engages proprioceptive feedback circuits. The prevailing view is that the recruitment of these neural pathways activates central-pattern generating networks [69] [74] and raises the excitability of spinal circuits to a level that enables sensory information to become a source of motor control [32]. This framework enacted two fundamental limitations in the clinical application of electrical neuromodulation therapies. First, the spatial location of stimulation remains confined to single spinal cord regions that are selected based on empirical mapping experiments [69] [75]. Second, the temporal structure of stimulation protocols is restricted to non-modulated patterns that remain constant during motor execution, regardless of the current state of lower-limb movements [68] [69] [72].

The production of lower-limb movements involves the activation of spatially distributed motoneurons [76] [39] following precise temporal sequences [77] [78] that are continuously adjusted through sensory feedback [79]. Current stimulation protocols do not attempt to reproduce these spatiotemporal patterns of motoneuron activation to facilitate movement. Here, we hypothesized that electrical neuromodulation therapies integrating spatial selectivity and temporal structure matching the natural dynamics of motoneuron activation will improve stimulation efficacy, enhancing the quality and vigor of lower-limb movements after SCI.

In order to address this hypothesis, we first conducted anatomical and functional experiments to visualize the spatiotemporal pattern of hindlimb motoneuron activation in healthy rats. We found that walking involves the alternating activation of spatially restricted hotspots underlying extensor versus flexor muscle synergies. We then developed neuromodulation strategies that specifically target proprioceptive feedback circuits in the dorsal roots in order to access these hotspots. Computer simulations determined the optimal electrode locations to recruit specific subsets of dorsal roots. These results steered the design of spatially selective spinal implants and real-time control software to modulate extensor versus flexor muscle synergies with

Chapter 3. Spatiotemporal neuromodulation therapies engaging muscle synergies to improve motor control after spinal cord injury

precise temporal resolution adjusted through movement feedback. Spatiotemporal neuromodulation therapies reinforced extension versus flexion components for each hindlimb independently, which improved a range of important gait features after complete SCI. This conceptually new stimulation strategy improved dynamic balance and skilled descending control during quadrupedal locomotion in rats with clinically relevant SCI.

3.3 Results

3.3.1 Dynamics of hindlimb motoneuron activation during gait

We first injected pairs of antagonist muscles spanning each hindlimb joint with Fluorogold in order to visualize the spatial location of hindlimb motoneurons. To combine tracings from multiple rats, we elaborated a 3D digital model of lumbar segments using the tibialis anterior motoneurons as a landmark (Fig. 3.1a). As expected, we found that motoneurons were segregated into well-defined columns of motor pools that each innervates a target muscle. Each column occupied a reproducible spatial location that created a rostrocaudal gradient of flexor and extensor motoneurons innervating proximal to distal hindlimb muscles (Fig. S3.1).

We then implanted bipolar electrodes into hindlimb muscles of seven intact rats to record the electromyographic activity of all traced muscles simultaneously during locomotion (Fig. 3.1b). The normalized muscle activity was projected onto the reconstructed motoneuron locations to visualize the spatiotemporal maps of motoneuron activation (Fig. 3.1c). These maps revealed that locomotion involves a burst of motoneuron activity in L4-L6 segments during stance and a burst of motoneuron activity mostly centered around L2-L4 segments during swing. The maps were remarkably consistent across rats (Fig. S3.2a). Gaussian clustering analysis identified these two spatial locations mathematically ($p < 0.01$), which we termed hotspots (Fig. 3.1c).

To identify the functionality and temporal structure underlying the activation of these hotspots, we decomposed muscle activity in functional modules termed muscle synergies [78] [80] using non-negative matrix factorization [81]. Four temporal activation profiles coalescing weighted combinations of the recorded muscle activity were sufficient to reconstruct more than 92 % of the variance in the original signals (92.0 ± 1.1 , Fig. 3.1d). To link muscle synergies to the activation of hotspots, we extracted the spatiotemporal map of motoneuron activation for each synergy independently (Fig. 3.1e). This analysis revealed that the first and fourth synergies produced hindlimb extension and enabled resisting gravity through the activation of the first hotspot,

which we termed extensor hotspot. These synergies were activated during stance and prior to foot strike. The third synergy promoted hindlimb flexion during swing through the activation of the second hotspot, which we termed flexor hotspot. The second synergy emerged during the stance to swing transition, and involved the simultaneous recruitment of both hotspots. These experiments uncover the function and temporal structure underlying the successive activation of spatially restricted extensor and flexor hotspots during locomotion (Fig. 3.1f). This pattern was captured in the spatiotemporal trajectory of the hindlimb endpoint (Fig. 3.1g).

3.3.2 Electrode position to target extensor vs. flexor hotspots

Epidural electrical stimulation of lumbar segments primarily recruits large-diameter proprioceptive fibers in the dorsal roots [46] [82] [45]. The resulting neural volleys provide monosynaptic and polysynaptic excitatory drives to motoneurons through the recruitment of proprioceptive feedback circuits [56] [46] [45] [33]. These previous results suggest that the recruitment of specific subsets of dorsal roots may provide access to motoneurons embedded in spatially restricted spinal segments. We tested this hypothesis to identify optimal electrode positions to modulate extensor and flexor hotspots.

We reconstructed the 3D location of dorsal roots innervating each lumbar segment (Fig. S3.1b-c) and integrated this anatomical data into an experimentally validated computational model of epidural electrical stimulation [46]. We then performed computer simulations using an optimization function that searched optimal electrode locations to recruit the dorsal roots projecting to spinal segments containing the identified extensor and flexor hotspots on each side of the spinal cord (Fig. S3.3). Simulations revealed that electrodes located 1.00 mm laterally at the border between L2 and L3 segments, and 0.75 mm laterally at the S1 segment preferentially recruited the dorsal roots projecting to extensor versus flexor hotspots, respectively (Fig. 3.2a-b).

To verify these predictions, we delivered stimulation at the identified electrode locations during acute experiments. Simultaneous electromyographic recordings of mono- and poly-synaptic motor responses in hindlimb muscles enabled the reconstruction of spinal segment activation for each site of stimulation (Fig. 3.1). These experiments confirmed the ability to target the spatially restricted hotspots unilaterally using electrode locations identified with computer simulations (Fig. 3.2c-d).

Chapter 3. Spatiotemporal neuromodulation therapies engaging muscle synergies to improve motor control after spinal cord injury

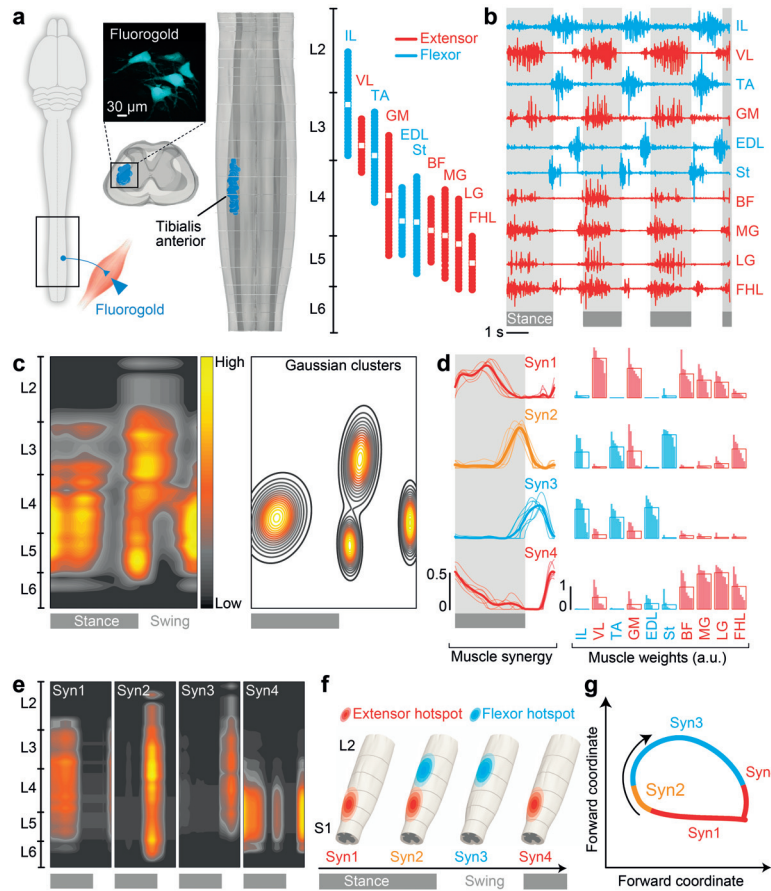


Figure 3.1 – Spatiotemporal dynamics of hindlimb motoneuron activation during locomotion (a) Diagram illustrating injections of the retrograde tracer Fluorogold into the tibialis anterior (TA) muscle to label motoneurons, as shown in the confocal image. Top-down and coronal snapshots of 3D lumbar reconstructions; each TA motoneuron is represented by a single dot. The same procedure was applied to gluteus medius (GM), iliopsoas (IL), vastus lateralis (VL), semi-tendinosus (St), biceps femoris (BF), gastrocnemius medialis (MG), gastrocnemius lateralis (LG), extensor digitorum longus (EDL), and flexor hallucis longus (FHL) muscles to reconstruct hindlimb motoneuron location within lumbar segments. The rostrocaudal location and center (white dot) of each motoneuron column is indicated in red and blue for muscles acting functionally for extension and flexion movements, respectively. (b) Hindlimb muscle activity during locomotion in an intact rat. (c) The muscle activity was projected onto the motoneuron location matrix to elaborate the spatiotemporal map of motoneuron activation during gait. The spatially restricted hotspots emerging during stance and swing were extracted by applying a Gaussian cluster algorithm onto the spatiotemporal map of motoneuron activation. (d) Mean and individual (thin lines, $n = 7$ rats) temporal activation profiles of muscle synergies, and histogram plots reporting muscle weighting for each rat (vertical bars) and muscle on each muscle synergy. (e) Spatiotemporal maps of muscle synergy activation, elaborated by representing the temporal activation profiles onto the weighted motoneuron matrix. (f) Model of spinal segments depicting the temporal sequence underlying the recruitment of muscle synergies, and the corresponding activation of extensor and flexor hotspots. (g) Activation of muscle.

3.3.3 Hardware: spatially selective spinal implants

We exploited microfabrication techniques to design spinal implants integrating the electrode configuration identified with computer simulations (Fig. S3.4a). The topolo-

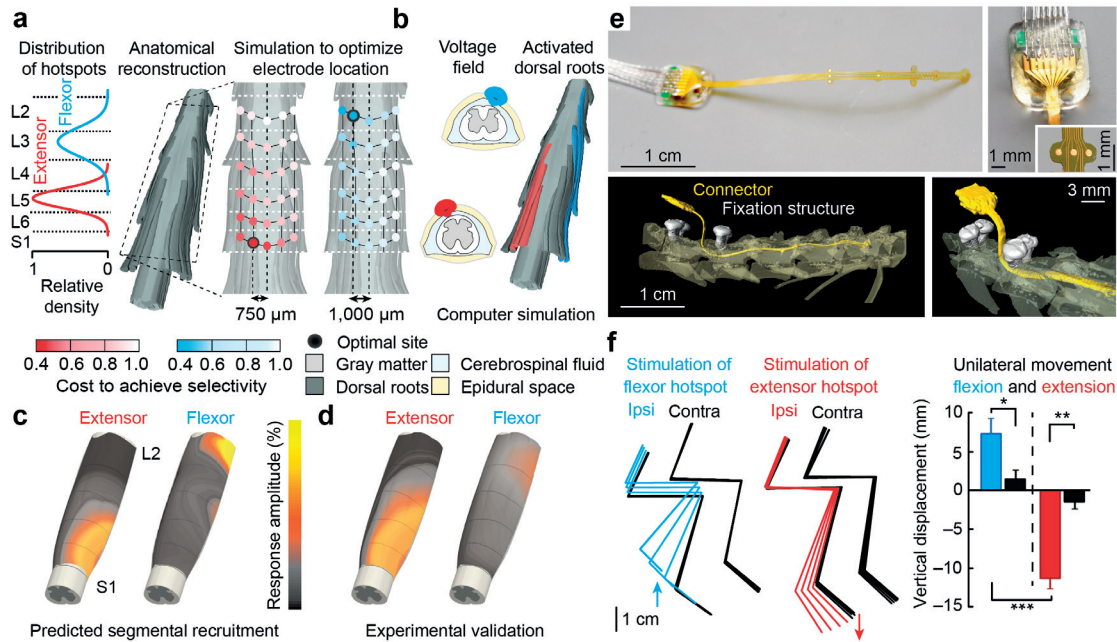


Figure 3.2 – Design, fabrication and validation of spatially selective spinal implants. (a) Experiments to identify the optimal electrode location to target extensor and flexor hotspots through the recruitment of dorsal roots. (1) Dorsal roots innervating S1 to L1 segments were reconstructed in 3D. The Gaussian curves display the spatial distribution of extensor and flexor hotspots along the spinal cord. Computer simulations were iterated over a grid of electrodes covering the lumbosacral segments and dorsal roots. An optimization algorithm identified the cost to preferentially activate dorsal roots projecting to extensor versus flexor hotspots. The black circles indicate the optimal mediolateral and longitudinal locations of electrodes. (3) Computer simulations showing isopotential 1V surface following a 150 μ A stimulation at each identified electrode location, including the resulting dorsal root activation. (4) Spatial maps of spinal segment activation for the optimal electrodes predicted by computer simulations, and (5) experimental validation in anesthetized rats. The map is computed from motor responses recorded from 8 hindlimb muscles, as described in Figure 3.1. (b) Photographs, including zooms on electrodes and connector, showing polyimide-based spinal implants. The 3D rendering was reconstructed from high-resolution μ -computed tomography (μ CT) scans performed after 5 weeks of implantation. (c) Under suspended conditions, a series of 4 pulses (40 Hz) was delivered through the electrodes targeting the extensor versus flexor hotspot. The resulting stick diagram decomposition of hindlimb movements is shown for the ipsilateral and contralateral side to the stimulation. Histogram plots report the mean ($n = 6$ rats) vertical displacement of the hindlimb endpoint for the ipsilateral (color) and contralateral (black) side to the stimulation. Error bar, SD. *, $p < 0.05$; **, $p < 0.01$; ***, $p < 0.01$.

gies and dimensions of the implants were tailored to the anatomy of the spinal cord and vertebrae structures (Fig. S3.1c).

We developed dedicated surgical procedures, including a tailored fixation structure, for locating and stabilizing the spinal implants overlying the targeted epidural spinal cord regions (Fig. 3.2e and S3.4c). Repeated impedance and electrophysiological evaluations over 6 weeks (S3.5a–b), and the absence of inflammatory responses after explantation (S3.5c–e) revealed the long-term functionality and bio-integration of

Chapter 3. Spatiotemporal neuromodulation therapies engaging muscle synergies to improve motor control after spinal cord injury

the spinal implants.

Delivery of short bursts (4 pulses at 40 Hz) of electrical stimulation through the spinal implants elicited the predicted unilateral movements of extension and flexion during suspended conditions in six intact rats (Fig. 3.2f and Supplementary Video 1).

3.3.4 Software: parameters adjusted through movement feedback

We next exploited an advanced real-time control platform [56] to implement spatiotemporal neuromodulation therapies. We elaborated signal-processing algorithms that detected the timing of gait events based on real-time tracking of bilateral hindlimb kinematics (Fig. 3.3). The continuous temporal sequence of gait events was derived from the angular displacements of the hindlimb endpoint (foot) around its center of rotation (Fig. 3.3). This progression of the foot in space resembles a clock that encodes the current timing of gait (Fig. 3.1g).

A finite-state machine logic triggered the activation of each individual electrode when the hindlimb endpoint trajectory crossed user-defined angular thresholds (Fig. 3.3 and Supplementary Video 2). Adjustments in amplitude or frequency could be tuned based on control policies [56] (Fig. 3.3). The time necessary to trigger stimulation based on movement feedback remained below 20 ms, which is 40 times faster than the average gait cycle duration in rats (800 ± 146 ms). Stimulation was triggered with 97.8% accuracy for a temporal window constrained within less than 5% of the relative gait cycle duration ($n = 140$ gait cycles). This computational infrastructure provides the technological framework for real-time adjustment of neuromodulation parameters over multiple electrodes based on high-fidelity kinematic feedback.

3.3.5 Spatiotemporal neuromodulation after complete SCI

We next exploited the developed hardware and software to test whether spatiotemporal neuromodulation therapies mediated superior gait improvements than continuous stimulation protocols. Adult rats received a complete transection of the T7 segment (Fig. 3.4a). The tailored spinal implant was inserted in the same surgery. Five weeks post-lesion, all rats exhibited complete hindlimb paralysis when positioned bipedally in a robotic bodyweight support system [7] (Fig. 3.4b). Ten minutes prior to testing, we administered a serotonergic replacement therapy [7] [31] that compensates for the interrupted source of monoaminergic modulation after injury. Continuous electrical neuromodulation delivered over the midline of L2-L3 and S1 segments enabled all the tested rats to perform coordinated locomotion in response to treadmill motion, as

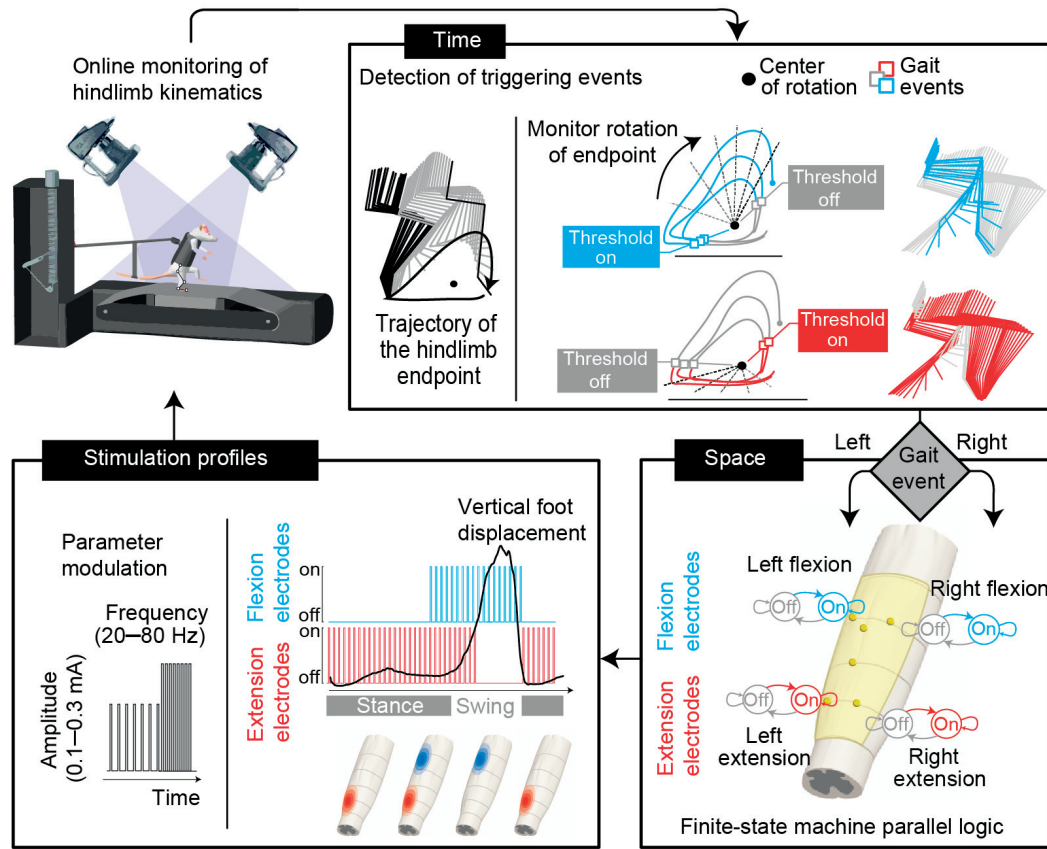


Figure 3.3 – Software to adjust spatiotemporal neuromodulation in real-time during locomotion. Computational platform to trigger adjustments of the temporal structure, spatial configuration and stimulation parameters of the neuromodulation therapies. Rats were supported bipedally in a robotic system provided vertical support during locomotion onto a motorized treadmill belt. A high-resolution video system allowed real-time monitoring of the left and right hindlimb endpoints (feet). The angular displacements of hindlimb endpoints around a calculated center of rotation were converted into angular coordinates, as indicated with the dotted grey lines. The On and Off states of electrodes targeting extensor- and flexor-related hotspots were triggered when the angular coordinates crossed user-defined thresholds, personalized for each rat. The stimulation profile module enabled tuning the amplitude and frequency of stimulation based on the therapist or control policies. The diagram represents the relationship between the vertical displacement of the foot and the activation of extensor and flexor hotspot, and how the spatially selective electrodes were turned On and Off to replicate this activation pattern.

previously reported [7] (Fig. 3.4b). However, the spatiotemporal map of motoneuron activation differed from those observed in intact rats (Fig. 3.4b), which translated into reduced vertical ground reaction forces ($p < 0.01$; Fig. 3.4b) and less extensive foot movement during swing ($p < 0.01$; Fig. 3.4b) in injured compared to intact rats.

To optimize the temporal structure of spatiotemporal neuromodulation therapies, we evaluated the impact of varying the onset or end of stimulation through the spatially selective lateral electrodes of the implant. Adjustment of the activation timing for

Chapter 3. Spatiotemporal neuromodulation therapies engaging muscle synergies to improve motor control after spinal cord injury

the electrode targeting the flexion hotspot led to a gradual tuning of flexion related variables such as flexor muscle activity, step height, and foot acceleration during swing (Fig. S3.6). The same modulation was detected for extensor related variables such as extensor muscle activity and vertical ground reaction force when varying the activation timing of the electrode targeting the extensor hotspot (Fig. S3.6). The concurrent activation of flexor and extensor hotspots at the end of stance was also critical to prevent foot dragging (Fig. S3.6). For each electrode, we selected the timing that yielded optimal values for this ensemble of gait parameters. The resulting temporal structure matched the temporal activation profiles of muscle synergies exposed in intact rats (Fig. S3.6c).

We tested whether this optimized stimulation protocol was capable of reproducing the spatiotemporal maps of motoneuron activation underlying locomotion of intact rats. In all tested rats, spatiotemporal neuromodulation therapies reinforced the amplitude of electromyographic signals and improved the activation timing in nearly all recorded hindlimb muscles (Fig. S3.10). This robust modulation led to spatiotemporal maps of hindlimb motoneuron activation that resembled those observed in intact rats (Fig. 3.4b, S3.2 and Supplementary Video 2).

Finally, we evaluated whether spatiotemporal neuromodulation improved locomotion compared to continuous neuromodulation. To quantify gait performance, we computed numerous parameters from kinematic, kinetic and muscle activity recordings ($n = 137$, Supplementary Table 1). To weight their relative importance objectively, we subjected the parameters to a principal component (PC) analysis [7] [31]. We visualized gait patterns in the new space created by PC1-2, where PC1 explained the highest amount of variance (27 %) and reflected the degree of similarity to intact rats (Fig. 3.4c). Analysis of scores on PC1 revealed that spatiotemporal neuromodulation promoted gait patterns closer to those of intact rats compared to continuous neuromodulation ($p < 0.05$; Fig. S3.8). We extracted parameters that highly correlated ($|\text{value}| > 0.5$, factor loadings) with PC1, and regrouped them into functional clusters corresponding to basic movement features. This analysis revealed that spatiotemporal neuromodulation normalized many key features of hindlimb movements (41 of 137 significantly improved parameters, $P < 0.05$ Fig. S3.8). Continuous stimulation delivered through the 4 spatially selective lateral electrodes failed to improve gait performance ($p < 0.05$; Fig. 3.4c and Fig. S3.8), confirming the synergy between spatial selectivity and temporal structure.

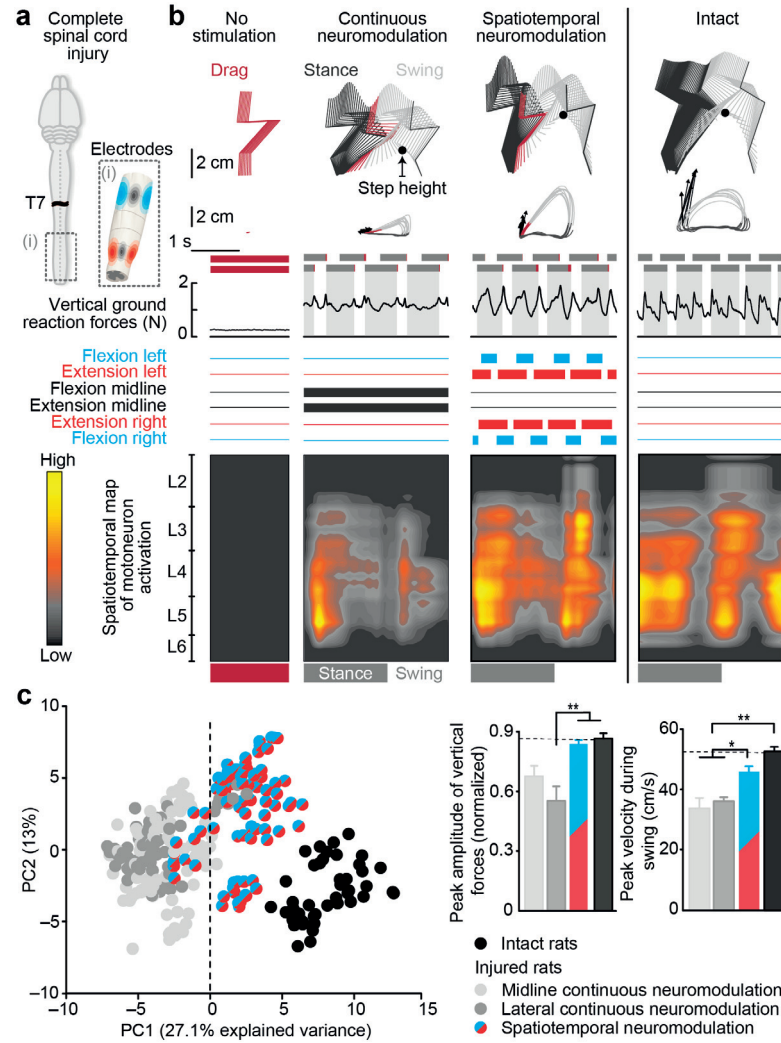


Figure 3.4 – Spatiotemporal neuromodulation reproduces the natural pattern of motoneuron activation (a) Rats receive a complete SCI and a spinal implant with conventional midline electrodes and spatially selective lateral electrodes, as depicted in (i). (b) Locomotion was recorded on a treadmill without stimulation, with continuous neuromodulation applied over the midline of lumbar and sacral segments, and during spatiotemporal neuromodulation. For each condition (same rat) and an intact rat, a stick diagram decomposition of left hindlimb movement is shown together with successive trajectories of the hindlimb endpoint, the velocity and orientation of the foot trajectory at toe off (vector with arrowheads), the stance (light grey), drag (red) and swing phases of both hindlimbs, and vertical ground reaction forces during a continuous sequence of steps. The horizontal bars (blue, red, black) indicate the current state of the electrodes. The corresponding spatiotemporal maps of motoneuron activation were calculated over 10 consecutive steps. Conventions are the same as in Fig. 3.1. (c) All the gait cycles recorded in 5 rats under the different conditions of neuromodulation are represented in a PC space. Histogram plots report mean peak amplitude of vertical ground reaction forces and the mean peak velocity of the foot during swing for the different neuromodulation conditions and for intact rats. Error bars, SEM. *, $p < 0.05$; **, $p < 0.01$.

Chapter 3. Spatiotemporal neuromodulation therapies engaging muscle synergies to improve motor control after spinal cord injury

3.3.6 Gradual adjustment of extension vs. flexion movements

We previously showed that modulation of stimulation amplitude and frequency led to gradual adjustments of hindlimb movements [56]. We asked whether this modulation could be superimposed onto spatiotemporal neuromodulation therapies in injured rats. We first varied the amplitude of stimulation delivered through one of the spatially selective lateral electrodes. A progressive increase of stimulation amplitude for the electrode targeting extension versus flexion hotspots promoted a selective and gradual augmentation of extensor versus flexor muscle activity on the stimulation side in all tested rats ($n = 5$, $P < 0.05$; Fig. 3.5a). This tuning translated into an incremental enhancement of extension versus flexion components (Fig. 3.5b), which supported the control of hindlimb extension during stance and foot trajectories during swing over ranges that reached the anatomical limits of motion (Supplementary Video 2). In contrast, increases in stimulation amplitude blocked hindlimb movements when stimulation was delivered without temporal structure (Supplementary Video 2). Muscle activity resulted from a succession of motor responses elicited after each pulse of stimulation (Supplementary S3.9), which likely originated from the recruitment of proprioceptive feedback circuits [56] [46] [33] [83]. Increase in stimulation amplitude led to commensurate augmentation of the amplitude of these responses (Supplementary Fig. S3.9)

We then verified that the previously observed modulation of step height with adjustment of stimulation frequency [56] was preserved during spatiotemporal neuromodulation (Fig. 3.5c). In all rats, adjustment of stimulation frequency led to a gradual increase in both extension and flexion components, which mediated a linear tuning of gait features such as foot height (Fig. 3.5d). These relationships support control over complex foot trajectories during locomotion [56], and can thus be combined with spatiotemporal neuromodulation.

3.3.7 Spatiotemporal neuromodulation after clinically relevant SCI

We finally evaluated the potential of spatiotemporal neuromodulation therapies to improve locomotion after clinically relevant SCI. Spinal cord damage in humans primarily results from contusions. To model such lesions, we delivered a robotically controlled impact onto thoracic segments (21.8 ± 1.7 % sparing, Fig. 3.6a and S3.10). Early after injury, all rats dragged both hindlimbs along the treadmill belt (Fig. 3.6b). Administration of the serotonergic replacement therapy failed to promote movement at this stage. The addition of continuous electrical neuromodulation instantly

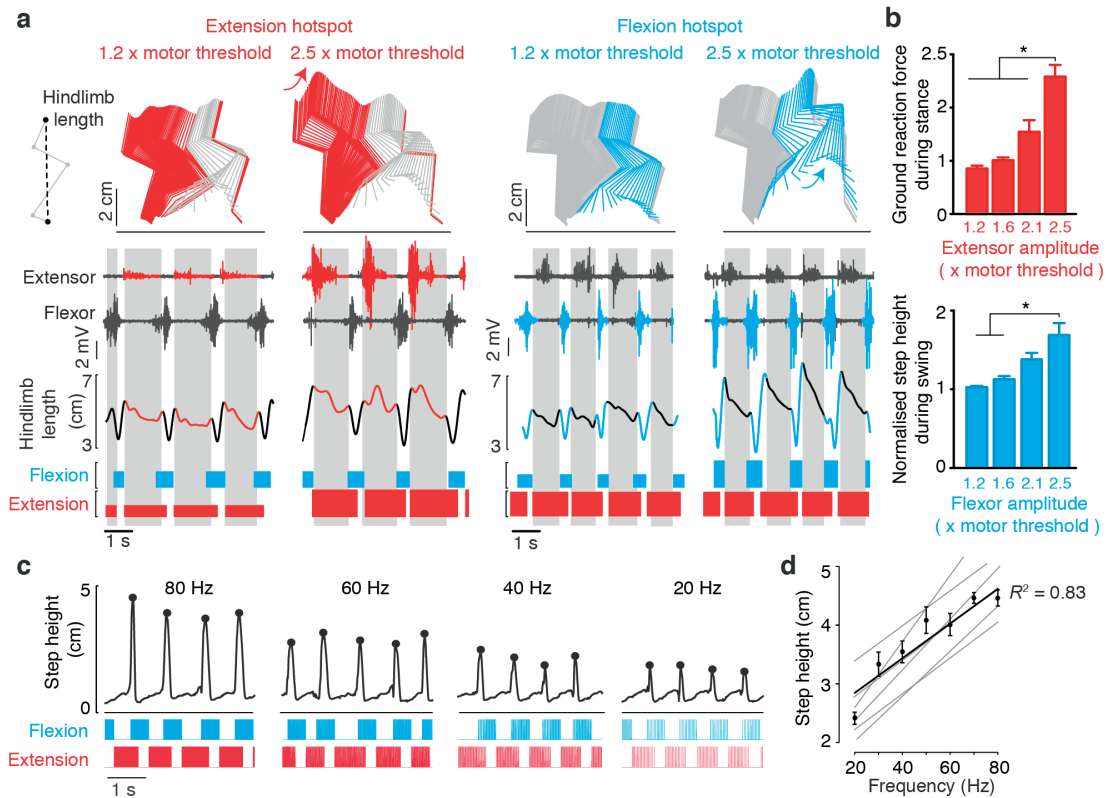


Figure 3.5 – Selective and gradual modulation of extension and flexion components. (a) Locomotor sequences recorded during spatiotemporal neuromodulation with two levels of stimulation amplitudes for the electrode targeting the extensor (left) versus flexor (right) hotspot. A representative stick diagram decomposition of hindlimb movement is shown for each condition. The colors correspond to the period during which the modulated electrode is turned on. Below, the electromyographic activity of extensor and flexor ankle muscles is displayed together with the changes in hindlimb length for a series of steps. The upper right diagram explains the calculation of the hindlimb length, which combines changes over multiple joints of the hindlimb. The spatiotemporal pattern of stimulation is shown at the bottom. The height of the bars is proportional to the stimulation amplitude. (b) Histogram plots reporting the mean vertical ground reaction forces measured during stance while modulating the amplitude of the extension electrode, and the mean step height measured during swing while modulating the flexion electrode. (c) Vertical foot displacements during locomotion under different stimulation frequency adjusted over both extension and flexion electrodes. The dots highlight the step height. Each pulse of stimulation is represented in the spatiotemporal patterns of stimulation shown at the bottom. The plot displays the relationships between the stimulation frequency and the step height for all the rats together, and each rat individually (thin line). The number of rats in indicated in each panel. Error bars, SEM. *, $p < 0.05$.

enabled locomotion. However, hindlimb movements extinguished after a few minutes since the rats were no longer able to support their bodyweight. Spatiotemporal neuromodulation instantly reestablished locomotion, enabling robust and powerful movements of both hindlimbs (Fig. 3.6b and Supplementary Video 3).

To quantify this improved gait performance, we measured the weight-bearing capacities and endurance during continuous versus spatiotemporal neuromodulation.

Chapter 3. Spatiotemporal neuromodulation therapies engaging muscle synergies to improve motor control after spinal cord injury

To determine weight-bearing capacities, we progressively decreased the amount of vertical robotic assistance by 5% increments until the rats failed to perform ten consecutive steps. Spatiotemporal neuromodulation mediated 25 to 60% augmentation of weight bearing capacities ($p < 0.05$, Fig. 3.6c), which correlated with substantial increase in vertical peak forces ($p < 0.05$, Fig. 3.6c) and extensor muscle activity ($p < 0.01$, Fig. 3.6c). To evaluate endurance, we provided optimal bodyweight support, and measured the time until the rats collapsed. Spatiotemporal neuromodulation extended the duration of locomotion from 40 to 270% ($p < 0.01$, Fig. 3.6d), maintaining step heights towards intact values during most of the testing (Fig. 3.6d).

In the chronic stage (8 weeks), the rats exhibited limited recovery of hindlimb motor control. When tested quadrupedally on a runway, gait performance ranged from limited movement of hindlimb joints to occasional plantar placements (Fig. S3.11). During spatiotemporal neuromodulation, the rats were capable of executing full weight bearing plantar steps ($p < 0.01$, Fig. S3.11 and Supplementary Video 3). Spatiotemporal neuromodulation significantly improved trunk dynamics and thus the maintenance of balance during quadrupedal locomotion ($p < 0.05$, Fig. 3.6e)

We then tested the rats during staircase climbing, a task requiring precise voluntary foot placement over consecutive steps to resist gravity and avoid tumbling against the stairs. Spontaneously, rats essentially tumbled against or hit the staircase. Spatiotemporal neuromodulation allowed both hindlimbs to pass the steps successfully without contact with the staircase in a substantial number of trials ($p < 0.01$, Fig. 3.6f and Supplementary Video 3).

3.4 Discussion

Therapeutic outcomes in animal models [7] [31] [56] [83] [84] and paraplegic patients [68] [69] [71] [72], have accelerated the deployment of clinical studies to evaluate the potential of epidural electrical stimulation for improving functional recovery after SCI [85]. In the absence of conceptual framework, however, stimulation protocols have remained unspecific, restricted to single regions, and delivered continuously. Here, we have introduced spatiotemporal neuromodulation therapies that are derived from biological principles. This conceptually new stimulation strategy reestablished lower-limb motor control when conventional protocols failed to facilitate movement. We expect that this approach will support the design of evidence-based neuromodulation therapies that improve motor control and gait rehabilitation in humans.

Various studies proposed that the motor command underlying the production of limb movement originates from a small set of motor primitives termed muscle synergies

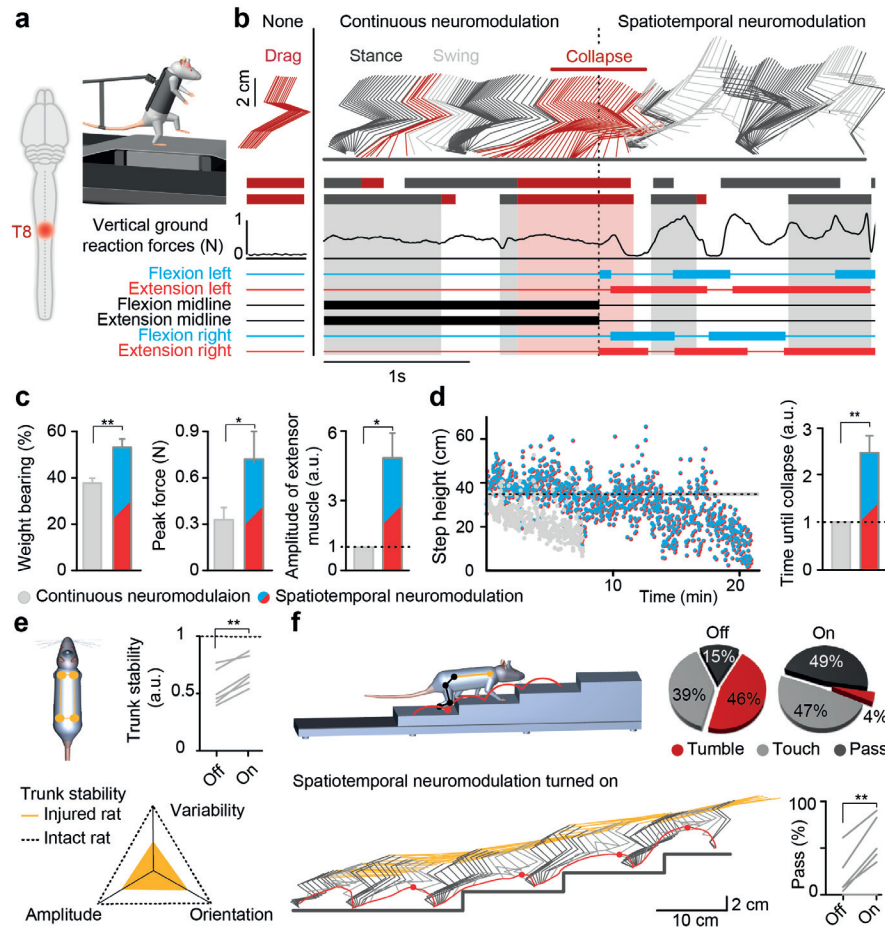


Figure 3.6 – Spatiotemporal neuromodulation improves motor control after clinically relevant SCI (a) Rats received a contusion at the thoracic level. (b) Locomotion was recorded on a treadmill without stimulation, and during a sequence during which continuous neuromodulation is applied over the midline electrodes until the rat collapses. At this moment, spatiotemporal neuromodulation is turned on. Conventions are the same as in Fig. 3.4 (c) Histogram plots reporting the maximum weight bearing capacities, the peak of vertical ground reaction forces, and amplitude of extensor muscle activity measured in the same rats during continuous versus spatiotemporal neuromodulation. (d) Successive step heights measured during a locomotor sequence recorded in the same rat under continuous versus spatiotemporal neuromodulation. The horizontal line corresponds to the mean step height of intact rats. Histogram plots reporting the normalized duration of locomotion under the rat collapsed under both conditions. (e) Rats were recorded during quadrupedal locomotion at 2 months post-SCI. Parameters related to the spatial orientation, movement amplitude, and movement variability of the trunk are each represented along an axis normalized to intact rats (dashed yellow lines). The inside of the triangle correspond to the stimulation off condition, whereas the colored surface quantifies the improvement for these balance related parameters during spatiotemporal neuromodulation, shown for all the rats (top, average) together, and for each rat individually (see Methods). The amount of tissue sparing is reported for each rat. (f) Stick diagram decomposition of hindlimb and trunk movements together with hindlimb endpoint trajectory during staircase climbing under spatiotemporal neuromodulation. The diagrams report the percent of tumbles, touches and passes against/over the steps recorded during 5 trials performed without or with spatiotemporal neuromodulation. The percent of successful passes over the step is shown for each rat individually. Error bar, SEM. *, $p < 0.05$; **, $p < 0.01$.

Chapter 3. Spatiotemporal neuromodulation therapies engaging muscle synergies to improve motor control after spinal cord injury

[74] [78] [86] [87]. These motor primitives help coping with the redundant degrees of freedom at muscles and joints [88], and are thus considered the building blocks for motor control [78] [86] [87] [89]. Previous work suggested that a control architecture based on muscle synergies would simplify the manipulation of natural limb dynamics in robotics [80] and neuroprosthetics [90]. We followed this approach to design and implement evidence-based neuromodulation therapies. As observed in humans [91], we found that rodent locomotion involves the sequential activation of spatially restricted hotspots associated with extensor versus flexor muscle synergies. These hotspots reflect the final motor command [76], which is elaborated by neuronal circuits located in the same regions [91] [92] [93]. These cells integrate supraspinal information and feedback signals to produce precisely timed muscle contractions [94] [48] [95]. Evidence suggested that these cellular nodes encode muscle synergies promoting extension versus flexion movements of the lower-limbs [91] [92]. These muscle synergy encoders receive dense synaptic contacts from proprioceptive afferents [92] [93]. Indeed, the proprioceptive regulation of neuronally encoded motor primitives [96] can predict the formation of lower-limb trajectory in the frog[97].

Epidural electrical stimulation leads to motor pattern formation through the recruitment of proprioceptive feedback circuits, both in rats [56] [46] [49] [45] and humans [72] [73]. We reasoned that spinal implants tailored to activate the proprioceptive afferents projecting to the identified hotspots would engage muscle synergy encoders related to extension versus flexion. By analogy, the recruitment of auditory afferent pathways related to specific tones has guided the development of cochlear implants to restore hearing [98]. Tailored spinal implants with electrodes targeting specific subsets of dorsal roots enabled a gradual control over the degree of flexion versus extension movements on the left and right hindlimbs. This hypothesis-driven neuromodulation therapy only required a few electrodes that were optimally located based on neuroanatomical reconstructions and computer simulations. In turn, the limited number of electrodes reduced technological challenges, allowing the development of highly reliable spinal implants that displayed long-term functionality and remarkable bio-integration.

This conceptual framework also simplified the architecture of the real-time control software. We found that the temporal activation profiles of muscle synergies were captured in the spatiotemporal trajectory of the foot, as previously reported during human walking [77]. Thus, a single parameter provided a simplified and reliable feedback signal to trigger simultaneous adjustments of neuromodulation parameters across multiple electrode configurations with high fidelity.

These new concepts and technologies will support the development of more refined

control policies. For example, we found that the predictive modulation of step height with changes in stimulation frequency [56] was well preserved during spatiotemporal neuromodulation. Algorithms incorporating adjustments of spatial, temporal, amplitude and frequency parameters under the guidance of dynamic computational models have the potential to further improve gait performance.

Habitual bipedalism elicited a series of adaptations in the dynamics of lower-limb motoneuron activation during human walking [78] [99]. Despite these evolutionary adaptations, both muscle synergies [78] [89] and proprioceptive feedback circuits [100] appear remarkably conserved across mammals. Moreover, the neuroanatomical [101], electrophysiological [72] [73], computational [74] [78] and modeling [43] concepts that guided the design and implementation of our hypothesis-driven neuromodulation therapies are directly applicable to humans.

Existing wearable and implanted wireless sensors [102] provide off-the-shelf solutions to monitor foot trajectory during locomotion. Neuromodulation platforms have been developed [103] to enable integration of feedback signals for closed-loop electrical stimulation of the human nervous system. These neurotechnologies are well suited to conduct clinical evaluations on the ability of spatiotemporal neuromodulation therapies to facilitate motor control and gait rehabilitation in humans. While challenges lie ahead, we believe that spatiotemporal neuromodulation of the spinal cord will become a viable therapy to enhance functional recovery in humans with SCI.

3.5 Online methods

3.5.1 Animal Models and surgical procedures

Animal species

All experiments were conducted in accordance with Swiss federal legislation and under the guidelines established at EPFL. Local Swiss Veterinary Offices approved all the procedures. Experiments were performed on Lewis rats (LEW/ORLj) with initial weight of 180-220 g that were ordered from Janvier Labs in France.

Surgical procedures

General surgical procedures for the majority of interventions carried out have been described previously [31] [56] [104]. All the interventions were performed under full general anesthesia with isoflurane in oxygen-enriched air (1-2%). After surgery, the rats were placed in an incubator for optimized recovery from anesthesia.

Implantation of intra-muscular electrodes

To record electromyographic activity, bipolar electrodes were implanted into selected hindlimb muscles. Combinations of the following muscles were implanted depending on experiments: gluteus medius, iliopsoas, vastus lateralis, semi-tendinosus, biceps femoris, gastrocnemius medialis, gastrocnemius lateralis, tibialis anterior, extensor digitorum longus, flexor hallucis longus. Briefly, recording electrodes were fabricated by removing a small part (0.5 mm notch) of insulation from each the implanted wire (AS631, Cooner wires). A common ground wire was created by removing about 1cm of Teflon from the distal extremity of the wire, which was inserted subcutaneously over the right shoulder. All electrode wires were connected to a percutaneous amphenol connector (Omnetics Connector Corporation) cemented to the skull of the rats. The proper location of the electrodes was verified post-mortem.

Surgical insertion of spinal implants

The surgical methods to insert and stabilize the spinal implant into the epidural space are detailed in Fig. S3.6. Briefly, 2 partial laminectomies were performed at vertebrae levels L3-L4 and T12-T13 to create entry and exit points for the implant. The implant was gently pulled above the dura mater using a surgical suture. Electrophysiological testing was performed intra-operatively to fine-tune positioning of electrodes. The

connector of the implant was secured into a protective cage plastered using freshly mixed dental cement on top of the L3-L4 vertebra.

Spinal cord injury models

Two models of spinal cord injuries were used in the present experiments. All the main experiments were conducted in rats that received a complete transection of the mid-thoracic spinal cord, towards T8 spinal segment. Under aseptic conditions and general anesthesia, a dorsal midline skin incision was made from vertebral level T5 to L2 and the underlying muscles were removed. A partial laminectomy was performed around T8 vertebra to expose the spinal cord. The exposed spinal cord was then cut with customized tools. The complete transection lesions were verified post-mortem by confirming the absence of neural tissues throughout the dorsoventral extent of the spinal cord. The second group of rats received a spinal cord contusion. A partial laminectomy was made at the T9 vertebra to expose T7/T8 segments. A 230 kdyn (1 dyn = 10 μ N) contusion injury was applied using a force-controlled spinal cord impactor (IH-0400 Impactor, Precision Systems and Instrumentation LLC, USA). The amount of damaged spinal tissue was evaluated using coronal sections stained with antibodies against glial fibrillary acidic protein (GFAP). The contours of the spared and damaged spinal tissues were reconstructed in the Neurolucida image analysis software to reconstruct the lesion in 3D.

Rehabilitation procedures after spinal cord injury

All the injured rats were trained daily for 30 min, starting 7 days post-injury. The neurorehabilitation program was conducted on a treadmill using a robotic bodyweight support system (Robomedica) that was adjusted to provide optimal assistance during bipedal stepping⁷. To enable locomotion, a serotonergic replacement therapy combining the 5HT_{2A} agonist quipazine and the 5HT_{1A/7} agonist 8-OHDPAT was administered systemically 10 min prior to training. Electrical neuromodulation was delivered throughout the training session.

3.5.2 Multimodal recordings and data analysis

Recordings of whole-body kinematics, kinetics, and muscle activity

Procedures to record kinematics, kinetics, and muscle activity have been detailed previously [56]. Briefly, whole-body kinematics was recorded using the high-speed motion capture system Vicon (Vicon Motion Systems), combining 12 infrared cameras

Chapter 3. Spatiotemporal neuromodulation therapies engaging muscle synergies to improve motor control after spinal cord injury

(200 Hz). Reflective markers were attached bilaterally overlying iliac crest, greater trochanter (hip), lateral condyle (knee), lateral malleolus (ankle) and distal end of the fifth metatarsal (limb endpoint). During quadrupedal locomotion, an additional marker was placed on the shoulders. 3D position of the markers was reconstructed offline using Vicon Nexus software. The body was modeled as an interconnected chain of rigid segments, and joint angles were generated accordingly. In addition we computed changes in the angle and length of the virtual telescopic limb linking the hip to the foot, which we termed hindlimb. Electromyographic signals (2 kHz) were amplified, filtered (10–2000 Hz bandpass), stored and analyzed off-line. Ground reaction forces in the vertical, anteroposterior and mediolateral directions were monitored using a force plate (2 kHz, HE6X6, AMTI) located in the middle of the runways, or below the treadmill belt. Concurrent video recordings (200 Hz) were obtained using two cameras (Basler Vision Technologies) oriented at 90 deg and 270 deg with respect to the direction of locomotion.

Analysis of whole-body kinematics, kinetics, and muscle activity

A minimum of 10 step cycles was typically extracted for each hindlimb in each experimental task and rat. A total of 137 parameters quantifying kinematics ($n = 118$), kinetic ($n = 6$) and muscle activity ($n = 13$) features were computed for each gait cycle using custom written Matlab scripts and according to methods described in details previously [56]. All the computed parameters are reported in Supplementary Table S3.12. To demonstrate the effects of experimental conditions, and extract the parameters that captured the largest amount of variance across rats or between conditions, we implemented a multi-step procedure based on principal component (PC) analysis [31] [56] [52]. PC analyses were applied on all the computed parameters from all individual gait cycles for all the rats together. Gait cycles were visualized in the new synthetic PC space, and PC scores were extracted to quantify differences between groups or experimental conditions. Parameters highly correlated (factor loadings) with PCs that discriminated the experimental conditions were extracted, and regrouped into functional clusters corresponding to basic movement features, which were named for clarity.

Dynamic trunk balance

To quantify improvement of dynamic trunk movement during quadrupedal locomotion, we computed an ensemble of parameters related to the orientation of the trunk, the variability of trunk movement, and the amplitude of trunk movement. Parameters are all reported in Supplementary Table S3.12. For each component of trunk

movement (amplitude, orientation and variability), we expressed these parameters along a dedicated axis that report the degree of similarity of these parameters to those measured in intact rats. In Figure 3.6d, these features are represented in the same rats without stimulation (inside triangles) and under spatiotemporal neuromodulation, since all the parameters improved for all tested rats. Therefore, the distance between the inside and outside of the triangles quantifies the improvements observed during stimulation. The overall increase in the surface of the colored area (difference between both conditions) reflects improvement in dynamic trunk movement during spatiotemporal neuromodulation.

Muscle Synergy extraction

Muscle activation signals (electromyographic data) were high-pass filtered (30 Hz) with a zero lag fourth-order Butterworth filter, full-wave rectified, smoothed with a zero lag fourth-order low-pass (20 Hz) Butterworth filter, time interpolated over individual gait cycles to fit a normalized time base with 200 points, and averaged across all gait cycles performed by the individual rat. The electromyographic signal of each muscle was normalized to its peak value. We then applied a non-negative matrix factorization algorithm on these curated muscle activation signals to derive the weighting components and temporal activation profiles of muscle synergies [78].

Spatiotemporal map of motoneuron activation

To visualize spatiotemporal map of motoneuron activation, electromyographic signals were mapped onto the rostrocaudal distribution of the reconstructed motoneuron matrix [76]. This approach provides an interpretation of the motoneuron activation at a segmental level rather than at the individual muscle level. The maps were constructed by adding up the contributions of each muscle to the total activity at each spinal segment. The motor output pattern of each spinal segment S_i was estimated by the following equation:

$$S_i = \frac{\sum_{j=1}^{n_i} \frac{MN_{ij}}{MN_j} EMG_j}{\sum_{j=1}^{n_i} \frac{MN_{ij}}{MN_j}} Ni \quad (3.1)$$

where n_i is the number of EMG_j s corresponding to the i^{th} segment, EMG_j represents the normalized muscle activity, MN_{ij} is the number of motor neurons related to muscle j for the segment i , MN_j is the total number of motor neurons for the muscle j , N_i is the number of muscles innervated by the i^{th} spinal segment.

Chapter 3. Spatiotemporal neuromodulation therapies engaging muscle synergies to improve motor control after spinal cord injury

Gaussian Cluster algorithms

Clusters of activity were extracted from the spatiotemporal map of motoneuron activation using Gaussian Mixture Models (GMM). GMM was applied to the temporal activation profiles of motoneuron activation within each spinal segment. Four clusters maximized fitting quality according to Bayesian information criteria. This analysis highlighted two main hotspots along the rostrocaudal direction, and three main timings of activation corresponding to stance, stance-to-swing transition, and late swing.

3.5.3 Anatomical and imaging procedures

Spatial distribution of hindlimb motoneurons

Rats ($n = 20$) received injections of Fluorogold (2% in sterile saline, 30-80 μl per muscle) into the tibialis anterior muscle, and in the same surgery, into one additional muscle on the contralateral side. The following muscles were traced: gluteus medius, iliopsoas, vastus lateralis, semi-tendinosus, biceps femoris, gastrocnemius medialis, gastrocnemius lateralis, extensor digitorum longus, and flexor hallucis longus. The location of the retrogradely traced motoneurons was reconstructed in 3D from serial spinal cord sections using Neurolucida. To merge reconstruction from several rats into a unified digital library, the tibialis anterior motor column was used as a landmark in each rat.

Micro-Computed Tomography

Repeated imaging of spinal implants in vivo was conducted using the micro-computer tomography scanner Skyscan 1076 (Bruker μCT). Scanner settings were adjusted to avoid artefacts induced by metallic parts of the vertebral orthosis (0.5-1 mm aluminum filter, voltage 70-100 kV, current 100-140 μA , exposure time 120-160 ms, rotation step 0.5 deg). The resulting projection images were reconstructed into 3D renderings using NRecon and GPURecon Server (Bruker μCT). Rats were kept under isoflurane anesthesia during the scan to reduce motion artifacts. Segmentation and 3D model were constructed with Amira® (FEI Visualization Sciences Group).

Measurement of vertebrae and spinal segments

The shape of vertebrae was measured using micro-computed tomography imaging. The spinal cords of 3 rats were imaged, and the entire bone structure was reconstructed

in 3D. The 3D renderings were exported in the virtual reality modeling language file format WRL that was later merged with spinal tissue and dorsal root reconstructions. Measurements of relationships between vertebra and spinal segment morphologies were performed on fresh tissue. For each subject, the spinal segments were identified based on the innervation of the dorsal roots. The center of the segment was defined as the entry point of the rootlets. After measuring the length of vertebra, and the relationships between vertebra and spinal segments, the entire spinal cord was extracted, and the roots moved perpendicular to the spinal cord to clearly visualize the segments. The location and length of each segment was then calculated.

Reconstruction of spinal segments

At the end of the experimental procedures, rats were perfused with Ringer's solution containing 100'000 IU/L heparin and 0.25% NaNO₂ followed by 4% phosphate buffered paraformaldehyde, pH 7.4 containing 5% sucrose. The spinal cords were dissected, post-fixed overnight, and transferred to 30% phosphate buffered sucrose for cryoprotection. After 4 days, the tissue was embedded and the entire lumbosacral spinal cord sectioned in a cryostat at a 40 µm thickness. To reconstruct spinal segment morphology in a 3D model, a Nissl staining was performed on 25 evenly cross-sections of lumbar and sacral segments, each separated by 0.8 mm. The slides were assembled into the Neurolucida image analysis software (MBF Bioscience) to reconstruct lumbosacral segments in 3D.

Reconstruction of dorsal root trajectories

After fixation, the spinal cord was extracted from the vertebral canal. The dura mater was opened along the rostrocaudal axis, and gently moved on the side. For each spinal segment, the dorsal root ganglions were identified. The corresponding root was retracted cranially and laterally. The entire length of the root was painted, from the cut extremity to the entrance into the spinal segment. All the painted roots from S3 to L1 were repositioned in their original location along spinal segments, and the dura mater was sutured using surgical wire (Ethilon 6.0). The spinal cord was then frozen and cut into 80 µm thick slices using a cryostat (Leica Instruments). Reconstructions were conducted using every other section, corresponding to intervals of 160 µm. The slides were assembled into the Neurolucida image analysis software (MBF Bioscience) to reconstruct the color-coded dorsal roots in 3D.

Chapter 3. Spatiotemporal neuromodulation therapies engaging muscle synergies to improve motor control after spinal cord injury

Histology of explanted spinal cord with long-term implants

After 8 weeks of implantation, rats were perfused, and their spinal cords sectioned, as explained above. Astrocytic reactivity was revealed by performing immunohistological staining against glial fibrillary acidic protein (GFAP). Coronal sections of the spinal segments located below the implant were incubated overnight in serum containing anti-Iba1 (1:1000, Abcam, USA) or anti-GFAP (1:1000, Dako, USA) antibodies. Immunoreactions were visualized with appropriate secondary antibodies labeled with Alexa fluor® 488 or 555. Sections were mounted onto microscope slides using anti-fade fluorescent mounting medium and covered with a cover glass. The tissue sections were observed and photographed with a laser confocal fluorescence microscope (Leica). Immunostaining density was measured offline using 6 representative confocal images of each lumbar segment per rat. Images were acquired using standard imaging settings that were kept constant across rats, and analyzed using custom-written Matlab scripts according to previously described methods⁵. All analyses were performed blindly.

Morphology of the entire spinal cord

All the 3D reconstructions derived from micro-computed tomography imaging and anatomical experiments were merged to generate a global model including the bony structure of vertebrae, the shape of spinal segments, and the trajectory of each dorsal root. We generated a database (Supplementary Database) using the STereoLithography (.stl) file format that is supported by many software packages, and is widely used for rapid prototyping and computer-aided manufacturing. This database is available for download at <http://cortine-lab.epfl.ch>.

3.5.4 Computational model

Hybrid computational model of electrical spinal cord stimulation

We previously elaborated and validated experimentally a hybrid computational model of epidural electrical stimulation of the rat spinal cord [46]. The model combines (i) finite element modeling of the entire lumbosacral spinal cord to compute the electrical fields elicited by electrical spinal cord stimulation, and (ii) anatomically and biophysically realistic neural structures to derive the type of fibers and neurons activated by the stimulation. In the present experiments, we integrated all the results from the traced hindlimb motoneurons (Fig. S3.1) and updated the positioning of the dorsal roots in the model with the new 3D reconstructions (Supplementary Database

).

Computer simulations and model predictions

We conducted simulations to identify the optimal electrode locations to activate interneurons and motoneurons located within extensor- and flexor-related hotspots of lumbar segments during gait. Computerized simulations, neurophysiological experiments, and pharmacological testing revealed that epidural electrical stimulation activates interneurons and motoneurons indirectly through the recruitment of proprioceptive fibers feedback circuits fibers within the dorsal roots [56] [46] [45]. Therefore, we performed computerized simulations that searched optimal electrode locations to activate proprioceptive afferent fibers ($A\alpha$ fibers) running in the dorsal roots projecting to the targeted spinal segments. The segmental distribution of extensor- and flexor-related hotspots during gait was derived from Gaussian clustering analysis (Fig. 3.1, See below). To optimize electrodes configurations, a grid of electrodes was positioned over the modeled lumbosacral segments. The grid combined 5 active sites per segment, resulting in a total of 30 electrodes. Active sites were located over the midline, and at 750 and 1500 μm from the midline for the more caudal segments (L4-S1), and at 1000 and 1500 μm from the midline for the more rostral segments (L2-L3) in order to conform the enlargement of lumbosacral segments. The spacing of electrodes along the mediolateral direction was selected to maximize left-right specificity¹². To evaluate the ability of each electrode to access the targeted dorsal roots, we elaborated an optimization algorithm that calculated the cost to achieve specificity based on 4 factors: (i) stimulation specificity for the targeted segments; (ii) ipsilateral vs. contralateral specificity; (iii) minimum threshold; and (iv) specificity of the neighboring sites. The later term was important to ensure robustness in case of electrode misplacement, inter-individual variability, and post-implantation migration. For each active site, stimulations were delivered at increasing amplitudes ranging from 50 to 600 μA . The resulting recruitment of $A\alpha$ fibers was evaluated for each segment at each current level. The total number of implemented simulations reached 112'500, which required approximately 8 days of computer time. Equations of the optimization algorithm are reported in Fig. S3.4.

3.5.5 Acute electrophysiological experiments

Motor evoked potentials to validate model predictions

Adult rats were anesthetized with urethane (1 g/kg, i.p.). Bipolar electrodes were implanted into a pair of antagonist muscles spanning each joint of the hindlimb: gluteus

Chapter 3. Spatiotemporal neuromodulation therapies engaging muscle synergies to improve motor control after spinal cord injury

medius, iliopsoas, vastus lateralis, semi-tendinosus, gastrocnemius medialis, tibialis anterior, extensor digitorum longus, flexor hallucis longus. An extensive laminectomy was performed to expose all the lumbar and sacral segments, and visualize the dorsal roots projecting to each segment. Motor evoked potentials were simultaneously recorded in all the implanted muscles while delivering rectangular pulses (0.2 ms duration) at 0.5 Hz through epidural electrodes. The electrode was positioned at the locations identified by simulations using dorsal roots and the spinal cord midline as anatomical landmarks. The intensity of the electrical stimulation was increased progressively from 20 to 300 μ A. Electromyographic signals (12.207 kHz) were amplified, filtered (1–5000 Hz bandpass), and stored for off-line analysis. The root mean square (RMS) of the motor evoked potentials were calculated for each muscle, and represented in color-coded spatial maps of motoneuron activation that were directly meshed onto the spinal cord model. The methodology to compute these maps is explained above.

3.5.6 Spinal implant design and fabrication

Epidural implants were fabricated using ultra-violet (UV) photolithographic patterning of a photosensitive polyimide, as well as micro electroforming to create gold electrodes and embedded gold interconnects. Polyimide is a mechanically and chemically robust polymer material that showed a high level of biocompatibility[52]. Processing of the implants was performed on wafer scale, which allowed parallel fabrication of 10 devices or more on a 125 mm silicon wafer serving as carrier wafer. Processing started with deposition of a 20 μ m thick polyimide film by spin coating on the silicon substrate. UV lithography was used to shape the polyimide-based bottom layer, which constituted the footprint of the implant. A 200 nm thick gold layer was deposited using vacuum evaporation and lithographically structured providing a conductive seed pattern. Gold was then electroplated to a height of approximately 6 μ m to create the electrodes and leads. A 20 μ m cover layer of photosensitive polyimide resist was applied by spin coating to uniformly cover the bottom and electrode structure. A final UV lithography step was conducted to structure the top layer of the implant, and create openings over the electrodes and contact pads. Before peeling off the implants from the carrier wafer, holes were punctuated through the polyimide using mechanical punching to promote the growth of conjunctive tissues that stabilized implants over time. To create a connector, the contact pads located at the extremity of the implant were glued to a small support plate made of medical grade PMMA sheet material. Precision milled alignment structures allowed fine adjustment of the support plate to the polyimide-based implant, and to the extremity of the leads. The support plate contained a seat in which a tiny printed circuit board (PCB) with

conductive stripes was fixed. Stainless steel leads with FEP (Fluorinated Ethylene Propylene) insulation (AS-632, Cooner Wire) were directly soldered to the contact pads of the implant via the contact stripes located on the PCB. The resulting implants and connective leads were highly reliable mechanically and electrically. Finally, the entire contact area was covered with a UV-curable, methacrylate-based resin that provided tight sealing. For improved bio-integration, the contact interface was over-molded with a thin layer of medical grade silicone. The process flow, shape and dimensions of the spinal implant are detailed in Fig. S3.5.

3.5.7 Long term functionality of spinal implants

Motor evoked potentials and induction of movement

The ability to spinal implants to engage specific muscles and to elicit distinct movements was tested using short bursts of stimulation delivered through chronic spinal implants. After recovery from implantation (around 2 weeks), rats ($n = 6$) were lightly anesthetized with ketamine, and suspended in the air in a custom-made jacket. Electromyographic activity was recorded at 2 kHz in conjunction with bilateral hindlimb kinematics (see above). Stimulations were delivered at 0.5 Hz, and synchronized with recordings of motor evoked potentials and kinematic data. To verify the long-term functionality of electrodes, motor evoked potentials were recorded weekly in fully awake rats. For each electrode of the spinal implant, single-pulses (0.2 ms, 0.5 Hz) were delivered at increasing intensities. The current threshold necessary to elicit motor evoked potentials in the left and right tibialis anterior muscles was measured. The obtained values were normalized to baseline recordings, and averaged across rats and electrodes.

Electrode impedance

The impedance of electrodes embedded in the spinal implants was recorded using a bipolar electrode configuration. The counter electrode was created by removing the insulation of a Teflon-coated stainless wire at its extremity, and implanted the electrode into the bony part of vertebra L1. Impedance at 1kHz was obtained with a potentiostat equipped with a frequency response analyzer (Reference 600, Gamry Instruments). Weekly electrochemical impedance spectroscopy measurements of all the electrodes of the spinal implants were made in fully awake rats.

3.5.8 Real-time monitoring platform and control policies

The real-time monitoring and control platform was implemented within a multi-threaded C++ code (Visual Studio 2010, Microsoft) running on a quad core Microsoft Windows 7 computer. Stimulation patterns were applied via an RZ5 processing unit (Tucker-Davis Technologies) connected to an MS16 Stimulus Isolator (Tucker-Davis Technologies). The integrated Vicon recording system generated raw 3D positions of the markers, which were imported into the C++ environment in (soft) real time via Ethernet using the DataStream SDK software. We developed a custom algorithm for online interpolation of missing markers through triangulation and relabeling of each marker to the appropriate joint landmark. All signals were filtered online using least mean squares adaptive filters. The control logic triggered individual electrodes based on trajectory of left and right hindlimb endpoints. Triggering-events were extracted for each electrode individually. Control algorithms continuously calculated the angular trajectory of the foot around a virtual center of rotation in the sagittal plane. The change in on/off state of each electrode configuration was triggered when the angular values crossed user-defined thresholds that were previously optimized for each electrode and rat during mapping experiments (Fig. S3.9). The algorithm calculated for each gait-cycle k the estimated position of the virtual center of rotation \hat{C}_k derived from the trajectory T_k of each foot in the sagittal plane as:

$$(X_C, Y_C) = \left(x_{max}, \frac{1}{N} \sum_{j=1}^N y_j \right) \quad (3.2)$$

where x_{max} is the x-coordinate at the point of highest step-height (y_{max}), and N the number of data-points recoded per gait cycle. In order to prevent jittering due to cycle-to-cycle variability, the estimate of the center of rotation was iteratively updated at every gait cycle as:

$$\hat{C}_k = \hat{C}_{k-1} + \mu(\hat{C}_k - \hat{C}_{k-1}) \quad (3.3)$$

with an updating factor $\mu = 0.2$. This approach captured the natural alternation of stance and swing phases during gait despite intrinsic variability within and in-between gait cycles. This procedure was also inherently invariant to scaling, and compliant enough to detect triggering-times with high fidelity compared to other methods that exhibit increase in variability with deteriorated gait movements. These control algorithms provide a flexible tool to study and implement phase-dependent modulation of neuroprosthetic system in real-time during gait. To evaluate the delay in the process-

ing time of this loop, we simulated an input and recorded the time necessary to adapt the stimulation parameters. This delay included the processing of video recordings by the motion capture system, the transfer of this data via Ethernet to a real-time control computer, the processing of this data using dedicated libraries, the changes in the parameters of the stimulus isolator, and the delivery of the modified stimulation pulse through the plug mounted on the head of the rat. We sent concomitant pulses at opposite ends of the loop, and calculated the discrepancy between both signals after each iteration, for more than 100 successive cycles. The computed delays remained below 20 ms. Custom-developed C++ and TDT (Tucker-Davis Technologies) codes will be made available through material transfer agreement upon request to G.C.

3.5.9 Behavioral recordings

Behavioral conditions

Rats were recorded under two conditions. First, bipedal locomotion was recorded on a treadmill while the robotic bodyweight support system provided optimal support against the direction of gravity and prevented lateral falls. Second, quadrupedal locomotion was recorded along a straight runway with a flat surface, and along a staircase that combined a succession of 4 steps, as described previously [41]. All the experimental conditions within and between recording sessions were randomized.

Spatiotemporal neuromodulation in rats with complete SCI

Electrochemical stimulation protocols were selected based on an extensive amount of previous studies in rats with complete and incomplete SCI [31] [56]. The serotonergic replacement therapy used during training was administered systemically prior to testing. After a few minutes, monopolar electrical stimulation currents were delivered between relevant electrodes of the implants and an indifferent ground located subcutaneously. The intensity of electrical spinal cord stimulation was tuned (40 Hz, 20-200 μ A, biphasic rectangular pulses, 0.2 ms duration) to obtain optimal stepping visually. To optimize the timing of stimulation onset and end for each relevant electrode of the spinal implant, we performed a comprehensive mapping that linked the timing of stimulation with functional effects in rats with complete transection of the thoracic spinal cord. For each rat ($n = 5$), the duration of the gait cycle (800 ± 156 ms, SD) was normalized, and then divided into 10 equal bins that served as triggering events to turn the stimulation on or off. For electrodes targeting extensor versus flexor hotspots, the stimulation was turned on or off over the entire range of bins. A total of 10 steps were usually recorded for each electrode and bin. Temporal structure was optimized

Chapter 3. Spatiotemporal neuromodulation therapies engaging muscle synergies to improve motor control after spinal cord injury

based on the modulation of a few gait parameters that characterized the expected effects of the stimulation. The timing of the electrodes targeting the extensor hotspot was driven by the amplitude of ankle extensor muscle activity, the amount of vertical ground reaction forces, and the intensity and amount of foot acceleration at push off (Fig. S3.9). The timing of the electrodes targeting the flexor hotspot was driven by amplitude of flexor muscle activity, the amount of foot dragging, step height, and the intensity and orientation of foot acceleration at swing onset (Fig. S3.9). These parameters were weighted equally for identification of the optimal temporal structure for each hotspot. After optimization of the temporal structure, the ability of spatiotemporal neuromodulation to mediate superior facilitation of locomotion compared to continuous neuromodulation was tested in the same rats during bipedal locomotion on a treadmill. A total of 10 to 20 successive steps were recorded during continuous neuromodulation (40 Hz, 20-200 μ A, biphasic rectangular pulses, 0.2 ms duration) applied through electrodes located over the midline of spinal segments L2/L3 and S1 (conventional protocols), and through spatially selective electrodes located on the lateral aspect of the same segments. Locomotor performance was compared with neuromodulation applied through the same spatially selective lateral electrodes with the identified temporal structure. The amount of robot-assisted bodyweight support was maintained constant across conditions. The amplitude of stimulation was adjusted for each condition. The amplitudes optimal for spatiotemporal neuromodulation could not be used for continuous neuromodulation since these values led to diminished performances, and could occasionally block hindlimb movements. The maximum weight bearing capacities of each rat with contusion SCI was tested under continuous neuromodulation and spatiotemporal neuromodulation around 3 weeks post-SCI. From an optimal vertical weight support condition, the amount of assistance was decreased by 5% increments after each sequence of 10 successful steps, until the rats collapsed. Kinematic and muscle activity was recorded throughout these evaluations. The endurance of rats with contusion SCI was recorded on two different days that were randomized across animals, around 3 weeks post-SCI. From an optimal vertical weight support condition, rats stepped with continuous neuromodulation or spatiotemporal neuromodulation until they collapsed onto the treadmill. Concomitant kinematic recordings were used to measure the step height of each step. Rats with contusion SCI were evaluated during quadrupedal locomotion at 2 months post-SCI, when functional recovery had plateaued⁵. Rats performed 10 successive trials without stimulation with the serotonergic replacement therapy and spatiotemporal neuromodulation, both along the runway and staircases. Bilateral hindlimb and trunk kinematics were recorded during these trials. The percent of tumbles, touches, and passes over the steps was computed based on video recordings. Tumbles were defined as dragging throughout the execution over the step, whereas

touches characterized gait cycles during which the paw entered into contact with the steps but passed it successfully. The events were classified as “pass” when the paw had no contact with the step during the entire swing phase.

3.5.10 Statistics analysis

All the computed parameters were quantified and compared between tested groups, unless otherwise specified. Statistics were performed on averaged values per rat. All data are reported as mean values \pm SEM, unless specified otherwise. Significance was analyzed using paired Student's t-test, ANOVA or repeated measures ANOVA when data were distributed normally. Post.hoc comparisons were performed using the Kruskal-Wallis test. The non-parametric tests Mann-Whitney was used comparisons with less than 6 rats.

3.6 Supplementary videos

3.6.1 Video 1: Tailored spinal implant to achieve spatial selectivity.

This movie illustrates the spatial distribution of hindlimb motoneurons, the design of spatially selective spinal implant targeting specific subsets of dorsal roots, and the ability of stimulation delivered through this implant to elicit limb and direction specific motor responses.

3.6.2 Video 2: Spatiotemporal neuromodulation therapies after complete SCI.

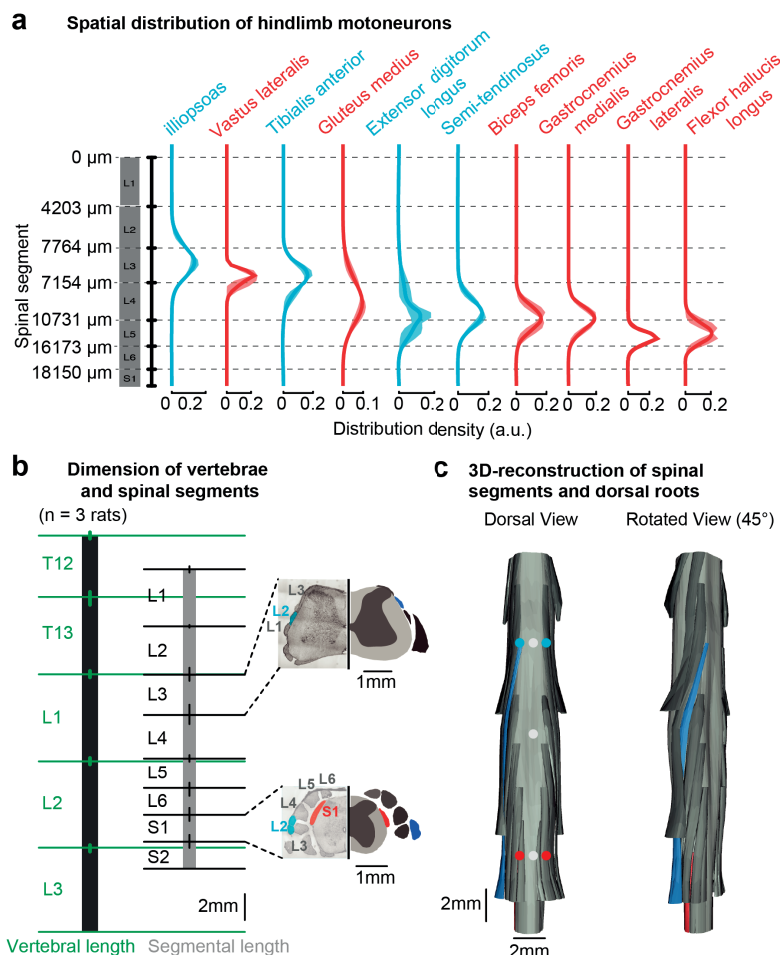
This movie shows the reconstructed spatiotemporal map of motoneuron activation during locomotion in intact rats, the online monitoring system, the complete SCI model, the ability of spatiotemporal neuromodulation to reproduce natural motoneuron activation dynamics during locomotion, and the tuning of extension versus flexion hotspots with increase in stimulation amplitude.

3.6.3 Video 3: Spatiotemporal neuromodulation improves motor control after clinically relevant SCI.

This movie shows the anatomical impact of the contusion SCI, the ability of spatiotemporal neuromodulation to enable robust locomotion early after the injury, and the ability of spatiotemporal neuromodulation to enable locomotion overground and along a staircase in the chronic stage of the SCI.

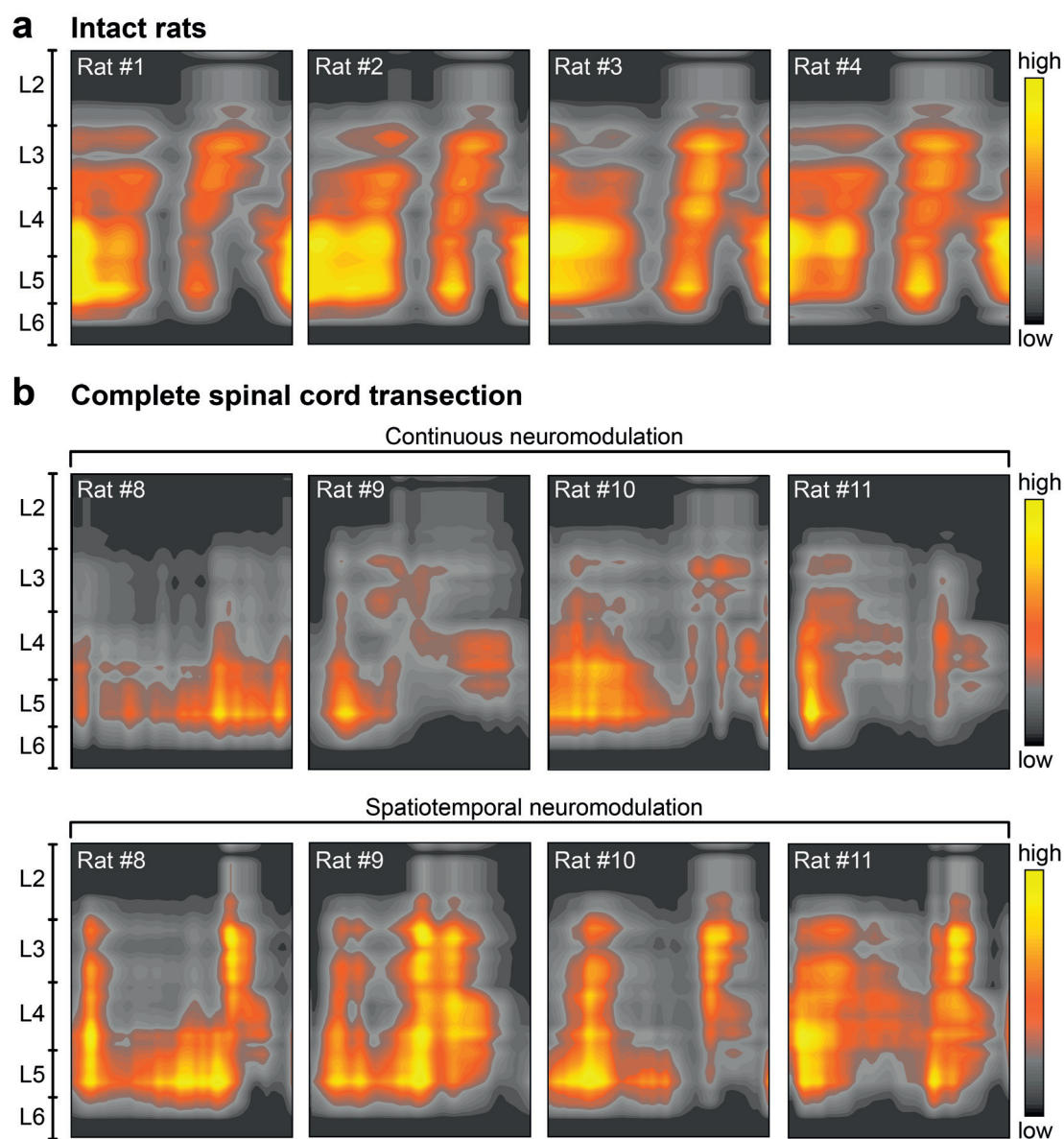
Videos are available on Nature website: <https://www.nature.com>

3.7 Supplementary figures



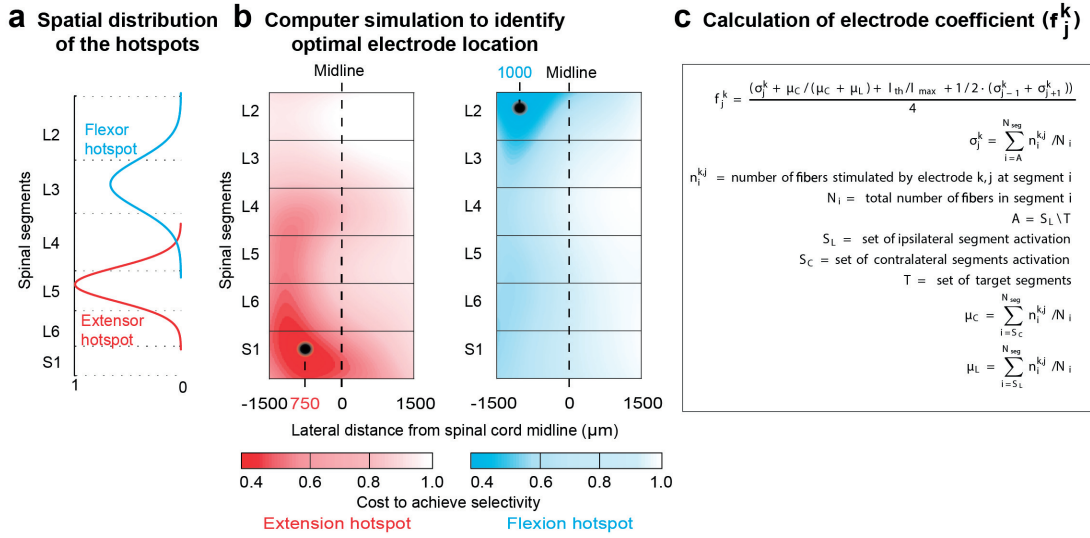
Supplementary Figure S3.1 – Spatial distribution of hindlimb motoneurons and 3D reconstruction of vertebrae, spinal cord and dorsal roots in Lewis rats. (a) Plots reporting the relative spatial distribution of motoneuron density along the rostrocaudal extent of lumbosacral segments for each traced muscle. Each distribution is the average (\pm SEM) of motoneuron densities calculated for 2 to 3 rats per muscle. The density is normalized to the total number of detected motoneurons for each muscle and rat, which corresponds to 1. (b) Quantification of the length of vertebra T12 to L3–L4, and of spinal segments L1 to S1 in three rats. The vertical bars on each diagram indicate the standard deviation of measurements across rats. The photographs show coronal views of the entire half of the spinal cord, including the dura mater, dorsal roots, and spinal tissue. The complementary views show camera Lucida reconstructions of the white and grey matter, and of the dorsal roots. Coronal sections were extracted from spinal segments L3 and S1. The dorsal roots projecting to L2 and S1 spinal segments are color-coded to visualize their respective location. (c) 3D reconstruction of the entire lumbosacral spinal cord and dorsal roots. The dorsal roots innervating L2 and S1 spinal segments are color-coded to help visualizing their respective spatial trajectory. The 3D reconstructions are displayed from a dorsal view, and from a view that is rotated by 45° leftward around the rostrocaudal axis in order to visualize the trajectory of the dorsal roots along spinal segments. The color-coded dots indicate the locations of electrodes targeting extensor and flexor hotspots through the recruitment of dorsal roots.

Chapter 3. Spatiotemporal neuromodulation therapies engaging muscle synergies to improve motor control after spinal cord injury



Supplementary Figure S3.2 – Spatiotemporal maps of motoneuron activation (a) Spatiotemporal map of motoneuron activation recorded in four intact rats. (b) Spatiotemporal map of motoneuron activation recorded in four rats with complete SCI during continuous versus spatiotemporal neuromodulation.

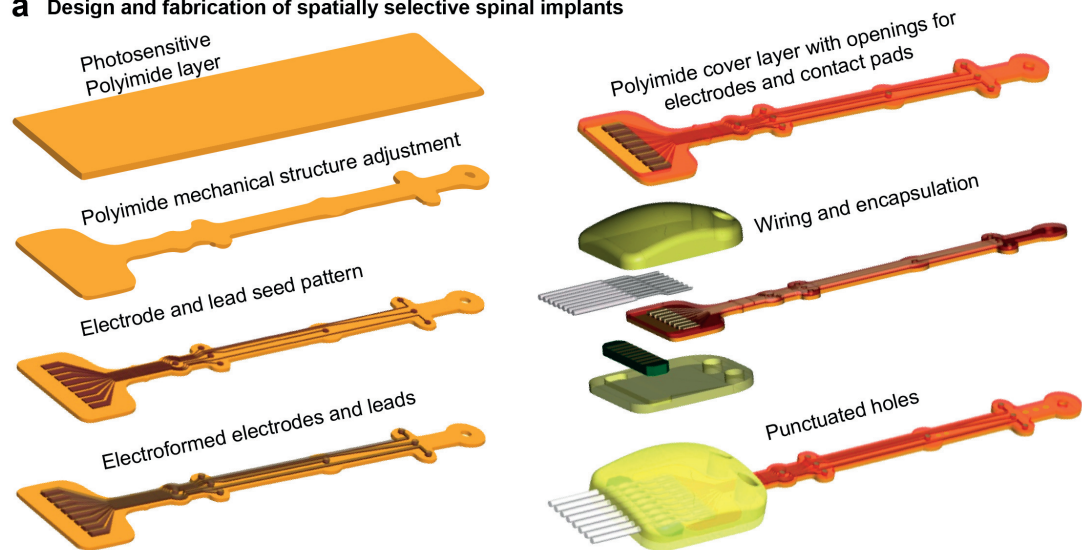
function-01.png function-01.png



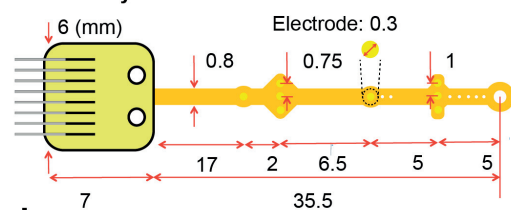
Supplementary Figure S3.3 – Computer simulations to identify optimal electrode locations to target extensor versus flexor hotspots (a) Spatial distribution of extensor and flexor motoneuron activation profiles along the rostrocaudal extent of lumbar segments. The spatial distribution was extracted using a Gaussian clustering algorithm applied on spatiotemporal maps of motoneuron activation during gait (Fig. 3.1). (b) Equations describing the optimization algorithm that calculated the cost to activate a given spinal segment, while minimizing activation of other segments. The cost function combined 4 optimization factors: (i) stimulation specificity for the targeted segments; (ii) ipsilateral vs. contralateral specificity; (iii) minimum threshold; and (iv) specificity of neighboring sites. The targeted activation of each segment was defined by the spatial distribution of extensor- and flexor-related motoneuron activation profiles displayed in (a). The color-coded maps report the computed cost to preferentially activate extensor versus flexor hotspots on one side of the spinal cord. Implants were designed with electrodes located at the mediolateral and rostrocaudal positions where the cost reached a local minimum, as highlighted by the black circles.

Chapter 3. Spatiotemporal neuromodulation therapies engaging muscle synergies to improve motor control after spinal cord injury

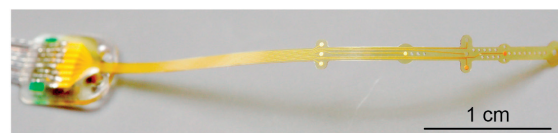
a Design and fabrication of spatially selective spinal implants



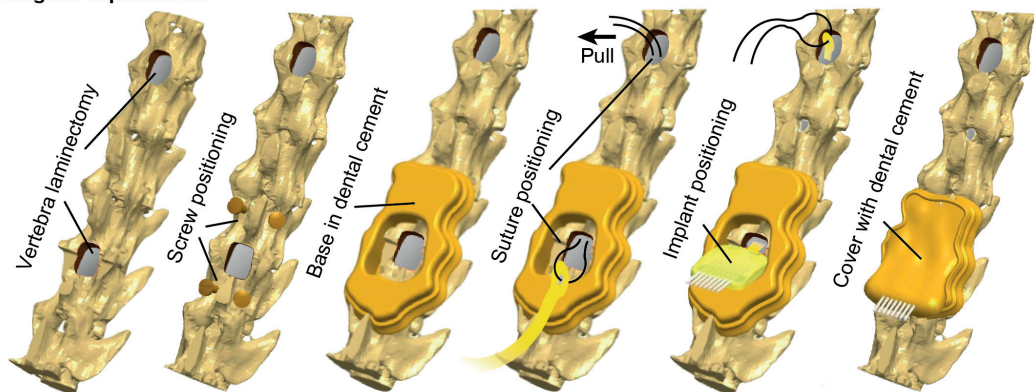
b Mask layout



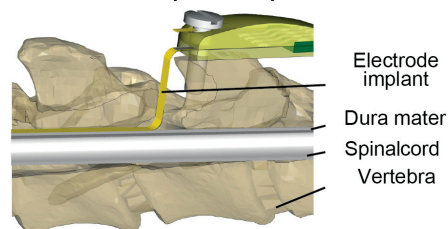
c Final spinal implant with connector



d Surgical implantation



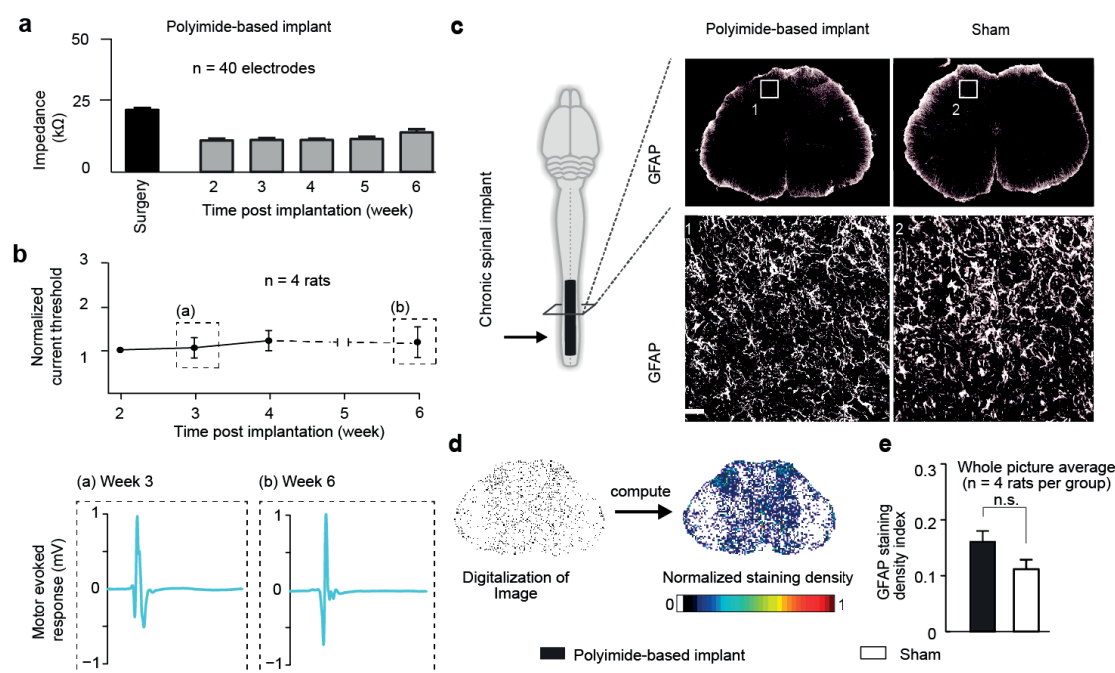
Vertebral orthosis for epidural implantation in rat



3.7. Supplementary figures

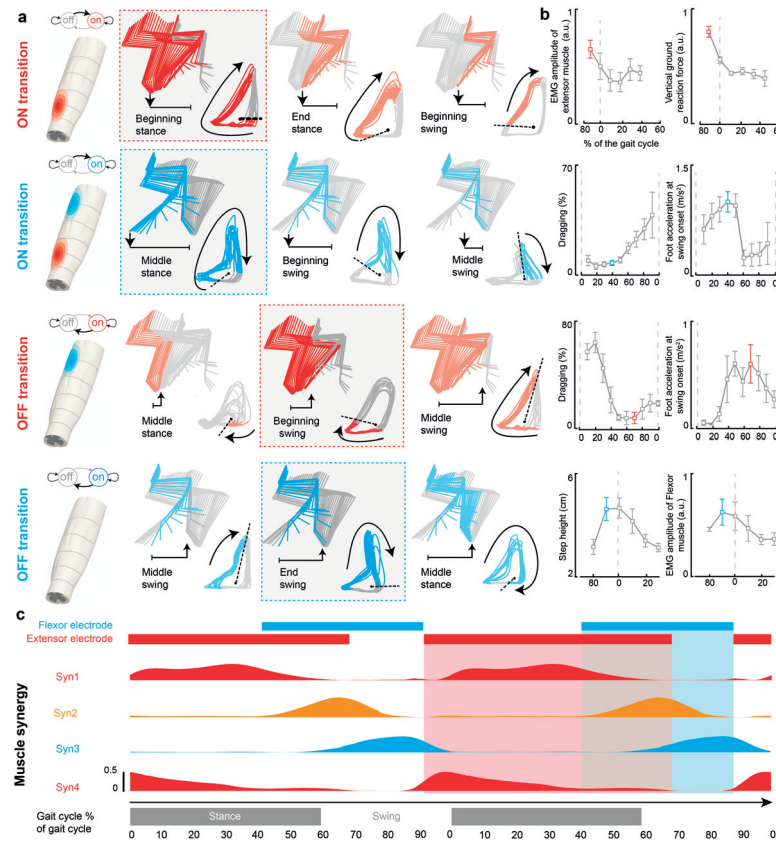
Supplementary Figure S3.4 – Design, fabrication and surgical procedures of spatially selective spinal implants. (a) Processing starts with deposition of a 20 μm thick Polyimide film by spin coating on the silicon substrate. The Polyimide-based bottom layer constituting the footprint of the implant is realized through ultra-violet lithography. A 200 nm thick gold layer is deposited using vacuum evaporation and lithographically structured to create a conductive seed pattern. An additional gold layer is electroplated to a height of approximately 6 μm to create the electrodes and interconnects. A 20 μm cover layer of photosensitive Polyimide is then applied by spin coating to uniformly cover the bottom and electrode structure. A final ultra-violet lithography is applied to structure the top layer of the implant, and to create openings over the electrodes and contact pads. The implants are gently released from the carrier wafer. To create a connector, the contact pads located at the extremity of the implant are glued to a small support plate made of medical grade PMMA sheet material. Precision milled alignment structures allow fine adjustment of the support plate to the polyimide-based spinal implant, and to the extremity of the leads. The support plate contained a seat in which a tiny printed circuit board (PCB) with conductive stripes is fixed. Stainless steel leads with silicone rubber insulation are directly soldered to the contact pads of the implant via the contact stripes located on the PCB. The resulting implants and connective leads were highly reliable mechanically and electrically. Finally, the entire contact area was covered with a ultra-violet curable, methacrylate-based resin that provides tight sealing. For improved bio- integration, the contact interface is over-moulded with a thin layer of medical grade silicone. (b) Electrode layout and dimensions (mm) of the implants. (c) Photograph showing the final fabrication of the spinal implants.

Chapter 3. Spatiotemporal neuromodulation therapies engaging muscle synergies to improve motor control after spinal cord injury



Supplementary Figure S3.5 – Long-term functionality and bio-integration of epidural spinal implants
(a) Histogram plots reporting changes in the mean values of electrode impedance of polyimide-based epidural spinal implants in rats. The impedance was measured for all the electrodes of the implants in the same rats during the surgical implantation, and on a weekly basis during the subsequent weeks. (b) Plots reporting the normalized current threshold necessary to elicit motor evoked responses in the tibialis anterior muscle with a single pulse of electrical stimulation (0.5 ms, 0.1 Hz) delivered through the same electrode over several weeks post implantation. Measurements could not be obtained on week 5 due to technical problems. The windows display motor evoked responses recorded in the tibialis anterior muscle at week 3 and week 6 post- implantation when delivering stimulation at 150 μ A through the same electrode of the spinal implant. (c) Rats (n = 4 per group) were sacrificed 8 weeks after the surgical insertion of Polyimide-based spinal implants over the epidural surface of lumbosacral segments. Representative confocal images of the L4 spinal segment (middle of implant) stained for the neuro-inflammatory marker GFAP (reactive astrocytes) are shown for the implanted and sham rats. Scale bars, 500 μ m and 40 μ m for the overviews and insets, respectively. (d) Images were digitalized, color-filtered, and binarized by means of an intensity threshold that was maintained constant across sections and rats. Images were divided into square regions of interest (ROI), and GFAP densities were computed within each ROI. (e) Histogram plots reporting the mean and SEM values of computed GFAP density for rats with spinal implants and sham rats. Spinal implants had a negligible impact on the inflammatory environment of spinal tissue located underneath the implant. n.s. = non-significant.

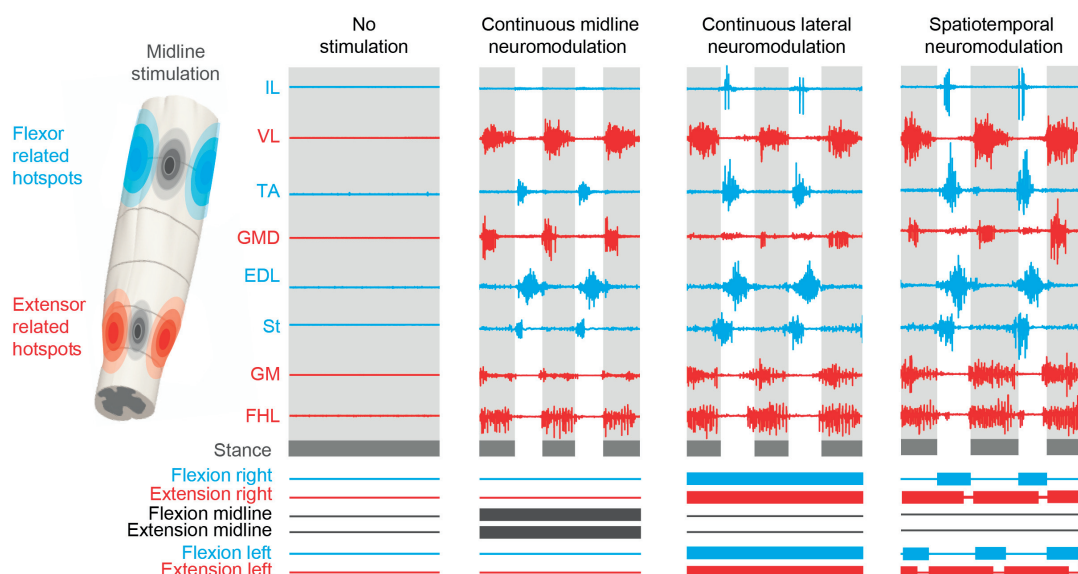
3.7. Supplementary figures



Supplementary Figure S3.6 – Experiments to identify optimal temporal structure (a) Experiments were performed in rats with complete SCI. A serotonergic replacement therapy was administered 10 min prior to experiments. Rats stepped bipedally on a treadmill while neuromodulation (40 Hz, 0.2 ms, 100-200 μ A) was delivered through the electrodes targeting extensor versus flexor hotspots on one side. The spinal cord diagrams illustrate the intended activation or inactivation of a given hotspot. The lines with an arrowhead indicate the onset (beginning of line) and end (arrowhead) of the stimulation. The arrowhead highlights the timing of the transition between states represented in each panel. A stick diagram decomposition of hindlimb movements during a complete gait cycle is displayed for 3 selected triggering times per transition state. The successive ($n = 10$ steps) trajectories of the hindlimb endpoint are also reported. Both stick diagrams and hindlimb endpoint trajectories are colored when the state of the tested electrode is ON. The dotted line indicates the angular value that triggered the transition between ON/OFF states, reported as percent of the gait cycle duration. The shaded background highlights the optimal triggering time, defined from combinations of parameters (see Methods). (b) Plots reporting the mean values (10 steps per data point, $n = 5$ rats) of relevant gait parameters related to extension or flexion across the entire range of tested triggering times. For each rat, the normalized gait cycle duration was divided into 10 bins of equal durations, reported along the x-axis as percent of cycle duration. The triggering times leading to optimal gait parameters are colored in red and blue for electrodes targeting extensor and flexor hotspots, respectively. (c) Diagram reporting the optimal temporal structure to deliver stimulation through the electrodes targeting extensor versus flexor hotspots in order to facilitate locomotion. The temporal activation profiles of muscle synergies are displayed at the bottom to emphasize the coincidence between the optimal temporal structure of stimulation and the activation of muscle synergies. Note that the optimal temporal structure involved co-activation of electrodes targeting the extensor and flexor hotspots at the stance to swing transition, which coincided with the activation of synergy 3 combining extensor and flexor motoneurons (see Fig. 3.1). The lower bar indicates the division of gait into bins of equal durations that defined the relative timing to triggering events.

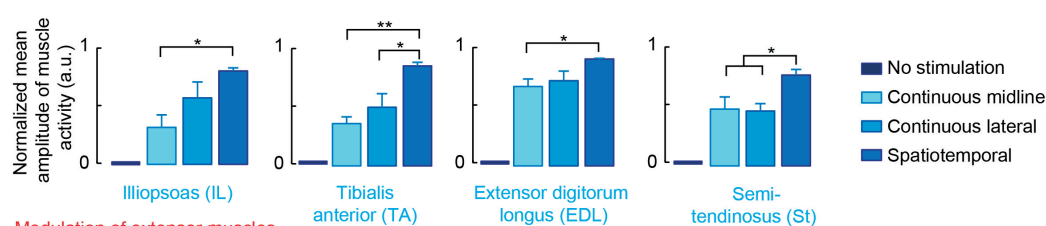
Chapter 3. Spatiotemporal neuromodulation therapies engaging muscle synergies to improve motor control after spinal cord injury

a Muscle activity during locomotion under different neuromodulation conditions



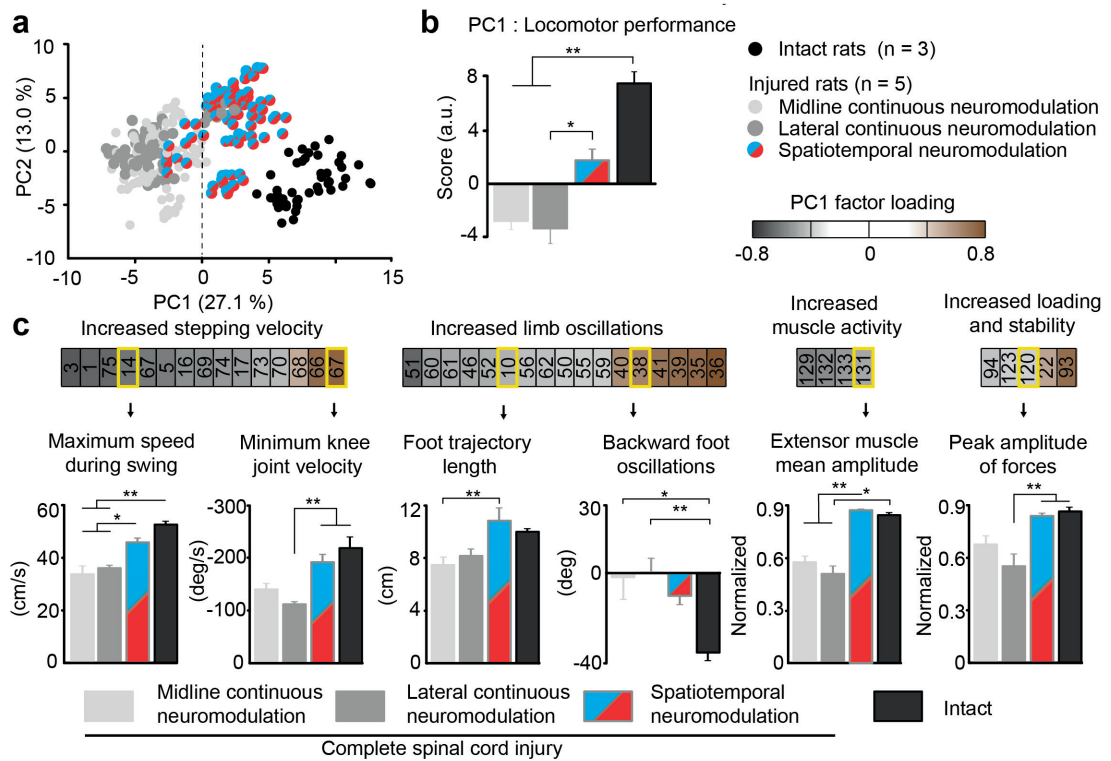
b Quantification of muscle activity

Modulation of flexor muscles



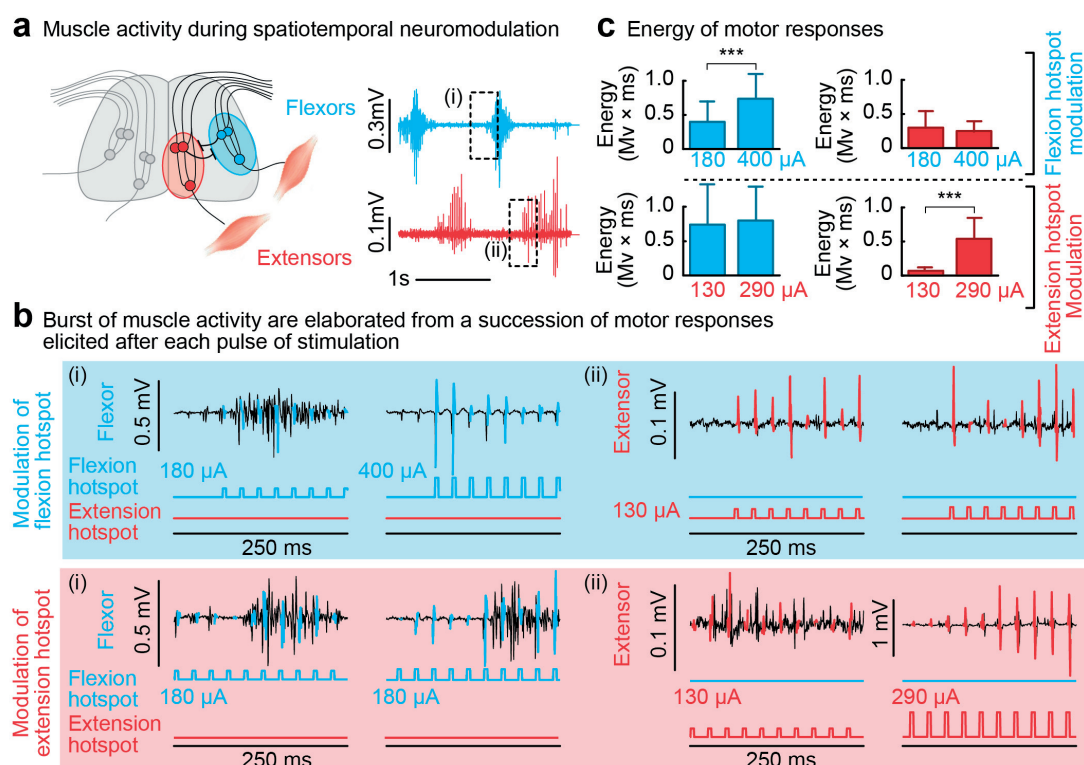
Supplementary Figure S3.7 – Changes in hindlimb muscle activity across conditions of neuromodulation (a) Electromyographic activity recorded from pairs of antagonist muscles spanning each hindlimb joint without stimulation (paralysis), during locomotion under continuous neuromodulation applied over the midline of lumbar and sacral segments, during continuous neuromodulation delivered through all the four lateral electrodes targeting extensor and flexor hotspots on the left and right sides, and during spatiotemporal neuromodulation through the lateral electrodes using the temporal structure identified in Fig. S3.9. The recordings were obtained on the same day. The horizontal bars at the bottom (blue, red, black) indicate the On/Off state of each electrode, which is controlled in real-time. Experimental conditions and conventions are the same as in Fig. 3.4. (b) Histogram plots reporting the mean ($n = 4$ rats, except $n = 5$ rats for MG and TA muscles) amplitude of each muscle burst during each experimental condition. The mean amplitude of EMG activity was normalized to the maximum value recorded during locomotion in each rat. **, $p < 0.05$; ***, $p < 0.01$.

3.7. Supplementary figures

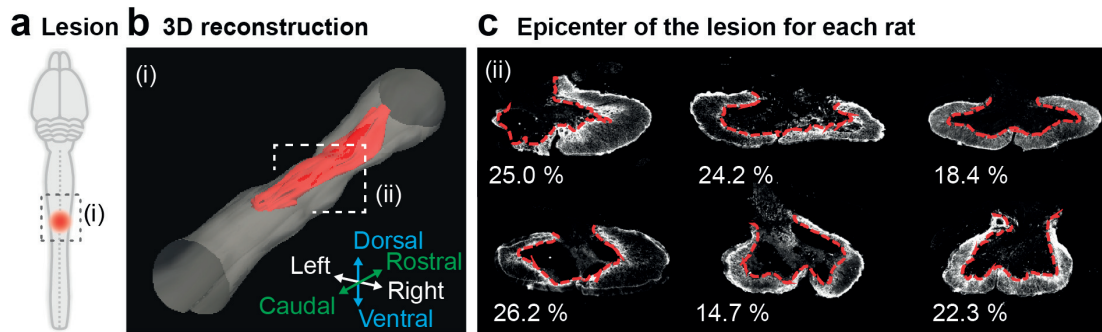


*Supplementary Figure S3.8 – Quantification of gait patterns in rats with complete SCI (a) A total of 137 parameters providing comprehensive gait quantification (Supplementary Table 1) were computed from kinematic, kinetic, and muscle activity recordings. Principal component (PC) analysis was applied on all the computed parameters for all the gait cycles under each experimental condition. Experimental conditions are the same as in Fig. 3.4. The analyzed gait cycles are represented by individual dots in the new 2D space created by PC1-2, which explained more than 40% of the total data variance. The histogram plots report the mean values of scores on PC1, which quantified the degree of difference between gait patterns of intact and injured rats during locomotion under the various experimental conditions. Scores on PC1 are thus related to locomotor performance. This analysis demonstrated significant improvement of locomotor performance during spatiotemporal neuromodulation compared to continuous neuromodulation applied over the midline, or through lateral electrodes targeting extensor versus flexor hotspots. (b) To identify the specific features that improved during spatiotemporal neuromodulation, the parameters correlating with PC1 (factor loadings) were extracted and regrouped them into functional clusters, which are named for clarity. The numbers refer to parameters described in Supplementary Table 1. (c) The histogram plots report the mean (n = 5 rats) values of parameters with high factor loadings on PC1 for each of the identified functional clusters. Error bars, SEM. *, $p < 0.05$; **, $p < 0.01$; ***, $p < 0.001$.*

Chapter 3. Spatiotemporal neuromodulation therapies engaging muscle synergies to improve motor control after spinal cord injury

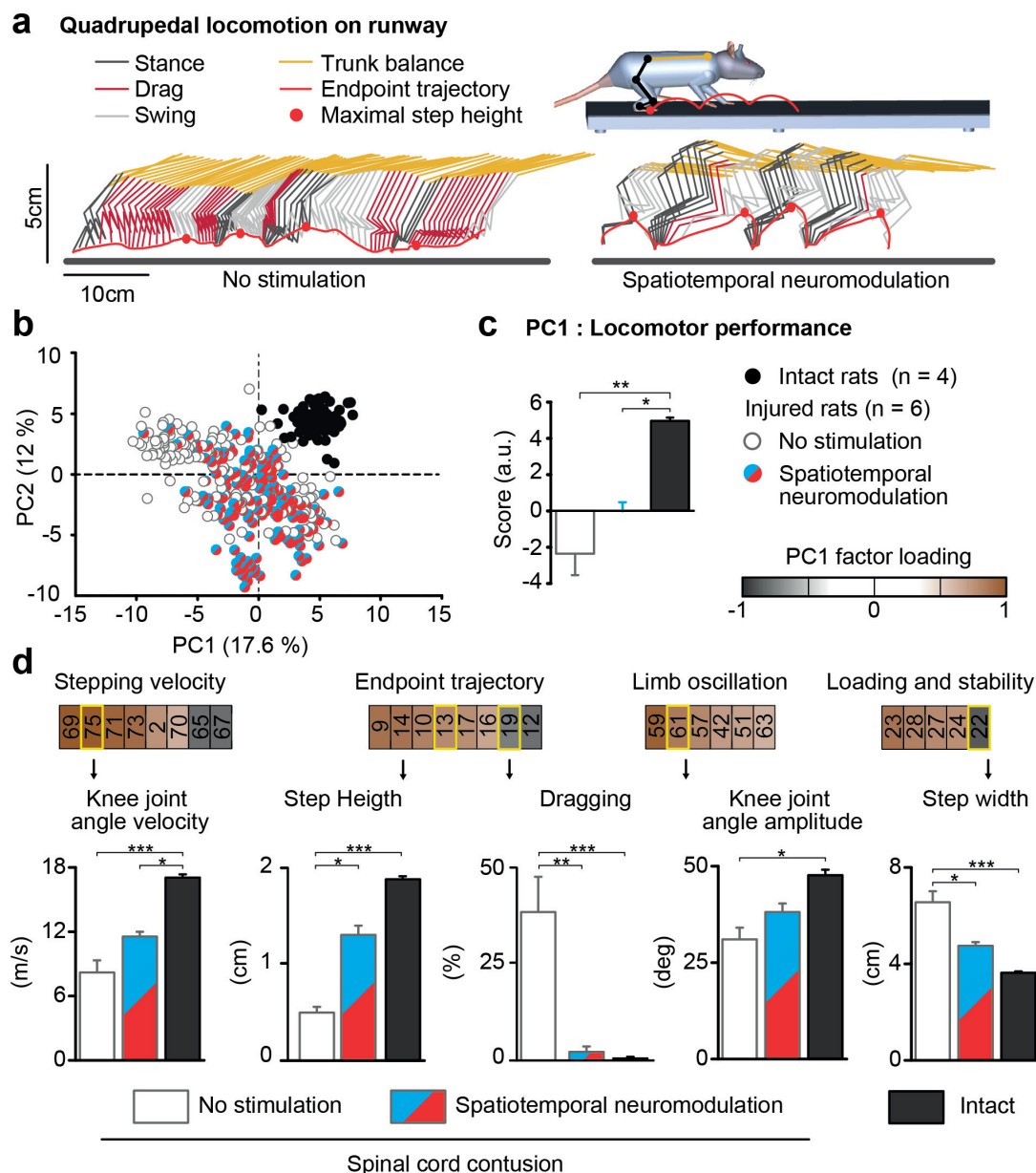


Supplementary Figure S3.9 – Modulation of motor responses during increase in stimulation amplitude (a) The diagram shows the proprioceptive feedback circuits that are thought to be recruited by epidural electrical stimulation. Electromyographic activity of flexor and extensor ankle muscles is shown for two successive steps performed under spatiotemporal neuromodulation. The dashed rectangles (i) and (ii) highlight the temporal window over which the muscle activity is displayed in panel (b). (b) Extensor and flexor muscle activity recorded with two levels of stimulation amplitudes for the electrode targeting the extensor versus flexor hotspot. Motor responses resulting from each stimulation pulse, indicated below each trace, are shown in color. (c) Histogram plots reporting the mean energy of motor responses in flexors and extensors muscles for the different experimental conditions. Energy was calculated as the square root of the second power of the signal, which was integrated over 2 ms. Bars show the median and 75% of the distribution. Non-parametric ANOVA statistical test was applied over 3000 responses. ***, $p < 0.001$.



Supplementary Figure S3.10 – Quantification of spared tissue in rats with contusion SCI. (a) Diagram illustrating the contusion SCI at the mid-thoracic level. (b) 3D reconstruction of a lesion cavity. (c) Photograph of coronal spinal cord sections taken at the lesion epicenter for each experimental rat. The tissues are stained against GFAP (reactive astrocyte) in order to delimitate the border between the lesioned and healthy tissues, shown with the red dashed lines. The calculated percent of tissue sparing is reported for each rat.

Chapter 3. Spatiotemporal neuromodulation therapies engaging muscle synergies to improve motor control after spinal cord injury



Supplementary Figure S3.11 – Quantification of locomotor performance during quadrupedal locomotion. (a) Stick diagram decomposition of hindlimb and trunk movements together with hindlimb endpoint trajectory during quadrupedal locomotion without stimulation and under spatiotemporal neuromodulation. Rats were recorded 2 months after the contusion SCI, when recovery had plateaued. (b) A PC analysis was applied using same methods as those described in Fig. S3.11, and displayed with the same convention as in this figure. Error bars, SEM. *, $p < 0.05$; **, $p < 0.01$; ***, $p < 0.001$.

3.7. Supplementary figures

KINEMATIC VARIABLES					
Temporal features					
	1	Cycle duration		84	Correlation between hip and knee oscillations
	2	Cycle velocity		85	Correlation between knee and ankle oscillations
	3	Stance duration	Cross-correlation	86	Correlation between ankle and MTP oscillations
	4	Swing duration		87	Temporal lag between backward positions of crest and thigh oscillations
	5	Relative stance duration (percent of the cycle duration)		88	Temporal lag between forward positions of crest and thigh oscillations
				89	Temporal lag between backward positions of thigh and leg oscillations
Limb endpoint (Metatarsal phalange) trajectory			Relative coupling	90	Temporal lag between forward positions of the thigh and leg oscillations
	6	Interlimb temporal coupling		91	Temporal lag between backward positions of leg and foot oscillations
	7	Duration of double stance phase		92	Temporal lag between forward positions of leg and foot oscillations
	8	Stride length		93	Lag of the cross correlation function between hindlimb oscillations
	9	Step length	Inter-segmental coordination compared to	94	Maximum R-value of the cross correlation function between hindlimb oscillations
	10	3D limb endpoint path length		95	Lag of the cross correlation function between hip oscillations
	11	Maximum backward position	Able-bodied rats	96	Maximum R-value of the cross correlation function between hip oscillations
	12	Minimum forward position		97	Lag of the cross correlation function between knee oscillations
	13	Step height		98	Maximum R-value of the cross correlation function between knee oscillations
	14	Maximum speed during swing		99	Lag of the cross correlation function between ankle oscillations
	15	Relative timing of maximum velocity during swing		100	Maximum R-value of the cross correlation function between ankle oscillations
	16	Acceleration at swing onset		101	Lag of the cross correlation function between endpoint oscillations
	17	Average endpoint velocity		102	Maximum R-value of the cross correlation function between endpoint oscillations
	18	Orientation of the velocity vector at swing onset		103	Phase of the first harmonic of the FFT of the hip elevation angle
	19	Dragging		104	Amplitude of the first harmonic of the FFT of the hip elevation angle
	20	Relative dragging duration (percent of swing duration)		105	Phase of the first harmonic of the FFT of the knee elevation angle
				106	Amplitude of the first harmonic of the FFT of the knee elevation angle
				107	Phase of the first harmonic of the FFT of the ankle elevation angle
				108	Amplitude of the first harmonic of the FFT of the ankle elevation angle
Stability			Left-right hindlimb coordination	109	Phase of the first harmonic of the FFT of the endpoint elevation angle
Base of support	21	Positioning of the foot at stance onset with respect to the pelvis		110	Amplitude of the first harmonic of the FFT of the endpoint elevation angle
	22	Stance width		111	Phase of the first harmonic of the FFT of the hindlimb elevation angle
Trunk and pelvic position and oscillations	23	Maximum hip sagittal position		112	Amplitude of the first harmonic of the FFT of the hindlimb elevation angle
	24	Minimum hip sagittal position	Hindlimb coordination	113	Lag of the cross correlation function between crest and thigh limb elevation angles
	25	Amplitude of sagittal hip oscillations		114	Lag of the cross correlation function between thigh and hindlimb elevation angles
	26	Variability of sagittal crest position		115	Lag of the cross correlation function between hip and thigh elevation angles
	27	Variability of sagittal crest velocity		116	Lag of the cross correlation function between hindlimb and foot elevation angles
	28	Variability of vertical hip movement		117	Lag of the cross correlation function between thigh and ankle elevation angles
	29	Variability of sagittal hip movement		118	Lag of the cross correlation function between ankle and foot elevation angles
	30	Variability of the 3D hip oscillations			
	31	Length of pelvis displacements in the forward direction			
	32	Length of pelvis displacements in the medio-lateral direction			
	33	Length of pelvis displacements in the vertical direction			
	34	Length of pelvis displacements in all directions			
Joint angles and segmental oscillations			KINETIC VARIABLES		
Backward	35	Crest oscillations		119	Mean amplitude of vertical forces (normalized to maximum value)
	36	Thigh oscillations		120	Peak amplitude of vertical forces (normalized to maximum value)
	37	Leg oscillations		121	Peak to peak amplitude of vertical forces (normalized to maximum value)
	38	Foot oscillations		122	Root mean square of vertical forces (normalized to maximum value)
Forward	39	Whole limb oscillations		123	Integral of vertical forces (normalized to maximum value)
	40	Crest oscillations		124	Weight-bearing level
	41	Thigh oscillations			
	42	Leg oscillations			
Flexion	43	Foot oscillations	MUSCLE ACTIVITY VARIABLES		
	44	Whole limb oscillations	Timing (relative to cycle duration, paw contact to paw contact)		
	45	Hip joint angle	Extensor	125	Relative onset of ipsilateral extensor muscle activity burst
	46	Knee joint angle		126	Relative end of ipsilateral extensor muscle activity burst
Abduction	47	Ankle joint angle		127	Relative onset of ipsilateral flexor muscle activity burst
	48	Whole limb abduction	Flexor	128	Relative end of ipsilateral flexor muscle activity burst
	49	Foot abduction			
	50	Hip joint angle	Duration		
Extension	51	Knee joint angle	Extensor	129	Duration of ipsilateral extensor muscle activity burst
	52	Ankle joint angle	Flexor	130	Duration of ipsilateral flexor muscle activity burst
	53	Whole limb adduction	Amplitude		
	54	Foot adduction	Extensor	131	Mean amplitude of ipsilateral muscle activity burst
Adduction	55	Crest oscillations		132	Integral of ipsilateral extensor muscle activity burst
	56	Thigh oscillations		133	Root mean square of ipsilateral extensor muscle activity burst
	57	Leg oscillations		134	Mean amplitude of ipsilateral flexor muscle activity burst
	58	Foot oscillations		135	Integral of ipsilateral flexor muscle activity burst
Amplitude	59	Whole limb oscillations	Flexor	136	Root mean square of ipsilateral flexor muscle activity burst
	60	Hip joint angle			
	61	Knee joint angle			
	62	Ankle joint angle			
Velocity	63	Whole limb medio-lateral oscillations	Muscle coactivation	137	Co-contraction of flexor and extensor muscle
	64	Foot abduction/adduction			
	65	Whole limb oscillation velocity			
	66	Hip joint angle velocity			
Minimum	67	Knee joint angle velocity			
	68	Ankle joint angle velocity			
	69	Whole limb oscillation velocity			
	70	Hip joint angle velocity			
Maximum	71	Knee joint angle velocity			
	72	Ankle joint angle velocity			
	73	Whole limb angle velocity			
	74	Hip joint angle velocity			
Amplitude	75	Knee joint angle velocity			
	76	Ankle joint angle velocity			
Inter-limb coordination					
PC analysis	77	Degree of linear coupling between joint oscillations			
FFT	78	Temporal coupling between crest and thigh oscillations			
decomposition	79	Temporal coupling between thigh and leg oscillations			
	80	Temporal coupling between leg and foot oscillations			
	81	Correlation between crest and thigh oscillations			
	82	Correlation between thigh and leg oscillations			
	83	Correlation between leg and foot oscillations			

Supplementary Figure S3.12 – Computed kinematic, kinetic, and muscle activity parameters

A brain-spinal interface alleviating gait deficits after spinal cord injury in primates

Marco Capogrosso^{1,2,*}, Tomislav Milekovic^{1,*}, David Borton^{1,3,*}, Fabien Wagner^{1,£}, Eduardo Martin Moraud^{2,£}, Jean-Baptiste Mignardot¹, Nicolas Buse⁴, Jerome Gandar¹, Quentin Barraud¹, David Xing³, Elodie Rey¹, Simone Duis¹, Yang Jianzhong⁵, Wai Kin D. Ko⁵, Qin Li^{5,6}, Peter Detemple⁶, Tim Denison⁴, Silvestro Micera^{2,8}, Erwan Bezard^{5,6,9,10}, Jocelyne Bloch¹¹ & Grégoire Courtine^{1,11}

Nature, 2016

1. International foundation for Research in Paraplegia chair in Spinal Cord Repair, Center for Neuroprosthetics and Brain Mind Institute, School of Life Sciences, Swiss Federal Institute of Technology (EPFL), Lausanne, Switzerland
2. Bertarelli Foundation Chair in Translational Neuroengineering, Center for Neuroprosthetics and Institute of Bioengineering, School of Bioengineering, EPFL, Lausanne, Switzerland
3. School of Engineering, Brown University Providence, USA
4. Medtronic, Minneapolis, USA
5. Motac neuroscience Ltd, Manchester, UK
6. Institute of Lab Animal Sciences, China Academy of Medical Sciences, Beijing, China
7. Fraunhofer ICT-IMM, Mainz, Germany
8. The BioRobotics Institute, Scuola Superiore Sant'Anna, Pisa, Italy
9. University of Bordeaux, Institut des Maladies Neurodégénératives, UMR 5293, Bordeaux, France
10. CNRS, Institut des Maladies Neurodégénératives, UMR 5293, Bordeaux, France
11. Centre Hospitalier Universitaire Vaudois (CHUV), Lausanne, Switzerland

*, £ : contributed equally to this work

4.1 Abstract

Spinal cord injury disrupts the communication between the brain and the spinal circuits that orchestrate movement. To bypass the lesion, brain–computer interfaces [105] [61] [62] have directly linked cortical activity to electrical stimulation of muscles, which have restored grasping abilities after hand paralysis [105] [106]. Theoretically, this strategy could also restore control over leg muscle activity for walking [107]. However, replicating the complex sequence of individual muscle activation patterns underlying natural and adaptive locomotor movements poses formidable conceptual and technological challenges [108] [109]. Recently, we showed in rats that epidural electrical stimulation of the lumbar spinal cord can reproduce the natural activation of synergistic muscle groups producing locomotion [56] [110] [111]. Here, we interfaced leg motor cortex activity with epidural electrical stimulation protocols to establish a brain–spinal interface that alleviated gait deficits after a spinal cord injury in nonhuman primates. Rhesus monkeys were implanted with an intracortical microelectrode array into the leg area of motor cortex; and a spinal cord stimulation system composed of a spatially selective epidural implant and a pulse generator with real-time triggering capabilities. We designed and implemented wireless control systems that linked online neural decoding of extension and flexion motor states with stimulation protocols promoting these movements. These systems allowed the monkeys to behave freely without any restrictions or constraining tethered electronics. After validation of the brain–spinal interface in intact monkeys, we performed a unilateral corticospinal tract lesion at the thoracic level. As early as six days post-injury and without prior training of the monkeys, the brain–spinal interface restored weight-bearing locomotion of the paralyzed leg on a treadmill and overground. The implantable components integrated in the brain–spinal interface have all been approved for investigational applications in similar human research, suggesting a practical translational pathway for proof-of-concept studies in people with spinal cord injury.

Publication contributions

In this study, I implemented the real-time control software to connect the brain decoding to an implantable pulse generator. I helped to improve the firmware inside the Medtronic device. I participated to experiments to validate the communication between hardwares and softwares involved in the loop. I performed computerized tomography scans for 3D vertebrae reconstructions and participated to figures regarding the implant design.

4.2 Introduction

A century of research in spinal cord physiology has demonstrated that the circuits embedded in lumbar segments of mammals can produce coordinated patterns of leg motor activity without brain input [6] [112]. Various neuromodulation approaches have been developed to activate these circuits after injury to reestablish locomotion [56] [67] [69] [70] [74] [66]. For example, epidural electrical stimulation (EES) of lumbar segments restored adaptive locomotion in paralyzed rats[56]. Recent studies showed that EES is also capable of activating lumbar spinal circuits in people with paraplegia [69] [74]. These empirical observations prompted us to develop an evidenced-based framework to understand the interactions between EES and spinal circuits [56] [110] [111]. We aimed to exploit this knowledge to optimize stimulation protocols for clinical applications. Computational modelling and functional experiments revealed that EES engages spinal circuits through the modulation of proprioceptive feedback circuits [111]. This framework guided the design of spatiotemporal neuromodulation therapies that not only activate but also control the activity of spinal circuits engaging synergistic muscle groups [56] [110] [111], enabling robust modulation of locomotor movements in rats whose spinal cords were void of brain input. However, volitional locomotion requires the brain to control the activity of spinal circuits. Brain–computer interface technologies [105] [61] [62] [106] [113] provide the tools to link the intended motor states to EES protocols [63] [114] [115] to reestablish voluntary control of locomotion after injury. For these developments, nonhuman primates are more appropriate models than rodents since they exhibit cortical engagement during locomotion similar to humans [60], analogous recovery mechanisms from injury[59], and comparable technological requirements [57]. Here, we decoded motor states from leg motor cortex activity to trigger EES protocols facilitating extension and flexion of the corresponding leg. We show that this brain–spinal interface alleviated gait deficits after spinal cord injury in nonhuman primates.

4.3 Results

To support the development of the brain–spinal interface, we established a wireless recording and stimulation platform in freely behaving, unconstrained and untethered nonhuman primates (Fig.4.1 and Supplementary Video 1). Rhesus monkeys (Supplementary Table S4.11) were implanted with a microelectrode array into the leg area of the left motor cortex to record spiking activity from neuronal ensembles. Electromyographic signals were monitored using bipolar electrodes implanted into antagonist muscles spanning each joint of the right leg. Wireless modules enabled transmission of neural (20kHz) and electromyographic (2kHz) signals to external receivers [64].

Chapter 4. A brain-spinal interface alleviating gait deficits after spinal cord injury in primates

We simultaneously acquired video recordings (100Hz) to reconstruct whole-body kinematics [59]. To deliver EES, we used technologies previously developed in rats [110], which we adapted to the characteristics of spinal segments and vertebrae measured in three monkeys (Extended Data Fig.S4.1). These spinal implants were inserted into the epidural space over lumbar segments, and connected to an implantable pulse generator commonly used for deep brain stimulation therapy. We engineered wireless communication modules that enabled control over the spatial and temporal parameters of EES with a latency of about 100ms (Extended Data Fig.S4.2).

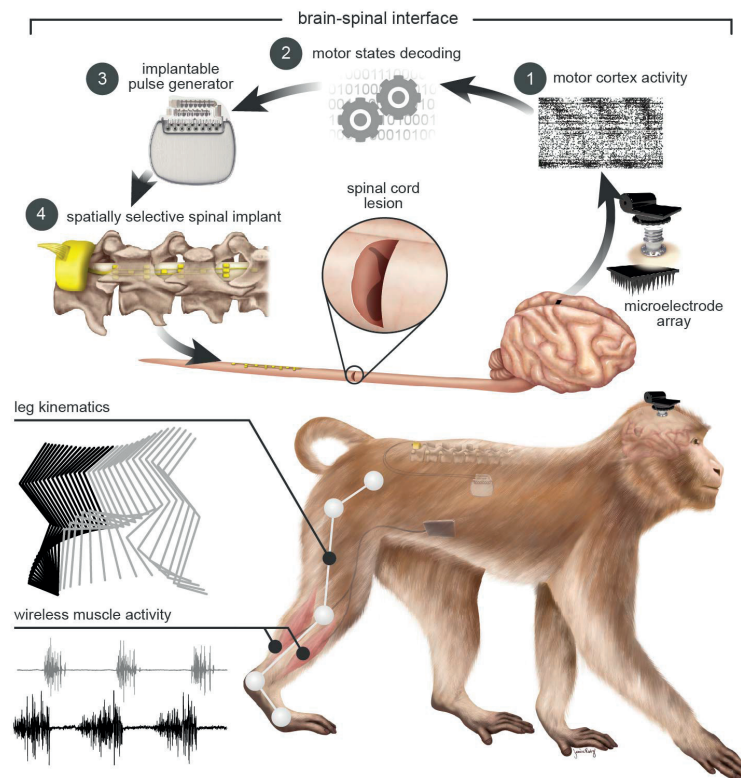


Figure 4.1 – The monkeys were implanted with a microelectrode array into the leg area of the left motor cortex. During recordings, a wireless module transmitted broadband neural signals to a control computer. (1) Raster plot recorded over three successive gait cycles. Each line represents spiking events identified from one electrode, while the horizontal axis indicates time. (2) A decoder running on the control computer identified motor states from these neural signals. (3) These motor states triggered electrical spinal cord stimulation protocols. For this, the monkeys were implanted with a pulse generator featuring real-time triggering capabilities. (4) The stimulator was connected to a spinal implant targeting specific dorsal roots of the lumbar spinal cord. Electromyographic signals of an extensor (grey) and flexor (black) muscles acting at the ankle recorded over three successive gait cycles are shown together with a stick diagram decomposition of leg movements during the stance (grey) and swing (black) phases of gait.

We first used well-established methods [110] [76] to identify the natural spatiotemporal pattern of motoneuron activation underlying locomotion. Our aim was to reproduce this pattern after injury. We conducted an anatomical tracing to identify

the spatial distribution of motoneuron pools innervating antagonist muscles spanning each joint of the leg (Fig. 4.2a). We then projected the muscle activity recorded during locomotion onto motoneuron locations to visualize the spatiotemporal maps of motoneuron activation (Fig. 4.2c). These maps showed that locomotion involves the successive activation of well-defined hotspots located in specific regions of the spinal cord that were reproducible across monkeys (Extended Data Fig. S4.3). The most intense hotspots emerged in the caudal (L6/L7) and rostral (L1/L2) compartments of lumbar segments around the transitions between stance and swing phases. We labelled these hotspots extension and flexion hotspots, respectively. EES activates motoneurons through the recruitment of large-diameter proprioceptive fibres within the dorsal roots [111] [43]. To access the extension and flexion hotspots, we targeted the dorsal roots projecting to spinal segments containing these hotspots. We reconstructed the spatial trajectory of the dorsal roots innervating each lumbar segment, and integrated this information together with motoneuron distribution into a unified library (Fig. 4.2a). We utilized the entry points of the dorsal roots as the targeted anatomical landmarks that guided the design and positioning of spinal implants (Fig. 4.2b and Extended Data Fig. S4.1). Experiments in three sedated monkeys confirmed that single EES pulses delivered through the electrodes targeting the extension and flexion hotspots led to spinal segment activation that correlated with the activation of these hotspots during locomotion (Fig 4.2c-d and Extended Data Fig. S4.3).

We next exploited cortical signals to decode the temporal structure of extensor and flexor hotspot activation. The spiking activity recorded from the left motor cortex displayed cyclic modulations that were phase-locked with right leg movements (Extended Data Fig. S4.4a). We developed a decoder that calculated the probability of foot strike and foot off events from this modulation to anticipate the activation of extensor and flexor hotspots associated with right leg movements (Extended Data Fig. S4.4b). Evaluations in two intact monkeys showed that the decoder accurately predicted these gait events in real-time over extended periods of locomotion, including when initiating and terminating gait, and during rest (Extended Data Fig. S4.5). We then exploited our wireless platform to implement a brain–spinal interface — a system wherein the decoded motor states triggered EES protocols targeting the extension and flexion hotspots. We tested the capacity of the brain–spinal interface to modulate the extension and flexion hotspots independently and simultaneously in two intact monkeys during locomotion on a treadmill. We calibrated the decoder with temporal offsets that were tuned to trigger and terminate stimulation protocols concomitantly to the activation of each hotspot (Fig. 4.3a and Supplementary Methods). We used data without and with stimulation to calibrate the decoders[106], which substantially improved decoding accuracy (Extended Data Fig. S4.5). Without prior training of the monkeys, brain-controlled stimulation of the extension and flexion

Chapter 4. A brain-spinal interface alleviating gait deficits after spinal cord injury in primates

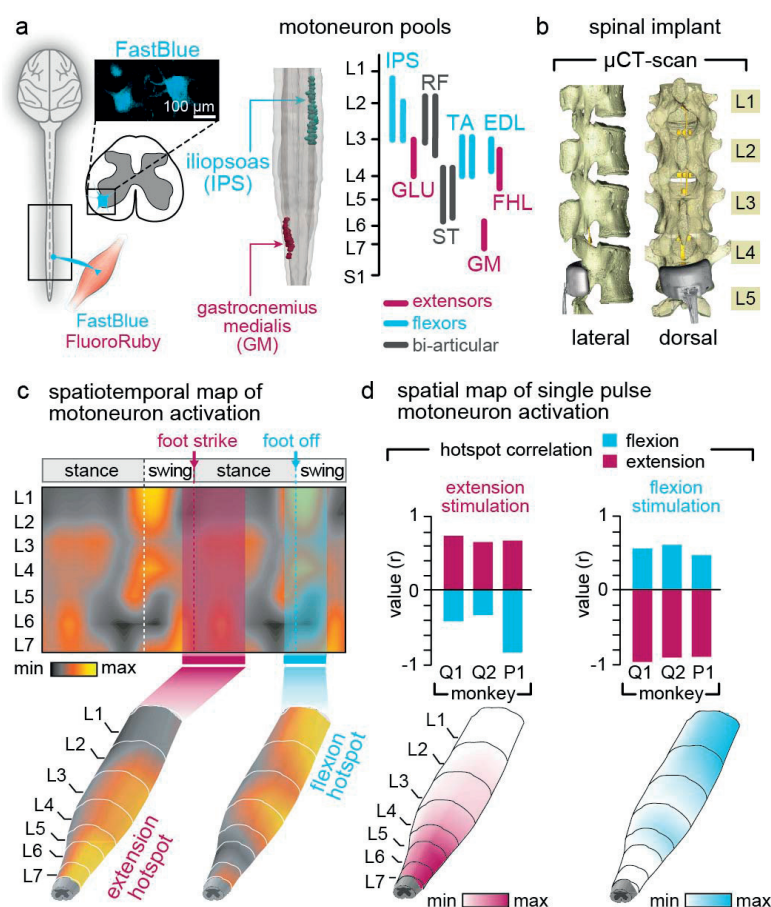


Figure 4.2 – (a) Diagram illustrating injections of retrograde anatomical tracers into leg muscles to label motoneurons. The inset shows a confocal photograph of labelled motoneurons. The 3D reconstruction shows each labelled motoneuron innervating iliopsoas (IPS) and gastrocnemius medialis (GM) muscles. The same procedure was applied to the gluteus medius (GLU), rectus femoris (RF), semitendinosus (ST), extensor digitorum longus (EDL), and flexor hallucis longus (FHL) muscles. The diagram reports the averaged ($n = 1$ to 3 monkeys per muscle) distribution of leg motoneurons within the spinal cord. (b) Representative micro-computed tomography (μ CT) scans of the spinal implant (monkey Q1). (c) Electromyography of the recorded leg muscles (monkey Q1) was projected onto the motoneuron locations in the spinal cord to compute the mean ($n = 73$ gait cycles) spatiotemporal map of motoneuron activation during locomotion. Maps recorded around foot off (-10% to $+20\%$ of gait cycle) and foot strike (-10% to $+30\%$) were extracted to highlight extension and flexion hotspots (data from other monkeys in Extended Data Fig. 3). (d) Median ($n = 6$ pulses) spatial map of motoneuron activation resulting from single pulses of stimulation delivered through the electrodes targeting the extension and flexion hotspots. For each monkey, the bar plots report the correlation between these spatial maps and the maps corresponding to the extension and flexion hotspots.

hotspots immediately modulated kinematic and muscle activity parameters related to the extension and flexion of the leg ipsilateral to stimulation (Fig. 4.3). A gradual increase in the frequency or amplitude of EES pulses led to a monotonic modulation of these parameters (Extended Data Fig.S4.6). We previously documented similar responses in rodents [56] [110] [111], suggesting that the mechanisms underlying the

modulation of spinal activity with EES are similar across mammals including humans [69] [74].

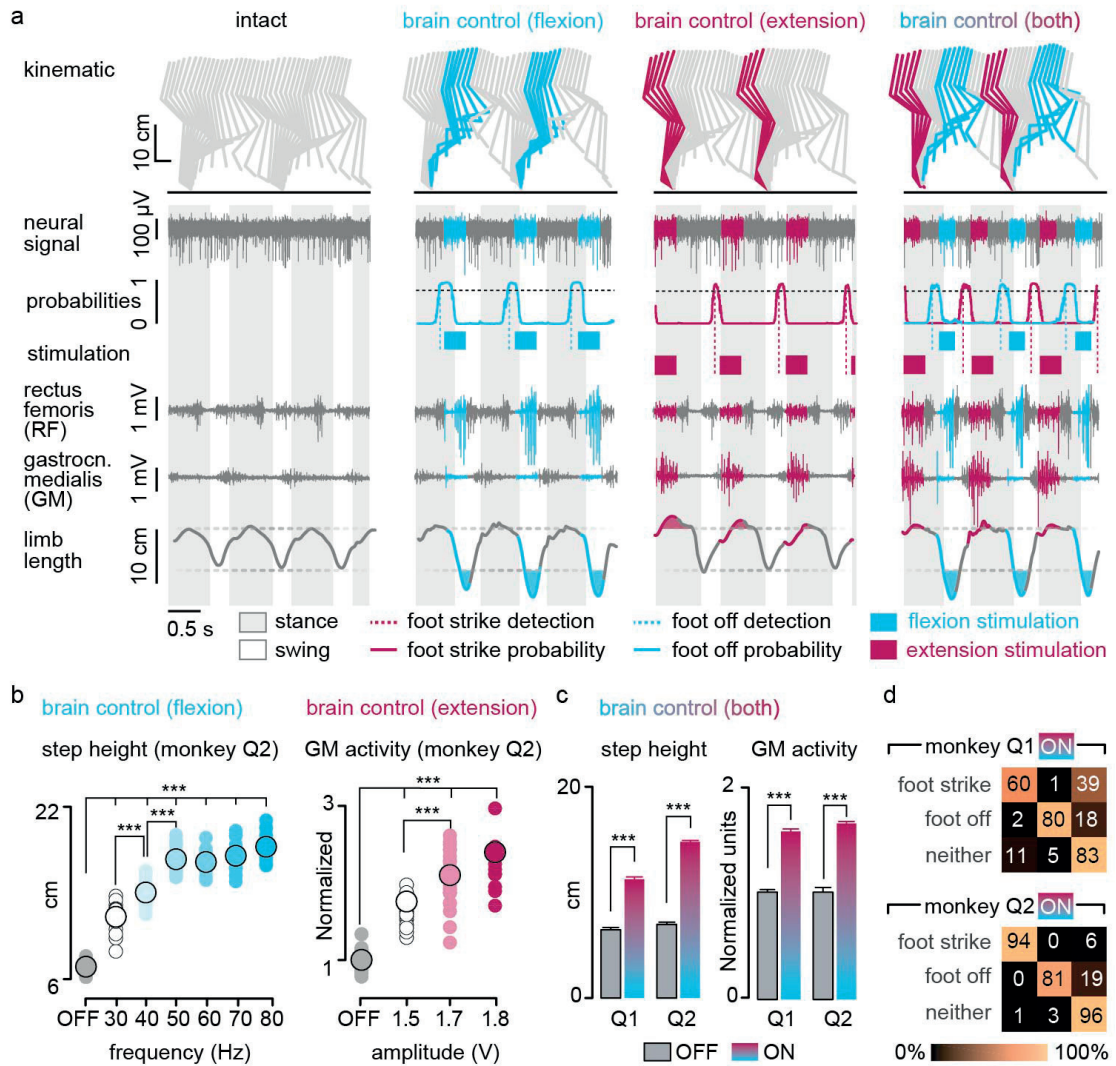


Figure 4.3 – (a) Two successive gait cycles recorded during locomotion without stimulation and during brain-controlled stimulation of the flexion hotspot, extension hotspot, or both (monkey Q2). From top to bottom: stick diagram decompositions of right leg movements; example of single channel neural recording; probability of foot off and foot strike motor states; detected motor states (cyan and magenta broken lines), periods of stimulation through the electrodes targeting the flexion and extension hotspots; electromyographic signals; limb length calculated as distance from the hip to the fifth metatarsal joint. The grey and white backgrounds correspond to stance and swing, respectively. (b) Relationship between frequency of brain-controlled flexion stimulation and step height, and between the stimulation amplitude and the activity of the GM muscle during brain-controlled extension stimulation. Values for individual gait cycles (smaller dots) and mean values (larger dots) are shown. (c) Bar plots reporting the mean step height and mean GM activity without stimulation and during brain-controlled stimulation for monkeys Q1 ($n = 125$ steps) and Q2 ($n = 119$ steps). (d) Decoder confusion matrices calculated during brain-controlled stimulation for monkeys Q1 ($n = 125$ steps) and Q2 ($n = 119$ steps).

Chapter 4. A brain-spinal interface alleviating gait deficits after spinal cord injury in primates

Finally, we tested the ability of the brain–spinal interface to alleviate locomotor deficits after a lesion of the corticospinal tract extending in the right dorsolateral column of mid-thoracic segments in two monkeys (Fig. 4.4a). Additional pathways were damaged, including the rubrospinal tract, dorsal column and reticulospinal fibres. This lesion initially led to a paralysis of the leg ipsilateral to the lesion, followed by an extensive yet incomplete recovery (Fig. 4.4b and Extended Data Fig. S4.7). During the first week after lesion and without training of the monkeys, the brain–spinal interface restored weight-bearing locomotion on a treadmill (Fig. 4.4b-c) and overground (Extended Data Fig. S4.8), improving both the quantity and quality of steps performed by the impaired leg (Fig. 4.4d-e, Extended Data Fig. S4.9 and Supplementary Video 1). The quantity and quality of steps was directly linked to the temporal structure of the stimulation (Extended Data Fig. S4.10). Decoding accuracy declined shortly after lesion. Improvement of decoding performance during the following week suggested that this decrease was primarily due to the reorganization of cortical dynamics (Extended Data Fig. S4.9). This recovery coincided with improvement in the quantity and quality of steps, indicating that the monkeys had spontaneously regained some degree of neural control over the impaired leg (Extended Data Fig. S4.7). At this stage, the brain–spinal interface alleviated many of the remaining gait deficits (Fig. 4.4d-e). Tuning EES frequency maximized the quantity and quality of steps, whereas the same stimulation protocols applied continuously failed to facilitate locomotion or were markedly less efficient than brain-controlled stimulation (Extended Data Fig. S4.10).

4.4 Discussion

The recovery of coordinated, weight-bearing locomotion in a primate model of spinal cord injury emphasizes the therapeutic potential of the brain–spinal interface for clinical applications. We have integrated intracortical arrays [61] [62], wireless modules [64] and pulse generators that have been approved for research applications in humans, opening realistic perspectives for proof-of-concept clinical studies.

Our brain–spinal interface exploits neuronal ensemble modulation that naturally occurs during locomotion, immediately linking cortical dynamics with spatiotemporal neuromodulation therapies without prior training of the monkeys. This ecological approach [116] enabled a smooth cooperation between residual supraspinal signals and the brain–spinal interface in generating leg movements. Imaging [117] and electrophysiological [106] studies showed that leg motor cortex dynamics is preserved in people with paralysis. Moreover, cortical activity modulates with intended movements in people with long-lasting tetraplegia, which allowed them to control robotic arms [61] [62] and neuromuscular stimulators [106]. These results suggest that the

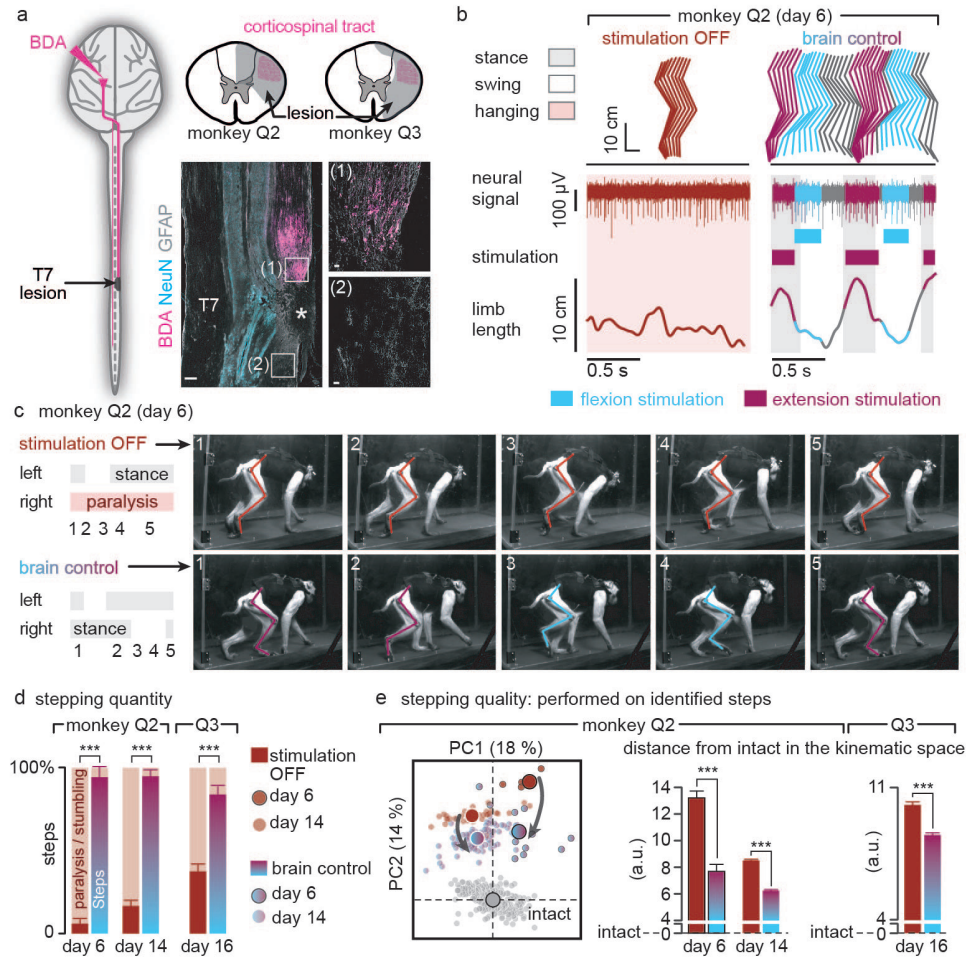


Figure 4.4 – (a) Diagram illustrating the location of the lesion and corticospinal tract labelling using biotinylated dextran amine (BDA). Right, anatomical reconstructions of spinal segments containing the lesion (grey), for monkeys Q2 and Q3. Photographs including insets, showing a longitudinal view of the lesioned spinal cord wherein astrocytes (GFAP, grey), neurons (NeuN, cyan) and corticospinal tract axons (BDA, pink) are labelled. Asterisk, lesion. Scale bars, overview: 500µm. Insets: 50µm. (b) Gait cycles performed during locomotion without stimulation and during brain-controlled stimulation of both flexion and extension hotspots in monkey Q2 at 6 days post-lesion. Conventions, same as Figure 3. Limb paralysis in red. (c) Snapshots extracted from video recordings showing a sequence of leg movements without stimulation and during brain-controlled stimulation (monkey Q2, 6 days post-injury). Timeline indicates video snapshot timing. Legend refers to panels d and e. (d) Bar plots reporting the ratio between of steps performed by the affected versus unaffected leg by each monkey without stimulation ($n = 6$ for day 6 and $n = 39$ for day 14 for Q2, $n = 68$ for Q3) and during brain-controlled stimulation ($n = 12$ for day 6 and $n = 93$ for day 14 for Q2, $n = 31$ for Q3). (e) Principal component (PC) analysis applied on 26 gait parameters for Q2. All the gait cycles corresponding to limb paralysis or stumbling have been excluded from this analysis. Each gait cycle is shown in the space defined by PC1 and PC2. Bar plots reporting the mean Euclidean distance between pre-lesion and post-lesion gait cycles corresponding to steps, calculated in the entire kinematic space. **, *** significant difference at $p < 0.01$ and $p < 0.001$, respectively using bootstrapping (panel d) or Wilcoxon ranksum test (panel e).

Chapter 4. A brain-spinal interface alleviating gait deficits after spinal cord injury in primates

decoding strategy employed in this study may have useful application in people with paraplegia. Our model of paralysis avoided many of the complications associated with severe injuries that are difficult to manage and ethically debatable in primates [57]. The use of a brain–spinal interface to restore bipedal locomotion in humans after severe injuries may require additional interventions, including monoaminergic replacement therapies [67] [63] compensating for the interrupted source of serotonin from brainstem centres and robotic systems to sustain balance. Nevertheless, individuals with motor complete injuries regained weight-bearing standing and stepping-like movements during continuous EES [69] [74]. Therefore, the conditions now exist to test the efficacy of the brain–spinal interface to enhance neuroplasticity [115] [31] during rehabilitation in people with spinal cord injury.

4.5 Methods

4.5.1 Animal husbandry, surgical intervention and behavioral training

Animal husbandry

Experiments were approved by the Institutional Animal Care and Use Committee of Bordeaux (CE50 – France) under the license number 50120102-A and performed in accordance with the European Union directive of September 22, 2010 (2010/63/EU) on the protection of animals used for scientific purposes in an AAALAC-accredited facility (Chinese Academy of Science, Beijing, China). Nine healthy male rhesus monkeys (*Macaca mulatta*, China; Supplementary Table S4.11) aged between 4 and 9 years old, and weighing between 4.3 and 8.4 kg (6.5 ± 0.5 kg) were housed individually in cages designed according to European guidelines (2 x 1.6 x 1.26 m). Environmental enrichment included toys and soothing music. All the monkeys are included in the manuscript. Only two monkeys received a spinal cord injury.

Surgical procedures

All the surgical procedures were performed under full anaesthesia induced with atropine (0.04 mg/kg) and ketamine (10 mg/kg, intramuscular injection) and maintained under 1-3% isoflurane after intubation. A certified functional neurosurgeon (J.B.) supervised all the surgical procedures. Surgical implantations were performed during a single operation lasting approximately 8 hours. We implanted a 96-channel microelectrode array (Blackrock Microsystems, pitch, 1.5 mm) into the leg area of the left primary motor cortex [105] (F4, Extended Table S4.11). The monkeys also received a wireless system [61] (T33F-4, Konigsberg Instruments, USA) to record electromyographic signals from the following leg muscles: gluteus medius (GLU), iliopsoas (IPS), rectus femoris (RF), semitendinosus (ST), gastrocnemius medialis (GM), tibialis anterior (TA), extensor digitorum longus (EDL), and flexor hallucis longus (FHL). A custom-made spinal implant was inserted into the epidural space of the lumbar spinal cord according to previously described methods [110]. The implant was inserted at L4-L5 vertebrae and pulled until T13-L1 vertebrae. Electrophysiological testing was performed intra-operatively to adjust the position of the electrodes. Specifically, we verified that a single pulse of stimulation delivered through the most rostral and most caudal electrodes induced motor responses in the IPS and GM muscles, respectively. The connector of the implant, enclosed into a titanium orthosis, was secured to the vertebral bone using titanium screws (Vis MatrixMIDFACE, diameter 1.5 mm, length

Chapter 4. A brain-spinal interface alleviating gait deficits after spinal cord injury in primates

8 mm, Synthes). The wires were routed subcutaneously to an implantable pulse generator inserted between intercostal muscles (See Supplementary Information). Monkeys Q2 and Q3 received a spinal cord injury. A partial laminectomy was made at the T7/T8 level. A micro-blade was used to cut approximately two thirds of the dorsoventral extent of the spinal cord. The lesion was completed using micro-scissors under microscopic observation. Animals retained bowel, bladder, and autonomic function after the injury. The veterinary team continuously monitored the monkeys during the first hours after surgery, and numerous times daily during the seven subsequent days. A few hours after completion of surgical interventions, the animals were able to move around and feed themselves unaided. Clinical rating and monitoring scales were used to assess post-operative pain. Ketophen (2 mg/kg; s.c.) and Metacam (0.2 mg/kg; s.c.) were administered once daily. Lidocaine cream was also applied to surgical wounds twice per day. The antibiotics ceftriaxone sodium (100 mg/kg; i.m.) was given immediately following surgery, and then once daily for 7 days.

4.5.2 Experimental recordings

Monkeys were trained to walk on a treadmill and overground along a corridor (300 x 35 x 70 cm). Plexiglas enclosures were used to maintain the monkeys within the field of view of the cameras. Food pellets and fruits rewarded appropriate behaviours. Additional food to complete daily dietary requirement was provided after training.

Single pulse stimulation in sedated monkeys

Monkeys were lightly sedated with ketamine (3.5 mg/kg), and suspended in the air using a jacket that did not impede leg movements. Single pulses of cathodic monopolar, charge-balanced stimulation (0.3 ms, 1 Hz) were delivered through the electrodes to elicit compound potentials in leg muscles. We selected the active sites whose corresponding spatial maps of motoneuron activation showed the highest correlation with the hotspots.

Brain-controlled stimulation during locomotion on a treadmill in intact monkeys

Brain-controlled stimulation protocols were tested during locomotion on a treadmill at a comfortable speed (Q1, 2.0 km/h; Q2, 1.6 km/h). Recording sessions were organized as follows: first, we recorded two to five blocks of 1-2 minutes-long during stepping without stimulation. These baseline recordings were used to calibrate the decoders for real-time detection of foot off and foot strike gait events. Second, monkeys were recorded during brain-controlled stimulation protocols involving (i) solely the

electrode targeting the extensor hotspot, (ii) solely the electrode targeting the flexor hotspot, and (iii) both electrodes. We tested the effects of stimulation frequency and amplitude over functional ranges (30 to 80 Hz; 1.5 to 3.9 V). See Supplementary Table S4.12.

EES during locomotion in lesioned monkeys

Monkey Q2 and Q3 were recorded after injury as soon as they were able to sustain independent locomotion on the treadmill, which corresponded to 6 days and 16 days post-injury, respectively. Q3 recovered more slowly than Q2, probably due to more extensive ventral and lateral spinal cord damage (Extended Data Fig. S4.9). Therefore, monkey Q3 could only be recorded when appropriate behavioural and physical conditions were reached, which occurred two weeks post-injury. Due to restrictions on the total duration of the experiments (2 weeks), only one entire session could be conducted with this monkey. Following this experiment, the monkey rapidly recovered, which prevented evaluating the efficacy of the brain-spinal interface. The monkeys were recorded on the treadmill at their most comfortable speed (1.2-1.4 km/h for monkey Q2 and 1.0 km/h for monkey Q3). Recording sessions were organized as follows. First, we recorded two to six blocks of 1-2 min without stimulation. These recordings were used to calibrate the decoders. Second, the decoders were used to test brain-controlled stimulation of both the extension and flexion hotspots over a range of stimulation frequencies. The effects of continuous stimulation using the same stimulation features as during brain-controlled stimulation were also tested. Within functional range of stimulation parameters, brain-controlled stimulation did not trigger undesired movements or spasms that impaired locomotor movements. See Supplementary Table S4.12.

4.5.3 Data acquisition

Procedures to record kinematics and muscle activity have been detailed previously [64] [118]. Whole-body kinematics was measured using the high-speed motion capture system SIMI (Simi Reality Motion Systems, Germany), combining 4 or 6 video-cameras (100 Hz). Reflective white paint was directly applied on the shaved skin of the monkey overlying the following body landmarks of the right side: iliac crest, greater trochanter (hip), lateral condyle (knee), lateral malleolus (ankle), 5th metatarsophalangeal (mtp), and the outside tip of the fifth digit (toe). The Simi motion tracking software was used to obtain the 3D spatial coordinates of the markers. Joint angles were computed accordingly. Electromyographic signals were recorded simultaneously (2 kHz, Kronenberg, USA) and synchronized through the Blackrock Cerebrus system (Blackrock

Chapter 4. A brain-spinal interface alleviating gait deficits after spinal cord injury in primates

Microsystems, USA), which also recorded neural signals. For this, the Cereplex wireless system [64] was mounted on the head of the monkeys. Six antennae and a receiver were used to transmit [64] broadband neural signals (0.1 Hz – 7.8 kHz, sampled at 22 kHz). The signals were band-pass filtered (500 Hz - 7.5 kHz) and spiking events were extracted through threshold crossings [61] [62] [119] [120] [121]. Specifically, a spiking event was defined on each channel (96 in total) if the signal exceeded 3.0 to 3.5 times its root mean square value calculated over a period of 5 s. This procedure resulted in a binary signal from 96 multiunits, each originating from one of the 96 electrode of the array. Signals from all 96 multiunits have been integrated in the decoder.

4.5.4 Decoding of motor states from neural signals

Our aim was to deliver stimulation over the extensor and flexor hotspots around the times at which these hotspots are active during natural locomotion. To this end, we decoded gait-related motor states from neural activity and used those detections to trigger the stimulation protocols at the appropriate times. The control computer was connected to the local network and continuously received UDP packets containing neural recordings. We designed a custom in-house software application running on the control computer (Visual Studio C++ 2010), which analysed the neural signals in real time. Every 20 ms, the application made a decision whether to trigger one of the spinal cord stimulation protocols. The decision was made based on probabilities of observing a “foot off” or a “foot strike” motor state given the history of neural data (300 ms pre-lesion and 400 ms post-lesion), as calculated by our decoders.

Natural activations of the extension and flexion hotspots were time-locked to foot off and foot strike gait events (fo and fs, respectively). In turn, we defined the foot off and foot strike motor states as the neural activity preceding foot off and foot strike gait events by Δt_{FO} and Δt_{FS} temporal offsets, respectively. The offsets were derived in order to maximize the overlap between the stimulation over the hotspots and the natural activation of those hotspots. In effect, the offsets integrated the latencies between the gait events and the hotspot activations, as well as latencies related to wireless communication between our devices, into the design of our decoders.

Extraction of motor states used for decoder calibration

We calibrated the decoders on data from two to seven no stimulation blocks recorded at the beginning of each session. Gait events were identified from electromyographic recordings (Q1) or from video recordings (Q2 and Q3). Identification of fo and fs gait events from electromyographic recordings was performed using signals from the

iliopsoas muscle, which was active around the time of swing onset and remained active throughout most of the swing phase of gait. The fo and fs events were estimated by thresholding the envelope of the rectified electromyographic signal. Identification of fo and fs gait events from video recordings was performed visually. After injury and while the monkeys only exhibited minimal movements of the limb ipsilateral to lesion, fo and fs gait events were defined according to residual hip/knee oscillations, which correlated with the attempt to execute steps.

Calibration procedure to account for stimulation-induced changes in neural signals

Analysis of the decoding temporal precision in Q1 revealed that decoded foot off and foot strike motor states during brain-controlled stimulation differed from the times of the motor states estimated from the foot off and foot strike gait events (median difference: foot off: 68ms; foot strike: -90 ms). We did not observe such difference when detecting motor states in the absence of stimulation (median difference: foot off: 11ms; foot strike: 3 ms). A range of factors could have decreased decoding performance including: changes in somatosensory feedback influenced by the stimulation, monkeys' attempts to adapt its gait, changes in stability, etc. To improve temporal accuracy of our decoder, we introduced a decoder recalibration process. The initial decoder, trained on data without stimulation, was used to trigger stimulation through the extension hotspot or flexion hotspot independently for 2 to 3 blocks each. The data collected during these blocks was then combined to the blocks without stimulation to calibrate a new, second decoder. This decoder successfully compensated for stimulation-induced changes in motor cortex activity (Fig 4.3. and Extended Data Fig. S4.5).

Duration of hotspot stimulation protocols

We sought to stimulate flexion and extension hotspots throughout the duration of their natural activation during locomotion. We determined the duration of the flexion and extension hotspot stimulation protocols by setting this duration to 300 ms. We then recorded a few steps during brain-controlled stimulation, and adjusted the duration of the stimulation protocols for each monkey when necessary in order to obtain a clear modulation of leg kinematics. This procedure was performed only once for all pre-injury sessions and was repeated for each post-injury session.

Chapter 4. A brain-spinal interface alleviating gait deficits after spinal cord injury in primates

4.5.5 Data processing and analysis

Code availability

The software routines utilized for data analysis will be made available upon reasonable request to the corresponding author.

Blinding

Data analyses, except identification of the steps and the marking of foot off and foot strike gait events from video recordings, were performed by automatic computer routines. When analyses required involvement of investigators, they were blind to the experimental conditions.

Spatiotemporal map of motoneuron activation

To visualize spatiotemporal maps of motoneuron activation, electromyographic signals were mapped onto the rostrocaudal distribution of the motoneurons reconstructed from histological analyses. This approach provides an interpretation of the motoneuron activation at a segmental level rather than at the individual muscle level.

Identification of extensor and flexor hotspots activation

Flexion and extension hotspots were identified from the mean spatiotemporal map of motoneuron activation for each monkey independently ($n = 3$ for Q1, P2 and P3). Single maps computed between two consecutive foot strike events were time-interpolated to a 1000 point map and averaged to obtain the mean spatiotemporal map of motoneuron activation. Flexion and extension hotspots were then identified by time-averaging the mean map around the foot off event (-10% + 20% of the gait cycle) for the flexion hotspot and around the foot strike event (-10% + 30% of the gait cycle) for the extension hotspot.

Analysis of muscle recruitment curves

The compound potentials recorded in leg muscles were rectified and integrated for each muscle and stimulation amplitude, and represented in color-coded spatial maps of motoneuron activation. Instead of measuring specific flexor and extensor muscle selectivity we selected the electrodes that elicited spatial maps similar to those extracted during activation of the flexion and extension hotspots, regardless of muscle

specificity. The correlation between the resulting map and the maps recorded during locomotion was calculated for each monkey to identify the voltage range over which the correlation was maximal. The derived voltage range was then used during behavioural experiments (Extended Data Fig. S4.3c).

Decoding performance quantification

We quantified the performance of our asynchronous decoders using confusion matrices and normalized mutual information, as described before [122]

Steps classification for kinematic analysis.

In order to evaluate the efficacy of the brain-spinal interface and assess the importance of the timing of stimulation in correcting gait deficits, we conducted a post-hoc classification of the steps based on the temporal accuracy of the decoder to reproduce the desired hotspot activation timings. We defined optimal and sub-optimal steps according to the initiation of flexion and extension hotspot stimulation. All the gait cycles that contained only one correct extension activation (stimulation occurring at Foot Strike \pm 125 ms) and only one correct flexion activation (stimulation occurring between Foot Off -200 ms and Foot Off +50 ms) were defined as optimal steps (Extended Data Fig. S4.10).

Stepping quantity

After the spinal cord lesion, the monkeys typically walked with the three intact limbs while the leg ipsilateral to the lesion was either dragging along the walking surface or maintained in a flexed posture. Occasionally, monkeys hopped to move both legs forward and avoid bumping against the back of the treadmill enclosure due to their inability to move at the selected treadmill belt speed. We counted the numbers of these “hop” and “bump” steps, as well as the numbers of normal steps. Experimenters were blinded to stimulation conditions during this analysis. To quantify the functional improvement mediated by the brain-spinal interface, we calculated the proportion of normal steps over all recorded blocks on a given day. To quantify the ability of the monkeys to sustain locomotion, we extracted all the events marked as steps, and measured the relative number of steps that were not performed while bumping into the back of the treadmill enclosure.

Chapter 4. A brain-spinal interface alleviating gait deficits after spinal cord injury in primates

Stepping quality

A total of 26 parameters quantifying kinematics (Supplementary Table S4.13) were computed for each step according to methods described in details previously [56] [110] [118]. We used principal component analysis (PCA) to visualize the changes in gait over time and for different conditions (Fig. 4.4, Extended Data Fig. S4.7, S4.8). To quantify locomotor performance, we calculated the mean Euclidian distance between steps corresponding to a given experimental condition and the mean of steps recorded before the lesion in the same monkey in the entire 26-dimensional space of kinematic parameters.

4.5.6 Anatomical procedures

Tissue processing

Monkeys were deeply anesthetized and perfused transcardially with a 4% solution of paraformaldehyde. The spinal cord dura was removed and the spinal cord was cut using a cryostat, and stored at 4°C in 0.1M PBS azide (0.03%).

Anterograde tracing of motor cortex projections

Monkeys Q2 and Q3 underwent anterograde tracing of corticospinal projections from the leg and trunk area of the left motor cortex using anatomical tracers. All animals were anesthetized as described above. Biotinylated dextran amine (BDA; 10% solution in water; 10,000 Da; Molecular Probes, TSA PLUS Biotin KIT PerkinElmer, cat. NEL749A001KT) was injected at 300 nl/site into 40 sites spanning the leg and trunk regions of the left motor cortex.

Quantification of the spinal cord lesion

Camera lucida reconstructions of the lesion (Neurolucida 11.0, MBF biosciences, USA) were performed using evenly spaced horizontal sections (1:4) throughout the whole dorsoventral axis on sections labelled for astrocytic (glial fibrillary acidic protein, GFAP; 1:1000, Dako, USA, cat. Z0334), NeuN (anti-NeuN; 1:300, Millipore, cat. MAB377) and BDA reactivity. Immunoreactions were visualized with secondary antibodies labelled with Alexa fluor® 488 (1:400, Invitrogen, cat. A-11034) and 647 (1:300, Invitrogen, cat. A-21235).

4.5.7 Statistical procedures

All the computed parameters were quantified and compared within each monkey. All data are reported as mean values \pm standard error of the mean (s.e.m.). Significance was analysed using the non-parametric Wilcoxon rank sum test, bootstrapping or a Monte-Carlo approach.

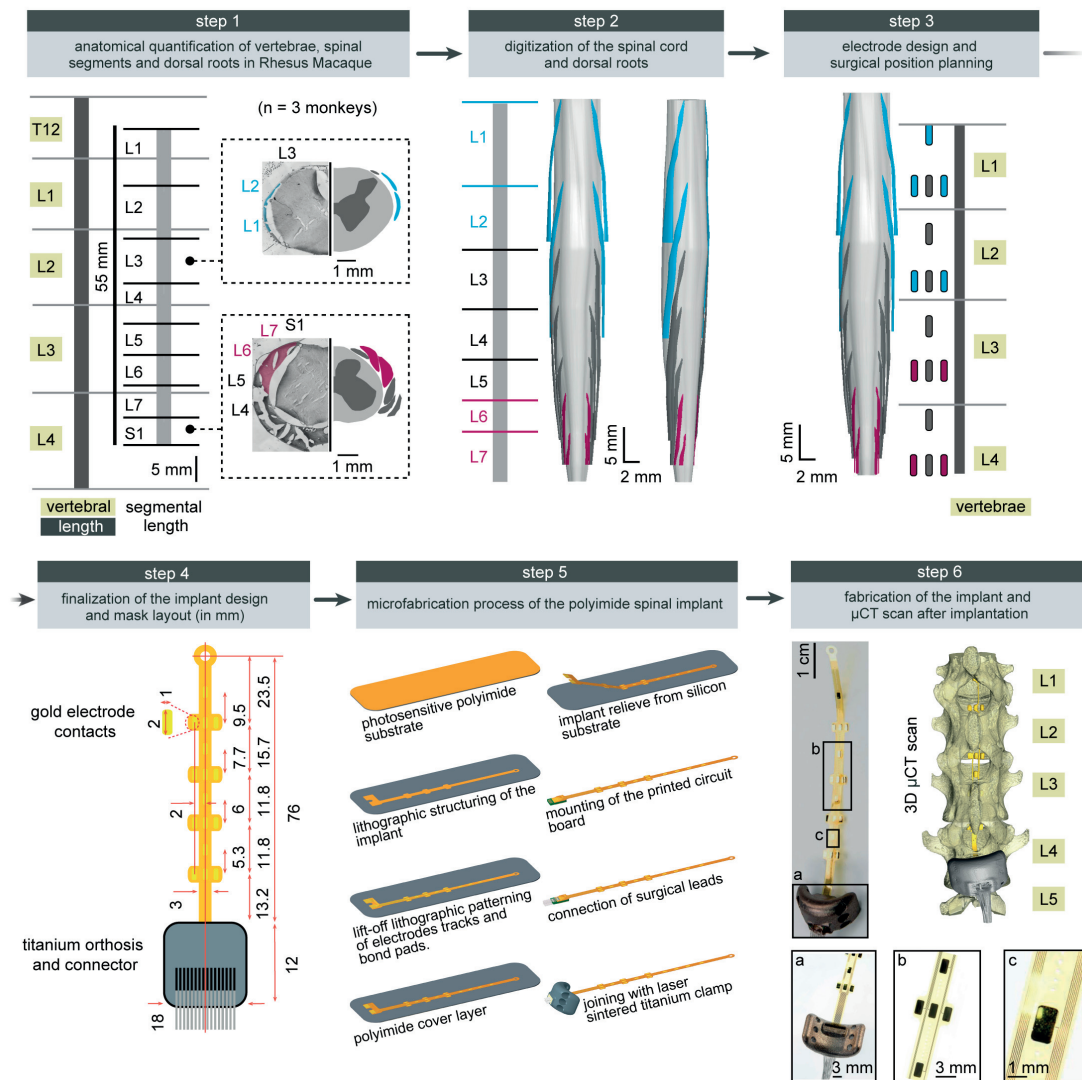
4.6 Supplementary video

4.6.1 Video 1: Technical design and therapeutic effects of the brain–spinal interface.

This video explains the design of the spinal cord stimulation system and brain decoding algorithms. The ability of the brain–spinal interface to modulate extension and flexion movements of the leg during continuous locomotion is then illustrated in intact monkeys. Finally, the video shows the recovery of functional leg movements during locomotion on a treadmill and overground in two monkeys with a spinal cord injury.

Videos are available on Nature website: <https://www.nature.com>

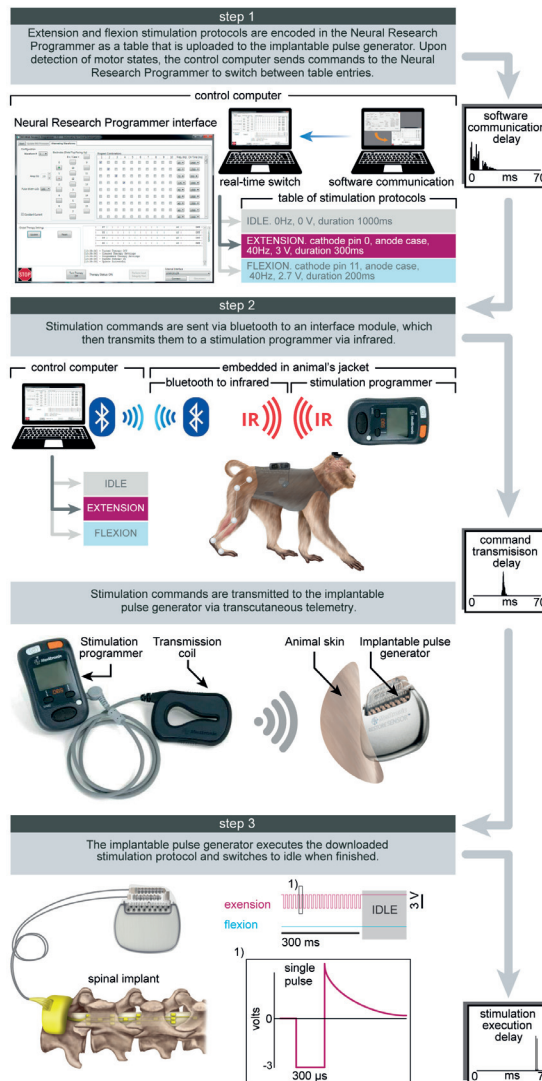
4.7 Supplementary figures



Chapter 4. A brain-spinal interface alleviating gait deficits after spinal cord injury in primates

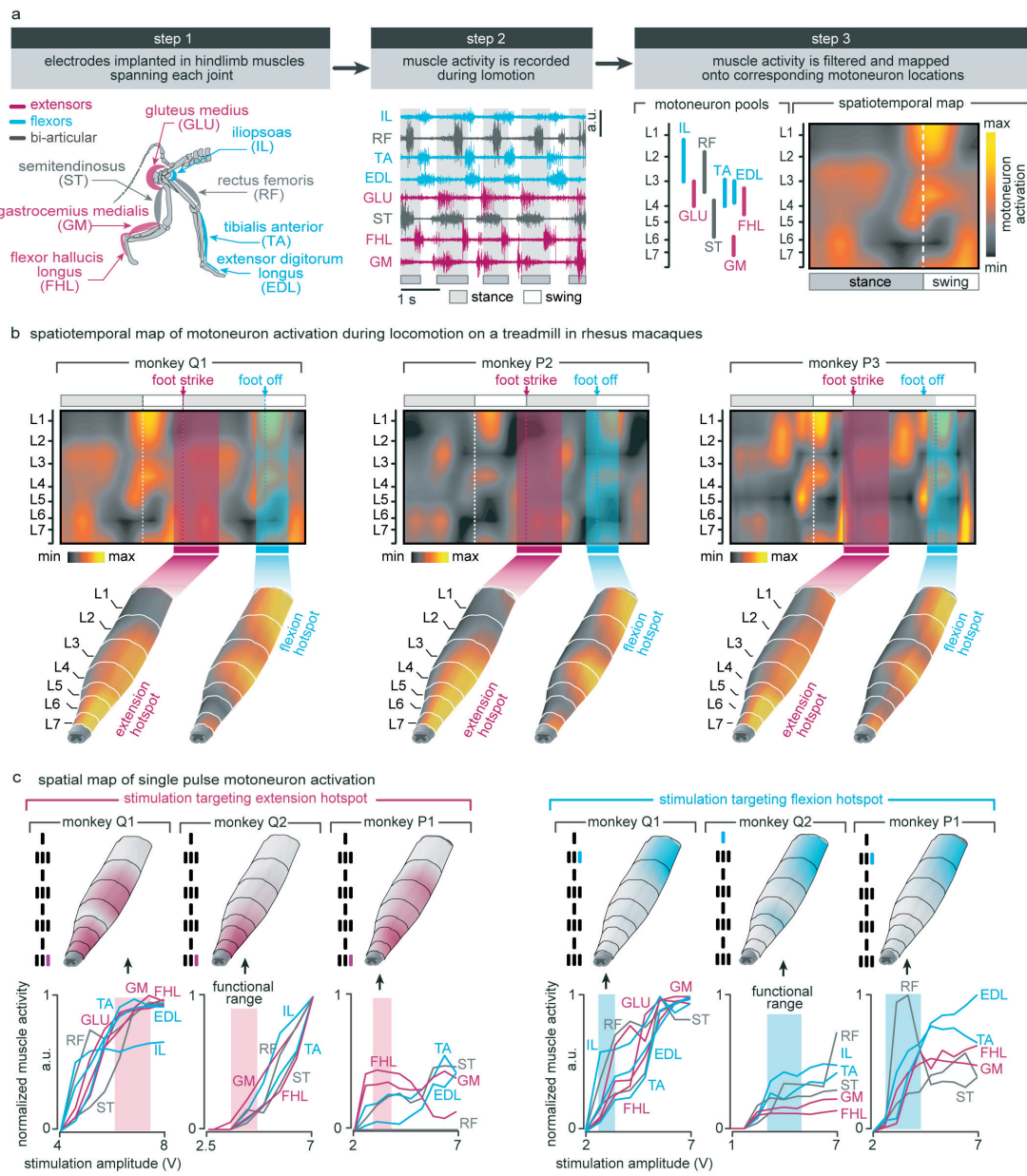
Supplementary Figure S4.1 – Design and fabrication of the spatially selective spinal implant. Step 1: Quantification of the length of vertebra T12 to L4, and of spinal segments L1 to S1. The photographs show coronal sections of the the left halves of the L3 and S1 spinal segments, including the dura mater, dorsal roots and spinal tissue. The complementary views show camera Lucida reconstructions of the dorsal roots, white and grey matter. The dorsal roots projecting to L1/L2 and L6/L7 spinal segments are color-coded to visualize their respective location. Step 2: 3D reconstruction of the entire lumbosacral spinal cord and dorsal roots. The dorsal roots innervating spinal segments containing the targeted extension (L6, L7) and flexion (L1, L2) hotspots are color-coded to help visualize their respective spatial trajectory. The 3D reconstructions are displayed from a dorsal view, and from a view that is rotated by 45 deg leftward around the rostrocaudal axis in order to visualize the trajectory of the dorsal roots along spinal segments. Step 3: Design of the spatially selective spinal implants, including the location of the electrodes with respect to the dorsal roots, and positioning of the implants with respect to the vertebra. The cyan and magenta shapes highlight the electrodes targeting the flexor and extensor hotspots, respectively. Step 4: Mask layout of the spatially selective epidural spinal implant. Step 5: Fabrication of the spinal implants. Processing starts with deposition of a 40 μm thick Polyimide film by spin coating on the silicon substrate. The Polyimide-based bottom layer constituting the footprint of the implant is realized through ultra-violet lithography. A 200 nm thick gold layer is deposited using vacuum evaporation and lithographically structured to create a conductive seed pattern. An additional gold layer is electroplated to a height of approximately 6 μm to create the electrodes and interconnects. A 20 μm cover layer of photosensitive Polyimide is then applied by spin coating to uniformly cover the bottom and electrode structure. A final ultra-violet lithography is applied to structure the top layer of the implant, and to create openings over the electrodes and contact pads. The implants are gently released from the carrier wafer. To create a connector, the contact pads located at the extremity of the implant are glued to a small support plate made of medical grade poly-methyl methacrylate (PMMA) sheet material. Precision milled alignment structures allow fine adjustment of the support plate to the spinal implant, and to the extremity of the leads. The support plate contained a seat in which a tiny printed circuit board with conductive stripes is fixed. Stainless steel leads with silicone rubber insulation are directly soldered to the contact pads of the implant via the contact stripes located on the printed circuit board. The resulting implants and connective leads were highly reliable mechanically and electrically. A fixation structure was realized by using 3D laser sintering of medical grade titanium. Step 6: Photographs, including zoomed insets, showing a fabricated spinal implant and a micro-computed tomography scan performed after implantation.

4.7. Supplementary figures



Supplementary Figure S4.2 – Protocols and technology of the spinal cord stimulation system. Step 1: A Neural Research Programmer interface (screen snapshot) encodes stimulation protocols that are pre-programmed into a table uploaded to the implantable pulse generator. Each row of this table corresponds to a specific electrode configuration (cathodes and anodes) and stimulation features (amplitude, frequency, pulse width and duration of stimulation). During experiments, the control computer selects the rows to be executed. The plot reports the distribution of temporal delays introduced by the communication between the decoder and the Neural Research Programmer ($n = 5000$). Step 2: stimulation commands are transmitted to the implantable pulse generator. Commands are first broadcasted via Bluetooth to a module that converts them into infrared signals transferred to the stimulation programmer device. The Bluetooth to infrared module and the stimulation programmer were embedded into a jacket worn by the monkeys during the experiments. The stimulation programmer transmitted the stimulation commands into the implantable pulse generator via induction telemetry. The antenna was placed under the jacket, in contact with the skin and aligned to the implantable pulse generator. The plot reports the distribution of delays needed to transmit the stimulation commands from the Neural Research Programmer to the implantable pulse generator. Step 3: The implantable pulse generator executed the selected stimulation protocols. After execution of the stimulation command, the implantable pulse generator switched to idle mode. The shape of a single charge balanced cathodic pulse is shown in the inset (1). The plot reports the distribution of time delays required to execute a single stimulation command by the implantable pulse generator.

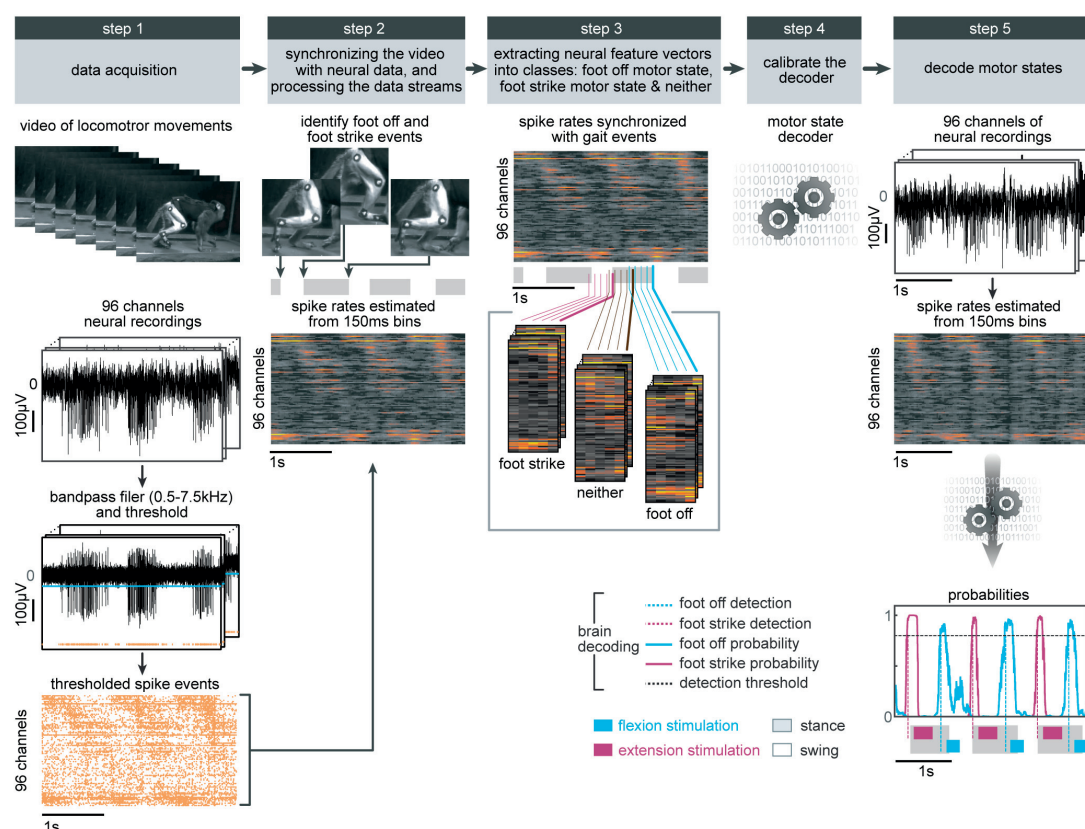
Chapter 4. A brain-spinal interface alleviating gait deficits after spinal cord injury in primates



4.7. Supplementary figures

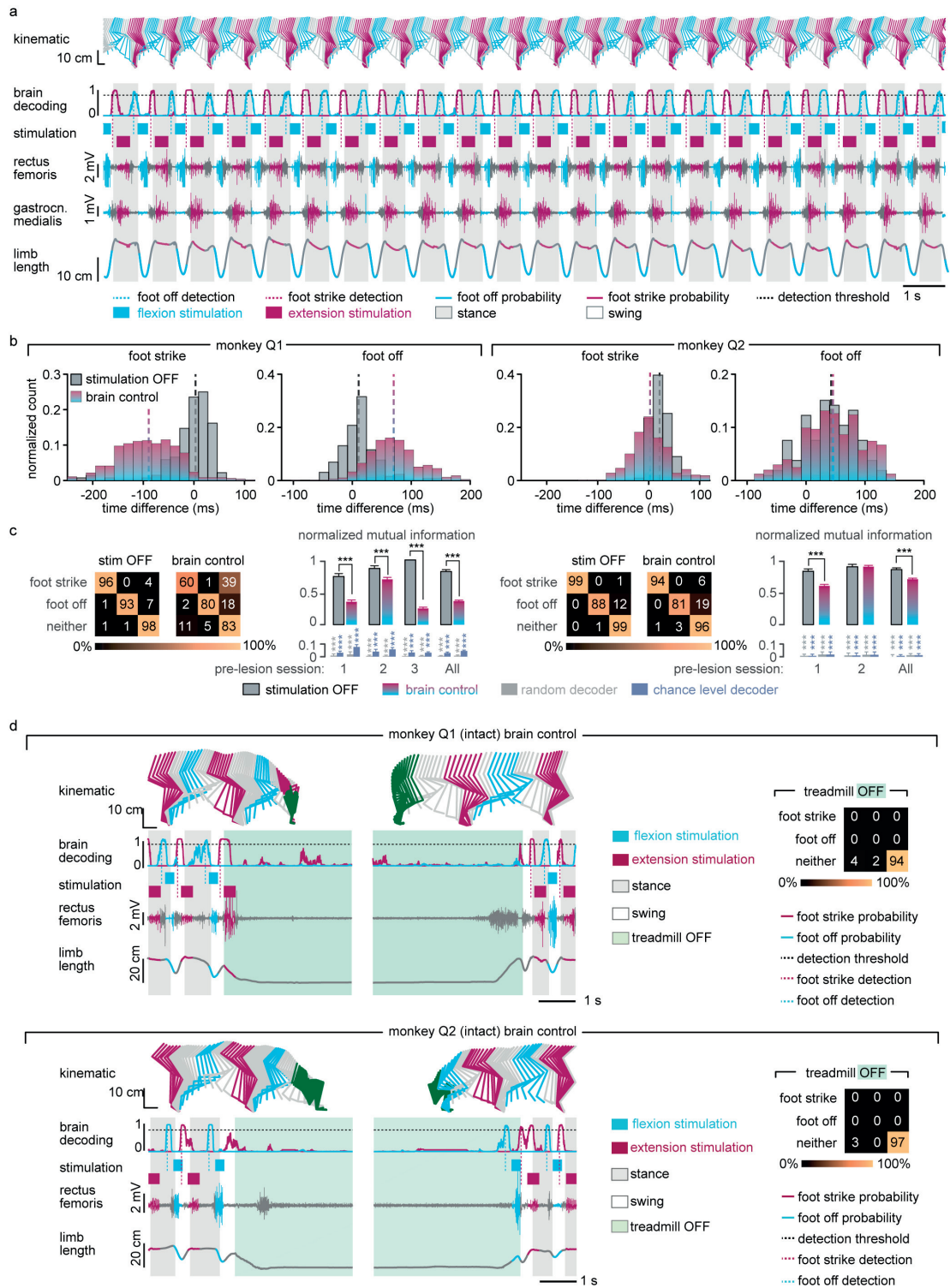
Supplementary Figure S4.3 – Anatomical, computational, and functional experiments allowed the identification of stimulation protocols to access flexion and extension hotspots. (a) Computational procedure to estimate spatiotemporal maps of motoneuron activation during locomotion. Step 1: Four pairs of antagonist muscles spanning each joint of the leg are implanted with bipolar electrodes to record electromyographic signals during locomotion. Step 2: Muscle activity recorded during locomotion on a treadmill is band pass filtered using a Butterworth 3rd order filter (30-800 Hz, monkey P3), Step 3: The signals are rectified, filtered with a low pass at 10 Hz, normalized to the maximum activity recorded across all the gait cycles, and then projected onto the location of the corresponding motoneuron columns in the spinal cord for each of the recorded muscles. The estimated motoneuron activation is represented as a color-coded spatiotemporal map of motoneuron activation. (b) Spatiotemporal maps of motoneuron activation recorded in three intact monkeys (Q1, P2 and P3). The maps were obtained by averaging electromyographic signals recorded during continuous locomotion on a treadmill ($n = 73, 25$ and 24 steps for monkey Q1, P2 and P3, respectively). The maps underlying the activation of extension and flexion hotspots were extracted by averaging the estimated motoneuron activation around the foot strike and foot off events, respectively. For this, a window was defined from -10% to $+30\%$ of the gait cycle duration for the foot strike event, and from -10% to $+20\%$ of the gait cycle duration for the foot off event. The maps were reproducible across monkeys: correlation between monkey Q1, P2 and P3 for the flexion hotspot was $0.94, 0.90$ and 0.90 for Q1-P2, Q1-P3 and P2-P3, respectively. Correlation between monkey Q1, P2 and P3 for the extension hotspot was $0.88, 0.90$ and 0.60 for Q1-P2, Q1-P3 and P2-P3, respectively. The resulting maps were projected onto the reconstructed spinal segments (Extended Data Fig. 1). (c) Recruitment curves showing the relationships between motor evoked potentials elicited by single pulses of epidural electrical stimulation in each of the recorded hindlimb muscles and the stimulation amplitude for three intact monkeys (Q1, Q2 and P1). Stimulation was delivered through the electrodes targeting the extension and flexion hotspots. The compound responses elicited in leg muscles were rectified and integrated to calculate the amplitude of the responses, and then projected on the reconstructed spinal segments. The spatial maps of motoneuron activation corresponding to the optimal range of stimulation amplitudes to access the hotspots stimulation are displayed for each monkey, including the location of the electrodes with respect to spinal segments. To compute the optimal range of stimulation amplitudes to access each hotspot, we extracted the stimulation amplitudes for which the spatial map of motoneuron activation displayed the highest values of correlation with the spatial maps of the targeted hotspots. The cyan and magenta shadings highlight the functional range of stimulation amplitude for each hotspot and monkey.

Chapter 4. A brain-spinal interface alleviating gait deficits after spinal cord injury in primates



Supplementary Figure S4.4 – Procedure to calibrate the decoders for real-time detection of motor states. Step 1: The locomotor movements of the right leg were recorded using the video camera system. In parallel, neural signals were recorded from the microelectrode array implanted into the leg area of the primary motor cortex. The signals were band-pass filtered (0.5-7.5 kHz). A threshold was at 3 to 3.5 times the standard deviation in order to obtain spike events. The two data streams were saved onto computers. Step 2: Visual inspection of the video frames allowed the identification of foot off and foot strike gait events. We estimated the spike rates from overlapping 150ms bins that were updated every 20 ms. Gait events were then synchronized with the spike rate estimates using a trigger saved with the neural data that marked the onset of video recordings. Step 3: We extracted feature vectors that originated at foot off and foot strike events and assigned them to foot off and foot strike motor state classes, respectively. All other feature vectors were assigned to the neither class. Step 4: Motor state classes of feature vectors were used to calibrate a regularized linear discriminant analysis decoder. Step 5: The decoder was uploaded into our real-time analysis application running on the control computer. Neural data was collected in real-time, processed into spike rate estimates, and passed through the decoder that calculated the probabilities of foot off and foot strike motor states. When one of the motor state probabilities crossed a threshold of 0.8, a command to trigger the flexion or extension hotspot stimulation protocols was sent to the neural research programmer, which relayed this instruction to the implanted pulse generator. Due to the wireless communication, the command was executed 178 ms (Q1) or 105 ms (Q2-3) after the detection of the motor states.

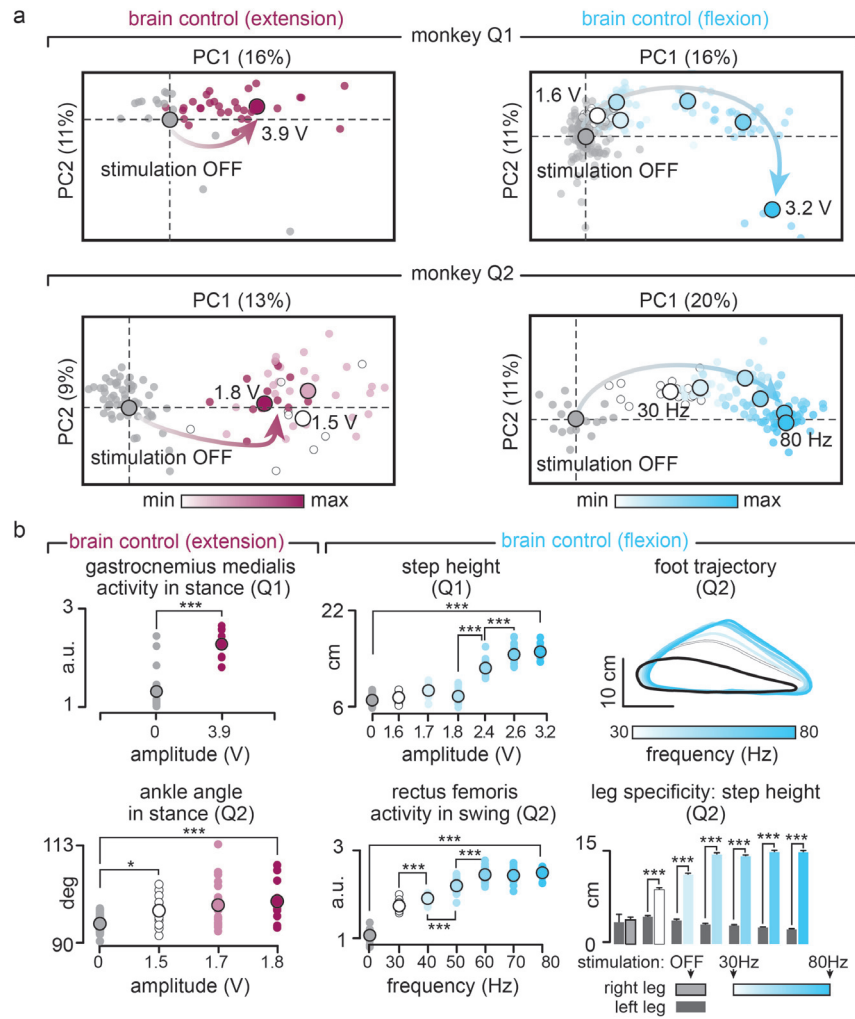
4.7. Supplementary figures



Chapter 4. A brain-spinal interface alleviating gait deficits after spinal cord injury in primates

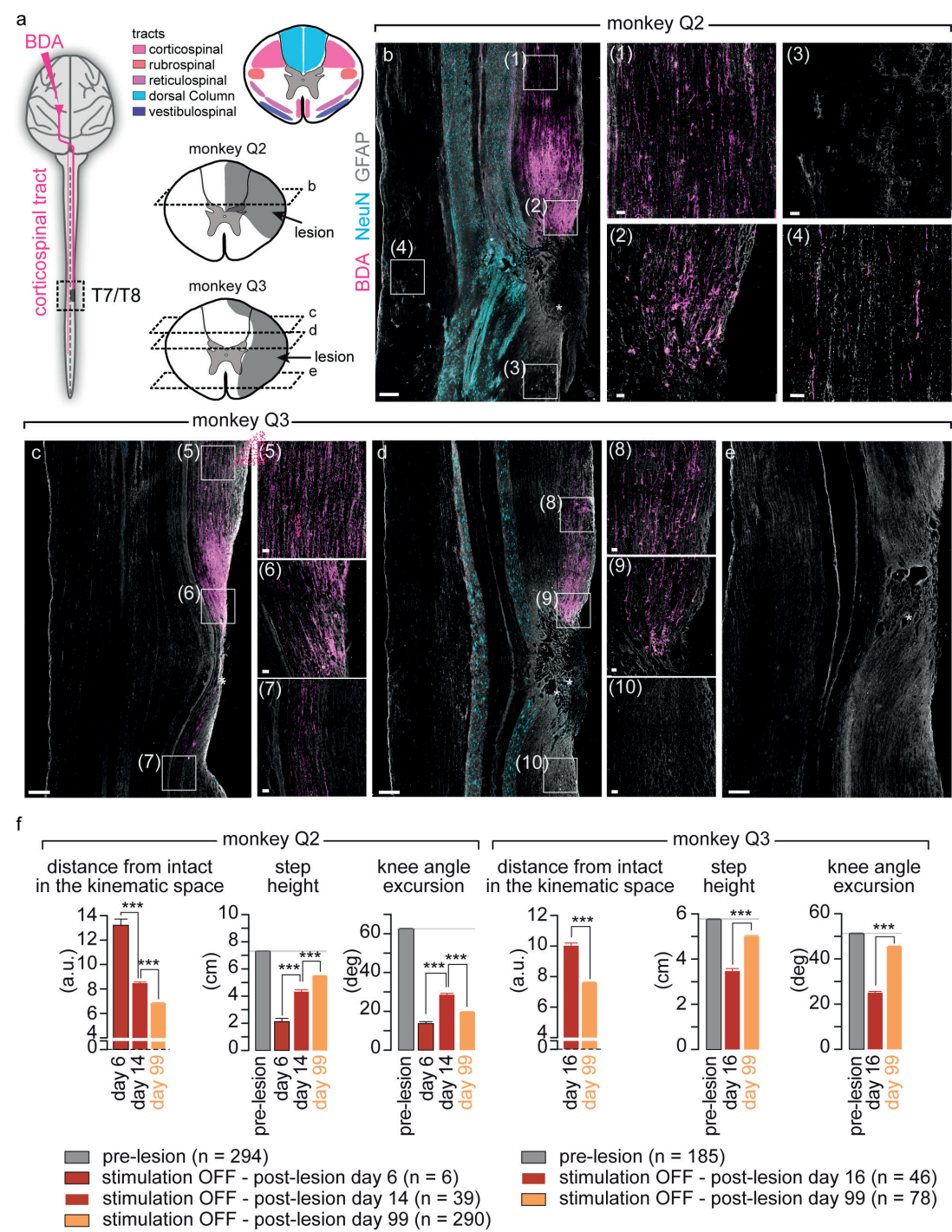
Supplementary Figure S4.5 – The real-time decoder accurately detected the motor states and triggered stimulation protocols during locomotion and when initiating and terminating it in intact monkeys. (a) Example of a continuous sequence of locomotion (20 s) during brain-controlled flexion and extension stimulation in an intact monkey (Q2, pre-lesion session 2, Extended Table S4.12). Conventions are the same as in Figure 3. The real-time decoder correctly detected the succession of 22 foot off and foot strike motor states occurring in this sequence (vertical dotted lines), and appropriately triggered the relevant stimulation protocols throughout the locomotor sequence. (b) Histograms showing the distribution of the temporal differences between the actual occurrence of foot off and foot strike events and the decoded occurrence of these motor states for all the recording sessions of the tested intact monkeys (Q1, Q2). The dotted lines indicate the median for each distribution. For the monkey Q1, the decoders were calibrated using recordings without stimulation only. For the monkey Q2, we improved the accuracy of the decoders by performing the calibration twice. First, the decoders were recalibrated using recordings without stimulation. These decoders were used to collect recordings during brain-controlled flexion or brain-controlled extension independently. New decoders were then calibrated using all the combined recording blocks together. (c) Confusion matrices reporting the accuracy of the real-time decoders without stimulation and during brain-controlled stimulation, given a tolerance window of ± 125 ms. The bar plots report the normalized mutual information calculated for the real-time decoders compared to random decoders and chance level decoders. Random decoders were the same decoders calibrated using shuffled gait events. The chance level decoders randomly assigned motor states with chance level probabilities, which were estimated from the data used to calibrate the online decoders, and at the same rate as the online decoders. (d) Two examples of recordings collected while monkey Q1 and Q2 initiated or terminated sequences of continuous locomotion on a treadmill. The green shaded area indicates the period during which the treadmill was turned off. The brain-spinal interface was kept on throughout the recordings. Conventions are the same as in Figure 3. Probability of foot strike and foot off motor states remained low during the periods of rest, and recommenced to modulate with the occurrence of motor states when the monkey resumed continuous locomotion. The decoder confusion matrices were calculated during brain-controlled stimulation across all the sessions with intact monkeys during which the treadmill was turned off ($n = 345$ and $n = 127$ temporal windows for Q1 and Q2). False positive detections were rare.

4.7. Supplementary figures



Supplementary Figure S4.6 – Modulation of leg locomotor movements during brain-controlled stimulation in intact monkeys. (a) PC analysis was applied on individual gait cycles extracted from locomotion on a treadmill without stimulation ($n = 125$ and $n = 119$ for Q1 and Q2) and during brain-controlled stimulation of the extension ($n = 33$ and $n = 54$ gait cycles with stimulation for Q1 and Q2, respectively) or flexion ($n = 98$ and $n = 120$ total stimulation steps for Q1 and Q2, respectively) hotspots for the intact monkeys Q1 and Q2. Conventions are the same as in Figure 3 and Extended Data Figure 7. This analysis emphasizes the graded modulation of gait parameters when increasing the frequency or amplitude of stimulation for extension and flexion hotspots independently. (b) Plots showing relationships between the amplitude or frequency of extensor (magenta) or flexor (cyan) hotspot stimulation and relevant kinematic or muscle activity parameter related to the extension or flexion of the right leg. The upper right plot shows the average foot trajectories during each experimental condition, illustrating the graded modulation of flexion during brain-controlled stimulation of the flexion hotspot. The lower right plot highlights the high degree of leg-specific modulation over the entire extent of tested stimulation parameters. Results were comparable in monkey Q1 and Q2. ***, * $p < 0.001$ and $p < 0.05$, respectively. Wilcoxon rank sum test. Error bars, s.e.m.

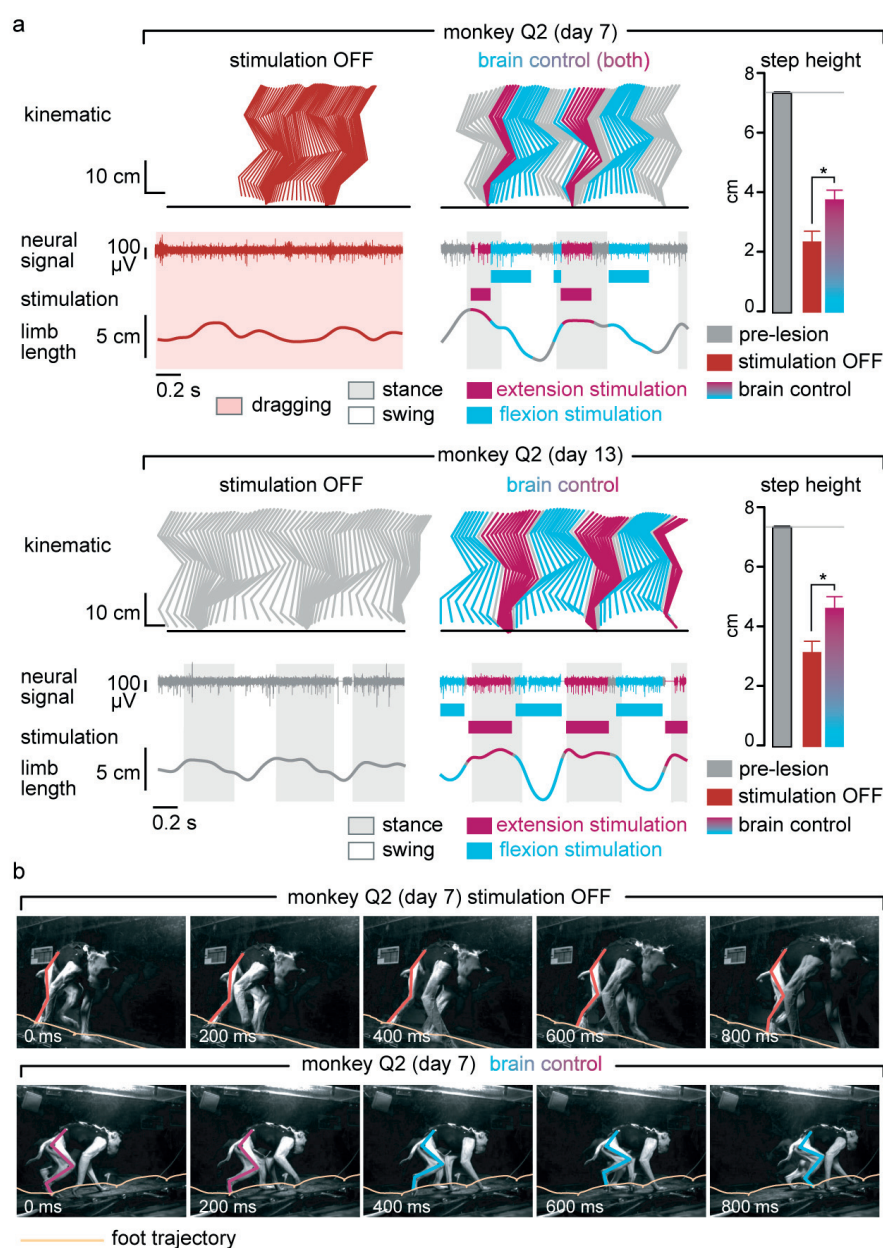
Chapter 4. A brain-spinal interface alleviating gait deficits after spinal cord injury in primates



4.7. Supplementary figures

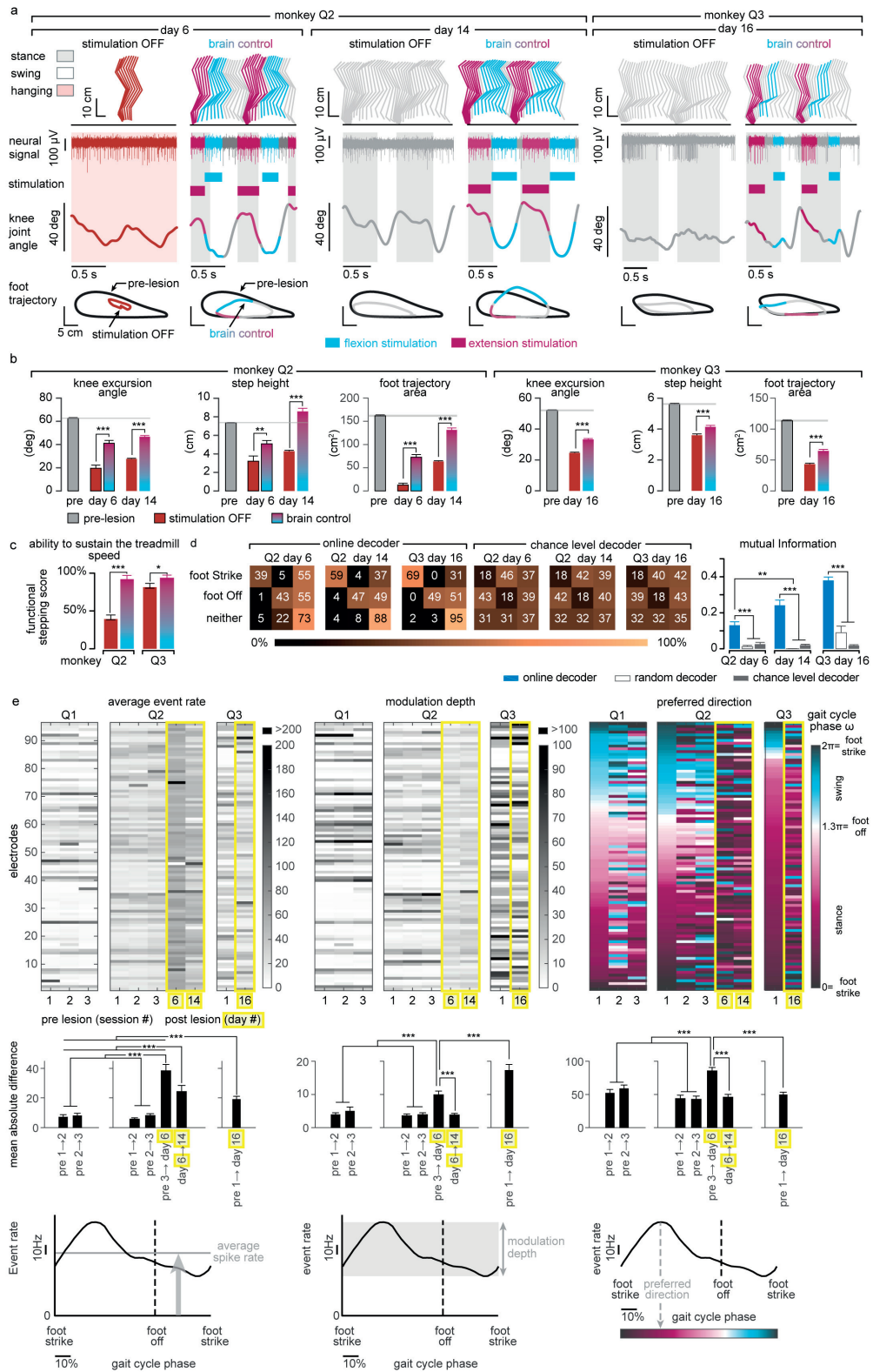
Supplementary Figure S4.7 – Quantification and reconstruction of the spinal cord lesions and quantification of gait deficits and spontaneous recovery after the spinal cord lesion. (a) Scheme illustrating the anatomical experiments to quantify the lesion of the corticospinal tract. The anterograde anatomical tracer BDA was injected into the leg and trunk regions of the left primary motor cortex to label corticospinal tract fibres in the spinal cord, shown in pink in the photographs. Top-right scheme shows the approximate pathways of the dorsal ascending tract and all descending tracts identified from [123], [124]. For monkey Q2 and Q3, the area of maximal damage was reconstructed in 2D by identifying the border of the glia scar on evenly spaced sagittal sections spanning the entire dorsoventral extent of the lesioned spinal cord. (b,c,d,e) For each monkey, confocal photographs show longitudinal sections of the lesioned spinal cord at specific dorsoventral levels, as indicated with dotted lines. In each photograph, the following anatomical elements are labelled: astrocytes (GFAP, grey), neural cell bodies (NeuN, cyan) and corticospinal tract axons (BDA, pink). The insets show high-resolution photographs of selected (white square) regions of the same photograph that illustrates intact corticospinal tract axons above the injury, axon retraction bulbs right above the lesion, and the absence of axons below the injury. Monkey Q2 displayed a small subset of spared corticospinal tract axons in the more dorsal aspect of the dorsolateral column. The asterisks indicate the location of the lesion. Scale bars, overviews: 500 μm . Insets: 50 μm . (f) Gait cycles were extracted from locomotion recorded in monkey Q2 and Q3 pre-lesion, during the first two weeks after the lesion, and at 99 days after the lesion. Analysis was only applied to gait cycles classified as steps, i.e. gait cycles classified as limb paralysis or stumbling were not included. The number of analysed gait cycles is directly reported into the figure. The bar plots report the mean Euclidean distance between all the steps under a given recording day without stimulation and steps recorded before the lesion, computed in the entire space of the 26 kinematic parameters. The other bar plots report mean values of relevant kinematic parameters. This analysis illustrates the progressive yet incomplete recovery of locomotion. ***, $p < 0.001$, Wilcoxon rank sum test. Error bars, s.e.m.

Chapter 4. A brain-spinal interface alleviating gait deficits after spinal cord injury in primates



*Supplementary Figure S4.8 – Restoration of leg locomotor movements during overground locomotion after the spinal cord lesion. (a) Representative sequences of locomotion along a straight corridor without stimulation and during brain-controlled stimulation recorded at 7 days and 13 days after the lesion for monkey Q2. Conventions are the same as in Figure 4. The bar plots report the mean step height of the right (lesioned) leg during swing. *, $p < 0.05$, Wilcoxon rank sum test. Error bar, s.e.m. (b). Snapshots extracted from video recordings showing a representative sequence of leg movements during one gait cycle without stimulation and during brain-controlled stimulation at 7 days post-injury for monkey Q2. The stick diagrams overlying the right (lesioned) leg and the trajectory of the foot are color-coded using the same color scheme as the stick diagram decomposition in panel a. Without stimulation, the monkey dragged the leg along the ground, whereas brain-controlled stimulation restored weight-bearing locomotion with plantar placement.*

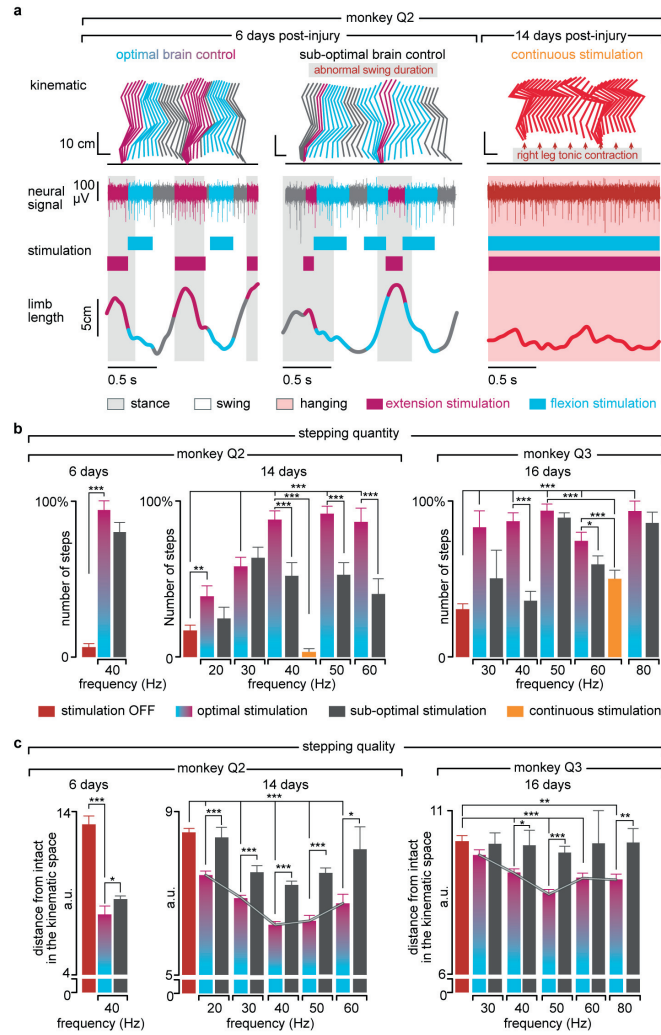
4.7. Supplementary figures



Chapter 4. A brain-spinal interface alleviating gait deficits after spinal cord injury in primates

Supplementary Figure S4.9 – Quantification of gait improvements and decoding accuracy during brain-controlled stimulation after the spinal cord lesion (a) Two successive gait cycles performed during locomotion on a treadmill without stimulation and during brain-controlled stimulation in monkey Q2 at 6 and 14 days post-lesion, and in monkey Q3 at 16 days post-injury. Conventions are the same as in Figure 4.4. In addition, the average foot trajectories calculated over all the recorded gait cycles are displayed for each experimental condition including during pre-lesion locomotion, illustrating the marked improvement of foot movements during brain-controlled stimulation. (b) Bar plot reporting the mean values of the total excursion of the angle, step height and foot trajectory area for monkey Q2 and Q3 during locomotion pre-lesion and post-lesion without stimulation and with brain-controlled stimulation. Analysis was only applied to gait cycles classified as steps, i.e. gait cycles classified as limb paralysis or stumbling were not included (Q2: pre-lesion $n = 294$; day 6 post-lesion no stimulation: $n = 6$; brain control: $n = 12$; day 14: no stimulation: $n = 39$; brain control: $n = 93$. Q3: pre-lesion $n = 185$; day 16 post-injury no stimulation: $n = 98$; brain control: $n = 31$). ***, ** $p < 0.001$ and $p < 0.01$, respectively. Wilcoxon rank sum test. Error bars, s.e.m. (c) Bar plots reporting the capacity of the monkeys to sustain walking at the imposed treadmill belt speed. The functional score is computed as the percentage of regular steps in which the animal is able to walk at the treadmill belt speed i.e. animal does not bump into the back of the treadmill. Gait cycles classified as hops or stumbling were not included. ***, * $p < 0.001$ and $p < 0.05$, respectively, Bootstrap. Error bars, s.e.m. (d) Decoding accuracy increases during recovery after the spinal cord lesion. Decoder confusion matrices calculated reporting the accuracy of the real-time decoders and chance level decoder during brain-controlled stimulation for monkey Q2 at day 6 ($n = 76$ foot strikes, $n = 74$ foot offs) and day 14 post-injury ($n = 264$ foot strikes, $n = 264$ foot offs) and for monkey Q3 at 16 days post-injury ($n = 319$ foot strikes, $n = 321$ foot offs). The tolerance window was set at ± 125 ms. The bar plots report the normalized mutual information calculated for the real-time decoders compared to random decoders and chance level decoders. (e) Top, from left to right: mean event rate, modulation depth and preferred direction for the neuronal spiking signal recorded obtained by regressing spike rates against the phase of the gait cycle for monkeys Q1-3. Preferred direction was defined as the angle for which the fitted tuning function was at a maximum. Bottom, from left to right: mean absolute single-electrode difference for mean event rates, modulation depths and preferred directions between two consecutive sessions shown in (e) top. Analysis shows substantial changes both before and after the spinal-cord lesion. Nevertheless, the rate of change between the last pre-lesion and the first post-lesion sessions was substantially higher than between any two other session pairs, thus indicating increased level of plasticity following spinal cord lesion. ***, ** significant difference at $p < 0.001$ and $p < 0.01$, respectively. Monte Carlo, Wilcoxon ranksum test, signed Wilcoxon ranksum test and Bootstrap. Error bars, s.e.m.

4.7. Supplementary figures



Supplementary Figure S4.10 – The temporal structure and features of stimulation determine the quantity and quality of steps (a) Two successive gait cycles performed during locomotion on a treadmill during brain-controlled stimulation with optimal and suboptimal temporal structures at 6 days post-injury, and during continuous stimulation at 14 days post-lesion for monkey Q2. The gait cycles were classified as suboptimal temporal structures when stimulation occurred outside an ± 125 ms tolerance window. Conventions are the same as in Figure 4.4. (b) Bar plots reporting the quantity of steps calculated during locomotion with optimal and suboptimal temporal structures over a range of stimulation frequencies and during continuous stimulation for monkey Q2 and Q3 at 6, 14 and 16 days post-injury. (c) Bar plots reporting the quality of stepping for the same conditions as in panel b. The quality of stepping was measured as the mean Euclidean distance between pre-lesion and post-lesion gait cycles calculated in the kinematic space defined by the 26 gait parameters, as reported in Figure 4.4. These results show that the optimal temporal structure leads to an increased number of steps and improved quality of stepping compared to sub-optimal temporal structures. Moreover, brain-controlled stimulation with both optimal and suboptimal temporal structure promoted markedly improved locomotor performance compared to continuous stimulation delivered with the same stimulation features. These results also highlight the ability to optimize locomotor performance when tuning the stimulation frequency. ***, **, * significant difference at $p < 0.001$, $p < 0.01$ and $p < 0.05$, respectively. Bootstrap (panel b). Wilcoxon ranksum test (panel c). Error bars, s.e.m.

Chapter 4. A brain-spinal interface alleviating gait deficits after spinal cord injury in primates

Animal ID	Micro electrode array	Spinal implant	Wireless muscle activity system	Spinal cord injury	Retrograde motoneuron tracing	Intact walking experiments	Single pulse spinal cord stimulation	Pre-lesion brain-control stimulation	Post-lesion brain-control stimulation
Q1	✓	✓	✓	-	✓	✓	✓	✓	-
Q2	✓	✓	✓	✓	✓	✓	✓	✓	✓
Q3	✓	✓	*	✓	✓	✓	*	*	✓
P1	✓	✓	✓	-	-	-	✓	-	-
P2	✓	-	✓	-	✓	✓	-	-	-
P3	✓	-	✓	-	-	✓	-	-	-
P4	-	-	-	-	✓	-	-	-	-
P5	-	-	-	-	✓	-	-	-	-
P6	-	-	-	-	✓	-	-	-	-

- ✓ Performed
 - Not Performed
 * Could not be performed due to technical issues or animal conditions

Supplementary Figure S4.11 – Experimental procedures conducted on the animals.

Monkey	Session	# of blocks Stimulation Off	# of blocks Brain control: Flexion	# of blocks Brain control: Extension	# of blocks Brain Control: Both	# of blocks Continuous stimulation
Q1	Pre-lesion 1: treadmill 28.7.2014	<u>5</u>		1 at 40 Hz	4 at 40 Hz	
	Pre-lesion 2: treadmill 29.7.2014	<u>4</u>	1 at 40Hz	1 at 40 Hz	4 at 40 Hz	
	Pre-lesion 3: treadmill 30.7.2014.	<u>4</u>	5 at 40 Hz		5 at 40 Hz	
Q2	Pre-lesion 1: treadmill 24.3.2015.	<u>2</u>	3 at 60 Hz 1 at 60 Hz	3 at 60 Hz 1 at 60 Hz	3 at 60 Hz	
	Pre-lesion 2: treadmill 26.3.2015.	<u>4</u>	2 at 60 Hz 1 at 60 Hz	2 at 60 Hz	3 at 60Hz	
	Pre-lesion 3: treadmill 28.3.2015.	<u>3</u>	2 at 60 Hz 4 at 30 to 80 Hz	2 at 60 Hz		
	Post-lesion day 6: treadmill 23.06.2015.	<u>4</u>			4 at 40Hz	
	Post-lesion day 7: corridor 24.06.2015.	<u>5</u> 2	2 at 40 Hz	3 at 40 Hz	2 at 40Hz	
	Post-lesion day 13: treadmill 30.06.2015.	<u>6</u>			13 at 20 to 60 Hz	1 at 40Hz
	Post-lesion day 14: Corridor 01.07.2015.	<u>6</u> 1			6 at 30Hz	
	Post-lesion day 99: treadmill 24.9.2015.	8				
Q3	Pre-lesion 1: treadmill 16.1.2015.	2				
	Post-lesion day 16: treadmill 3.7.2015.	<u>2</u>	2 at 40Hz	2 at 60Hz	8 at 30 to 80Hz	
	Post-lesion day 99: treadmill 24.9.2015.	8				
P2	Intact: treadmill 26.11.2013.	1				
P3	Intact : treadmill 12.12.2013.	1				

Supplementary Figure S4.12 – Behavioral experiments conducted with each animal. Trials in bold and underlined were used to calibrate the brain decoders used on that session.

4.7. Supplementary figures

PARAMETERS	VARIABLE	DETAILED EXPLANATION
Limb endpoint (Metatarsal phalange) trajectory		
	1	Step length
	2	Maximum backward position of the foot
	3	Maximum forward position of the foot
	4	Step height
	5	Speed of the foot at swing onset
	6	Angular acceleration of the foot velocity vector at swing onset
Stability		
<i>Trunk and pelvic position and oscillations</i>	7	Maximum hip sagittal position
	8	Minimum hip sagittal position
	9	Length of pelvis displacements in the forward direction
	10	Length of pelvis displacements in the vertical direction
Joint angles		
<i>Backward</i>	11	Crest oscillations
	12	Thigh oscillations
	13	Leg oscillations
	14	Foot oscillations
<i>Forward</i>	15	Crest oscillations
	16	Thigh oscillations
	17	Leg oscillations
	18	Foot oscillations
<i>Flexion</i>	19	Knee joint angle
	20	Ankle joint angle
<i>Abduction</i>	21	Whole limb abduction
	22	Foot abduction
<i>Extension</i>	23	Knee joint angle
	24	Ankle joint angle
<i>Adduction</i>	25	Whole limb adduction
	26	Foot adduction

Supplementary Figure S4.13 – Computed kinematic parameters.

Electronic dura mater for long-term multimodal neural interfaces

Ivan R. Minev^{1*}, Pavel Musienko^{2,3*}, Arthur Hirsch¹, Quentin Barraud², Nikolaus Wenger², Eduardo Martin Moraud⁴, Jérôme Gandar², Marco Capogrosso⁴, Tomislav Milekovic², Léonie Asboth², Rafael Fajardo Torres², Nicolas Vachicouras^{1,2}, Qihan Liu⁵, Natalia Pavlova^{2,3}, Simone Duis², Alexandre Larmagnac⁶, Janos Vörös⁶, Silvestro Micera^{4,7}, Zhigang Suo⁵, Grégoire Courtine^{2&}, Stéphanie P. Lacour^{1&}

Science, 2015

1. Bertarelli Foundation Chair in Neuroprosthetic Technology, Laboratory for Soft Bioelectronic Interfaces, Centre for Neuroprosthetics, Institute of Microengineering and Institute of Bioengineering, Ecole Polytechnique Fédérale de Lausanne (EPFL), Switzerland.
2. International Paraplegic Foundation Chair in Spinal Cord Repair, Centre for Neuroprosthetics and Brain Mind Institute, EPFL, Switzerland.
3. Pavlov Institute of Physiology, St. Petersburg, Russia.
4. Translational Neural Engineering Laboratory, Center for Neuroprosthetics and Institute of Bioengineering, EPFL, Lausanne, Switzerland.
5. School of Engineering and Applied Sciences, Kavli Institute for Bionano Science and Technology, Harvard University, Cambridge, MA, USA.
6. Laboratory for Biosensors and Bioelectronics, Institute for Biomedical Engineering, University and ETH Zurich, Switzerland.
7. The BioRobotics Institute, Scuola Superiore Sant'Anna, Pisa 56025, Italy. *These authors contributed equally to this work.

*,& equal contributions

5.1 Abstract

The mechanical mismatch between soft neural tissues and stiff neural implants hinders the long-term performance of implantable neuroprosthesis. Here, we designed and fabricated soft neural implants with the shape and elasticity of dura mater, the protective membrane of the brain and spinal cord. The electronic dura mater, which we call e-dura, embeds interconnects, electrodes and chemotrodes that sustain millions of mechanical stretch cycles, electrical stimulation pulses, and chemical injections. These integrated modalities enable multiple neuroprosthetic applications. The soft implants extracted cortical states in freely behaving animals for brain machine interface, and delivered electrochemical spinal neuromodulation that restored locomotion after paralyzing spinal cord injury. Electronic dura mater offers a novel platform for long-term multimodal neural interfaces in basic research and neuroprosthetics.

Publication contributions

In this chapter, I performed computerized tomography scans for ex-vivo mechanical characterizations and in-vivo compliance validations. I assisted to surgeries, participated to training and recording of the behavioral experiments regarding walking rehabilitation in rat after a spinal cord injury. I contributed to the preparation of the figures and methods related to behavioral testing.

5.2 Introduction

Implantable neuroprostheses are engineered systems designed to study and treat the injured nervous system. Cochlear implants restore hearing in deaf children, deep brain stimulation alleviates Parkinsonian symptoms, and spinal cord neuromodulation attenuates chronic neuropathic pain [19]. New methods for recording and modulation of neural activity using electrical, chemical and/or optical modalities open promising therapeutic perspectives for neuroprosthetic treatments. These advances have triggered the development of myriad neural technologies to design multimodal neural implants [125] [126] [31] [127]. However, the conversion of these sophisticated technologies into implants mediating long-lasting therapeutic benefits has yet to be achieved. A recurring challenge restricting long-term bio-integration is the substantial biomechanical mismatch between implants and neural tissues [128] [129] [130]. Neural tissues are viscoelastic [131] [132] with elastic and shear moduli in the 100 to 1,500 kPa range. They are mechanically heterogeneous [133] [134] and endure constant body dynamics [135] [136]. In contrast, most electrode implants, even thin, plastic interfaces, present high elastic moduli in the GPa range, thus are rigid compared to neural tissues [126] [137]. Consequently, their surgical insertion triggers both acute and long-term tissue responses [128] [129] [130] [136]. Here, we tested the hypothesis that neural implants with mechanical properties matching the statics and dynamics of host tissues will display long-term bio-integration and functionality within the brain and spinal cord.

5.3 Results

We designed and engineered soft neural interfaces that mimic the shape and mechanical behavior of the dura mater (Fig. 5.1A-B, S5.1). The implant, which we called electronic dura mater or e-dura, integrates a transparent silicone substrate (120 μm in thickness), stretchable gold interconnects (35 nm in thickness), soft electrodes coated with a platinum-silicone composite (300 μm in diameter), and a compliant fluidic microchannel (100 μm x 50 μm in cross-section) (Fig. 5.1C-D, S5.2, S5.3, S5.4). The interconnects and electrodes transmit electrical excitation and transfer electrophysiological signals. The microfluidic channel, termed chemotrode [27], delivers drugs locally (Fig. 5.1C, S5.4). The substrate, encapsulation and microchannel silicone layers are prepared with soft lithography and assembled by covalent bonding following oxygen plasma activation (Fig. 5.1D, S5.2). Interconnects are thermally evaporated through a stencil mask, while electrodes are coated with the soft composite by screen-printing (fig. S5.2). Microcracks in the gold interconnects [54] and soft

Chapter 5. Electronic dura mater for long-term multimodal neural interfaces

platinum-silicone composite electrodes confer exceptional stretchability to the entire implant (Fig. 5.1B, Movie S1).

Most implants used experimentally or clinically to assess and treat neurological disorders are placed above the dura mater [137] [16] [69] [47]. The compliance of the soft implant enables surgical insertion below the dura mater through a small opening (Fig. 5.1A-C, S5.5). This location provides an intimate interface between electrodes and targeted neural tissues (Fig. 5.1E), and allows direct delivery of drugs into the intrathecal space. To illustrate these properties, we fabricated implants tailored to the spinal cord, one of the most demanding environments of the central nervous system. We developed a vertebral orthosis to secure the connector (Fig. 5.1F), and dedicated surgical procedures for subdural implantation (fig. S5.5). The soft implant smoothly integrated the subdural space along the entire extent of lumbosacral segments (2.5 cm in length and 0.3 cm in width), conforming to the delicate spinal neural tissue (Fig. 5.1E-F).

We next tested the long-term biointegration of soft implants compared to stiff, plastic implants (6 weeks). A stiff implant was fabricated using a 25 μm thick polyimide film, which corresponds to standard practices for flexible neural implants [53] and is robust enough to withstand the surgical procedure. Both types of implants were inserted into the subdural space of lumbosacral segments in healthy rats. A sham-operated group of animals received the headstage, connector, and vertebral orthosis but without spinal implant. To assess motor performance, high-resolution kinematic recordings of whole-body movement were conducted during basic walking and skilled locomotion across a horizontal ladder. In the chronic stages, the behavior of rats with soft implants was indistinguishable from that of sham-operated animals (Fig. 5.2A, S5.6 and Movie S2). By contrast, rats with stiff implants displayed significant motor deficits that emerged around 1-2 weeks post-implantation and deteriorated over time. They failed to accurately position their paws onto the rungs of the ladder (Fig. 5.2A). Even during basic walking, rats with stiff implants showed pronounced gait impairments including altered foot control, reduced leg movement, and postural imbalance (fig. S5.6). The spinal cords were explanted after 6 weeks of implantation. Both soft and stiff implants occupied the targeted location within the subdural space. Minimal connective tissue was observed around the implants. To evaluate potential macroscopic damage to the spinal cord that may explain motor deficits, the explanted lumbosacral segments were reconstructed in 3D. A cross-sectional circularity index was calculated to quantify changes in shape. All the rats with stiff implants displayed significant deformation of spinal segments under the implant ($p < 0.05$, Fig. 2B), ranging from moderate to

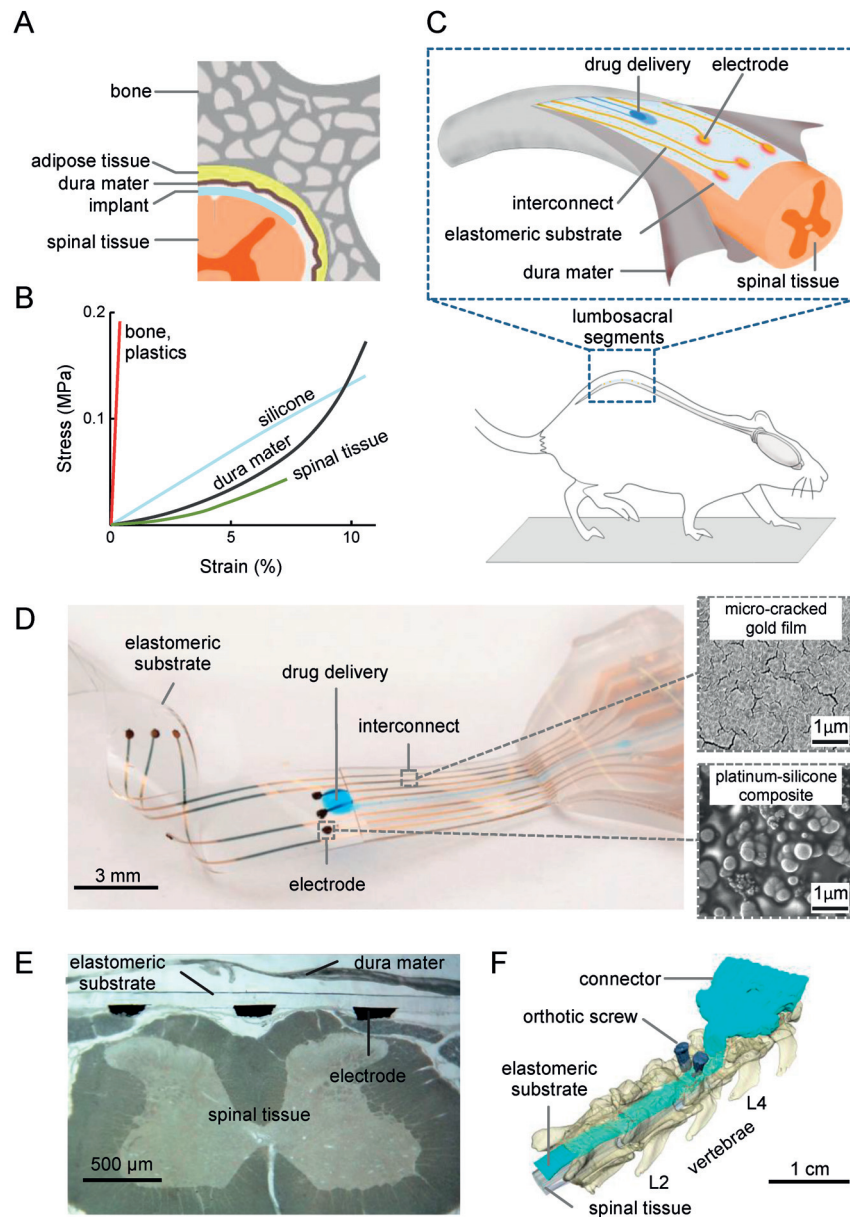


Figure 5.1 – Electronic dura mater, “e-dura,” tailored for the spinal cord. (A) Schematic cross-section of the vertebral column with the soft implant inserted in the spinal subdural space. (B) Strain-stress curves of spinal tissues, dura mater, implant materials, and complete e-dura. Plastics (polyimide), silicone, e-dura, and dura mater responses are experimental data. Spinal tissue response is adapted from the literature (see supplementary materials). (C) Illustration of the e-dura implant inserted in the spinal subdural space of rats. (D) Optical image of an implant, and micrographs of the gold film and the platinum-silicone composite. (E) Cross-section of an e-dura inserted in the spinal subdural space. (F) Reconstructed 3D micro-computed tomography scans of the e-dura inserted in the spinal subdural space covering L2 to S1 spinal segments in rats. The scan was obtained *in vivo* at week 5 after implantation.

extreme compression (fig. S5.7, Movie S2). Neuro-inflammatory responses at chronic stages were visualized using antibodies against activated astrocytes and microglia (Fig.

Chapter 5. Electronic dura mater for long-term multimodal neural interfaces

5.2C), two standard cellular markers for foreign body reaction [129]. As anticipated from macroscopic damage, both cell types massively accumulated in the vicinity of stiff implants ($p < 0.05$, Fig. 5.2C,S5.8). In striking contrast, no significant difference was found between rats with soft implants and sham-operated animals (Fig. 5.2C, S5.8). These results demonstrate the long-term biocompatibility of the soft implants.

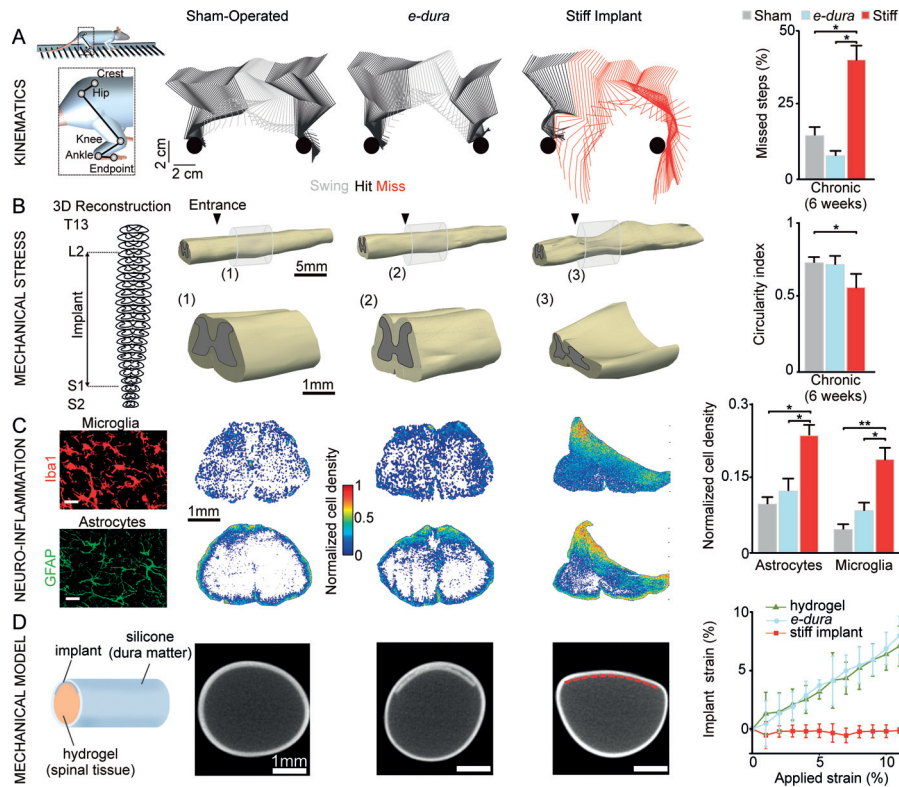


Figure 5.2 – Biointegration. (A) Hindlimb kinematics during ladder walking 6 weeks after implantation. Histogram plots reporting mean percentage of missed steps averaged per animal onto the rungs of the ladder ($n = 8$ trials per rat, $n = 4$ rats per group). (B) 3D spinal cord reconstructions, including enhanced views, 6 weeks after implantation. The arrowheads indicate the entrance of the implant into the subdural space. Bar plots reporting mean values of spinal cord circularity index ($4\pi \times \text{area}/\text{perimeter}^2$). (C) Photographs showing microglia (Iba1) and astrocytes (GFAP, glial fibrillary acidic protein) staining reflecting neuroinflammation. Scale bars: 30 mm. Heat maps and bar plots showing normalized astrocyte and microglia density. (D) Spinal cord model scanned using micro-computed tomography without and with a soft or stiff implant. e-dura implant is 120 μm thick. The red line materialized the stiff implant (25 μm thick), not visualized because of scanner resolution. Plot reporting local longitudinal strain as a function of global strain. Statistical test: Kruskal-Wallis one-way analysis of variance (* $P < 0.05$; ** $P < 0.01$). Error bars: SEM.

We manufactured a model of spinal cord using a hydrogel core to simulate spinal tissues, and a silicone tube to simulate the dura mater (fig. S5.9A). A soft or stiff implant was inserted into the model (Fig. 5.2D). The stiff implant induced a pronounced flattening of the simulated spinal cord, while the soft implant did not alter the circu-

larity of the model (Fig. 5.2D, S5.10). To provide the model with realistic metrics, the natural flexure of the spine was quantified in freely moving rats (fig. S9B). When the model was bent, the stiff implant formed wrinkles that induced local compressions along the hydrogel core. In contrast, the soft implant did not affect the smoothness of simulated spinal tissues (Fig. S5.11). When the model was stretched, the stiff implant slid relative to the hydrogel core, whereas the soft implant elongated together with the entire spinal cord (Fig. 5.2D, S5.11). Reducing the thickness of the plastic implant to $2.5\mu\text{m}$ improved bending stiffness and conformability. However, the ultra-thin, plastic implant still failed to deform during motion of the soft tissue (Fig. S5.10).

Patterning extremely thin films into web-like systems offers alternative mechanical designs for elastic surfaces [138] [139] [140]. For example, fractal-like meshes develop into out-of-plane structures during mechanical loading, which facilitates reversible and local compliance. Medical devices prepared with such 3D topologies can conform the curvilinear surface of the heart [141] and skin [139]. However, this type of interfaces requires complex, multi-step processing and transient packaging. In comparison, fabrication steps of e-dura are remarkably simple. Moreover, the shape and unusual resilience of the soft implant greatly facilitate surgical procedures.

The composite electrodes of the soft implant displayed low impedance ($Z = 5.2 \pm 0.8 \text{ k}\Omega$ at 1 kHz, $n = 28$ electrodes), and maintained the electrochemical characteristics of platinum (Fig. 5.3A-B). Cyclic voltammograms of the composite electrodes remained unchanged when the implant was stretched up to a strain of 45%. The high effective surface area of the platinum-silicone composite produced a large cathodal charge storage capacity of $46.9 \pm 3.3 \text{ mC/cm}^2$. This value is two orders of magnitude higher than that of smooth platinum [142], and is smaller but comparable to that of highly doped organic electrode coatings [143]. The composite electrode supported charge injection limit of $57 \pm 9 \mu\text{C/cm}^2$, which is comparable to the injection limit of platinum [142] (Fig. 5.3C, S5.12). These characteristics remained stable even after five million electrical pulses, which corresponds to more than 30 hours of continuous stimulation with clinically relevant parameters (40 Hz, charge-balanced, biphasic, $100 \mu\text{A}$ current pulse, 0.2 ms pulse width).

To demonstrate the robustness of the soft implant against deformation experienced by natural dura mater during daily living activities, we stretched the device to 20% strain over one million cycles. The implant, the chemotrode, and the seven embedded electrodes withstood the cyclic deformation, displaying minimal variation in impedance over time (Fig. 5.3D, S5.13, S5.14, Movie S1). Assuming radical postural changes approximately every 5 minutes, these results indicate that the soft implant

Chapter 5. Electronic dura mater for long-term multimodal neural interfaces

would survive mechanically for nearly a decade in a patient.

Electrode impedance and chemotrode functionality was evaluated over 5 weeks in 4 rats ($n = 28$ electrodes and 4 chemotrodes in total). Impedance at 1kHz remained constant throughout the 5 weeks of implantation (Fig. 5.3E), demonstrating stability of stretchable electrodes in vivo. Daily injections of drugs and hydrodynamic evaluations of microfluidic channels after explantation (fig. S5.4) confirmed that the chemotrodes remain operational for extended durations in vivo. These combined results demonstrate electrochemical stability, mechanical robustness, and long-term functionality of the soft electrodes and chemotrodes, abiding the challenging requirements for long-term implantation.

We exploited the soft neurotechnology to tailor electronic dura mater for the brain and spinal cord. An e-dura, consisting of a 3x3 electrode array, was placed over the motor cortex of mice expressing the light sensitive channel Channelrhodopsin-2 in the majority of neurons (Fig. 5.4A). The silicone substrate is optically transparent, enabling concurrent optical stimulation and neural recording. The cortical surface was illuminated with a laser focused on distinct locations to activate neurons locally. The spatial resolution of electrocorticograms recorded from the e-dura allowed extraction of neuronal activation maps that were specific for each site of stimulation (Fig. 5.4A).

An e-dura was then inserted between the dura mater and motor cortex tissues (fig. S5.5) to record electrocorticograms in conjunction with whole-body kinematic, and leg muscle activity in freely moving rats (Fig. 5.4B). Power spectral density analysis applied on electrocorticograms [144] identified standing and locomotor states over several weeks of recordings (Fig. 5.4B, S5.15). To verify whether neural recordings could also be obtained from an e-dura chronically implanted over spinal tissues, electrospinograms were measured in response to electrical stimulation of the motor cortex or the sciatic nerve. Descending motor command was reliably recorded (fig. S5.16), and peripheral sensory feedback was detected with remarkable spatial and temporal selectivity after 6 weeks of implantation (Fig. 5.4C, S5.16).

We finally exploited the e-dura to restore locomotion after spinal cord injury [31] [69]. Adult rats received a clinically relevant contusion at the thoracic level, which spared less than 10% of spinal tissues at the lesion epicenter, and led to permanent paralysis of both legs (Fig. 5.4D). An e-dura covering lumbosacral segments (Fig. 5.1) was used to engage spinal locomotor circuits located below injury. A serotonergic replacement therapy (5HT1A/7 and 5HT2 agonists) [145] was injected through the chemotrode, and continuous electrical stimulation was delivered on the lateral aspect of L2 and S1 segments (40 Hz, 0.2 ms, 50-150 μ A) [7]. The concurrent and co-localized

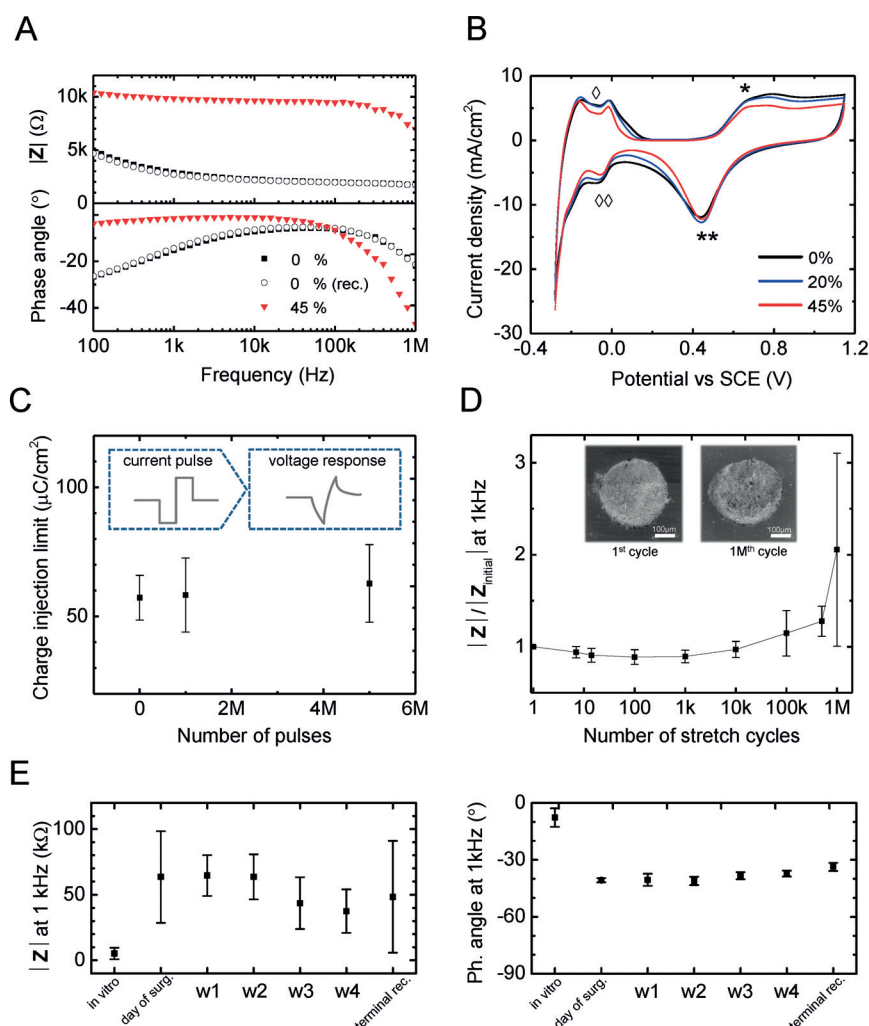


Figure 5.3 – Properties of e-dura electrodes. (A) Magnitude and phase of electrode impedance recorded in saline solution (pH 7.4). Spectra were collected before (■), at maximum elongation (▼), and after (○) a uniaxial stretch cycle to 45% strain. (B) Cyclic voltammograms recorded in diluted sulfuric acid (pH 0.9) during a uniaxial stretch cycle to 45% strain. Cyclic voltammetry (50 mV/s) reveals high current densities through the electrode even at large strain. Peaks correspond to oxide formation (*), oxide reduction (**), H⁺ adsorption (◇◇), and H⁺ desorption (◇) on Pt metal surfaces. (C) Charge injection limit of electrodes ($n = 4$, mean TSD) and evolution after repeated pulsing. (D) Relative impedance modulus of electrodes ($n = 7$, mean TSD) at 1 kHz and at rest and after uniaxial fatigue cycling to 20% strain. Inset: electron micrographs of an electrode after the first and one millionth stretch cycles. (E) Modulus and phase at 1 kHz ($n = 28$ total electrodes, mean TSD, across four rats) recorded in vitro, then in vivo immediately after implantation and weekly until terminal procedure.

electrical and chemical stimulations enabled the paralyzed rats to walk (Fig. 5.4E). Intrathecal delivery allowed a 4-fold reduction of injected drug volume compared to intraperitoneal injection required to obtain the same facilitation of stepping (fig. S5.17). Subdural drug delivery through the chemotrode eliminated side effects of serotonergic agents on autonomic systems (fig. S17). The distributed electrodes

delivered stimulation restricted to specific segments, which allowed facilitation of left versus right leg movements (fig. S5.18, Movie S3). The e-dura mediated reliable therapeutic effects during the 6-week rehabilitation period.

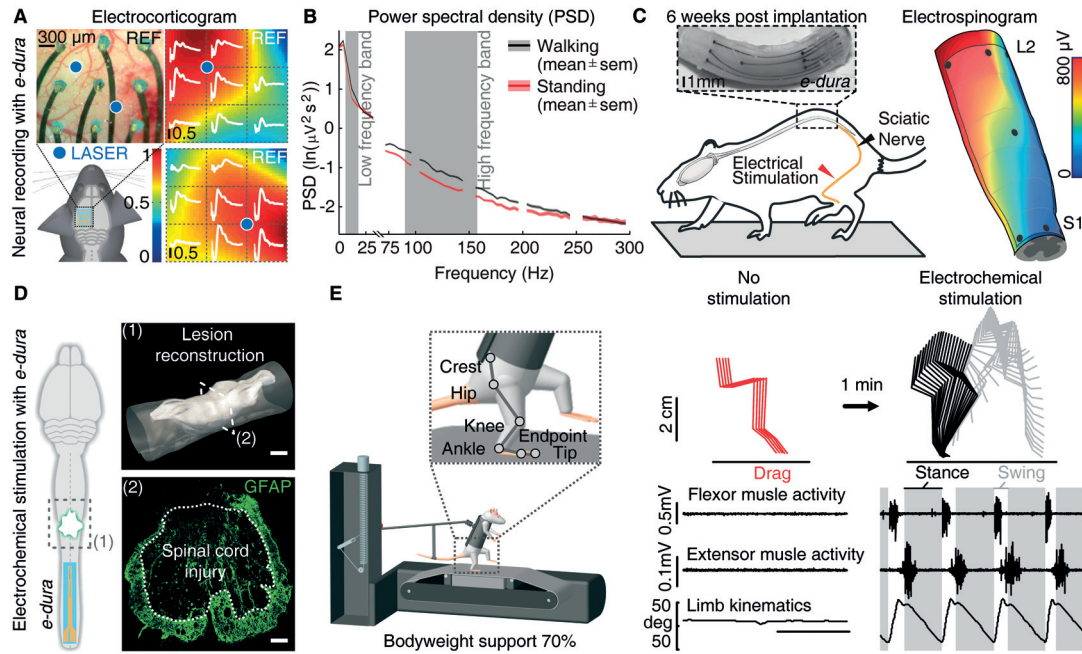


Figure 5.4 – Recordings and stimulation with e-dura. (A) e-dura implant positioned over the cortical surface of a Thy1-ChR2-YFP (yellow fluorescent protein) mouse. Blue spot indicates laser location. Cortical activation maps were reconstructed from normalized electrocorticograms, shown in white (150-ms duration). (B) Power spectral density computed from motor cortex electrocorticograms recorded 3 weeks after e-dura implantation in rats. Increased neural activity in low- and high-frequency bands differentiate cortical states during walking from those during standing. (C) Spinal cord activation map was reconstructed from electrospinochograms recorded 6 weeks after e-dura implantation in response to left sciatic nerve stimulation. (D) Rats were implanted with a spinal e-dura covering lumbosacral segments and received a severe spinal cord injury. (E) Recording without and with electrochemical stimulation during bipedal locomotion under robotic support after 3 weeks of rehabilitation. Stick diagram decompositions of hind-limb movements are shown together with leg muscle activity and hindlimb oscillations.

5.4 Discussion

We have introduced soft neural implants that show long-term bio-integration and functionality within the central nervous system. Computerized and mechanical simulations demonstrated that the biomechanical coupling between implants and neural tissues is critical to obtain this symbiosis. Neural implants prepared with elastic materials met the demanding static and dynamic mechanical properties of spinal and brain tissues. Even in the subdural space, the soft implant triggered limited foreign body reaction. This location enables local drug application reducing side

effects, high-resolution neuronal recordings, and concurrent delivery of electrical and chemical neuromodulation alleviating neurological deficits for extended periods of time. The integration of tissue-matched implants with higher electrode density, implantable pumps for drug delivery, and embedded electronics to read and write into the nervous system in real-time requires additional technological developments. While challenges lie ahead, e-dura holds promises for a new generation of diagnostic and clinical interfaces.

5.5 Materials and Methods

5.5.1 Soft e-dura materials and fabrication process

We designed and fabricated brain and spinal e-dura implants using soft neurotechnology. The spinal implant hosts seven electrodes, distributed along the length of the implant in a 3-1-3 configuration array, and a microfluidic delivery system (single channel). The brain implant consists of electrodes, patterned in a 3x3 matrix. A generic fabrication process is presented in fig. S5.2. The fabrication steps of the three components integrated in e-dura implants are detailed below.

Interconnects (fig. S5.2-1)

i) First a 100 μm thick substrate of polydimethylsiloxane (PDMS, Sylgard 184, Dow Corning, mixed at 10:1, w:w, pre-polymer:cross-linker) was spin-coated on a 3" silicon carrier wafer pre-coated with polystyrene sulfonic acid (water soluble release layer). The PDMS substrate was then cured overnight in a convection oven (80°C). ii) Then a customized Kapton© shadow mask patterned with the negative of the electrode layout was laminated on the PDMS substrate. Thermal evaporation of 5/35 nm of chromium/gold (Cr/Au) metal films through the shadow mask deposited the interconnect tracks (Auto 360, Edwards).

Electrical passivation layer (fig. S5.2-2)

i) The interconnect passivation layer was prepared in parallel. A 5" wafer sized, 5mm thick slab of PDMS was produced and its surface was functionalized with a 1H,1H,2H,2H-perfluorooctyltriethoxysilane (Sigma-Aldrich) release monolayer under weak vacuum. Two thin PDMS layers of 20 μm thickness were sequentially spin-coated on the thick PDMS slab, individually cured then treated with the debonding monolayer. In cross-section, the structure was a triple stack consisting of a thick PDMS slab and two thin PDMS layers. The release coatings allowed for each of the 20 μm thick layers to be peeled off independently at a later stage. ii) Using a hollow glass capillary of a pre-defined tip diameter, both 20 μm thick PDMS layers were simultaneously punctured at locations corresponding to the sites of the electrodes.

Encapsulation (fig. S5.2-3)

i) Both PDMS triple stack and interconnect wafers were exposed to brief air plasma activating the silicone surfaces. The triple stack was flipped upside down to align

the punctured holes with the underlying electrodes. ii) The two pieces were brought together to form a covalent bond. The thick PDMS slab was peeled off, leaving behind the two 20 μm thick PDMS layers on top of the interconnects.

Soft platinum-silicone composite preparation and patterning (fig. S5.2-4)

i) e-dura electrode sites were coated with a customized platinum-silicone composite. The conductive composite was a blend of platinum nano-micro particles and PDMS (Sylgard 184, Dow Corning). The PDMS pre-polymer, mixed with its cross-linker, was diluted in heptane in a 1:2 w:w ratio to create a low viscosity liquid. In a small container, 100 mg of platinum microparticles (Pt powder, particle size 0.5-1.2 μm , Sigma-Aldrich) was added to 5mg of PDMS (15 μL of heptane diluted PDMS). This mixture was thoroughly stirred and put aside for evaporation of the heptane fraction. The addition of 5mg doses of PDMS was repeated until the mixture (after heptane evaporation) became a paste. Paste formation occurs when the PDMS content is 15-20% by weight. Immediately before dispensing onto the electrode sites, the paste may be thinned with a drop of pure heptane. ii) To form the active electrode coating, a bolus of conductive composite paste was “printed” i.e. spread and pressed into the holes of the upper encapsulation layer. iii) The upper encapsulation layer was then peeled off, leaving bumps of conductive composite precisely at the active electrode sites. The bottom 20 μm thick PDMS layer remained permanently bonded to the electrode-interconnect e-dura substrate, thereby providing electrical encapsulation. The array was placed in a convection oven at 60°C overnight to ensure full polymerization of the conductive paste.

Microfluidic and connector integration (fig. S5.2-5)

i) To form the microfluidic delivery system, an additional 80 μm thick PDMS layer was bonded to the metallized e-dura substrate. This layer covered approximately a third of the length of the implant and contained a central microfluidic channel (100x50 μm^2 in cross section), terminating 2 mm caudally from the 3 caudal electrodes (Movie S1). The connector side of the microchannel was interfaced with a polyethylene capillary (0.008” i.d., 0.014” o.d., Strategic Applications Inc.) and sealed with a bolus of fast-cure silicone (KWIK-SIL, World Precision Instruments). ii) A custom-made soft-to-wires electrical connector was assembled for all the e-dura implants. De-insulated ends of ‘Cooner’ wires (multistranded steel insulated wire, 300 μm o.d., Cooner wire Inc.) were carefully positioned above the terminal pads of the gold film interconnects. The electrical contact was enhanced by ‘soldering’ the wires to the contact pads with a conductive polymer paste (H27D, component A, EPO-TEK) deposited below and

Chapter 5. Electronic dura mater for long-term multimodal neural interfaces

around each electrical wire. To stabilize the connector, the ‘solder’ connection area was flooded with a silicone adhesive to form a package (One component silicone sealant 734, Dow Corning) (Fig. 5.1D).

Release (fig. S5.2-6)

i) The contour of the finished implant was cut out from the wafer using a razor blade. The implant was released from the carrier wafer upon a brief immersion in water.

5.5.2 Description of the implants prepared for the biocompatibility study

For the purpose of the biocompatibility study, we designed and fabricated soft e-dura and stiff implants. Four copies of each type were fabricated and implanted chronically in the subdural space of the lumbosacral spinal cord in healthy rats.

Soft implants

The e-dura were functional silicone implants, including both the microfluidic channel and seven electrodes, and were designed to fit the intrathecal space of the spinal cord. The implants were prepared following the process presented above.

Stiff implants

Stiff implants were cut out from 25 μm thick polyimide foil (KaptonTM-100HN, DuPont). The intraspinal dwelling portion of these devices was 3.2 mm wide and 3 cm long. The contour of the implant was cut out using a laser micromachining tool (LAB 3550, Inno6 Inc.) and had rounded edges to minimize tissue trauma during insertion. At its caudal end, the implant integrated the same trans-spinal electrical connector as the one used in the soft implants. However, neither electrodes nor interconnects were patterned on the polyimide foil. The dummy connector was 8mm long, 11mm wide and 2 mm thick and coupled seven insulated wires (multistranded steel insulated wire, 300 μm o.d., Cooner wire Inc.) that run sub-cutaneous away from the spinal orthosis to a head mounted socket (12 pin male micro-circular connector, Omnetics corp.).

Sham-operated rats

Sham-operated rats received an implant without intraspinal portion. The implant consisted of the same connector as that used in the other two types of implants, which was secured with the spinal orthosis, and then attached to seven wires running subcutaneously, and terminating in a head-mounted Omnetics connector.

5.5.3 Mechanical spinal cord model (fig. S5.9A)

We assembled a spinal cord model to simulate the mechanical interaction between spinal tissue and soft versus stiff implants after their positioning on the spinal tissue and during dynamic movement of the spinal cord. Artificial dura mater and spinal tissues were fabricated from PDMS and gelatin hydrogel, respectively ([146] [147]). One end of a polystyrene rod (20 cm long, 3.2 mm diameter) was attached to the drive shaft of a mixer. The mixer was positioned so that the rod was horizontal and rotating about its long axis, approximately a centimeter above the surface of a hotplate. Several grams of freshly prepared PDMS pre-polymer (Sylgard 184, Dow Corning) were dispensed along the length of the rotating rod. By adjusting the rotation speed, the distance between rod and hotplate, and the hotplate temperature, the thickness of the PDMS film that coated the polystyrene rod was controlled. Following thorough curing of the silicone coating, the polystyrene core was dissolved by immersion in acetone overnight. Thorough rinsing and de-swelling of the silicone in water left a PDMS tube with wall thickness ranging 80-120 μm . One end of the tube was pinched and sealed with a bolus of fast-cure silicone (KWIK-SIL, World Precision Instruments), the other end was trimmed to a total tube length of 8.5 cm. Artificial spinal tissue was fabricated by pouring warm ($\approx 40^\circ\text{C}$) gelatin solution (10% gelatin by weight in water, gelatin from bovine skin, Sigma-Aldrich) into a silicone mold containing a cylindrical cavity, 3.2mm in diameter and 10 cm long. The mold was then placed in a fridge for 1h to allow for the gel to set. The gelatin ‘spinal tissue’ was recovered from the mold and placed in a desiccator under mild vacuum for several hours. Partial loss of water content caused shrinkage and stiffening of the gelatin ‘spinal tissue’. This allowed for its insertion inside the surrogate dura mater tube together with a stiff or soft implant. The assembled model was then immersed in water overnight to re-hydrate the hydrogel ‘spinal tissue’ and secure the implant in the artificial intrathecal space. The open end of the model was then sealed with quick setting silicone and the model was ready for mechanical tests. Verification of the compression modulus of the hydrogel was conducted through an indentation test. A large slab (6 cm thickness, 12cm diameter) of gelatin hydrogel was prepared and indented with a spherical indenter (6 mm diameter) mounted on a mechanical testing platform (Model 42, MTS

Criterion). By fitting a Hertz contact model to experimental force versus displacement data we obtained a compressive elastic modulus of 9.2 ± 0.6 kPa ($n=5$ test runs) for the 10% gelatin hydrogel. Indentation of rat spinal cords yields closely comparable values [148].

5.5.4 In vitro electrochemical characterization of e-dura electrodes

In vitro Electrochemical Impedance Spectroscopy of e-dura electrodes under stretch (Fig. 5.3A, E, S5.13)

We developed an experimental set-up combining electrochemical impedance spectroscopy with cyclic mechanical loading. The e-dura implant under test was mounted in a customized uni-axial stretcher and immersed in saline solution to conduct electrochemical characterization of the electrodes following different stretching protocols. Electrochemical Impedance Spectroscopy measurements were conducted in phosphate buffered saline (PBS, pH 7.4, Gibco) at room temperature using a three-electrode setup and a potentiostat equipped with a frequency response analyzer (Reference 600, Gamry Instruments). A 5 cm long Pt wire served as counter electrode and a Standard Calomel Electrode (SCE) as reference. Impedance spectra were taken at the open circuit potential. The excitation voltage amplitude was 7mV. Impedance spectra of individual electrodes were measured at tensile strains of 0%, 20% and 45%. Stretching in PBS of the e-dura implants was conducted in a LabView-controlled, custom-built uniaxial tensile stretcher programmed to actuate two clamps moving in opposite directions along a horizontal rail. Each clamp held a stiff plastic rod pointing downwards from the plane of motion. The lower halves of the rods were submerged in a vessel holding electrolyte. The device under test was attached to the submerged part of the rods with silicone glue (KWIK-SIL, World Precision Instruments), so that the motion of the clamps was transferred to the device under test (Movie S1). The stretcher was programmed to hold the implant under test at a specific strain or to execute a pre-set number of stretch-relaxation cycles (for example 0%-20%-0% at a stretch rate of 40% /s).

Cyclic Voltammetry (CV) of electrodes under stretch (Fig. 5.3B)

CV responses were recorded in 0.15M H₂SO₄ (pH 0.9) under N₂ purge. A potential scan rate of 50 mV/s was used within the potential range of -0.28 V to +1.15 V (vs. SCE). Due to the difference in pH, this potential range corresponds to -0.6 V to +0.8 V (vs. SCE) in PBS. For each tested electrode, 20 priming cycles (1,000 mV/s) were applied to allow the electrode to reach a steady state.

Charge injection capacity (CIC) of e-dura electrodes (fig. S5.12, 5.3C)

CIC is a measure of the maximum charge per phase per unit area an electrode coating can deliver through reversible surface reactions. For CIC determination, electrodes with the platinum-silicone composite coating were immersed in PBS and cathodic-first, biphasic current pulses (200 μ s per phase) were passed between the electrode and a large platinum counter electrode. A pulse stimulator (Model 2100, A-M Systems) delivered the current pulses, and the electrode polarization (vs. SCE) was recorded on an oscilloscope (DPO 2024 Digital Phosphor Oscilloscope, Tektronix). The amplitude of the current pulses was gradually increased until the electrode under test was polarized just outside the water window (the instantaneous polarization of the electrodes due to Ohmic resistances in the circuit was subtracted from voltage traces). For experiments where the CIC was determined after cyclic pulse delivery, the repeating pulses were charge balanced, biphasic (200 μ s per phase) with amplitude of 100 μ A.

5.5.5 In vivo Electrochemical Impedance Spectroscopy of e-dura electrodes (fig. 5.3E)

The impedance of e-dura electrodes implanted over lumbosacral segments were recorded using a bipolar electrode configuration (working and counter electrode only). The counter electrode was a 'Cooner' wire whose de-insulated tip was implanted in the osseous body of vertebra L1. As with in vitro measurements, impedance spectra were obtained with a potentiostat equipped with a frequency response analyzer (Reference 600, Gamry Instruments) using the same settings. Weekly electrochemical impedance spectroscopy measurements of all electrodes were made in fully awake rats held by an experienced handler.

5.5.6 Scanning Electron Microscopy of e-dura electrodes (fig. S5.14)

Scanning electron microscopy (Zeiss Merlin FE-scanning electron microscope) was used to visualize e-dura electrodes under tensile strain. Prior to imaging, a 5nm thick layer of platinum was sputtered on the implant under investigation. To image the electrode active sites under tensile strain in situ, the e-dura implant was mounted and stretched in a custom-made miniature stretcher that can be inserted in the microscope chamber.

5.5.7 Mechanical characterization of the platinum-silicone composite (fig. S5.3)

A block of platinum-silicone composite was cut to produce a high aspect-ratio pillar of 3 mm height and $480\ \mu\text{m} \times 110\ \mu\text{m}$ rectangular base. The sample was glued to a glass slide so that the pillar's long axis was vertical (sticking out of the plane of the glass slide). A miniature force probe (FT-S10000 Lateral Microforce Sensing Probe, FemtoTools) applied a force at the tip of and normal to the pillar. Using beam bending theory, the geometry of the beam, and its force-displacement characteristics, we computed a value for the composite's Young's modulus of 10 MPa.

5.5.8 Tensile mechanical properties of rat spinal cord (Fig. 5.1B)

A section of rat dura mater was explanted from a 2-month old Lewis rat and cut to a strip with dimensions of 3.4 mm x 1 mm. Immediately post explantation, each end of the strip was secured to a glass cover slip using a fast acting cyanoacrylate adhesive. The cover slips were inserted into the clamps of a tensile testing platform (Model 42, MTS Criterion). Extension at strain rate of 0.5%/s was continuously applied until the dura mater sample failed. The thickness of the dura mater sample was determined from optical micrographs. During the process of mounting and stretching, the dura mater sample was kept hydrated with saline dispensed from a micropipette. The stress(strain) response plotted Fig. 5.1B for spinal tissues was adapted from ([147]).

5.5.9 Animal groups and surgical procedures

All surgical procedures were performed in accordance with Swiss federal legislation and under the guidelines established at EPFL. Local Swiss Veterinary Offices approved all the procedures. Experiments were performed on Lewis rats (LEW/ORLj) with initial weight of 180-200 g.

Animal groups

- In the biocompatibility study, rats received either a sham (n=4), stiff (n=4) or soft (n=4) implant. Prior to surgery rats were handled and trained daily in the locomotor tasks for three weeks. These tasks included walking overground along a straight runway, and crossing a horizontal ladder with irregularly spaced rungs. Prior to the training, rats underwent a mild food deprivation and were rewarded with yoghurt at the end of each trial. The body weight was monitored closely;

in case of weight loss the food deprivation was adjusted. The animals were terminated 6 weeks post-implantation.

- In the study with electrochemical spinal cord stimulation, rats (n=3) were first implanted with an e-dura over lumbosacral segments, and with bipolar electrodes into ankle muscles to record electromyographic (EMG) activity. After 10 days of recovery from surgery, they received a spinal cord injury.
- Recording of electrospinograms were obtained in a separate group of rats that were implanted with an e-dura over lumbosacral segments, and with bipolar electrodes into ankle muscles of both legs. Recordings were obtained after 6 weeks of implantation.
- Recording of electrocorticograms were obtained in a group of rats (n = 3) that were implanted with an e-dura over the leg area of the motor cortex, and with bipolar electrodes into ankle muscles of both legs. These rats followed the same behavioral training as rats in the biocompatibility group.
- Recording of electrocorticograms following optical stimulation were obtained in Thy1-ChR2-YFP transgenic mice (Jackson Laboratories, B6.Cg-Tg-(Thy1-COP4/EYFP)18Gfng/J) under acute, anesthetized conditions.

Implantation of e-dura into the spinal subdural space (fig. S5.5A-B)

The e-dura were implanted under Isoflurane/Dorbene anesthesia. Under sterile conditions, a dorsal midline skin incision was made and the muscles covering the dorsal vertebral column were removed. A partial laminectomy was performed at vertebrae levels L3-L4 and T12-T13 to create entry and exit points for the implant. To access the intrathecal space, a 3mm long mediolateral incision was performed in the dura mater at both laminectomy sites. A loop of surgical suture (Ethilon 4.0) was inserted through the rostral (T12-T13) dura mater incision and pushed horizontally along the subdural space until the loop emerged through the caudal (L3-L4) dura mater incision. The extremity of the implant was then folded around the suture loop. The loop was then retracted gently to position the implant over the spinal cord. A small portion of the implant protruded beyond the rostral dura mater incision and could be manipulated with fine forceps to adjust the mediolateral and rostrocaudal positioning of the implant. Electrophysiological testing was performed intra-operatively to fine-tune positioning of electrodes with respect to lumbar and sacral segments [7]. The protruded extremity of the implant became encapsulated within connective tissues, which secured positioning of the implant in the chronic stages. The soft-to-wires (and microfluidic) connector was secured to the bone using a newly developed vertebral

Chapter 5. Electronic dura mater for long-term multimodal neural interfaces

orthosis. The connector was first positioned above the vertebral bone. Four micro-screws (Precision Stainless Steel 303 Machine Screw, Binding Head, Slotted Drive, ANSI B18.6.3, # 000-120, 0.125) were inserted into the bone of rostral and caudal vertebrae. Surgical suture (Ethilon 4.0) was used to form a cage around the micro-screws and connector. The walls of the cage were plastered using freshly mixed dental cement (ProBase Cold, Ivoclar Vivadent) extruded through a syringe. After solidification of the dental cement, the electrical wires and microfluidic tube were routed sub-cutaneously to the head of the rat, where the Omnetics electrical connector and the microfluidic access port were secured to the skull using dental cement. The same method was used to create the vertebral orthosis for stiff and sham implants in the biocompatibility study.

Implantation of e-dura into the cortical subdural space (fig. S5.5C-D)

The e-dura were implanted under Isoflurane/Dorbene anesthesia. Under sterile conditions, 2 trepanations were performed on the left half of the skull to create two windows rostral and caudal to the leg area of the motor cortex. The first window was located cranially with respect to the coronal suture, while the second window was located cranially with respect to the interparietal suture. Both windows were located close to sagittal suture in order to position the center of the e-dura electrodes 1 mm lateral and 1mm caudal relative to the bregma. The surgical insertion technique developed for passing e-dura into the spinal subdural space was also used to implant e-dura into the cortical subdural space. Excess PDMS material was cut in the cranial window, and the edge of the implants sutured to the dura mater using a Ethilon 8.0 suture. The exposed parts of the brain and external part of the e-dura were covered with surgical silicone (KWIK-SIL). A total of 4 screws were implanted into the skull around the e-dura connector before covering the entire device, the connector, and the percutaneous amphenol connector with dental cement. Implantation of electrodes to record muscle activity All the procedures have been reported previously [7]. Briefly, bipolar intramuscular electrodes (AS632; Cooner Wire) were implanted into the tibialis anterior and medial gastrocnemius muscles, bilaterally. Recording electrodes were fabricated by removing a small part (1 mm notch) of insulation from each wire. A common ground wire (1 cm of Teflon removed at the distal end) was inserted subcutaneously over the right shoulder. All electrode wires were connected to a percutaneous amphenol connector (Omnetics Connector Corporation) cemented to the skull of the rat. The proper location of EMG electrodes was verified post-mortem.

Spinal cord injury

Under Isoflurane/Dorbene anesthesia, a dorsal midline skin incision was made from vertebral level T5 to L2 and the underlying muscles were removed. A partial laminectomy was performed from around T8 to expose the spinal cord. The exposed spinal cord was then impacted with a metal probe with a force of 250 kDyn (IH-0400 Impactor, Precision Systems and Instrumentation). The accuracy of the impact was verified intra-operatively, and all the lesions of the animals used in this study were reconstructed post-mortem.

5.5.10 Rehabilitation procedures after spinal cord injury

Rats with severe contusion spinal cord injury were trained daily for 30min, starting 7 days post-injury. The neurorehabilitation program was conducted on a treadmill using a robotic bodyweight support system (Robomedica) that was adjusted to provide optimal assistance during bipedal stepping [31] [7]. To enable locomotion of the paralyzed legs, a serotonergic replacement therapy combining quipazine (0.03 ml) and 8-OHDPAT (0.02 ml) was administered through the microfluidic channel of chronically implanted e-dura, and tonic electrical stimulation was delivered through the electrodes located overlying the midline of lumbar (L2) and sacral (S1) segments (40Hz, 0.2ms pulse duration, 50-200 μ A) [7].

5.5.11 Histology and Morphology of explanted spinal cord

Fixation and explantation

At the end of the experimental procedures, rats were perfused with Ringer's solution containing 100 000 IU/L heparin and 0.25% NaNO₂ followed by 4% phosphate buffered paraformaldehyde, pH 7.4 containing 5% sucrose. The spinal cords were dissected, post-fixed overnight, and transferred to 30% phosphate buffered sucrose for cryoprotection. After 4 days, the tissue was embedded and the entire lumbosacral tract sectioned in a cryostat at a 40 μ m thickness.

3D reconstruction of the spinal cord (Fig. 5.2B, S5.7)

To assess spinal cord morphology, a Nissl staining was performed on 25 evenly spaced lumbosacral cross-sections separated by 0.8 mm, for each rat. The slides were assembled into the Neurolucida image analysis software (MBF Bioscience, USA) to reconstruct lumbosacral segments in 3D. Spinal cord compression was quantified us-

Chapter 5. Electronic dura mater for long-term multimodal neural interfaces

ing a circularity index defined as $4\pi \text{ area/perimeter}^2$. Circularity index was measured for all the slices, and averaged for each rat to obtain a mean value that was compared across groups.

Immunohistochemistry protocols (Fig. 5.2C, S5.8)

Microglial and astrocytic reactivity was revealed by performing immunohistological staining against glial fibrillary acidic protein (GFAP) and ionized calcium binding adapter molecule 1 (Iba1), respectively. Briefly, lumbosacral spinal cord coronal sections were incubated overnight in serum containing anti-Iba1 (1:1000, Abcam, USA) or anti-GFAP (1:1000, Dako, USA) antibodies. Immunoreactions were visualized with appropriate secondary antibodies labeled with Alexa fluor® 488 or 555. A fluorescent counterstaining of the Nissl substance was performed with the Neurotrace 640/660 solution (1:50, Invitrogen, USA). Sections were mounted onto microscope slides using anti-fade fluorescent mounting medium and covered with a cover-glass. The tissue sections were observed and photographed with a laser confocal fluorescence microscope (Leica, Germany).

Immunostaining quantification

Immunostaining density was measured offline using 6 representative confocal images of lumbosacral segments per rat. Images were acquired using standard imaging settings that were kept constant across rats. Images were analyzed using custom-written Matlab scripts according to previously described methods [31]. Confocal output images were divided into square regions of interest (ROI), and densities computed within each ROI as the ratio of traced fibers (amount of pixels) per ROI area. Files were color-filtered and binarized by means of an intensity threshold. Threshold values were set empirically and maintained across sections, animals and groups. All the analyses were performed blindly.

5.5.12 μ -Computed Tomography

Spinal cord model (Fig 5.2D, S5.10)

Non-destructive computed tomography (CT) reconstructions of the spinal cord model were obtained with a Skyscan 1076 scanner (Bruker microCT, Kontich, Belgium). The following settings were used: accelerating voltage 40 kV, accelerating current 250 μ A, exposure time per image 180 ms, angular resolution 0.5°. The resultant projection images were reconstructed into 3D renderings of the model using NRecon

and GPURecon Server (Bruker microCT, Kontich, Belgium). The resultant volumetric reconstructions had a voxel size of 37 μm . This limit prevented the direct visualization of stiff implants, whose thickness was 25 μm .

In-vivo implant imaging (Fig. 5.1F)

Imaging of implanted e-dura (5 weeks post implantation) was conducted in the same scanner. Rats were kept under Isoflurane anesthesia during the scan to reduce motion artifacts. Scanner settings were adjusted to avoid artefacts induced by metallic parts of the spinal orthosis (typical settings were: 1 mm aluminum filter, voltage 100 kV, current 100 μA , exposure time 120 ms, rotation step 0.5). Prior to imaging, a contrast agent (Lopamiro 300, Bracco, Switzerland) was injected through the microfluidic channel of the implants to enable visualization of soft tissues and e-dura. Segmentation and 3D model were constructed with Amira® (FEI Visualization Sciences Group, Burlington, USA).

5.5.13 Recordings and analysis of muscle activity and whole-body kinematics (Fig. 5.2, 5.4, S5.6, S5.17, S5.18)

Bilateral hindlimb kinematics were recorded using 12 infrared motion capture cameras (200 Hz; Vicon). Reflective markers were attached bilaterally overlying iliac crest, greater trochanter (hip), lateral condyle (knee), lateral malleolus (ankle), distal end of the fifth metatarsal (limb endpoint) and the toe (tip). Nexus (Vicon) was used to obtain 3D coordinates of the markers. The body was modeled as an interconnected chain of rigid segments, and joint angles were generated accordingly. Muscle activity signals (2 kHz) were amplified, filtered (10–1000 Hz bandpass) and recorded using the integrated Vicon system. Concurrent video recordings (200 Hz) were obtained using two cameras (Basler Vision Technologies) oriented at 90° and 270° with respect to the direction of locomotion ([31] [7]). A minimum of 8 gait cycles was extracted for each experimental condition and rat. A total of 135 parameters quantifying gait, kinematics, ground reaction force, and muscle activity features were computed for each limb and gait cycle according to methods described in detail previously ([31] [7]). These parameters provide a comprehensive quantification of gait patterns ranging from general features of locomotion to fine details of limb motion. The entire list of 135 computed parameters is described in table S5.19.

Principal component analysis

The various experimental conditions led to substantial gait changes, which were evident in the modification of a large proportion of the computed parameters. In order to extract the relevant gait characteristics for each experimental condition, we implemented a multi-step statistical procedure based on principal component (PC) analysis ([31] [7]). PC analyses were applied on data from all individual gait cycles for all the rats together. Data were analyzed using the correlation method, which adjusts the mean of the data to zero and the standard deviation to 1. This is a conservative procedure that is appropriate for variables that differ in their variance (e.g. kinematic vs. muscle activity data). PC scores we extracted to quantify differences between groups or conditions. Analysis of factor loadings, i.e. correlation between each variable and PC, identified the most relevant parameters to explain differences illustrated on each PC.

5.5.14 Acute recordings of electrocorticograms in mice (Fig. 5.4A)

Thy1-ChR2-YFP mice were anesthetized with Ketamine/Xylazine and head-fixed in a stereotaxic frame (David Kopf Instruments). A 2x2 mm² craniotomy was performed over the leg area of the motor cortex, which was verified by the induction of leg movements in response to optogenetic stimulation. The e-dura was placed over the exposed motor cortex and covered with physiological saline. We employed a diode-pumped solid state blue laser (473 nm, Laserglow technologies) coupled via a FC/PC terminal connected to a 200 μ m core optical fiber (ThorLabs) to deliver optical stimulation. Using a micromanipulator, the fiber was placed at the center of each square formed by 4 adjacent electrodes. Optical stimulation was delivered through the transparent elastomeric substrate to illuminate the surface of the motor cortex. A train of light pulses was delivered at 4 Hz, 9 ms duration, 30 mW intensity for each site of stimulation. Electrocorticograms were recorded using the same methods as employed in rats. For each electrode, the amplitude of light-induced electrocorticograms was extracted, normalized to the maximum recorded amplitude for that electrode, and the peak to peak amplitude calculated. The values measured across all the electrodes were used to generate color-coded neuronal activation maps.

5.5.15 Long-term in vivo recordings of electrocorticograms in freely behaving rats (Fig. 5.4B, S5.15)

Electrocorticograms were measured in conjunction with whole body kinematics and muscle activity recordings during standing and walking in freely behaving rats (n=3

rats). The rats were tested every week for 3 weeks after chronic implantation of the e-dura over the hindlimb area of the motor cortex. A lateral active site integrated in the e-dura was used as a reference for differential amplification. A wire ground was fixed to the skull using a metallic screw. Differential recordings were obtained using a TDT RZ2 system (Tucker Davis Technologies), amplified with a PZ2 pre-amplifier, sampled at 25 kHz, and digital band-passed filtered (0.1-5000 Hz). Raw electrocorticograms were elaborated using previously described methods [145], which are summarized in fig. S5.15. Kinematic and muscle activity recordings were used to dissociate standing and walking states.

5.5.16 Chronic recordings of electrospinograms (Fig. 5.4C, S5.16)

Recordings of electrical potentials from the electrodes integrated in the chronically implanted e-dura, which we called electrospinograms, were performed after 6 weeks of implantation (n=3 rats). Experiments were performed under urethane (1 g/kg, i.p.) anesthesia. Both electrospinograms and muscle activity were recorded in response to stimulation delivered to peripheral nerve or motor cortex. The sciatic nerve was exposed, and insulated from the surrounding tissue using a flexible plastic support. A hook electrode was used to deliver single biphasic pulses of increasing amplitude, ranging from 150 to 350 μ A, and 100 μ s pulse-width, at 0.5 Hz. Each trial was composed of at least 30 pulses. Responses measured in chronically implanted muscles and from each electrode integrated in the e-dura, were extracted and triggered-averaged. To elicit a descending volley, a custom-made wire electrode was inserted overlying the leg area of the motor cortex, in direct contact with the dura mater. Current controlled bi-phasic pulses were delivered every minute using a 1mA, 1ms pulse-width stimulus. Responses were then extracted, and triggered-averaged. Signals were recorded using a TDT RZ2 system (Tucker Davis Technologies), amplified with a PZ2 Pre-amplifier, and sampled at 25 kHz with a digital band-passed filtered (1-5000 Hz). Electrospinograms were recorded differentially from each active site of the implants with respect to a reference fixed to one of the bony vertebrae. The latency, amplitude, and amplitude density spectrum of the recorded signals were analyzed offline.

5.5.17 Electrochemical stimulation of the spinal cord (Fig. 5.4E, S5.17)

Electrochemical stimulation protocols were selected based on an extensive amount of previous studies in rats with spinal cord injury ([31] [145] [7]). The chemical stimulation used during training was administered through the microfluidic channel integrated in the chronically implanted e-dura. After 1-2 minutes, subdural electrical stimulation currents were delivered between active electrodes located on the

lateral aspect or midline of sacral (S1) and lumbar (L2) segments, and an indifferent ground located subcutaneously. The intensity of electrical spinal cord stimulation was tuned (40 Hz, 20-150 μ A, biphasic rectangular pulses, 0.2 ms duration) to obtain optimal stepping visually. To demonstrate the synergy between chemical and electrical stimulation, we tested rats without any stimulation, with chemical or electrical stimulation alone, and with concurrent electrochemical stimulation. To demonstrate the previously inaccessible capacity to facilitate specific aspects of locomotion with subdural electrical stimulation, we delivered electrical stimulation using electrodes located on the lateral aspects of lumbar and sacral segments, and compared locomotor movements with stimulation delivered bilaterally.

5.5.18 Statistical analysis

All the displayed quantifications are reported as mean values \pm SEM (standard error of mean), unless otherwise stated. Statistical evaluations were performed using paired Student's t-test, one-way analysis of variance (ANOVA), repeated-measure ANOVA or Friedman test, depending on the experimental design. In case of limited number of measurements, we used their non-parametric equivalents: Wilcoxon ranksum test and Kruskal-Wallis one-way analysis of variance. The Tukey's range test and Bonferroni procedure were applied to test post-hoc differences when appropriate.

5.6 Supplementary text

5.6.1 Deformation analysis of the spinal cord - implant model (fig. S5.10)

The biomechanical coupling of the implant with the spinal cord depends on the implant's materials and geometry, and the mechanical response of the spinal cord.

Influence of implant bending stiffness

Bending stiffness is defined by eq. 5.1:

$$D = \frac{Et^3}{12(1 - \nu^2)} \quad (5.1)$$

where E and ν are Young's modulus and Poisson's ratio of the implant material, respectively, and t is the thickness of the implant. We neglected the contribution of the

thin metal interconnects on the overall implant mechanical behavior. If the bending stiffness of the implant is large compared to that of the surrounding tissue, the implant cannot accommodate the deformation of the tissue. In the context of an implant inserted in the intrathecal space, this translates in compression of the spinal tissue. We used plane strain finite element simulation to investigate the effect of bending stiffness of the implant on the deformation of spinal tissues and quantified the resulting maximum principal logarithmic strain inside the hydrogel ‘spinal tissue’. When the bending stiffness of the implant is much higher than that of dura mater, the implant distorts the spinal tissue. The lower the bending stiffness, the less interference is induced by the implant. Ideally the bending stiffness of the implant should be as low as possible. In practice, bending stiffness comparable to dura mater may be sufficient, as demonstrated with results obtained with the soft e-dura implants.

Influence of tensile stiffness mismatch (fig. S5.10C)

Tensile stiffness is defined in eq. 5.2:

$$S = EA \quad (5.2)$$

with A, the cross-sectional area of the structure perpendicular to the tensile/compression direction and E, the Young’s modulus of the implant material. We define three zones along the length of the spinal cord model: in zone 1, the spinal tissue is implant-free, in zone 2, the implant sits above the spinal tissues, and zones 3 depict the transition between zones 1 and 2.

Except for the transition region of the size comparable to the diameter of the spinal cord, the strain of the regions 1 and 2 should be homogeneous. By force balance we will have:

$$S_1\epsilon_1 = S_2\epsilon_2 \quad (5.3)$$

with ϵ_1 and ϵ_2 the strain in zone 1 and 2 respectively.

If the implant is very stiff, then $S_1 \gg S_2$. As a result, $\epsilon_1 \ll \epsilon_2$ and the implant will severely limit the motion of the spinal tissue. A stiff implant may also result in debonding during stretch. The debonded implant will slide relative to the spinal cord and dura mater as the animal moves. Such repetitive relative movements may trigger and maintain neuroinflammation in the spinal tissue. The energy release rate G for

Chapter 5. Electronic dura mater for long-term multimodal neural interfaces

debonding is expressed in eq. 5.4:

$$G = \frac{S_2 \epsilon_2^2}{2w} - \frac{S_1 \epsilon_1^2}{2w} \quad (5.4)$$

where is the bonding width of the implant (25). When an overall strain ϵ_{app} is applied along the spinal cord system,

$$l\epsilon_{app} = l_1\epsilon_1 + l_2\epsilon_2 \quad (5.5)$$

Once the implant material and geometry are selected, , and can be resolved with equations (5.3)-(5.4)-(5.5). The table below summarizes these parameters when the spinal cord-implant model is stretched by 10% strain, and compares the different coverage rate of the implant, characterized by the ratio l_1/l , for the soft (PDMS) and stiff (polyimide) implants. Two thicknesses of polyimide implants are simulated (25 μm and 2.5 μm). The bending stiffness of an extremely thin (2.5 μm) polyimide is negligible compared to that of a 25 μm thick polyimide film (fig. S5.10).

	120 μm PDMS ($S_1/S_2 = 1.33$)			25 μm Polyimide ($S_1/S_2 = 88.13$)			2.5 μm Polyimide ($S_1/S_2 = 9.71$)		
l_1/l	ϵ_1	ϵ_2	G	ϵ_1	ϵ_2	G	ϵ_1	ϵ_2	G
10%	7.7%	10.3%	1.0 J/m^2	0.1%	11.0%	4.4 J/m^2	0.1%	11.0%	3.9 J/m^2
50%	8.6%	11.4%	1.2 J/m^2	0.2%	19.8%	13.9 J/m^2	0.2%	18.1%	10.6 J/m^2
90%	9.7%	12.9%	1.5 J/m^2	1.0%	90.7%	291.9 J/m^2	5.0%	51.9%	86.7 J/m^2

A stiff implant, even extremely thin, severely constraints the motion of the underlying spinal tissues ($0.1\% < \epsilon_1 < 1\%$ for $\epsilon_{app}l = 10\%$). Furthermore, as the coverage rate increases, the strain in zone 2 (outside of the implant coverage) is rapidly increasing reaching 50% (2.5 μm thick implant) and 90% (25 μm thick implant) (for $\epsilon_{app}l = 10\%$) when the implant covers 90% of the length of the spinal cord. As the result of this strain concentration, the energy release rate for debonding is one order of magnitude higher than a soft e-dura implant made of PDMS.

5.7 Supplementary videos

5.7.1 Movie S1: Electronic dura mater.

This movie illustrates the resilience of the e-dura under various conditions, and shows a 3D rendering of a computed tomography scan of the e-dura inserted in the spinal subdural space of a rat.

5.7.2 Movie S2: e-dura bio-integration.

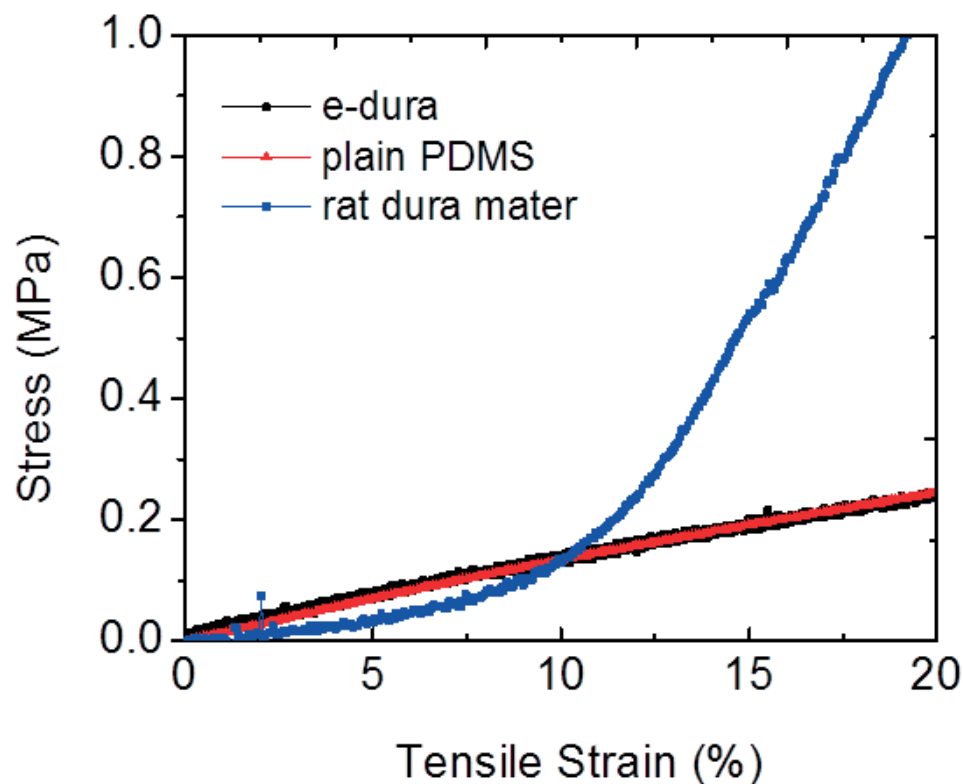
This movie shows leg kinematics during locomotion along a horizontal ladder for a sham-operated rat, a rat implanted with the e-dura and a rat implanted with a stiff implant, and a 3D rendering of the reconstructed spinal cords after 6 weeks of implantation.

5.7.3 Movie S3: e-dura applications.

This movie shows leg kinematics during bipedal locomotion on a treadmill under various combinations of chemical and electrical stimulation of lumbosacral segments for a rat that received a severe spinal cord injury leading to permanent paralysis.

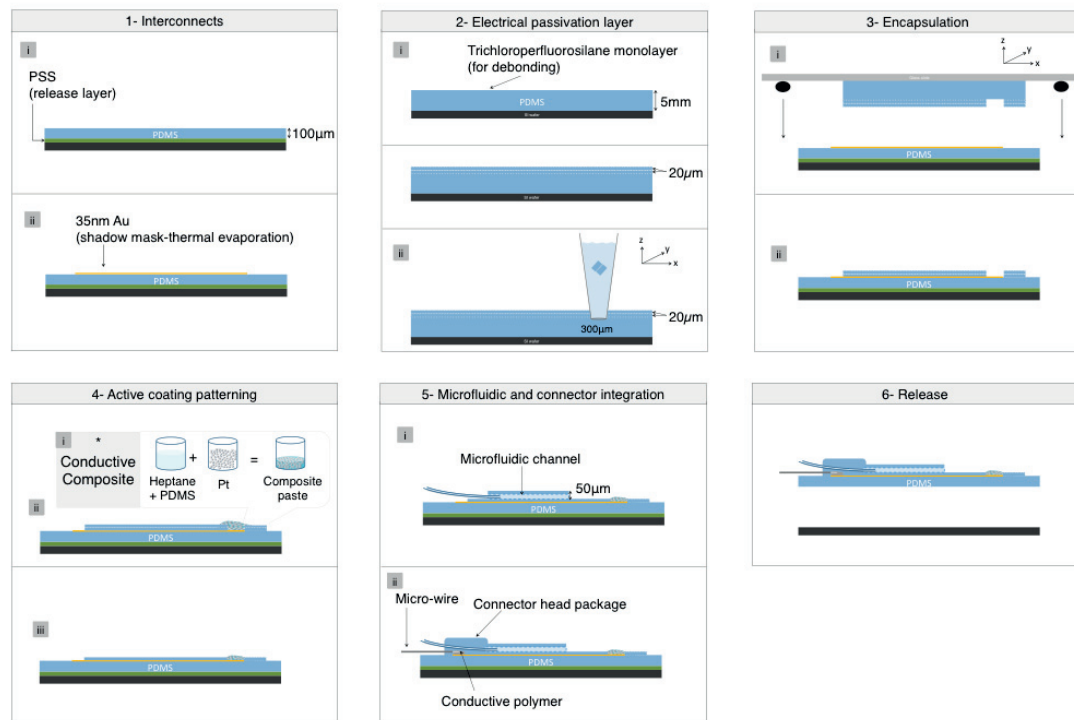
Videos are available on Science magazine website: <http://science.sciencemag.org>

5.8 Supplementary figures



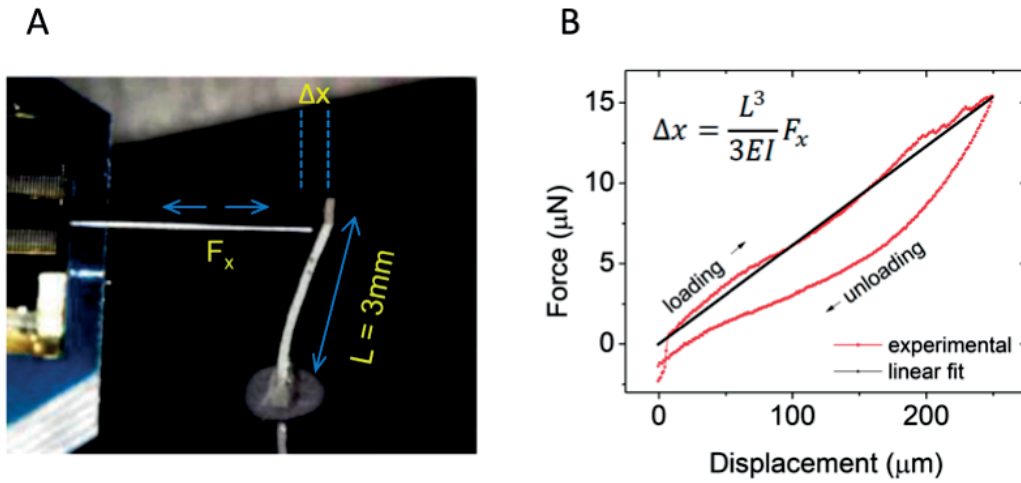
Supplementary Figure S5.1 – Tensile response of natural dura mater, silicone and e-dura implant. Stress-strain curves of explanted rat dura mater, e-dura and plain membrane of silicone (PDMS). Both e-dura (120 μm thick) and the plain silicone membrane (85 μm thick) are linearly elastic in the tested strain range and poses similar elastic moduli of approximately 1.2 MPa. Freshly explanted spinal rat dura exhibits a 'J' shaped stress-strain curve typical of collagen rich biomaterials. At elongations up to approximately 10%, natural rat dura and e-dura exhibit similar tensile properties. Strain rate is 0.5%/s.

5.8. Supplementary figures

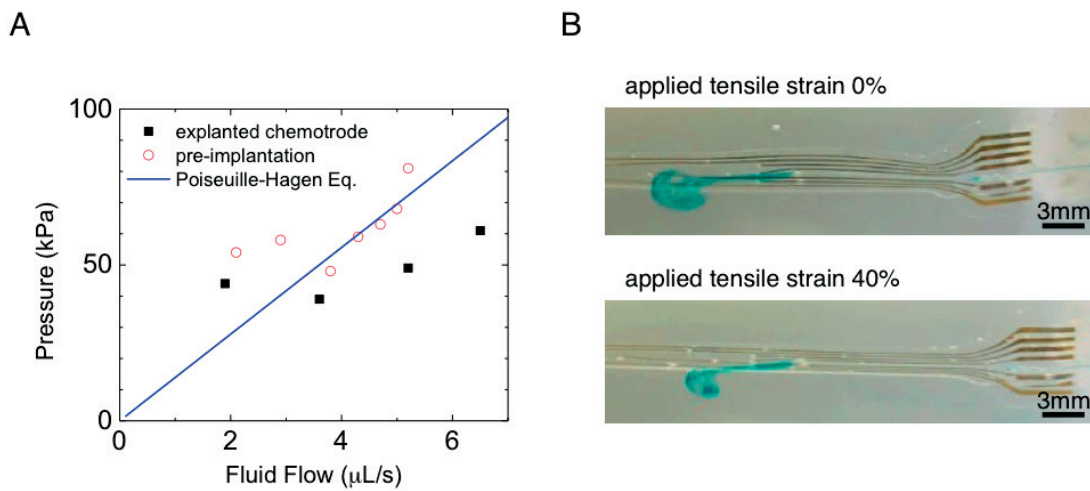


Supplementary Figure S5.2 – Soft neurotechnology for e-dura implants.

The process flow, illustrated in cross-sectional views, consists of 6 main steps. (1) Elastomeric substrate and stretchable interconnects fabrication. Patterning (2) and bonding (3) of interconnects' passivation layer. (4) Coating of the electrodes with a customized platinum-silicone composite screen-printed above the electrode sites. (5) Integration of the PDMS microfluidic channel and connector. (6) Release of the e-dura implant in water.

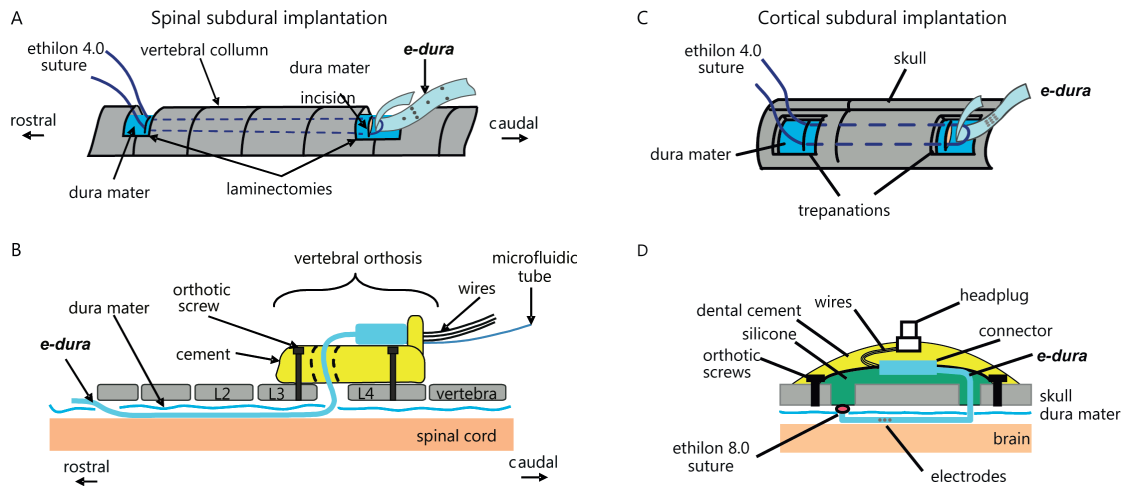


Supplementary Figure S5.3 – Mechanical characterization of the platinum-silicone composite. (A) To estimate the elastic modulus of the coating composite, we fabricated a high aspect ratio pillar with a rectangular cross-section ($L = 3 \text{ mm}$, $h = 113 \mu\text{m}$, $w = 480 \mu\text{m}$, 4:1 w:w Pt:PDMS composite). The pillar was then mounted vertically. (B) To obtain a force-displacement curve, we measured the force required to deflect the free end of the pillar by a small distance Δx . We used a linear fit to the loading portion of the force-displacement curve and bending beam theory to derive the Young's Modulus (E) of the composite. In this equation, I is the moment of inertia defined by the known cross-section dimensions of the beam, E is the elastic modulus of the beam, and F_x is the force needed to produce a displacement Δx . We found the elastic modulus of the platinum-silicone composite was approximately 10 MPa.

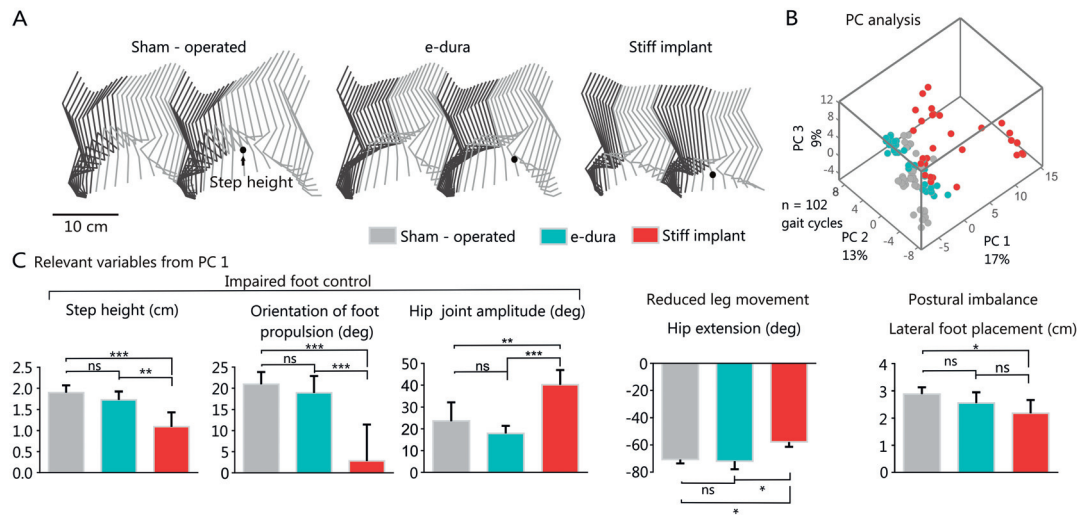


Supplementary Figure S5.4 – E-dura chemotrode: compliant fluidic microchannel. (A) Determination of the hydrodynamic resistance of the microfluidic system. The continuous line displays the fluid flow predicted by the Poiseuille-Hagen equation. Monitoring the hydrodynamic response of the chemotrode before surgery and after explantation following 6 weeks of chronic implantation demonstrated that the microfluidic channels do not become occluded with tissue or debris, and maintain functionality during prolonged subdural implantation. (B) Blue-colored water was injected through the chemotrode under different tensile conditions. The integrity and functionality of the microfluidic channel was maintained when the implants was stretched up to a strain of 40%.

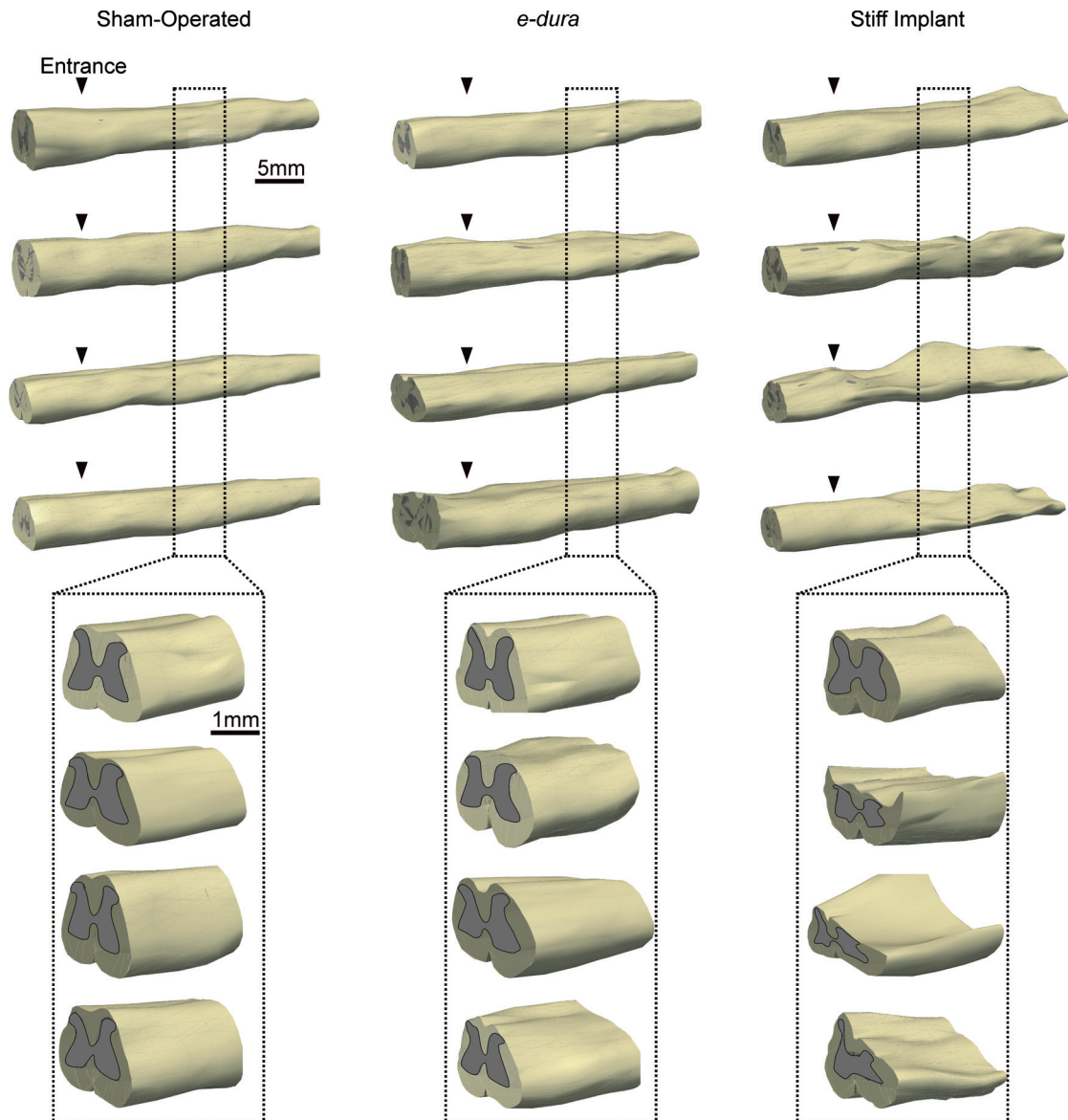
5.8. Supplementary figures



Supplementary Figure S5.5 – Orthoses and surgical procedures for chronic e-dura implantation. (A-B) Spinal e-dura. (A) Surgical procedure to slide the e-dura below the dura mater covering lumbar segments. (B) Side view of the engineered vertebral orthosis that secures the e-dura connector, and ensures long-term functionality of embedded electrodes and chemotrode in vivo. (C-D) Cortical e-dura. (C) Surgical procedure to slide the e-dura below the dura mater covering the motor cortex. (D) Side view describing the engineered cortical orthosis that secures the e-dura and its connector, ensuring chronic recordings of electrocorticograms in freely moving rats.

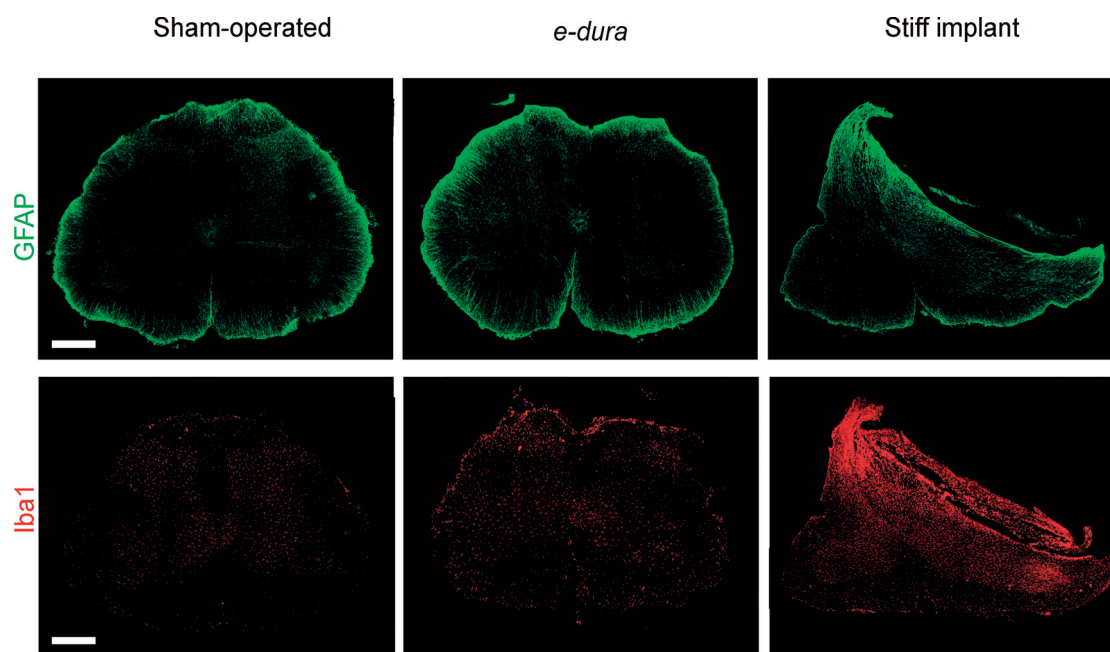


Supplementary Figure S5.6 – Kinematic analysis of gait patterns during basic overground locomotion. (A) Representative stick diagram decomposition of hindlimb movement during two successive gait cycles performed along a horizontal unobstructed runway. Recordings were obtained 6 weeks after surgery for a sham-implant rat, and for a rat implanted with an e-dura or a stiff implant, from left to right. (B) A total of 135 parameters providing comprehensive gait quantification (Table S1) were computed from high-resolution kinematic recordings. All the parameters computed for a minimum of 8 gait cycles per rat at 6 weeks post-implantation were subjected to a principal component (PC) analysis. All gait cycles ($n = 102$, individual dots) from all tested rats ($n = 4$ per group) are represented in the new 3D space created by PC1-3, which explained 40% of the total data variance. This analysis revealed that sham-operated rats and rats with e-dura exhibited similar gait patterns, whereas rats with stiff implants showed markedly different gait characteristics compared to both other groups. (C) To identify the specific features underlying these differences, we extracted the parameters with high factor loadings on PC1, and regrouped them into functional clusters (not shown), which we named for clarity. This analysis revealed that rats with stiff implants displayed impaired foot control, reduced amplitude of leg movement, and postural imbalance. To illustrate these deficits using more classic parameters, we generated plots reporting mean values (\pm SEM) of variables with high factor loadings for each of the 3 identified functional clusters. Statistical test: Kruskal-Wallis ANOVA. ***, $P < 0.001$. **, $P < 0.01$. *, $P < 0.05$. ns, non-significant. Error bars: standard error of mean, SEM.



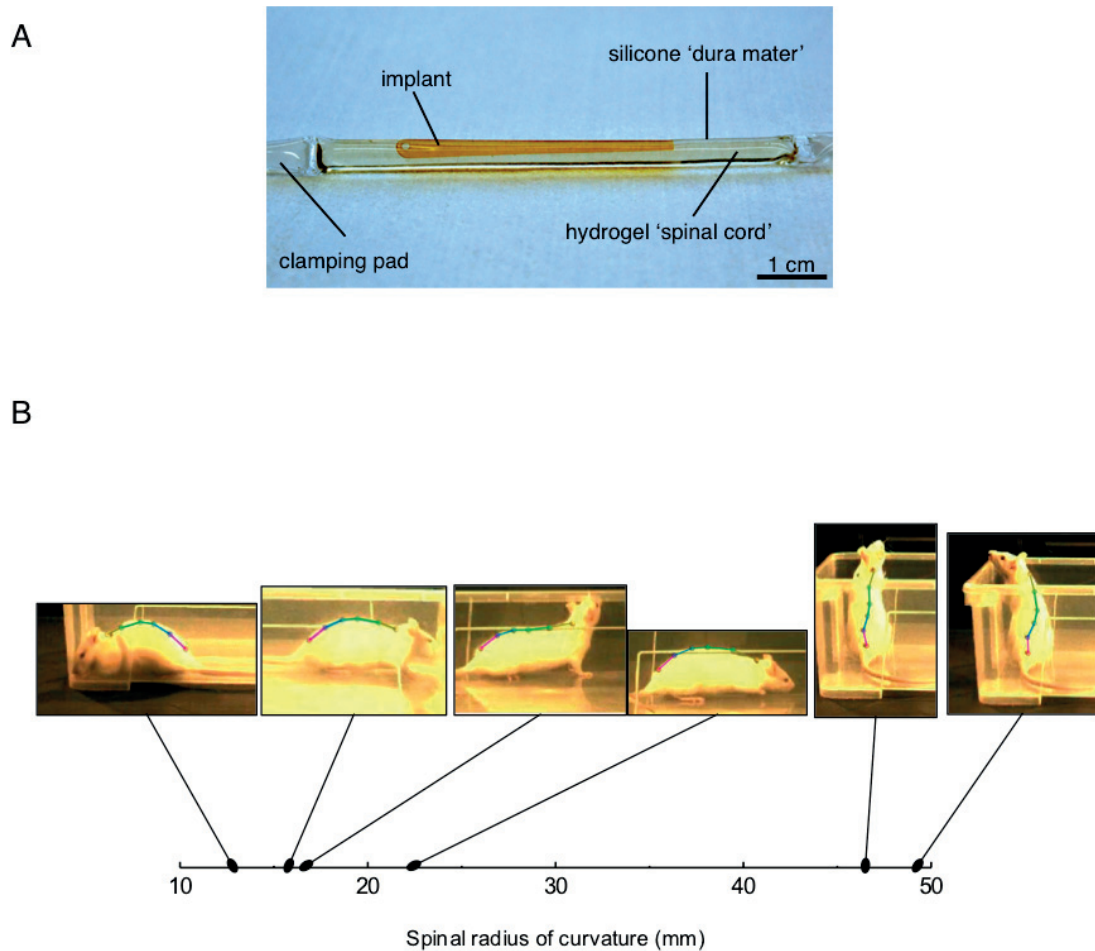
Supplementary Figure S5.7 – Damage of spinal tissues after chronic implantation of stiff, but not soft, implants.

3D reconstructions of lumbosacral segments for all 16 tested rats (3 groups of 4 animals), including enhanced views. The spinal cords were explanted and reconstructed through serial Nissl-stained cross-sections after 6-week implantation. Stiff implants induced dramatic damage of neural tissues, whereas the soft implant had a negligible impact on the macroscopic shape of the spinal cord. The arrowheads indicate the position of the entrance of the implant into the subdural space.



Supplementary Figure S5.8 – Significant neuro-inflammatory responses after chronic implantation of stiff, but not soft, implants.

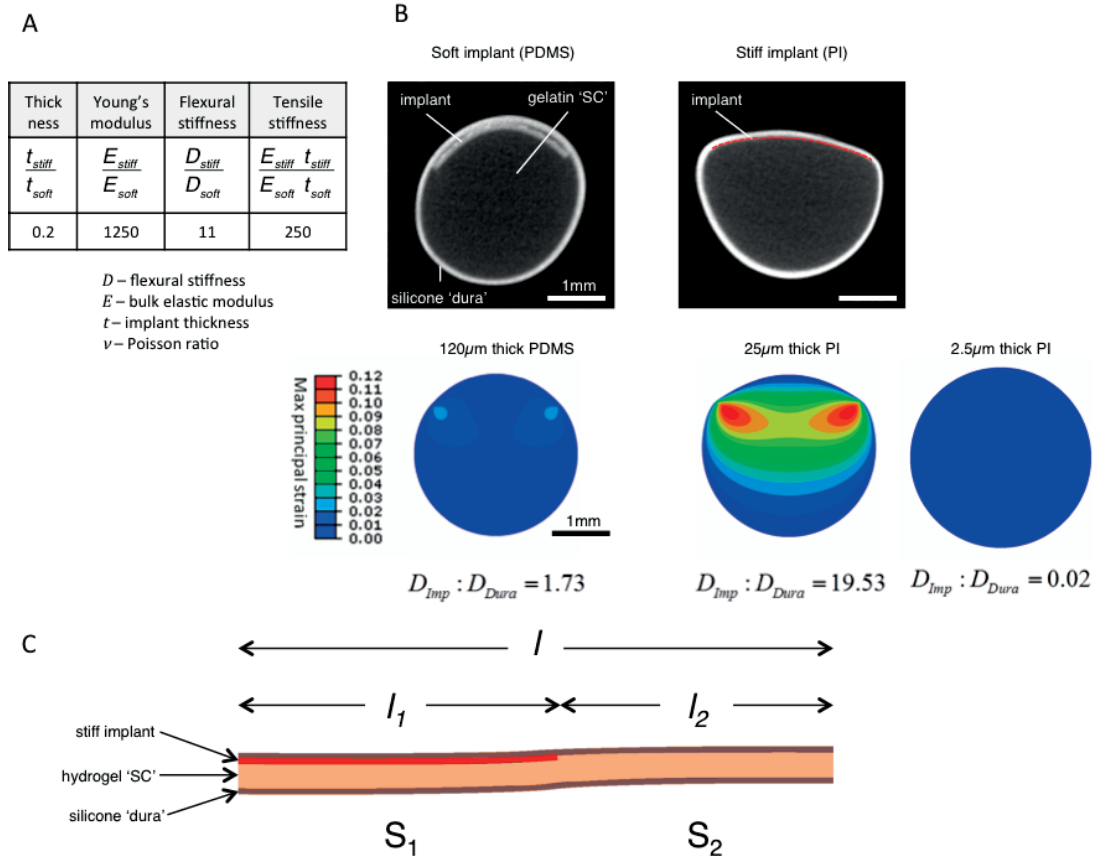
Cross-section of the L5 lumbar segment stained for the neuro-inflammatory markers GFAP (astrocytes) and Iba1 (microglia) after 6-week implantation. A representative photograph is shown for each group of rats. The stiff implant leads to a dramatic increase in the density of neuro-inflammatory cells, whereas the e-dura had a negligible impact on these responses. Scale bars, 500 μ m.



Supplementary Figure S5.9 – Model of spinal cord and experimental quantification of vertebral column curvatures in freely behaving rats.

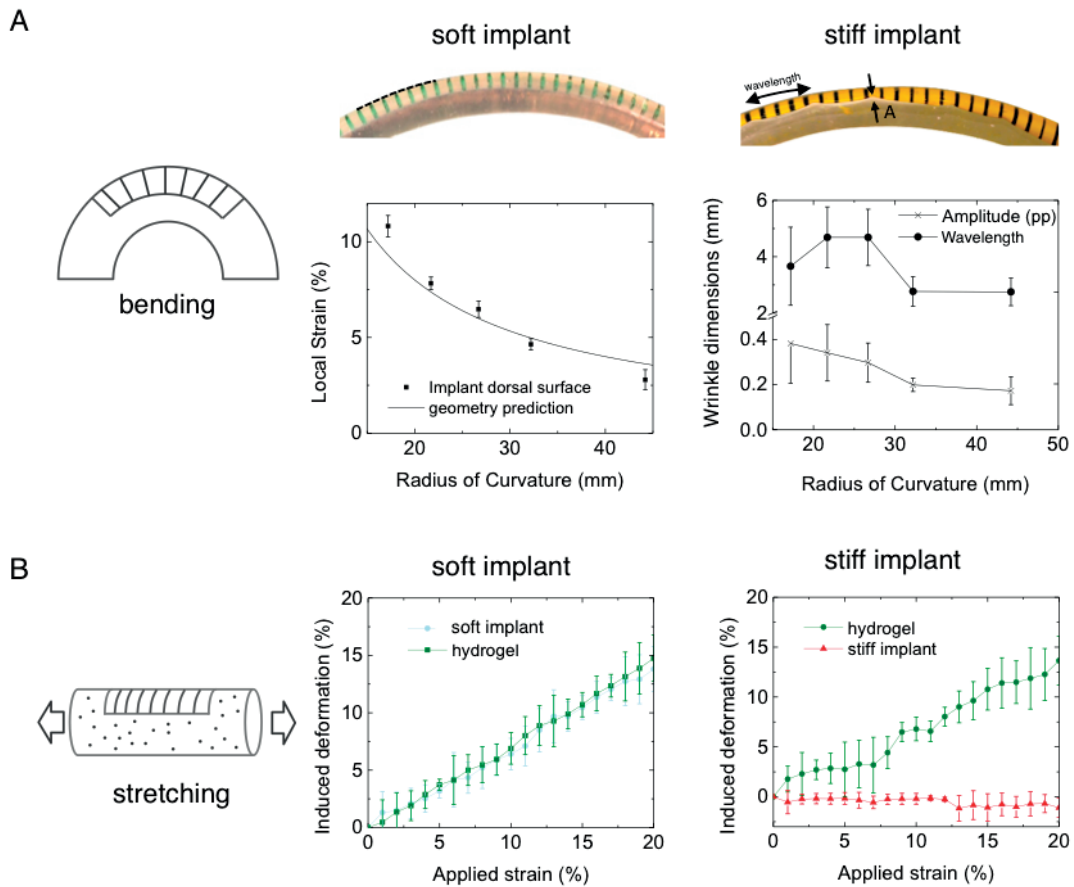
(A) The mechanical model of spinal cord is composed of a hydrogel that simulates spinal tissue, and a silicone membrane that simulates the dura mater. The soft or stiff implant was inserted between the hydrogel and the silicone membrane. The water trapped under the simulated dura mater ensured constant lubrication of the entire implant. Both ends of the model were sealed with silicone forming the clamping pads used in stretching experiments. (B) To measure the range of physiologically relevant vertebral column curvatures, we recorded spontaneous movement of a healthy rat during exploration of a novel environment. Reflective markers were attached overlying bony landmarks to measure motion of the vertebral column. The photographs displayed the stereotypical motor behaviors that were extracted for further analysis. For each behavior, we fitted a polynomial function through the inter-connected chain of markers. The resulting curvatures are reported along the x-axis. Since the markers were attached to the moving skin, the radii of curvature experienced by the vertebral column, and even more by the spinal cord itself, are expected to be at least 1 to 2mm smaller. We used the measured radii of curvature to define the bending limits applied to the spinal cord-implant model tested under flexion.

Chapter 5. Electronic dura mater for long-term multimodal neural interfaces



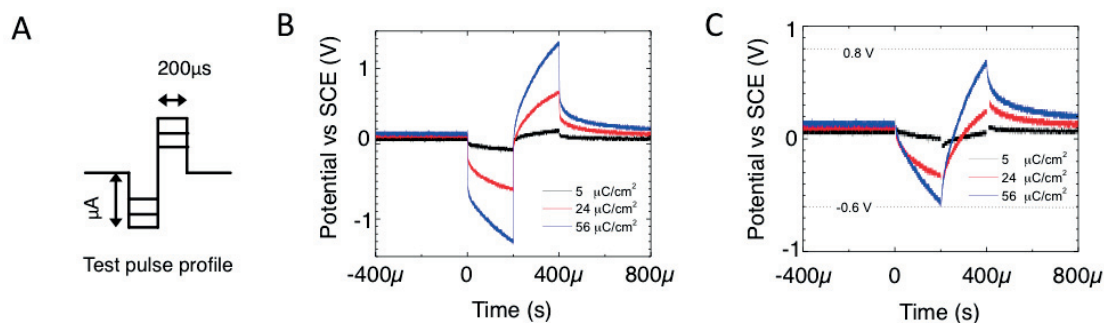
Supplementary Figure S5.10 – Mechanical effects of implants on the model of spinal cord.

(A) Ratios of the mechanical properties of the materials used to prepare the soft (i.e. silicone) and stiff (i.e. polyimide) implants. Bending stiffness describes the resistance of the implant towards flexion, while tensile stiffness refers to the resistance of the implant towards elongation. Although the stiff implant is five times thinner than the soft implant, its tensile and flexural stiffness are respectively two and one orders of magnitude larger. (B) Micro-Computed Tomography (μ CT) images and Finite Element (FE) Simulation strain maps of the cross-sections of the model of spinal cord carrying a soft or a stiff implant. No external deformation is applied to the model. The 25 μ m thick polyimide implant is highlighted with a dotted red line because the resolution of the μ CT is not high enough to distinguish the thin plastic film. The FE simulations depict the maximum logarithmic strain inside the model of spinal cord computed with the geometry and materials properties of the spinal cord models and three implant configurations (120 μ m soft PDMS, 25 μ m and 2.5 μ m thick polyimide films). (C) Schematic longitudinal cross-section of the model of spinal cord model carrying a stiff implant. The model system is stretched along the length of the implant by 20% strain. The high tensile stiffness $S_{stiff} = E_{stiff} \cdot t_{stiff}$ of the implant compared to that of the simulated spinal cord leads to nearly unstretched simulated spinal tissues immediately underneath the implant and highly deformed spinal tissues away from the implant.



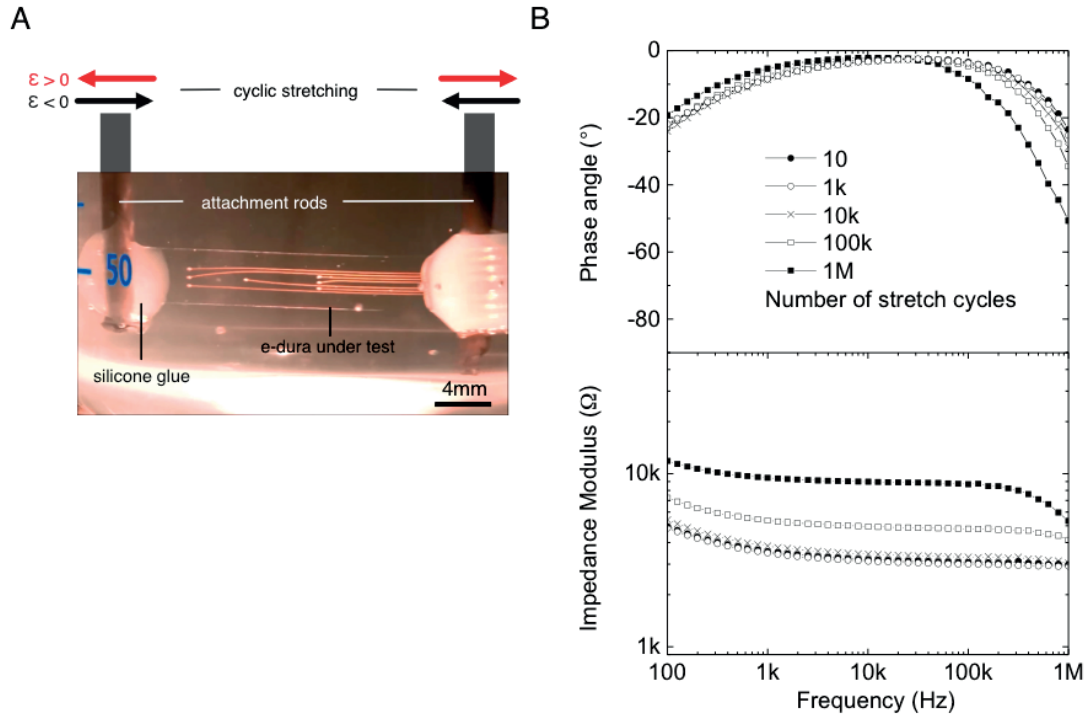
Supplementary Figure S5.11 – Effect of tensile deformations on the implants and on the model of spinal cord.

(A) To measure local strains, we tracked fiducial markers in the hydrogel ‘spinal tissue’ and on the soft or stiff implant. Graphite powder particles were mixed with the hydrogel during gel preparation. Parallel lines with 1mm inter-distance were drawn directly onto the surface of the implants. The model was flexed to controlled bending radii, which covered the entire range of physiologically relevant spinal movement determined *in vivo* (fig. S5.9). The soft implant conformed to the flexion of simulated spinal tissues. The strain along the sagittal crest of the model (broken line) was determined experimentally (discrete symbols) and compared to a geometrical prediction (continuous line). The stiff implant started wrinkling with radii smaller than 30 mm. The amplitude of wrinkles, termed *A*, and the wavelength depended on the bending radius. (B) The spinal cord - implant model was placed under uniaxial (global) tensile stretch. Local strain was measured by tracking the displacement of pairs of particles in the gel ($n=8$ pairs), or neighboring stripes on the implants ($n=10$ pairs). The graphs quantify locally induced strain in the implant and in the hydrogel core (spinal tissues) as a function of the global applied strain to the model. The soft implant stretched with the model of spinal cord. In contrast, there was a substantial mismatch between the local strain inside the model and the induced deformation of the stiff implant. Consequently, the stiff implant slid between the silicone and the hydrogel during stretch. Mean \pm standard deviation (SD).



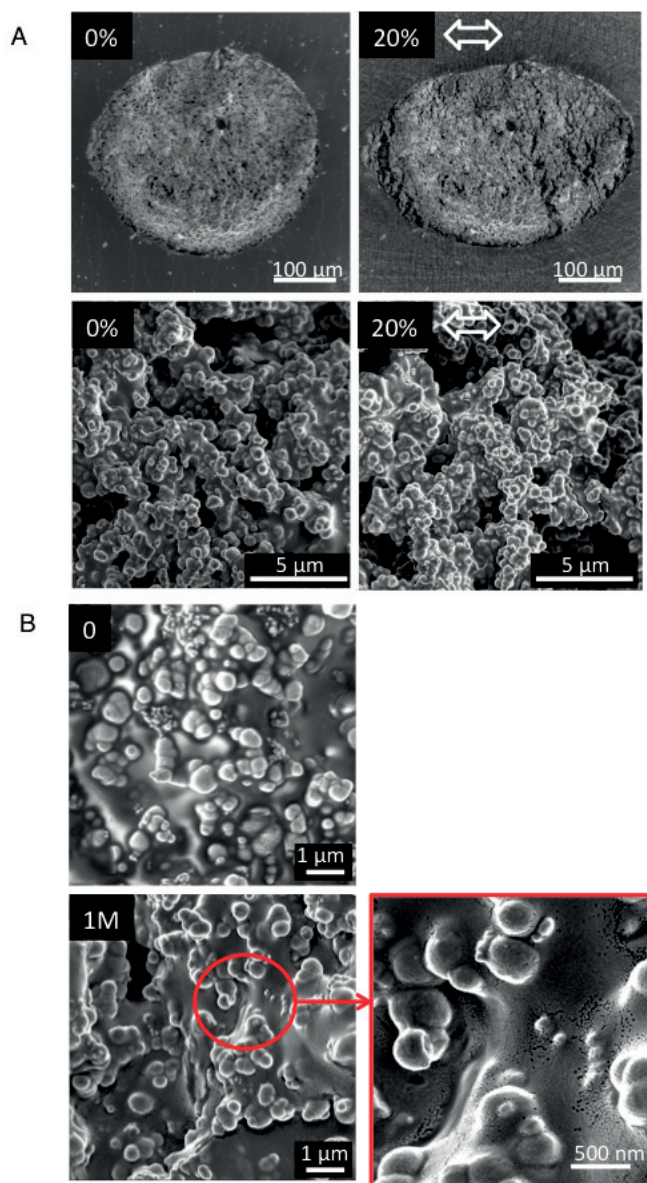
Supplementary Figure S5.12 – Determination of charge injection capacity of electrodes with platinum-silicone coating.

(A) Charge-balanced, biphasic current pulses were injected through electrodes immersed in Phosphate Buffer Saline solution (PBS). The duration of each pulse phase was fixed at 200 μs per phase, which corresponds to the typical pulse duration used during therapeutic applications. (B) The amplitude of the current pulses was gradually increased. As the current density flowing through the coating and its polarization increased, a significant portion of the recorded voltage drop occurred in the electrode interconnects and the electrolyte above the coating. (C) To obtain the true voltage transients at the coating surface with respect to the reference electrode, the instantaneous polarization of the cell was subtracted. The maximum safe current density was reached when the coating polarization exited the water window.



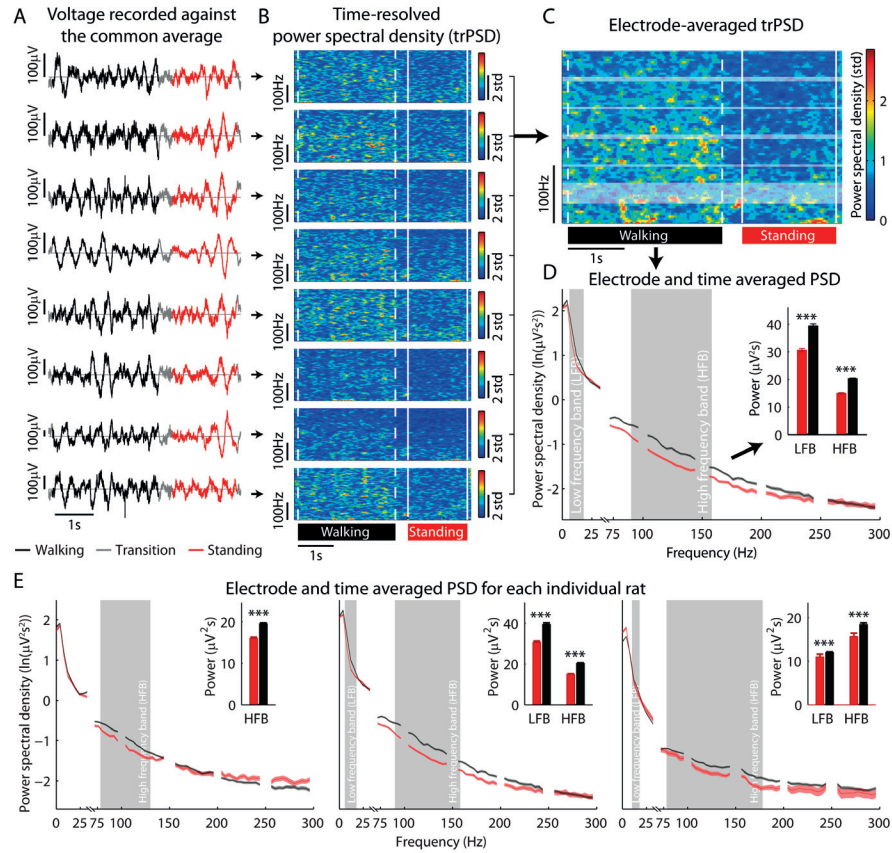
Supplementary Figure S5.13 – Impedance spectroscopy of the soft electrodes under cyclic stretching to 20% strain.

(A) Apparatus for conducting electrochemical characterization of soft implants under tensile strain. The ends of the implant were glued to two probes that are clamped to the jaws of a custom built extensometer. The implant and (partially) the probes were then submerged in Phosphate Buffered Saline solution (PBS). The extensometer applied pre-defined static strain to the implant, or performed a cyclic stretch-relax program. A counter and a reference electrode were submerged in the electrolyte to complete the circuit (not shown). (B) Representative impedance plots recorded from one electrode. The spectra were recorded at 0% applied strain after 10, 1,000, 10,000, 100,000 and 1 million stretch cycles. Each stretch cycle lasted 1s. The implants remained immersed in PBS throughout the evaluations. The remaining 6 electrodes in the tested implants exhibited a similar behavior.

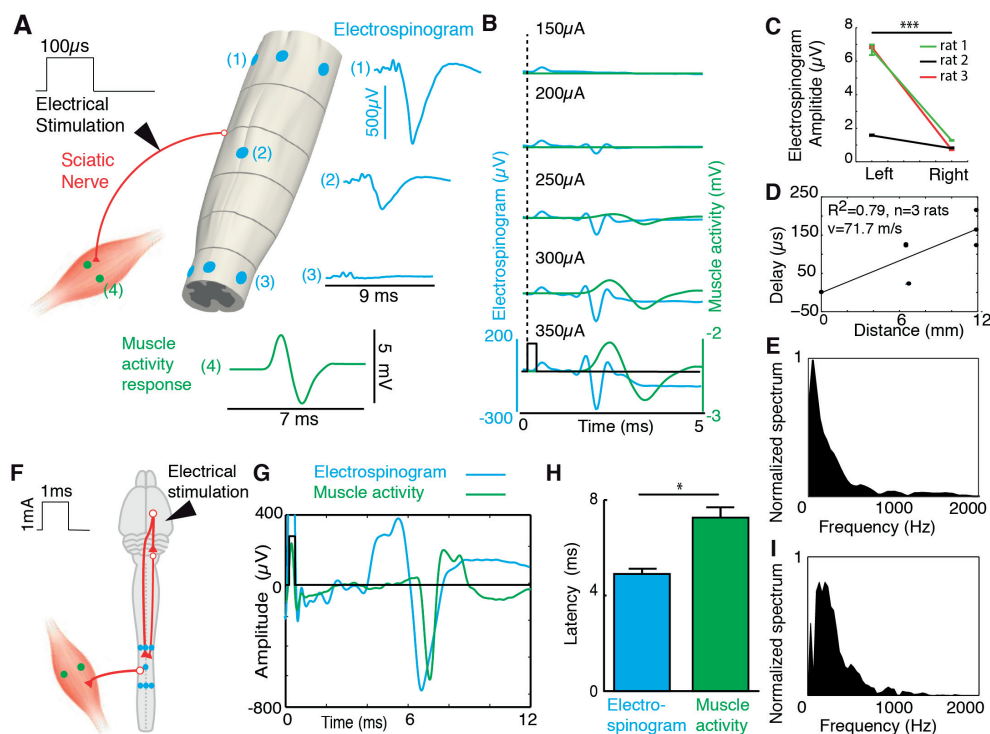


Supplementary Figure S5.14 – In-situ scanning electron micrographs of platinum-silicone coatings. (A) Images collected during the first stretch cycle to 20% applied strain (from pristine electrode). Low magnification scanning electron micrographs taken at 20% strain revealed the appearance of cracks, but the absence of delamination. The high effective surface area of the composite coating is clearly visible in medium magnification scanning electron micrographs (lower panels). (B) Images collected before (cycle 0) and after one million stretch cycles to 20% strain. All the images were taken at 0% strain. High-magnification scanning electron micrographs revealed the effects of fatigue cycling on the nano-scale morphology of the composite coating.

5.8. Supplementary figures

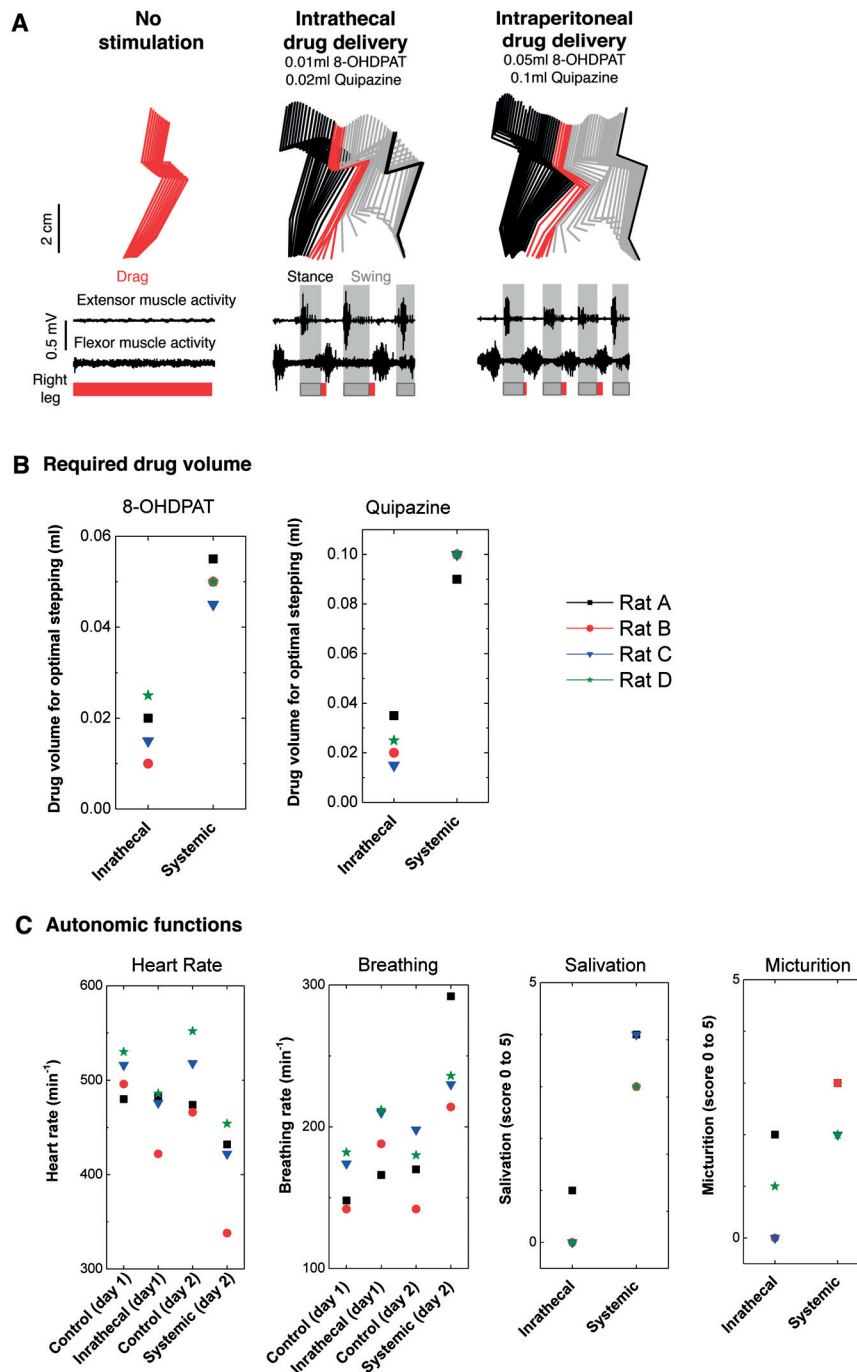


Supplementary Figure S5.15 – Motor cortex electrocorticograms reflect motor states in freely moving rats. (A) Raw color-coded electrocorticograms recorded against the common average for each electrode of the chronically implanted e-dura. Colors correspond to motor states (identified from video) and labeled as continuous walking, transition between walking and standing, and standing. (B) Each electrocorticogram was Fourier transformed into time resolved power spectral densities (trPSD), shown in units of standard deviation (std). (C) trPSDs averaged across all electrodes. Each trPSD was normalized to mean trPSD in each frequency in order to account for drop in power with increasing frequencies. The transparent regions corresponds to the frequency sub-bands that were excluded from the analysis to remove the effect of the 50Hz line noise and its higher order harmonics. (D) Mean \pm SEM of power spectral density for standing and walking states. To calculate the time-resolved power of electrocorticograms within each contiguous band, we integrated the electrode-averaged trPSD across that band. We then compared all time-resolved power measurements during walking periods against all time-resolved power measurements during standing periods for each band using Wilcoxon rank-sum test. The low (LFB) and high (HFB) frequency bands (shared areas) were identified as bands with the local minima of p values. Histogram plots report the mean values \pm SEM of electrode-averaged power in the identified bands. ***, $p < 0.001$. p value corrected for multiple comparisons using Bonferroni correction (n tests = 45,150 for each rat). (E) Electrode-averaged trPSD, identified low and high frequency bands, and histogram plots reporting means \pm SEM of power in identified bands for walking and standing states, are shown for each rat ($n = 3$ rats in total). Elevated power in low and high frequency bands during walking compared to standing is consistent with electrocorticogram recordings during hand movements in humans [pistohl2012decoding](#).



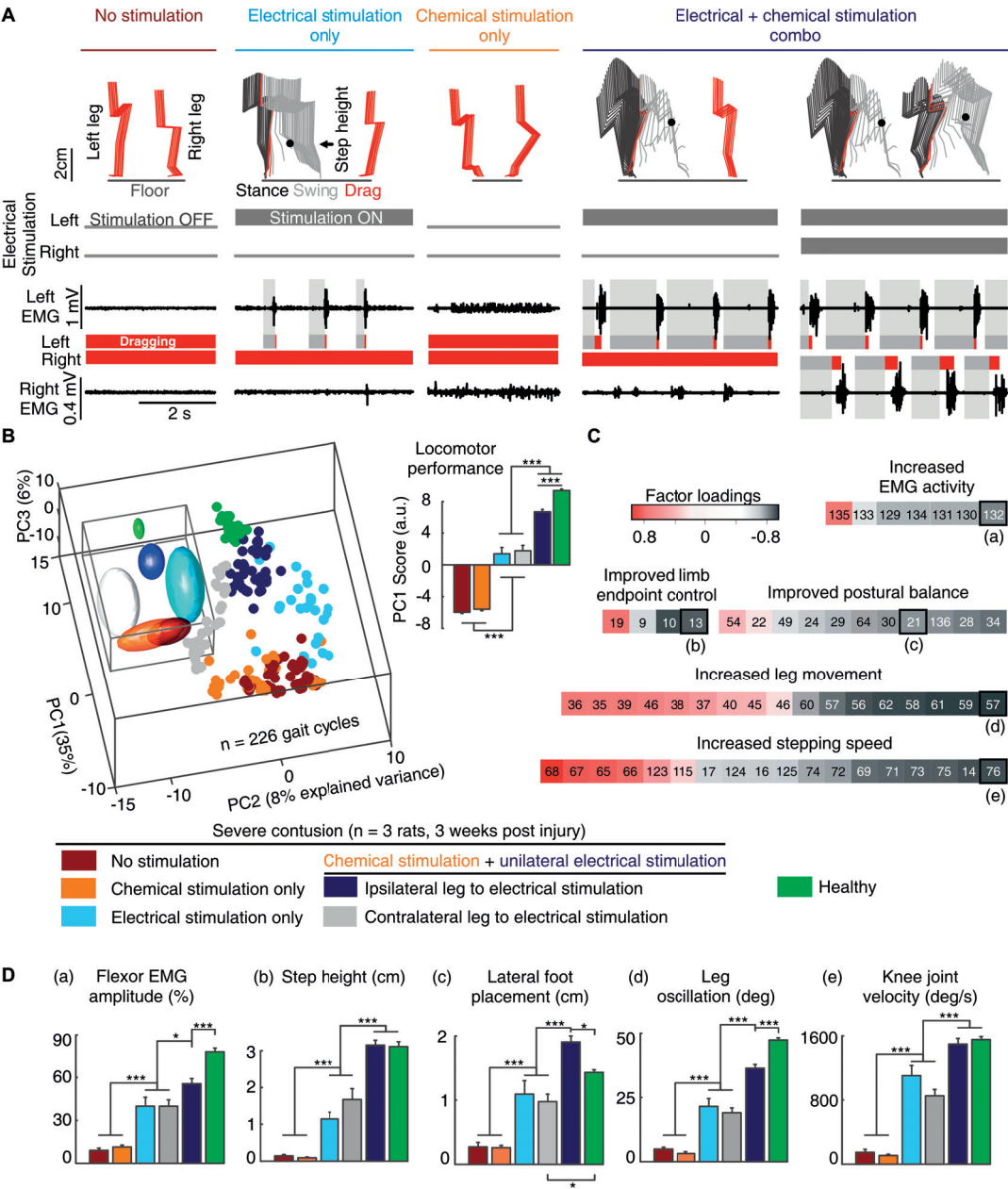
Supplementary Figure S5.16 – Recordings of electrospinograms following peripheral nerve and brain stimulation.

An e-dura was chronically implanted over lumbosacral segments for 6 weeks in 3 rats. Terminal experiments were performed under urethane anesthesia. (A) Electrospinograms and left medial gastrocnemius muscle activity were recorded in response to electrical stimulation of the left sciatic nerve. (B) Representative color-coded electrospinograms and muscle activity responses are displayed for increasing stimulation intensities. Electrospinograms appeared at lower threshold than muscle responses, suggesting that e-dura electrodes measured neural activity related to the recruitment of myelinated fibers. (C) Electrospinogram mean amplitudes for left versus right side electrodes (10 trials per rat). Responses were significantly larger on the stimulation side (t-test, ***, $P < 0.001$). (D) Correlation plot showing the relationship between electrode location and the latency of electrospinogram responses. The locations are referred to the left L2 electrode, which is the closest to sciatic nerve afferent neurons. The measured neural conduction velocity from lumbar to sacral segments, which was derived from the correlation line, is coherent with the conduction velocity of large-myelinated fibers. (E) Power spectrum of electrospinograms is condensed in the region below 1,000 Hz, which is consistent with a lead field potential signal, most likely arising from the afferent volley and related synaptic events. These combined results demonstrate the high degree of spatial and temporal selectivity in the neural recordings obtained with e-dura. (F) A stimulating electrode was positioned over the motor cortex of the same rats ($n = 3$) to elicit a descending volley. (G) Representative color-coded recording of an electrospinogram and muscle activity following a single pulse of motor cortex stimulation. (H) Bar plot reporting the mean (10 trials per rat) latency (\pm SEM) of electrospinograms and muscle activity responses following a single pulse of stimulation. Electrospinograms systematically preceded muscle evoked responses (t-test, *, $P < 0.05$). (I) The power spectrum of electrospinograms was condensed in the region below 1,000 Hz, which was consistent with a neural response related to multiple descending pathways.



Supplementary Figure S5.17 – Drug delivery through the chemotrode annihilates side effects. (A) Rats ($n = 4$) were tested during bipedal locomotion under robotic support after 1 week of rehabilitation. Recordings were performed without stimulation, and with concurrent electrochemical stimulation. Chemical stimulation was delivered either intrathecally through the chemotrode, or intraperitoneally. The drug volumes were adjusted to obtain the same quality of stepping. Color-coded stick diagram decompositions of hindlimb movements are shown together with muscle activity of antagonist ankle muscles. (B) Drug volumes required to obtain optimal facilitation of locomotion for each serotonergic agonist. ($n = 4$ rats). (C) Effects of optimal drug volumes on autonomic functions. Salivation and micturition are reported using a visual scaling system ranging from 0 (baseline, no drug) to 5 (maximum possible effects). ($n = 4$ rats).

Chapter 5. Electronic dura mater for long-term multimodal neural interfaces



5.8. Supplementary figures

Supplementary Figure S5.18 – The electrochemical neuroprosthesis e-dura mediates specific adjustments of locomotion.

(A) Spinal cord injured rats ($n = 3$) were recorded during bipedal locomotion on a treadmill after 3 weeks of rehabilitation. The rats were tested without stimulation (spontaneous) and during various combinations of chemical and/or electrical lumbosacral stimulations, as explained at the top and bottom of each panel. For each condition, a color-coded stick diagram decomposition of left and right hindlimb movements is displayed together with left and right muscle activity, and the color-coded duration of stance, swing, and drag phases. Without stimulation, both legs dragged along the treadmill belt. Electrical stimulation alone delivered at the level of lumbar (L2) and sacral (S1) electrodes, but only on the left side, induced rhythmic movement restricted to the left leg. Chemical stimulation alone, composed of 5HT1A/7 and 5HT2 agonists, did not induce locomotion, but raised the level of tonic muscle activity in both legs. After chemical injection, delivery of electrical stimulation on the left side induced robust locomotor movements restricted to the left leg. The combination of chemical and bilateral electrical stimulation promoted coordinated locomotor movements with weight bearing, plantar placement, and alternation of left and right leg oscillations. (B) A total of 135 parameters providing comprehensive gait quantification (Table S1) was computed from kinematic, kinetic, and muscle activity recordings. All the parameters were subjected to a PC analysis, as described in fig. S5.6. All the gait cycles ($n = 226$, individual dots) from all the tested rats ($n = 3$) and 3 healthy rats are represented in the new 3D space created by PC1-3, which explained nearly 50% of the total data variance. The inset shows elliptic fitting applied on 3D clusters to emphasize the differences between experimental conditions. The bar plot reports locomotor performance, which was quantified as the mean values \pm SEM of scores on PC1 (4). This analysis illustrates the graded improvement of locomotor performance under the progressive combination of chemical and bilateral electrical stimulation. Statistical test: Friedman test ANOVA. ***, $P < 0.001$. (C) To identify the specific features modulated with chemical and electrical stimulation, we extracted the parameters correlating with PC1 (factor loadings), and regrouped them into functional clusters, which we named for clarity. The numbers refer to variables described in Table S1. (D) Mean values \pm SEM of variables with high factor loadings, for each of the 5 functional clusters, as highlighted in panel C. Statistical test: Friedman test ANOVA. **, $P < 0.01$. *, $P < 0.05$. Error bars: standard error of mean, SEM.

Chapter 5. Electronic dura mater for long-term multimodal neural interfaces

PARAMETERS	VARIABLE	DETAILED EXPLANATION
KINEMATICS		
Temporal features	1	Cycle duration
	2	Cycle velocity
	3	Stance duration
	4	Swing duration
	5	Relative stance duration (percent of the cycle duration)
Limb endpoint (Metatarsal phalange) trajectory		
	6	Interlimb temporal coupling
	7	Duration of double stance phase
	8	Stride length
	9	Step length
	10	3D limb endpoint path length
	11	Maximum backward position
	12	Minimum forward position
	13	Step height
	14	Maximum speed during swing
	15	Relative timing of maximum velocity during swing
	16	Acceleration at swing onset
	17	Average endpoint velocity
	18	Orientation of the velocity vector at swing onset
	19	Dragging
	20	Relative dragging duration (percent of swing duration)
Stability		
Base of support	21	Positioning of the foot at stance onset with respect to the pelvis
	22	Stance width
Trunk and pelvic position and oscillations	23	Maximum hip sagittal position
	24	Minimum hip sagittal position
	25	Amplitude of sagittal hip oscillations
	26	Variability of sagittal crest position
	27	Variability of sagittal crest velocity
	28	Variability of vertical hip movement
	29	Variability of sagittal hip movement
	30	Variability of the 3D hip oscillations
	31	Length of pelvis displacements in the forward direction
	32	Length of pelvis displacements in the medio-lateral direction
	33	Length of pelvis displacements in the vertical direction
	34	Length of pelvis displacements in all directions
Joint angles and segmental oscillations		
Backward	35	Crest oscillations
	36	Thigh oscillations
	37	Leg oscillations
	38	Foot oscillations
	39	Whole limb oscillations
Forward	40	Crest oscillations
	41	Thigh oscillations
	42	Leg oscillations
	43	Foot oscillations
	44	Whole limb oscillations
Flexion	45	Hip joint angle
	46	Knee joint angle
	47	Ankle joint angle
Abduction	48	Whole limb abduction
	49	Foot abduction
Extension	50	Hip joint angle
	51	Knee joint angle
	52	Ankle joint angle
Adduction	53	Whole limb adduction
	54	Foot adduction
	55	Crest oscillations
Amplitude	56	Thigh oscillations
	57	Leg oscillations
	58	Foot oscillations
	59	Whole limb oscillations
	60	Hip joint angle
	61	Knee joint angle
	62	Ankle joint angle
	63	Whole limb medio-lateral oscillations
	64	Foot abduction/adduction
Velocity		
Minimum	65	Whole limb oscillation velocity
	66	Hip joint angle velocity
	67	Knee joint angle velocity
	68	Ankle joint angle velocity
	69	Whole limb oscillation velocity
Maximum	70	Hip joint angle velocity
	71	Knee joint angle velocity
	72	Ankle joint angle velocity
	73	Whole limb angle velocity
Amplitude	74	Hip joint angle velocity
	75	Knee joint angle velocity
	76	Ankle joint angle velocity
Inter-limb coordination		
PC analysis	77	Degree of linear coupling between joint oscillations
	78	Temporal coupling between crest and thigh oscillations
	79	Temporal coupling between thigh and leg oscillations
	80	Temporal coupling between leg and foot oscillations
	81	Correlation between crest and thigh oscillations
	82	Correlation between thigh and leg oscillations
	83	Correlation between leg and foot oscillations
	84	Correlation between hip and knee oscillations
	85	Correlation between knee and ankle oscillations
	86	Correlation between ankle and MTP oscillations
Cross-correlation	87	Temporal lag between backward positions of crest and thigh oscillations
	88	Temporal lag between forward positions of crest and thigh oscillations
Relative coupling	89	Temporal lag between backward positions of thigh and leg oscillations
	90	Temporal lag between forward positions of thigh and leg oscillations
	91	Temporal lag between backward positions of leg and foot oscillations
	92	Temporal lag between forward positions of leg and foot oscillations
	93	Lag of the cross correlation function between hindlimb oscillations
Inter-segmental coordination compared to	94	Maximum R-value of the cross correlation function between hindlimb oscillations
	95	Lag of the cross correlation function between hip oscillations
	96	Maximum R-value of the cross correlation function between hip oscillations
	97	Lag of the cross correlation function between knee oscillations
	98	Maximum R-value of the cross correlation function between knee oscillations
Able-bodied rats	99	Lag of the cross correlation function between ankle oscillations
	100	Maximum R-value of the cross correlation function between ankle oscillations
	101	Lag of the cross correlation function between endpoint oscillations
	102	Maximum R-value of the cross correlation function between endpoint oscillations
	103	Phase of the first harmonic of the FFT of the hip elevation angle
Left-right hindlimb coordination	104	Amplitude of the first harmonic of the FFT of the hip elevation angle
	105	Phase of the first harmonic of the FFT of the knee elevation angle
	106	Amplitude of the first harmonic of the FFT of the knee elevation angle
	107	Phase of the first harmonic of the FFT of the ankle elevation angle
	108	Amplitude of the first harmonic of the FFT of the ankle elevation angle
	109	Phase of the first harmonic of the FFT of the endpoint elevation angle
	110	Amplitude of the first harmonic of the FFT of the endpoint elevation angle
	111	Phase of the first harmonic of the FFT of the hindlimb elevation angle
	112	Amplitude of the first harmonic of the FFT of the hindlimb elevation angle
	113	Lag of the cross correlation function between crest and thigh limb elevation angles
Hindlimb coordination	114	Lag of the cross correlation function between thigh and hindlimb elevation angles
	115	Lag of the cross correlation function between hip and thigh elevation angles
	116	Lag of the cross correlation function between hindlimb and foot elevation angles
	117	Lag of the cross correlation function between thigh and ankle elevation angles
	118	Lag of the cross correlation function between ankle and foot elevation angles
KINETICS		
	119	Medio-lateral forces
	120	Anteroposterior forces
	121	Vertical forces
	122	Weight-bearing level
MUSCLE ACTIVITY		
Timing (relative to cycle duration, paw contact to paw contact)		
Extensor	123	Relative onset of ipsilateral extensor muscle activity burst
	124	Relative end of ipsilateral extensor muscle activity burst
Flexor	125	Relative onset of ipsilateral flexor muscle activity burst
	126	Relative end of ipsilateral flexor muscle activity burst
Duration		
Extensor	127	Duration of ipsilateral extensor muscle activity burst
Flexor	128	Duration of ipsilateral flexor muscle activity burst
Amplitude		
Extensor	129	Mean amplitude of ipsilateral muscle activity burst
	130	Integral of ipsilateral extensor muscle activity burst
	131	Root mean square of ipsilateral extensor muscle activity burst
	132	Mean amplitude of ipsilateral flexor muscle activity burst
Flexor	133	Integral of ipsilateral flexor muscle activity burst
	134	Root mean square of ipsilateral flexor muscle activity burst
Muscle coactivation	135	Co-contraction of flexor and extensor muscle

Supplementary Figure S5.19 – Computed kinematic, ground reaction force, and muscle activity variables.

Model-driven optimization of multipolar electrical stimulation of the lumbosacral posterior roots using transversal epidural implant

Jerome Gandar^{1,*}, Andreas Rowald^{1,2*}, Frederic Michoud^{3,*}, Nikolaus Wenger⁴, Polina Shkorbatova⁵, Arnaud Bichat¹, Stéphanie lacour^{3,&}, Marco Capogrosso^{2,&} and Gregoire Courtine^{1,&}

Manuscript in preparation

1. Center for Neuroprosthetics and Brain Mind Institute, School of Life Sciences, Swiss Federal Institute of Technology (EPFL), Lausanne, Switzerland
2. Department of Medicine, Platform of Translational Neuroscience, University of Fribourg, Fribourg, Switzerland
3. Center for Neuroprosthetics, School of Engineering, Institute of Microengineering and Bioengineering, Swiss Federal Institute of Technology (EPFL), Lausanne, Switzerland
4. Department of Neurology with Experimental Neurology, Charité–Universitätsmedizin Berlin, Berlin, Germany
5. Motor Physiology Laboratory, Pavlov Institute of Physiology, St. Petersburg, Russia.

*,& equal contributions

Chapter 6. Model-driven optimization of multipolar electrical stimulation of the lumbosacral posterior roots using transversal epidural implant

6.1 Abstract

Epidural electrical stimulation (EES) of lumbosacral segments engages leg muscles by recruiting afferent fibers in the posterior roots. These protocols improved motor control after spinal cord injury in animals and humans with spinal cord injury. However, inter-subject reproducibility, limited specificity and time consuming optimization procedures hinder large-scale clinical deployment of this technology. Here we designed a transversal spinal implant tailored to the anatomy of the rat posterior roots that maximizes stimulation specificity while being robust to inter-subject variability. We fitted the design of a spinal implant to the transversal functional organization of the posterior roots allowing for efficient current steering protocols. We then used a realistic computational model of the spinal cord to optimize multipolar stimulation patterns. Finally, we demonstrate that our tailored interface optimized for multipolar stimulation maximizes specificity and robustness in behavioral experiments in rats with spinal cord injury.

Publication contributions

I planned and coordinated the study and performed all experiments in rats. I oriented model construction and designed transversal implants. I performed surgeries, rat rehabilitation trainings, recordings and data analysis of the behavioral experiments. I supervised the creation of all figures and prepared figures related to animal experiments. I wrote the manuscript.

6.2 Introduction

After a spinal cord injury (SCI), the neural network below the lesion is deprived from supraspinal input. In consequence, the sensorimotor circuit of the lumbar spinal cord is heavily affected which leads to a range of motor dysfunctions. Neuromodulation therapies of this disconnected neural tissue demonstrated capabilities to generate functional motor outputs, which reflect the dormant state of this network [7]. Epidural electrical stimulations (EES) protocols over the spinal cord is rising as a solution to restore locomotion in paralyzed subject [68] [69] [70]. Promising results in animal model [31] [110] [46] opened new perspectives and hope to patients suffering a SCI.

EES applied with spatiotemporal protocols demonstrated their efficiency to restore enhanced locomotion in multiple paralyzed species [110] [149]. This technology required dedicated spinal implants to achieve spatially selective stimulations. Active sites had their own specificity and their placements were crucial to ensure desired activations. A misplacement could lead to a drastic therapy drop in efficacy. Computational models based on proprioceptive afferent recruitments steered the development of such implants [46]. However, novel soft implant technology allowed stimulation in area impossible to reach with previous multi-electrode array generations [104] [150]. Performances exhibited during a subdural implantation foresee a similar integration in narrow lateral aspects of epidural space where some roots could be found.

In addition, we tackled the concept of multipolarity [151]. Classic approaches delivered EES with a monopolar stimulation paradigm [31], which focus on activation of desired structures with cathodic pulses. However, multipolar stimulations could provide anodic electrical fields that will shield unwanted structures and prevent their activations. We hypothesized that computational models integrating a precise spinal cord anatomy and an electrode variable polarity would provide alternative electrode configurations to improve robustness of spatiotemporal neuromodulation.

We first performed a root trajectory analysis and build finite-element model closer to real anatomy. We ran simulations to extract new potential electrode patterns. These predictions steered the development of a soft transversal spinal implant design. We demonstrated in-silico and in-vivo array capacities to reach every roots involved in locomotion above only one spinal segment, and recruit selectively flexor and extensor muscles. A genetic algorithm ran through multipolar stimulation combinations to isolate candidates offering an enhanced specificity compared to monopolar stimulations. We confirmed an increased selectivity in some muscles with multipolar patterns and the capacity to balance electrical fields to correct implant misplacements. Such spatial reinforcements applied with a temporal sequence on paralyzed rats allowed

Chapter 6. Model-driven optimization of multipolar electrical stimulation of the lumbosacral posterior roots using transversal epidural implant

rehabilitation of locomotion.

6.3 Results

6.3.1 Precise rat spinal cord anatomy

To build a precise model closer to real anatomic dimension, a computed tomography scan was performed on rats to extract vertebral features (figure 6.1a). A MRI permitted to catch spinal cord and roots (figure 6.1a). Segmentations were conducted to follow their 3D trajectories. An alignment between MRI data and the rostrocaudal location of each motoneuron pool [110] involved for flexion and extension allowed to highlighted roots required (figure 6.1c). Instead of observing a spatial selectivity in transversal plane, we looked at it in a coronal plane and showed a possibility to recruit similar roots at sacral level (figure 6.1d).

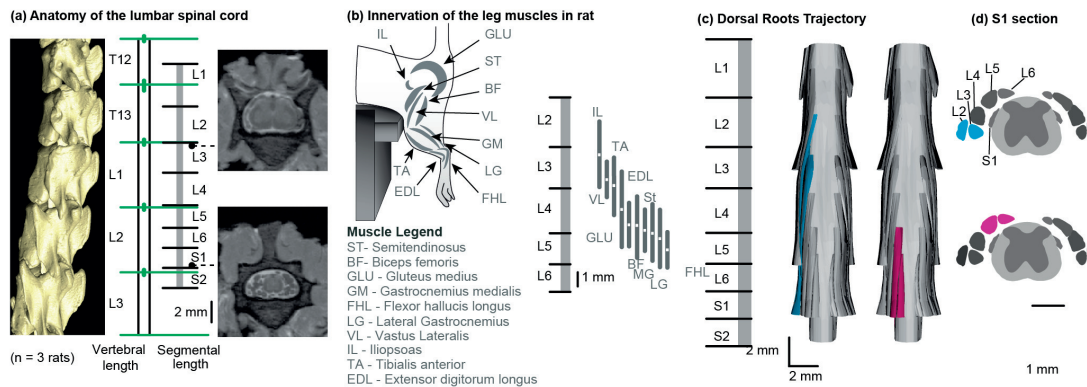


Figure 6.1 – Precise spinal cord anatomy. Model construction: (a) Ctscan imageries and their extracted 3D reconstructions define the vertebrae organisation and dimension. (b) MRI scanners are required to capture spinal cord and roots trajectories. (c) The rostrocaudal location and center (white square) of each motoneuron pool for muscles involved in flexion and extension were aligned and merged inside our 3D model. (d) Based on muscle activation during flexion and extension, respective muscle activities are projected on the spinal cord and activated roots are highlighted. A coronal section of S2 segment in humans and S1 segment in rat reveal the presence of roots containing every motoneuron pool labeled.

6.3.2 Modelization of belt strategy

To understand the activity of EES on such lateral aspect of the rat spinal cord, we integrate our realistic model inside a 3D hybrid finite-element method (FEM) (figure 6.2a) and neuron action potential propagation [46] (figure 6.2b). This model guided the build of an electromagnetic volume-conductor of lumbosacral anatomy, with anisotropic conductive properties proper to each different component inside. The FEM generated estimations of the 3D voltage potential spreading following a electrical

stimulation. Electrode active sites were located around the sacral spinal segment, like a half belt (figure 6.2a). To start, only monopolar cathodic stimulations were simulated for each electrode. The modelisation revealed that such electrode locations could recruit all roots innervating motoneuron pool locations involved in locomotion. Centered electrodes selectively activated extension related roots, while lateral electrodes recruited flexor one (figure 6.2c). To verify these predictions, a dedicate implant had to be design.

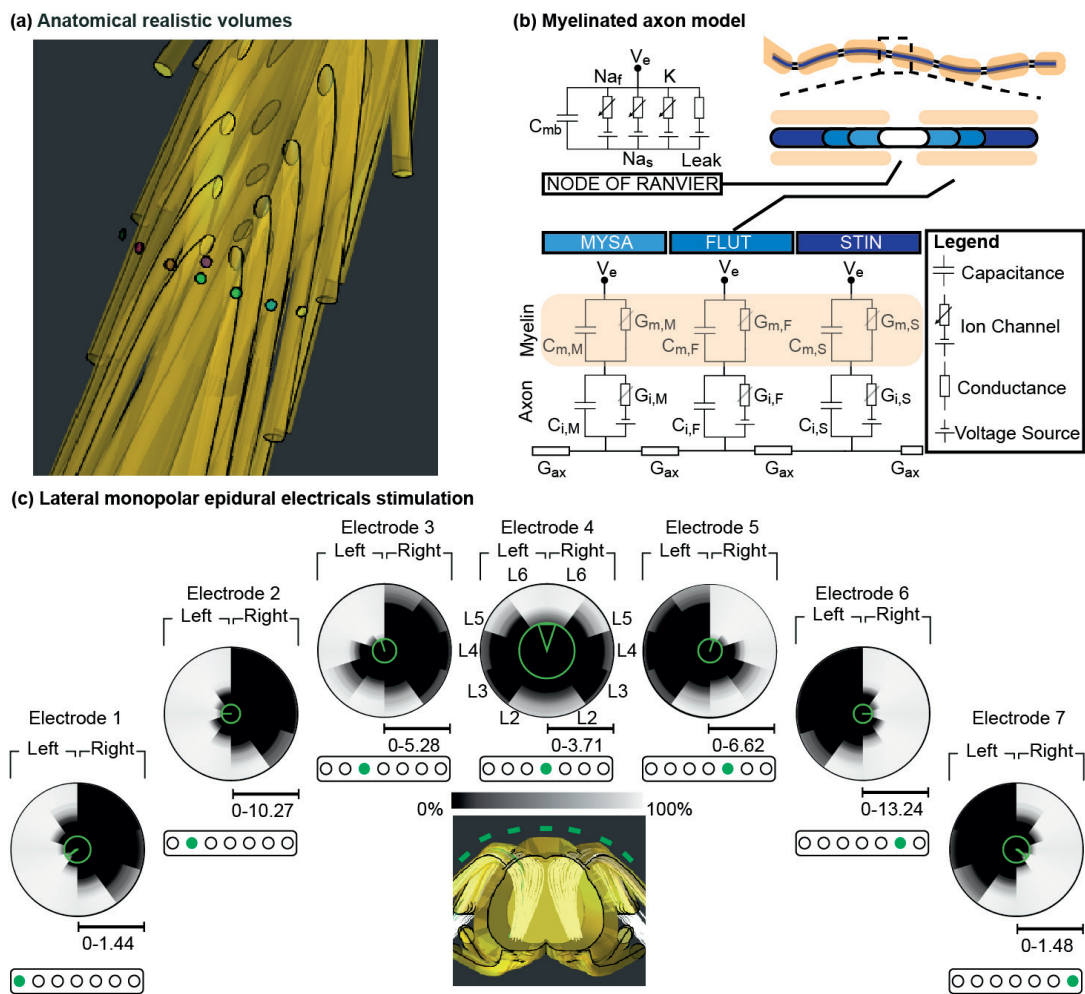


Figure 6.2 – Computational Model (a) Anatomically realistic volume conductor model of the rat spinal cord, as detailed in (Capogrosso et al., 2018) (b) Axon-cable model of myelinated nerve fibers. (c) Spinal recruitment curves of simulated monopolar stimulation at each active site individually.

Chapter 6. Model-driven optimization of multipolar electrical stimulation of the lumbosacral posterior roots using transversal epidural implant

6.3.3 Transversal spinal implants

In order to deliver tailored EES to the lateral aspects of the spinal cord, and based on the report of subdural neural implants [104] [150], we developed a transversal spinal electrode array to be implanted in the rat epidural space. The device compliance and its dimensions (thickness $< 100\ \mu\text{m}$) allow for a wide electrode distribution over the sacral spinal segments. Micro-cracked gold [54] in the interconnects and mechanically-soft silicones in the substrate and superstrate confer to this implant rare stretchability properties (Figure 6.3a-b). The mechanical match with the neural tissue promoted the implant biointegration over chronic implantation (Supp Figure S6.1). The platinum-silicone mesocomposite for electrode coating enables high performance and stable electrical stimulations under various conditions [104]. The low electrode impedance ($1.65\ \text{k}\Omega$ at $1\ \text{kHz}$) was maintained under large deformations ($13.78\ \text{k}\Omega$ at 40% strain) (Figure 6.3c). Cyclic voltammograms demonstrate the neural coating high effective surface area and its compliance to elongation, displaying larger cathodal storage capacity for larger strains (Figure 6.3d). Next, we investigated the electrode maximal charge injection limit without strain by applying biphasic charge balanced current pulses with gradually increasing current densities (Figure 6.3f). For a typical current density used in EES ($47\ \mu\text{C}/\text{cm}^2$), we measured the cathodal electrode potential (E_c) and the maximum negative voltage (V_{min}) under uni-axial strains. While V_{min} significantly decreased at 40% due to the interconnect resistive component, E_c remained relatively stable ($-0.19 \pm 0.05\ \text{V}$), demonstrating the electrode array ability to deliver fine EES in vivo (Figure 6.3e).

6.3.4 Transversal spinal implant selectivity

To validate the computational model and the implant design, we conducted acute electrophysiological experiment in intact anesthetized rat. Electrodes were slid epidural below the L2 vertebra targeting S1 spinal segment (Figure 6.4a, left). The ladder printed on implants helped to find the proper position (Figure 6.3a). Computed Tomography (CTscan) confirmed the soft implant compliance which fit the epidural space without visible pressure on spinal cord (Figure 6.4a, right).

In addition, bipolar wire electrode were implanted in a flexor (Tibialis Anterior) and extensor (Medialis Gastrocnemius) muscles of both side to record electromyographic (EMG) responses evoked by a low frequency current pulse ($0.2\ \text{ms}$). The quantification of the EMG monosynaptic pic for each EMG was used to draw recruitment curves. Monopolar EES were applied individually on each active site around the spinal cord. Circular plots transcribed the activity of each muscle in function of the current

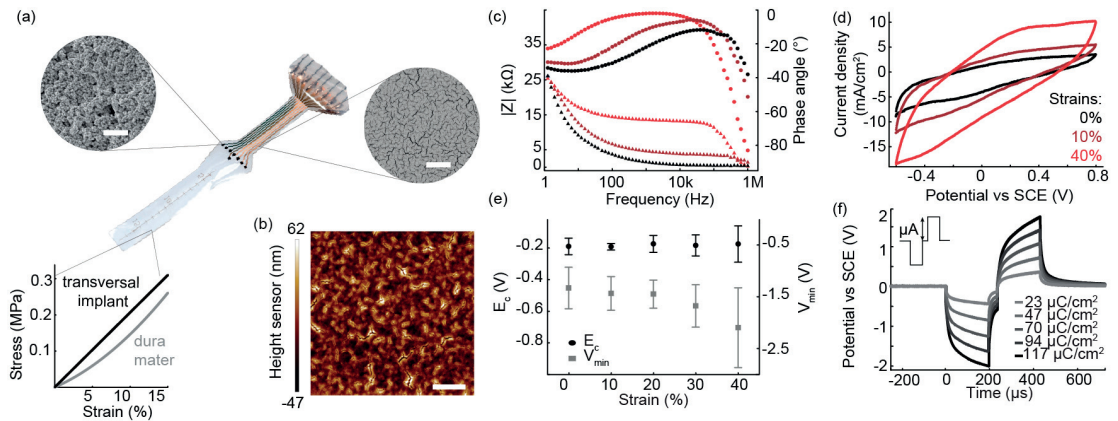


Figure 6.3 – A soft transversal electrode array. (a) Optical image of the spinal electrode array. SEM pictures of the interconnect thin film morphology and of the neural electrode coating are shown, top insets, right and left respectively. Stress-strain curves of the rat spinal dura mater and of the transversal implant (measured in saline) shows the implant relative softness with the interfaced tissue. (b) Representative AFM image of the non-encapsulated interconnect thin film. Tri-branched micro-cracks enables the film to sustain electrical conductivity under mechanical strain. (c) Magnitude (\square square) and phase (\bullet) of electrode impedance recorded in a 3-electrode setup configuration. Spectra were collected at 0% (black), 10% (blue) and 40% (red) uni-axial strains. (d) Cyclic voltammograms (50 mV/s) recorded in saline during a uni-axial stretch cycle. Larger cathodal charge storage capacity is observed for larger strains. (e) Voltage transients at the electrode coating surface recorded for different current densities. Charge-balanced, biphasic current pulses were injected through electrodes. The duration of each pulse phase was fixed to 200 μ s with an interphase period of 40 μ s. e, The cathodal electrode potential (E_c) and the maximum negative voltage (V_{min}) at the electrode coating surface were measured for different uni-axial strains ($n = 8$ electrodes, mean \pm s.d.). (f) The pulse current density was fixed to 47 μ C/cm, which corresponds to the typical maximum current pulse during in vivo experiments. Through the experiment, (E_c) remains within the water window (-0.6 V).

amplitude used, one for each active site. We confirmed here the fact that monopolar stimulations can achieve at S1 spinal cord segment some selectivity toward flexion versus extension. From Electrode 1 to 7 (left to right), (Figure 6.4b) stimulations described a selectivity gradient that started with left flexion, then a left extension. For E4, at the midline of the spinal cord, a bilateral extension is dominant. As stimulations continued to move to the right, muscles selectivity went to right extension, and flexion to finish.

6.3.5 Multipolar combination selection

We next exploited multipolar properties, capabilities to shape the electrical field in a way that some dorsal roots are recruited, while other are prevented to be activated [151]. With a multipolar stimulation paradigm, the number of combination possible within electrode exploded and it became illusive to test all of them.

Chapter 6. Model-driven optimization of multipolar electrical stimulation of the lumbosacral posterior roots using transversal epidural implant

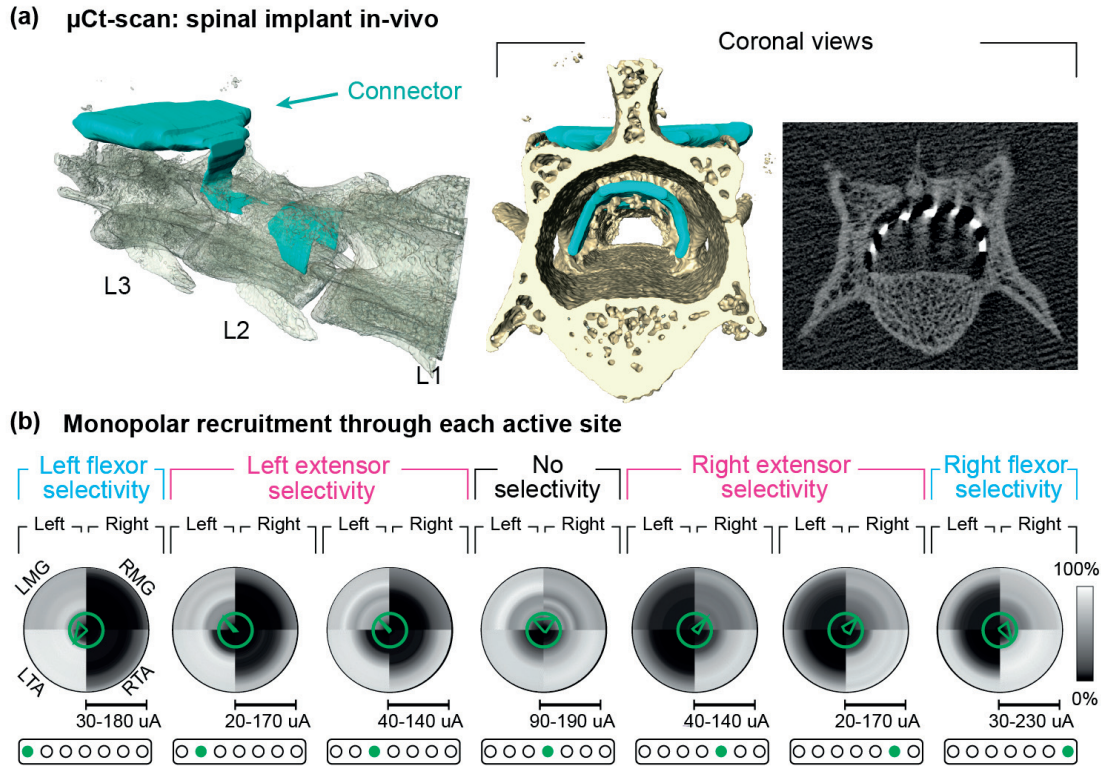


Figure 6.4 – Transversal implant integration and stimulation on spinal cord. (a) 3D rendering reconstructed from high-resolution microcomputed tomography scans conducted postmortem. A frontal view highlights the softness of the implant that embraces the shape of the spinal cord. One coronal slide of the reconstructed CTscan at implant level verified electrode location respectively to bone. (b) In-vivo experimental validations performed with each electrode individually show recruitment of flexor and extensor of both side. The white polygon represents the selectivity of each muscle at the amplitude of the maximum selectivity for the desired muscle and the white circle at which amplitude this occur.

To solve this situation, we developed a genetic algorithm (GA) to select a configuration suitable to elicit a flexion and another for extension (figure 6.5a). The “gene” to optimize is the vector of current for each electrode. Each generation involved a group of parent that generate children with random crossovers and mutations. Then, children feed the computational model and only the best are kept to be the next generation of parents. The cycle is repeated 500 times. We highlighted best outputs of this algorithm, one for the extension and one for the flexion. The extension privileged a centered stimulation while shielding the contralateral side (Figure 6.5b). The flexion targeted the stimulation on the extreme lateral aspect of the implant and shielded the ipsilateral extension (Figure 6.5c). Inside this virtual environment, the multipolar specificity doubled for the extension, while the flexion increased of 25% compared to monopolar recruitments (green shaded area).

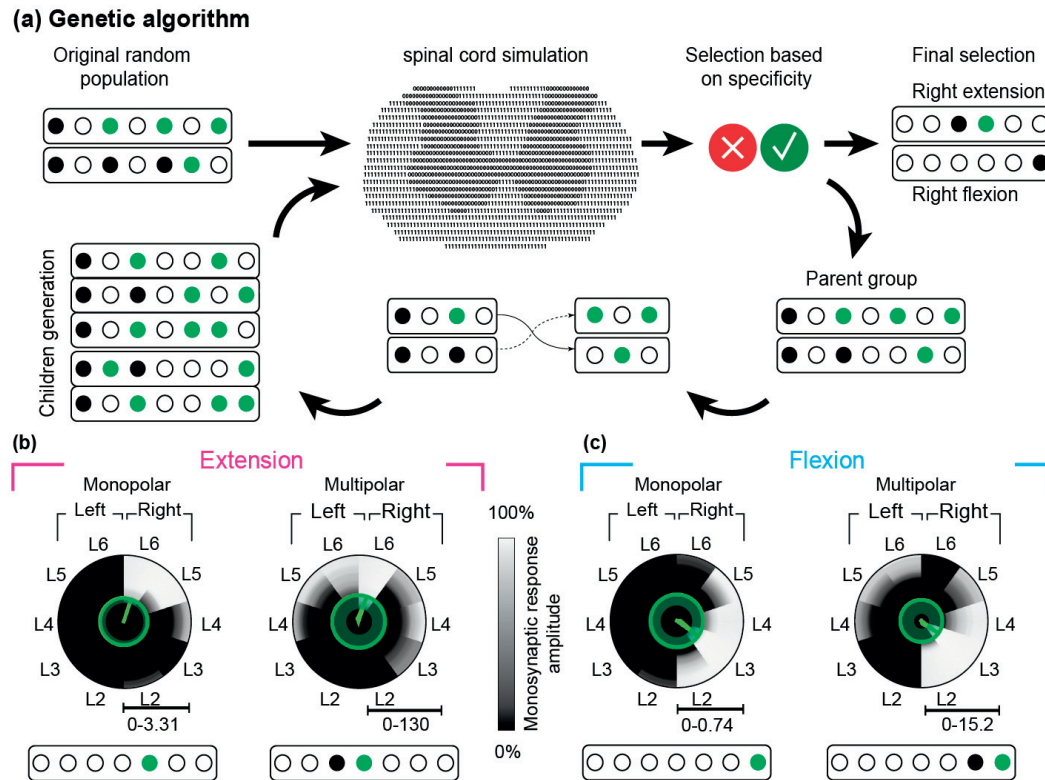


Figure 6.5 – Optimizing spinal selectivity. (a) A genetic algorithm was employed to minimize the euclidean distance between desired nerve fiber recruitment and actually observed recruitment pattern in each iteration. The genetic algorithm would follow the steepest descent method to find a local minima in the solution space for multiple iterations. After a local minima was identified, the search process was repeated multiple times with a randomly set starting point to identify a global minima within the solution space. (b) The fibers of the L6 dorsal root were chosen as a extensor hotspot. The GA was primed to find a configuration to highly selectively recruit the L6 root. The resulting stimulation paradigm was highly selective in the L6 root. (c) The fibers of the L2 dorsal root were chosen as a flexor hotspot. The GA was primed to find a configuration to highly selectively recruit the L2 root. The resulting stimulation paradigm was not highly selective for L2 root recruitment but first activated the L3 root, closely followed by the L2 root. The multipolar configuration is however more selective than a simple monopolar stimulation.

6.3.6 Multipolar experimental validation

We performed similar implantations as monopolar validation experiment and added iliopsoas (IL) muscles, in order to ensure a complete muscle coverage. We compared monopolar versus multipolar stimulations for both combinations extracted from the GA. In the first case, we saw a better selectivity of extensor muscles as predicted by the simulation (Figure 6.6a). The MG muscles were the only recorded muscle above threshold during wider range of amplitudes compare to monopolar stimulation ($n = 6$ rats, $* p < 0.05$) (Figure 6.6b). In the second case, we observed a tendency to be more selective (Figure 6.6c), but the increase was not significant. The monopolar configuration was already strongly specific for flexor muscle and the multipolar case

Chapter 6. Model-driven optimization of multipolar electrical stimulation of the lumbosacral posterior roots using transversal epidural implant

reinforced it without clear superiority ($n = 6$ rats, n.s. $p > 0.05$) (Figure 6.6d).

Multipolar stimulation can oriented electrical field and compensate the miss positioning. When the implant was left shifted, the midline electrode did not evoke a bilateral movement, here the extensor left is recruited first, than the right one (Figure 6.6e-right). With bipolar stimulations, the cathodic electric field was pushed back to the center and extensors were recruited both at the same amplitude to elicit a bilateral activation (Figure 6.6e-left). The amplitude difference between the first muscle activated and the second was normalized and compared with the multipolar condition ($n = 4$) (Figure 6.6f).

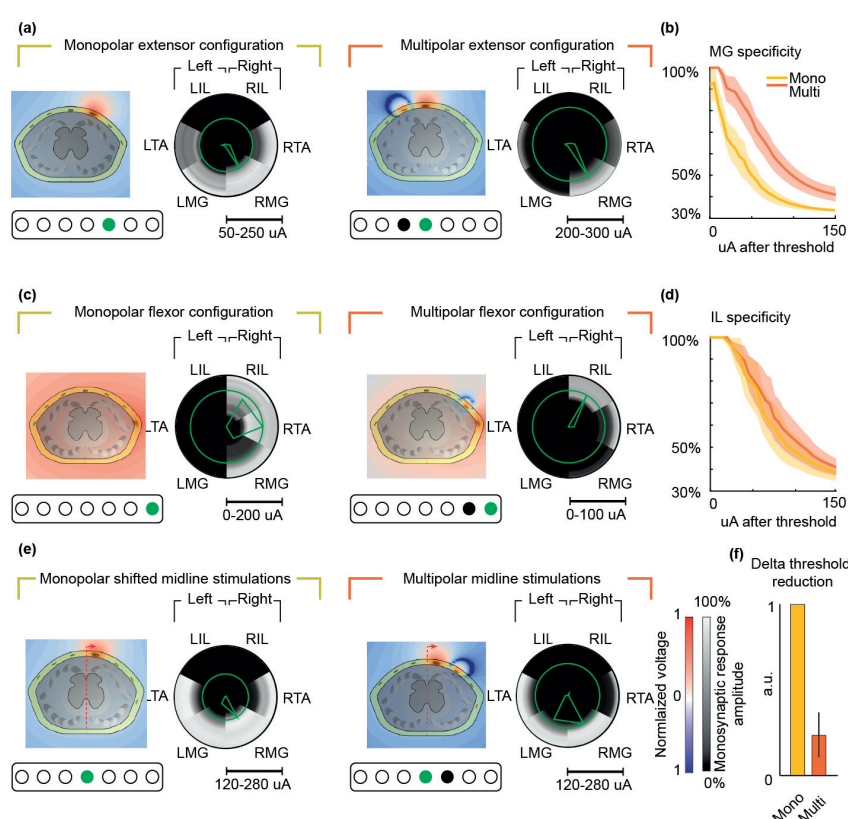


Figure 6.6 – In-vivo validation multipolar recruitment. Sedated rats with hanging legs received predicted stimulation pattern with incremental amplitudes. (a,c,e) example of muscle recruitment elicited by monopolar and multipolar stimulation in yellow and orange respectively; muscles represented are Medial Gastrocnemius (MG), Tibialis anterior (TA) and Ilisopsoase (IL) with prefix L and R according to the left or right side. Green polygons fit muscle selectivity index when the highest is reached for each recruitment and green circle radius match amplitudes. (a,c) Monopolar and predicted multipolar stimulation patterns with their respective muscle recruitment. (d) Graphs report the mean ($n = 6$ rats) of selectivity index after targeted muscle threshold, with the sem shaded, for extension and flexion. (e) In the case of misalignment, midline electrode will favor one side. With mutlipolar stimulation, threshold of each side can be equalized. (f)Histogram plot represent the normalized mean ($n=4$ rats) differential threshold between mono- and multi-polar stimulation, where a perfectly aligned implant should be 0.

6.3.7 Multipolar stimulation combined with spatiotemporal neuromodulation

We then tested multipolar neuromodulation could generate proper movement in rat after a SCI and integrate inside a rehabilitation protocol. Seven weeks after SCI including 6 weeks of rehabilitation over treadmill with continuous midline neuromodulation.

Then, we tested the implant in rats ($n = 6$) with a clinically relevant spinal cord injury. A contusion was performed on T8 spinal cord with a mechanic impactor (Figure 6.7a, Supp. Figure S6.2). The first step was to validate that the flexor muscles activity shown could elicit a functional leg movement usable for stepping. Here, rats hang in a jacket attached on a robotic body weight support and doesn't touch the floor (Figure 6.7b). Reflective markers that were placed on the leg and video recorded synchronously with a continuous burst of stimulation with the desired pattern - flexor or extensor. The vertical displacement of the foot marker was measured for the ipsilateral and contralateral leg. A clear unilateral, but antagoniste movement was observed in both case (Figure 6.7b, magenta for extension, cyan for flexion).

To finish the validation of spatiotemporal neuromodulation using the multipolar protocol, we tested same rats with a complete multipolar pattern alternating extension and flexion according to the gait cycle on a treadmill (Figure 6.7c, Supp. Figure S6.3). First recording condition was to control that rats did not spontaneously recovered from the contusion. The second despite a continuous neuromodulation and finally the third showed a full multipolar spatiotemporal neuromodulation. Sequences representing typical locomotion pattern for each condition was presented (Figure 6.7d). A principal component analysis (PCA) was run over 118 computed parameters during the rat stepping. We visualize each recorded gait in the new space created by the three first PCs which explain the highest amount of variance and reflect the progression from a paralyzed animal toward healthy rats (Figure 6.7d, top right). Analysis of PC1 factor weights allowed extracting numerous parameters highly correlated with the progression toward healthy state. This analysis revealed that spatiotemporal neuromodulation at S1 spinal cord segment with multipolar stimulation significantly improved key features of the locomotor system (Figure 6.7d, bottom right).

Multipolar stimulations followed amplitude modulation (Supp. figure S6.4). A progressive increase of stimulation amplitude for flexor activity led to an enhancement of the gait cycle - mainly the swing phase. An amplitude too strong led to a detrimental stepping pattern. Finally, we perform post mortem histologic analysis on the spinal cord, and confirm that such large and invasive implants did not damage the neural

Chapter 6. Model-driven optimization of multipolar electrical stimulation of the lumbosacral posterior roots using transversal epidural implant

tissue (Supp. figure S6.5).

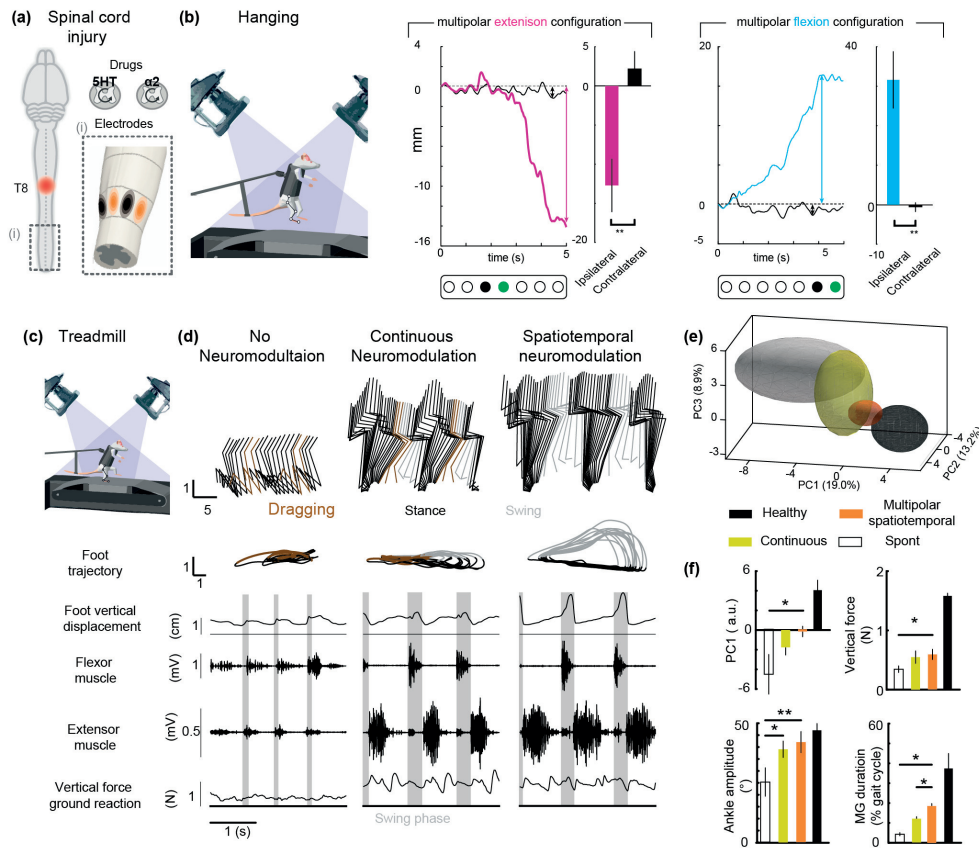


Figure 6.7 – Long-term multipolar neuromodulation. (a) Rat received a severe clinically relevant SCI and a transversal spinal cord implant designed for multipolar stimulations. (b) Rats were hanging in a body weight support harness and received a series of multipolar pulse with increasing amplitude through implant targeting extension, then flexion. The resulting foot trajectory is shown for ipsilateral (colored) and contralateral (black) side to the stimulation. Histogram plots report the mean ($n = 6$ rats) vertical displacement of the foot for both side. (c) Locomotion was recorded on a treadmill without stimulation, with continuous neuromodulation applied over midline sacral segments and during spatiotemporal neuromodulation. (d) For each condition (same rat), a stick diagram decomposition of the right limb movement is shown, in addition with successive foot trajectory, the swing (light grey), drag (brown) and stance phase, and vertical foot trajectory, flexor and extensor muscle activity and vertical ground reaction force during a continuous sequence of steps. Mean of the gait cycle recorded in 6 rats under the different condition of neuromodulation are presented in the PC space and computed with 12 consecutive steps. Histogram plots report mean of PC1, mean peaks amplitude of vertical ground reaction force, mean angle amplitude of the ankle and mean extensor muscle duration for the different neuromodulation conditions and for intact rats. (Error bar, SEM; * $p < 0,05$; ** $p < 0,01$)

6.4 Discussion

We built a 3D anatomical volume based on precise imaging methods and integrated it inside hybrid FEM [46]. Dorsal roots trajectories revealed a sacral area where are

all lying around the spinal cord and computational models proposed multipolar paradigm to reinforce selectivity. We conducted simulations and in-vivo validations that demonstrated selective stimulations for flexion and extension. Then, a dedicated spinal implant design delivered multipolar stimulation combined with spatiotemporal [110] paradigm to restore locomotion in paralyzed rat.

6.4.1 Lateral spinal cord recruitments led to novel spinal implant design

Computer models [44] [46] and experimental [56] validation found evidence that EES active large afferent fibers in dorsal roots. Recruitment of such pathway evoked motor response in animal model [45] and patients [73]. Here, we expanded these results to distal afferent fiber stimulations. This L3 recruitment around sacral spinal segment demonstrate the possible activation of flexor motoneurons located up to 4 spinal segment away with a remarkable selectivity. Roots from L3 to L6 are present at this level, so all motoneurons of muscle involved in locomotion should be accessible. Following the framework that target dorso-lateral root activation [110], we proposed a novel implant design. In opposition to previous generation with a longitudinal shape [110] [149] [69], our implants were transversal and conserved similar muscle recruitment properties in rat. The main advantage of this configuration was that for the first time all electrodes were located close to each other and offered the opportunity to try a multipolar strategy.

6.4.2 Multipolarity increased specificity

Until our novel implants, electrodes were located too far from each other to create interactions and generate multipolar electrical fields. Here, we covered roots from L2 to L6 with a restricted number of electrodes linked to the fabrication process [104]. The physical resolution offered by electrode could not be strong enough to achieve sufficient specificity. We overcame this issue by playing with electrode polarities. Multipolar strategy oriented voltage field to activate different sub cortical structures [151]. We demonstrated benefits to apply this strategy on spinal cord to increase extensor muscle selectivity. Computational models predicted an increase for each root specificity using multipolar stimulations. However, enhancements could not be significant regarding some roots already highly specific for monopolar configuration.

6.4.3 Paradigm compatibility: spatiotemporal multipolar protocols for long term rehabilitation

Multipolar stimulation paradigm does not affect other policies such as spatiotemporal neuromodulation or amplitude modulations [110]. We found that superiority of spatiotemporal neuromodulation over continuous stimulation is preserved. The new implant location activated similar pathway and conserved the previously defined muscles synergies temporal structure [110]. The increase in the specificity available with multipolar stimulations could lead to a redefinition of the synergies used, some could be divided to fit even more in spinal cord activity [41].

6.5 Conclusion

Spatiotemporal neuromodulation strategies appeared as a promising rehabilitation protocol after SCI in rat and non-human primate, pending to human clinical trials. This approach relied on the specificity of each electrode. Here, we have introduced novative spinal implants and a multipolar stimulation strategy to enhance selectivity. We expect this framework to guide next spinal cord implant generation and neuro-modulation protocols.

6.6 Methods

6.6.1 MicroComputed tomography (μ CT scan)

In vivo images of spinal implants were produced using the microcomputed tomography scanner Skyscan 1076 (Bruker μ CT). Based on X-ray technology, The scanner rotated around the sample and combined multiple angle of view to extract a 3D image. Scanner settings were adjusted to avoid artifacts induced by metallic parts of the vertebral orthosis (0.5–1 mm aluminum filter, voltage 70–100 kV, current 100–140 μ A, exposure time 120–160 ms, rotation step 0.5°). The reconstruction in 3D occurred in NRecon software using GPURecon Server (Bruker μ CT). The device is equipped with isoflurane to keep the rats under anesthesia during the scan to reduce motion artifacts. Amira software (FEI Visualization Sciences Group) was used to segment each component (vertebrae, implant, connector) and for the final rendering.

6.6.2 MRI

We developed a mixed contrast ad-hoc MRI image sequences on a 3 T SIEMENS PRISMA to visualize the spinal roots in human subjects. Moreover we performed similar ex-vivo scans in rats on a custom build 9.4 T MRI.

6.6.3 Computer Model

We translated the computational framework previously detailed in [150] to Sim4Life to elaborate a hybrid computational model capable of calculate the recruitment of neural structures during epidural electrical stimulation of the lumbar spinal cord in rats and humans. The model consists of a finite element part to characterize the electric potential and currents generated by EES, as well as a geometrically realistic biophysical model of the afferent fibers in the spinal roots and dorsal column of the lumbar and sacral spinal cord to identify the percentage of afferent fibers recruited by various stimulation configurations.

6.6.4 3D Geometry

We first extracted the volume conductor model representing the spinal segments L1 to S2 of the rat spinal cord, detailed in [150] and imported it into Sim4Life. We then built a volume conductor model representing the spinal segments L1 to S3 of the human spinal cord in the exact same fashion. Both geometries included seven distinct

Chapter 6. Model-driven optimization of multipolar electrical stimulation of the lumbosacral posterior roots using transversal epidural implant

compartments representing: the grey matter (GM), the white matter (WM) and spinal roots, the dural sac filled with cerebrospinal fluid (CSF), the epidural fat (Fat), the bony vertebral column (Bone), the tissue surrounding the spine (Saline), and the metallic electrode active sites (Elec). The relevant anatomical data was extracted by measuring the widths and lengths of each spinal segment identified in the MRI data of both rat and human. Finally, we represented the electrode active sites by cylinders that combined the same dimensions and inter-spacing as the ones used during the in-vivo experiments.

6.6.5 Physics

In analogy to [150] the electric potential distribution was computed under quasi-static approximation [152] [153] [154] [46]. Each compartment was assigned a scalar conductivity tensor, reflecting the isotropy of the material conductivity [155] [156] [154] [46].

Merely the joint white matter and spinal roots were assigned an anisotropic conductivity to account for the preferential flow direction of ions along the longitudinal axis of axons that run parallel to the roots and white matter in the spinal cord. For this purpose, we computed a local coordinates system in every point of the subdomain of the geometry composed by the white matter and roots to define the conductivity tensor. For this purpose, we performed a preliminary quasi-static electromagnetic simulation. We applied boundary conditions of $V = 0$ and $V = 1$ on the uppermost and lowermost side of the subdomain to allow the potential gradient to follow the curvature of the subdomain. We extracted the direction of the diffusion tensor in each mesh element and overlayed its directionality as Cartesian coordinates in each individual mesh element.

We modeled the stimulation pulse with a boundary current source injecting a unitary current of $1 \mu\text{A}$ applied on one surface of a single active site at a time. We assigned a zero-flux condition (Von Neumann) to the other faces of the stimulating active site to minimize the direct outward current flow away from the spinal cord. This was done to account for the shielding effect of the highly insulating PDMS-based paddle of the electrode array. Finally, we applied a Dirichlet condition ($V = 0$) at the outermost boundary of the model to approximate a zero-potential condition at infinity.

6.6.6 Biophysical Model

We coupled the FEM model with a realistic biophysical model of myelinated nerve fibers running in the dorsal roots of the spinal cord. Computational and Experimental efforts suggested that the primary mechanism of EES is the recruitment of large-diameter, myelinated afferent fibers in the dorsal roots [43] [46]. Hence, only type A α -fibers running in the dorsal roots were simulated. We used NEURON in Sim4Life to model 50 myelinated Group I afferent fibers per dorsal root as a log-norm function with a mean fiber diameter of 16 μm and a standard deviation of 4 μm [157]. An anatomically accurate trajectory of the afferent fibers was initialized and fitted around their entry and exit point determined by the anatomical parameters extracted from MRI and CT-data. A Sweeney model [158] was used to describe the equation of the active membrane at the nodes of Ranvier and at the passive intermodal segments. The electrical compartments were automatically initialized in Sim4Life. The resting potential was set to -80 mV. Finally, recruitment of Ia afferents was evaluated by linearly scaling the extracellular voltage applied at each fiber's compartment until an action potential was generated.

6.6.7 Genetic Algorithm

In order to identify optimal multipolar stimulation configurations a Genetic Algorithm (GA) was implemented in Python. The objective was to minimize the Euclidean distance f_e between desired spinal root recruitment N_d and simulated one N_s for each dorsal root.

The input of the model was a vector of multiplication factors corresponding to each active site. The resulting fields of the monopolar stimulation with unitary currents were superimposed and scaled by the multiplication vector, which is correct under a quasi-static approximation [152]. The newly generated electric potential distribution was used for the NEURON simulations. The GA was terminated when the best individual fitness was varying less than 5% for more than 30 generations. Basin-Hopping was implemented to search for other local minima. After 500 iterations of Basin-Hopping the global minima was chosen.

6.6.8 Selectivity

The capacity of a stimulation protocol to elicit nerve-fiber recruitment in one root over other was encapsulated in a selectivity index. It is desirable to activate as many nerve fibers in one root as possible while minimizing the amount of fibers activated

Chapter 6. Model-driven optimization of multipolar electrical stimulation of the lumbosacral posterior roots using transversal epidural implant

in any other dorsal root. The following selectivity index was defined to provide this useful information.

6.6.9 Spinal implant fabrication

The general fabrication process of the soft transversal spinal implant is depicted on supplementary figure 6.1. First, a 60 μm thick substrate layer of PDMS (Sylgard 184, Dow Corning, mixed at 10:1, w:w) was spin-coated on a 3" silicon wafer coated with a water-soluble layer of poly(4-styrenesulfonic acid) (PSS, Sigma-Aldrich, spin-coated at 2000 rpm for 1 minute). Following PDMS curing (80 °C overnight), a 23 μm thick PET stencil mask (Mylar, Dupont) was laminated on the PDMS substrate. The shadow mask was tailored to the interconnects layout using an excimer femtosecond laser (1030 nm, Amplitude Systemes, MM200-USP, Optec). Then, a 5 nm thick film of chromium and a 45 nm thick film of gold were successively thermally evaporated (Auto 306, Edwards) to the PDMS substrate, shaping the implant interconnects. The latter were encapsulated with a 30 nm thick layer of silicone rubber (Elastosil M 4600, Wacker). This passivation layer was spin-coated over a 23 μm PET film (Mylar, Dupont) laminated on a 4" silicon wafer. Following the silicone rubber curing (80 °C overnight), a second PET film was laminated over the silicone rubber using a dry film laminator (Photopro 33). The triple stack PET-rubber-PET was released from the wafer and then customized to the electrode negative layout using an excimer laser (Optec). Finally, the top PET film was carefully peeled off the stack and the silicone rubber superstrate was bonded to the PDMS substrate following oxygen plasma surface activation. The implant electrodes were coated with a platinum-silicone composite, as described in REF. Briefly, 100 mg of platinum microparticles (Pt powder, Goodfellow) were mixed to 110 μL of a PDMS/cyclohexane solution (200 mg/500 μL , Dow Corning, Sigma-Aldrich). The mixture was thoroughly stirred and the cyclohexane evaporated until the mixture became a paste. Finally, the paste was printed to the electrode sites by spreading the paste over the second PET film. Right before printing, the paste was diluted with a drop of cyclohexane. The PET film was then peeled off the superstrate and the platinum-silicone composite cured (60 °C overnight). The substrate-superstrate stack was precisely cut to the implant shape using an excimer laser (Optec). The last step consists in connecting the implant interconnects to stainless-steel wires (AS 632, Cooner Wire) via Ag paste (ref) drop casting to the connection pads. After the wiring sealed (734, Dow Corning), the soft transversal implant is released from the wafer after immersion in deionized water.

6.6.10 Surgical procedures

General condition of surgical procedures have been detailed in previous works [31] [56] [104]. Present In vivo experiments involved female Lewis rats with initial weight of 180–220 g (LEW-ORlj, Janvier Labs). Each surgical procedures were performed under full general anesthesia with isoflurane in oxygen-enriched air (1–2%). Rats recovered from anesthesia in an incubator after surgery.

Animal regulations

All experiments were approved by Local Swiss Veterinary Offices and conducted under the guidelines established at EPFL in accordance with the Swiss federal legislation (GE33/17). A total of 15 rats were used for experiments divided as follows: n= 3 rats; for the model development, n = 6; rats for acute muscle recruitments in mono and multipolar stimulations, n= 6 rats; for long term implantation, movement generation, spatiotemporal rehabilitation and biocompatibility.

Implantation of intramuscular electrodes

In order to record electromyographic activity, leg muscles were implanted with bipolar electrodes, the combinations depending on experiments: iliopsoas, gastrocnemius medialis and tibialis anterior, extensor digitorum longus. Recording electrodes were fabricated from stainless steel wires (AS631, Cooner Wire) where a small part (0.5-mm notch) of insulation was removed. A common ground was created with the same type of wire by removing about 1 cm of Teflon from the distal extremity and placed subcutaneously over the left shoulder. All electrode wires were connected to a transcutaneous amphenol connector (Omnetics Connector Corporation) cemented to the skull of the rats.

Surgical insertion of spinal implants

The surgical procedure to insert the spinal implant into the epidural space are detailed in [110]. Briefly, to create entry and exit points for the implant, we performed two partial laminectomies at vertebrae levels L3–L4 and L1–L2 . A surgical suture is used to pull the implant below vertebrae, but above the dura mater. The position of electrodes were fine-tuned with electrophysiological testing intra-operatively. To avoid any displacement of the implant, the connector was secured into a dental cement cage on top of the L3–L4 vertebra.

Chapter 6. Model-driven optimization of multipolar electrical stimulation of the lumbosacral posterior roots using transversal epidural implant

Spinal cord injury models

Rats received a spinal cord contusion, a clinically relevant model of injury. Under aseptic conditions and general anesthesia, the spinal cord segment T8-T9 was revealed after a partial laminectomy at T9 vertebra segment. A force-controlled spinal cord impactor (IH-0400 Impactor, Precision Systems and Instrumentation LLC, USA) applied a 230 kdyn (1 dyn = 10 μ N) to create severe contusion injury. The extent of the spinal lesion was evaluated using coronal tissue sections stained with antibodies against glial fibrillary acidic protein (GFAP) (Dako Z0334, USA).

6.6.11 Motor-evoked potential recruitments

Motor-evoked potential recruitments for model validation were performed with sedated rats (urethane 1 g/kg, i.p., Sigma-Aldrich). Intramuscular electrodes were implanted as defined in iliopsoas, gastrocnemius medialis and tibialis anterior muscles of both legs. Important laminectomy was performed to expose sacral segment and dorsal roots. Asymmetric pulses (0.2 ms duration, 1/5 amplitude ratio) at 0.5 Hz through epidural electrodes were delivered while motor-evoked potentials of each muscle were recorded simultaneously. The electrode location was defined by implant dimensions according spinal cord midline. The intensity of the electrical stimulation was increased progressively from 0 up to the first between 300 μ A or muscle saturations. Electromyographic signals were amplified, filtered (1–5,000 Hz bandpass), and recorded (48828 kHz) for offline analysis. The pick to pick amplitude of monosynaptic response of the motor-evoked potentials were calculated and normalized for each muscle, and represented in black and white polar maps of motoneuron activation. Threshold was defined as 10% of the total activation. When curve failed to reach plateau, we extrapolated missing values using Matlab fitting function for sigmoidal non-linear curves.

6.6.12 Rehabilitation procedures after spinal cord injury

Each rats followed a training protocol starting 7 days after the injury. The neurorehabilitation program was conducted on a treadmill using a robotic body weight support system (Robomedica) that was adjusted to provide optimal assistance during bipedal stepping, daily for 30 min. To enable locomotion, a serotonergic replacement therapy combining the 5HT_{2A} agonist quipazine and the 5HT_{1A-7} agonist 8-OHDPAT was administered systemically 5 min before training. 7 days after spinal implant surgery, the training was performed with electrical neuromodulation.

6.6.13 Kinematics, kinetics and muscle activity recording

Recording procedures have been detailed previously (Wenger et al., 2016). Briefly, an high-speed motion capture system Vicon (Vicon Motion Systems) tracked reflective markers with 12 infrared cameras (200 Hz). The iliac crest, greater trochanter (hip), lateral condyle (knee), lateral malleolus (ankle) and distal end of the fifth metatarsal (limb endpoint) of both legs are marked and their final 3D position was reconstructed offline using Vicon Nexus software. The same device allowed recording (2 kHz) of electromyographic activity after amplification and filter (10–2,000 Hz bandpass), and monitoring of ground reaction forces in the vertical, anteroposterior and mediolateral directions using a force plate (2 kHz, HE6X6, AMTI) located below the treadmill belt. The system was synchronized with two cameras recording video (100 Hz, Basler Vision Technologies) oriented at 90 degrees and 270 degrees with respect to the direction of locomotion.

6.6.14 Closed-loop platform

The Vicon recording system generated raw 3D positions of the markers and send them into a real-time algorithm via Ethernet using DataStream SDK software. A control platform implemented in a multi-threaded C++ environment (Visual Studio 2012, Microsoft) running on Windows 7 Microsoft with a quad-core computer. An RZ2 processing unit (Tucker-Davis Technologies) connected to an IZ2 Stimulator (Tucker-Davis Technologies) formed and delivered stimulation patterns. Inside a custom algorithm designed for online performance, we filtered signals, interpolated missing markers through triangulation and relabeled them to appropriate position. According each leg, the angular trajectory of the foot around a virtual center of rotation in the sagittal plane was continuously calculated. Based on angular values, the control algorithm triggered appropriate electrode combination [110].

6.6.15 Behavioral condition

Rats were recorded bipedally on treadmill while a robotic body weight support system provided optimal assistive force against gravity and preventing lateral falls. A serotonergic drug cocktail was injected systemically before each training and recording session. After a couple of minutes, EES were applied through relevant electrode combination and an external ground located far subcutaneously. Amplitude ratio inside a combinaison was driven by predictive algorithm, but the exact intensity of electrical stimulation was manually tuned (biphasic asymmetric rectangular pulses, 60 Hz, 50–300 μ A, 1/5 ratio, 0.2 ms duration) to get the best visual locomotion in

Chapter 6. Model-driven optimization of multipolar electrical stimulation of the lumbosacral posterior roots using transversal epidural implant

the rats. The temporal structure of each combinaison was conserved as previously described according to their expected function [110]. Spatiotemporal neuromodulation performance compared to continuous neuromodulation was tested in the same rats during bipedal locomotion on a treadmill. The assistive support body weight provided by robotic support was adapted and fixed for each animal, then maintained constant across conditions. Stimulation intensity was adjusted for each condition, since optimal high amplitudes of spatiotemporal neuromodulation could not be used for continuous neuromodulation. Using same values could block leg movements and led to diminished performances. We recorded 10 to 20 successive steps during continuous neuromodulation over midline of spinal cord S1 segment and through spatially multipolar stimulation located on the lateral aspect of the same segments with a temporal structure. All the experimental conditions within and between recording sessions were randomized for the analyze.

6.6.16 Biocompatibility

Histology for biocompatibility validation was performed after 10 weeks of implantation on $n=6$ rats. They were perfused and their spinal cord were extracted. The spine was first left in PFA solution, then in sucrose and conserved in PBS. The spinal cord was frozen and cut into 40 μm thick slices using a cryostat (Leica Instruments). We used immunohistological staining against glial fibrillary acidic protein (GFAP) to reveal Astrocytic reactivity. Slices were incubated overnight in anti-GFAP antibody solution (1:1000, Dako Z0334, USA) and visualized with a secondary antibody (Alexa fluor©488 or 555, Thermofisher). Each sections was observed and photographed with a slide scanner fluorescence microscope (Leica). Immunostaining density was measured offline using a custom-written Matlab scripts with 3 representatives images of sacral segment per rat. Conventional setting were used to acquire images and kept constant according to previously described methods [31].

6.6.17 Principal Component Analysis

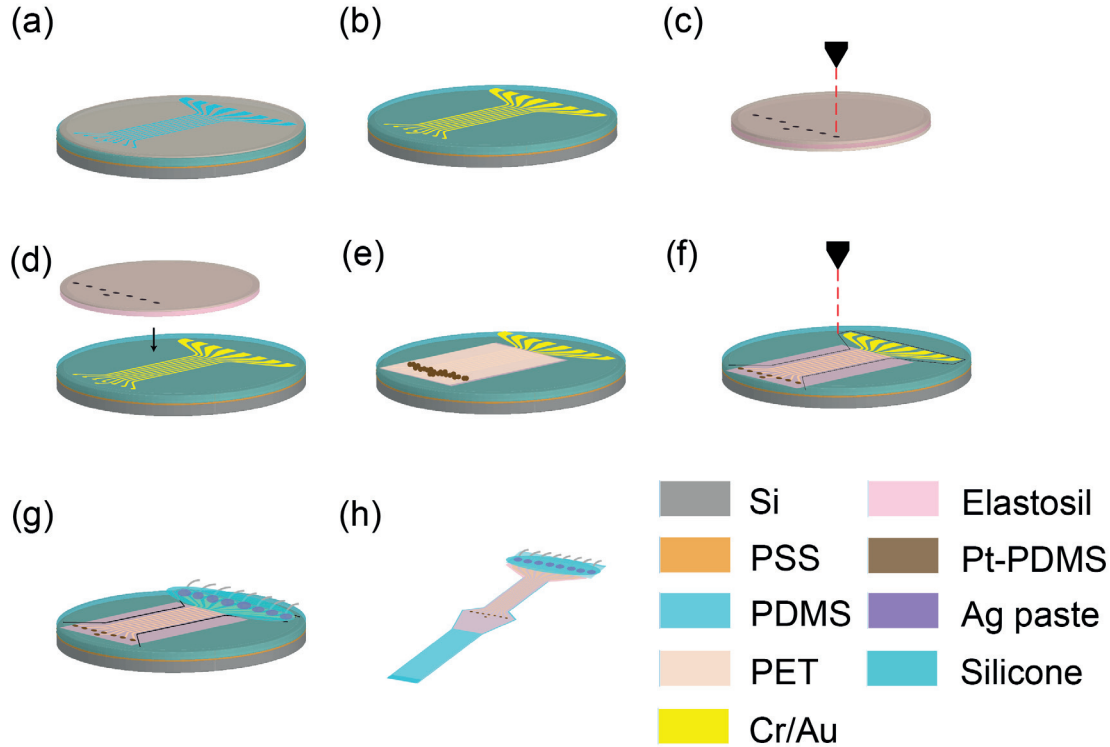
A minimum of 12 step cycles was typically extracted for each hindlimb in each experimental task and rat. A total of 118 parameters quantifying kinematics, kinetic and muscle activity features were computed for each gait cycle using custom-written Matlab scripts and according to methods described previously [7]. PC analyses were applied on all the computed parameters from all individual gait cycles for all the rats together. Gait cycles were visualized in the new synthetic PC space, and PC scores were extracted to quantify differences between groups or experimental conditions. Parameters highly correlated with PCs that discriminated the experimental conditions

were extracted.

6.6.18 Statistics

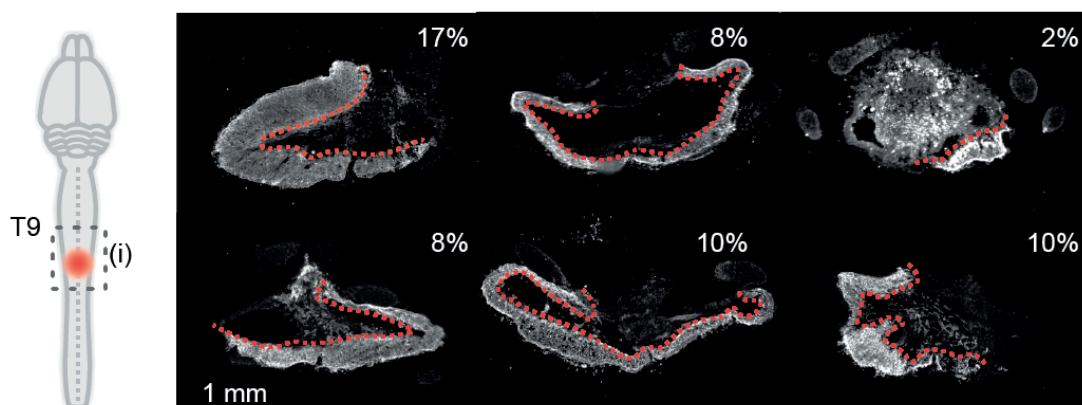
All computed parameters were quantified and compared between tested groups. Statistics were performed on average values per rat. All data are reported as mean *pm* s.e.m. unless specified otherwise. Significance was analyzed using paired Student's *t*-test, ANOVA or repeated-measures ANOVA when data were distributed normally. Post hoc comparisons were performed using the Kruskal-Wallis test. The nonparametric Mann-Whitney test was used in comparisons of $n < 6$ rats. The sizes of the experimental groups were arranged to minimize the number of sentient animals used in the studies while providing sufficient information to report significant and reliable results. Gait cycles were excluded from data analysis when stimulation profiles were delivered with incorrect timing during behavioral recordings. For continuous neuromodulation, none of the gait cycles had to be excluded.

6.7 Supplementary figures



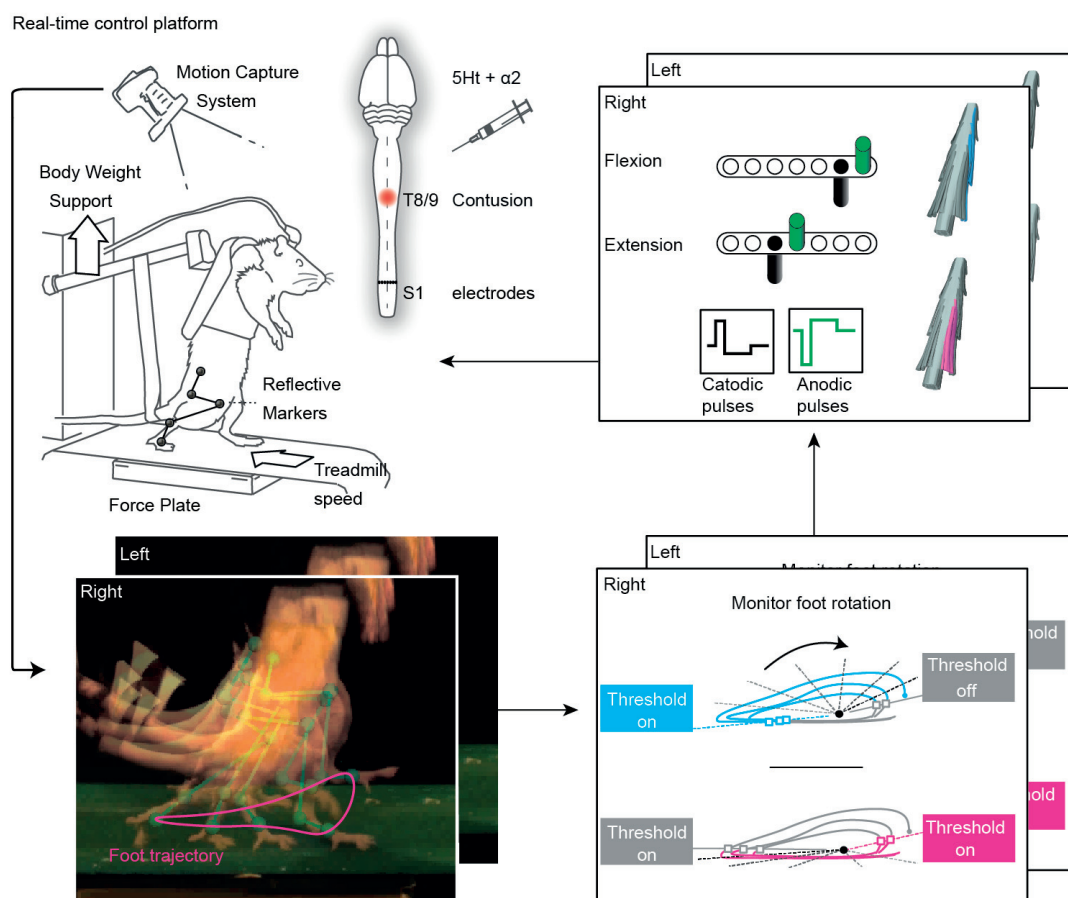
Supplementary Figure S6.1 – Transversal spinal electrode array microfabrication. (a) A PET stencil mask is laminated on a PDMS substrate. The latter was previously spin-coated and cured on a PSS-coated Si wafer. (b) The interconnect thin film is thermally evaporated and the stencil mask peeled off. (c) In parallel, an elastosil membrane laminated with PET films on both sides is prepared for the implant encapsulation. Laser ablation of this stack formed the electrode sites. (d) After a single PET film removal, the stack is aligned and O₂ plasma bonded to the metallized PDMS substrate. (e) The 2nd PET film is used as a stencil mask for the Pt-PDMS mesocomposite screen printing at the electrode sites. (f) After peeling-off the PET film, the implant shape is defined by laser ablation through the elastosil superstrate and PDMS substrate. (g) Stainless-steel micro-wires are carefully placed and connected to the implant interconnects via silver paste dispensing. The connector is eventually encapsulated with a room temperature vulcanized (RTV) silicone. (h) Finally, the implant is released from the wafer in deionized water.

Contusion



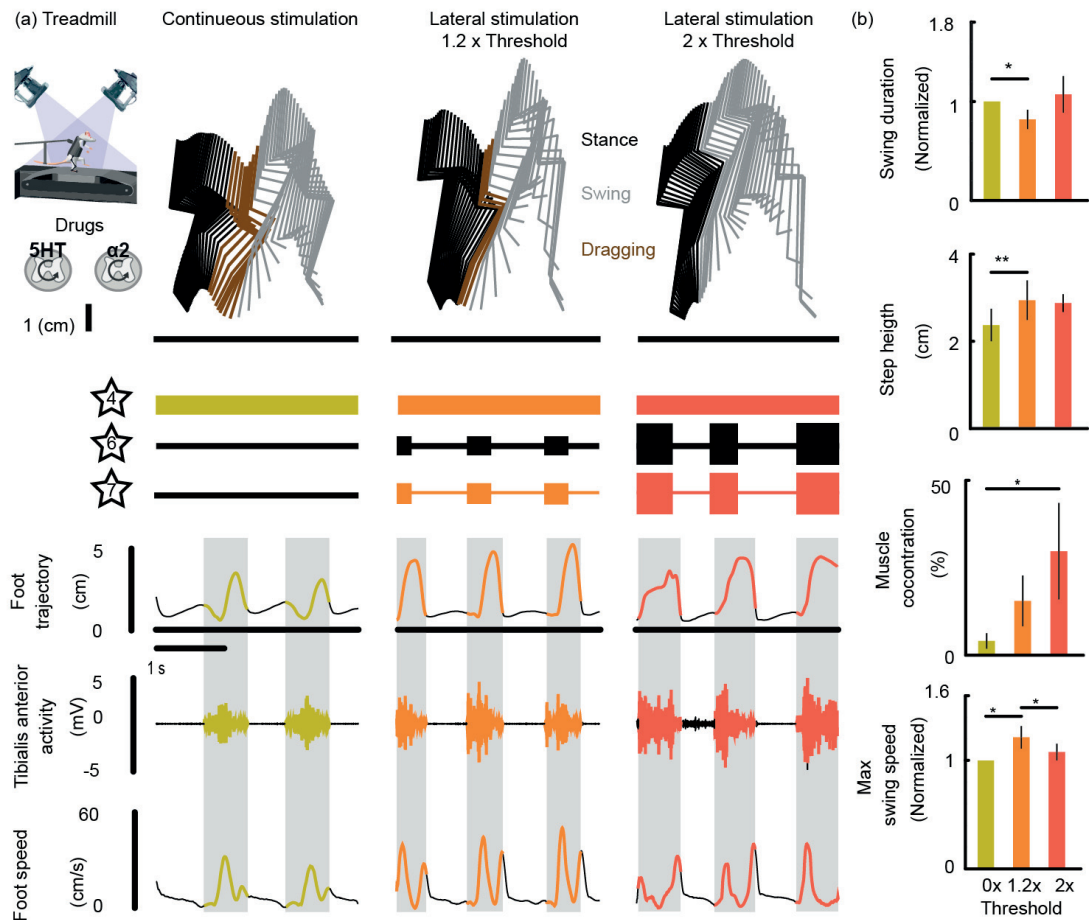
Supplementary Figure S6.2 – Quantification of spared tissue left by contusion SCI in rats. (a) Schema illustrate a contusion delivered between T8 and T9 vertebrae. (b) Scans of coronal spinal cord slides at lesion epicenter for each rat used during the study. To delimit border with the lesion, the tissues are stained to reveal GFAP. The boundary is shown with red dashed lines. The residual percentage is computed in comparison of healthy tissues above and below lesion site and reported in white for each rat.

Chapter 6. Model-driven optimization of multipolar electrical stimulation of the lumbosacral posterior roots using transversal epidural implant



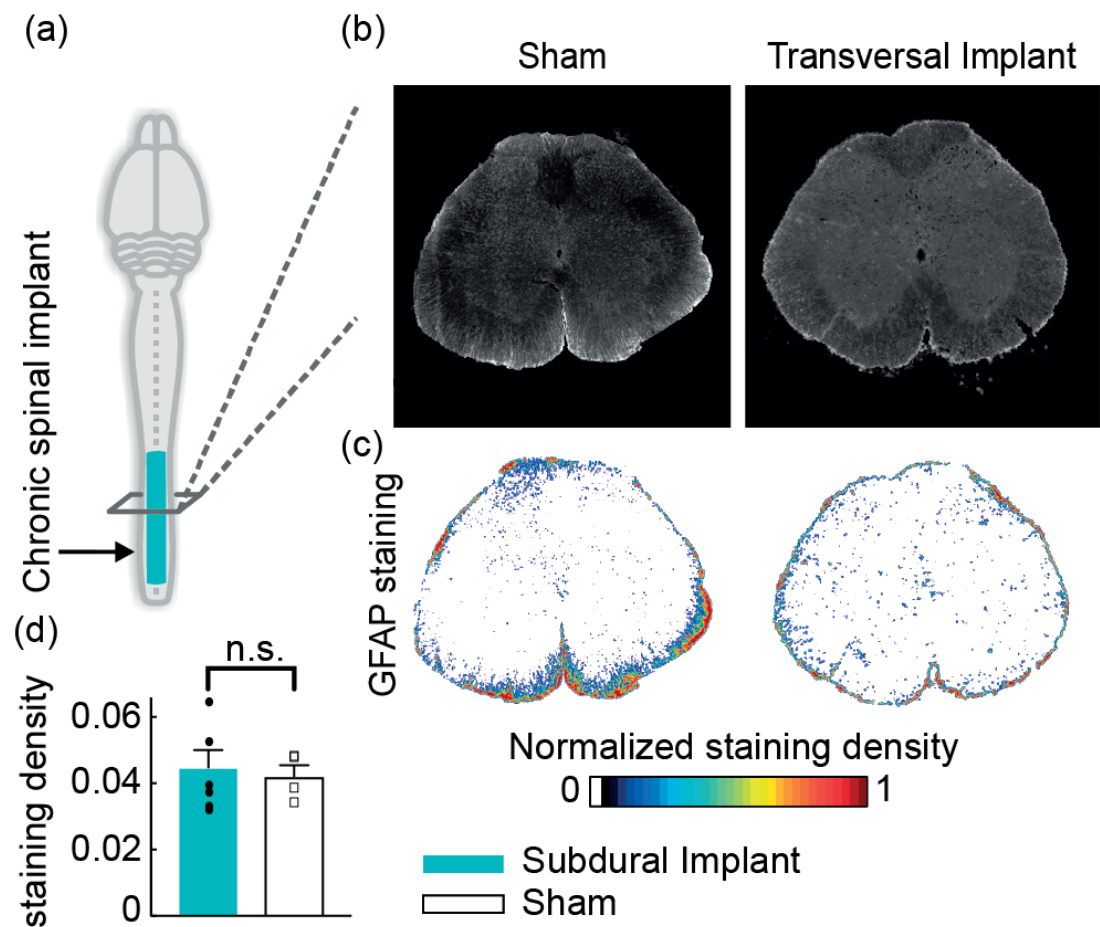
Supplementary Figure S6.3 – Real-time control platform. A software adjust stimulations to respect the temporal structure and spatial configuration required for the spinal cord. Rats were placed on a treadmill in bipedal position supported by a robotic system to compensate the missing weight bearing. A video motion tracking system send directly position of left and right foot trajectory. An angle is computed between the current foot position and a virtual center of gait cycle. This angle trigger on and off states of each electrode when a defined threshold is crossed. The stimulation pattern respect GA prediction, but enable amplitude tuning by user for fine adjustment. The asymmetric shape allow voltage balanced pulses and a dominant polarity.

6.7. Supplementary figures



Supplementary Figure S6.4 – Multipolar modulation. (a) After 6 weeks of rehabilitation, a rat with a SCI is placed on a treadmill stimulated electrochemically. (b) With a spatiotemporal pattern restricted to flexion, the amplitude of current is modulated. Below, traces of applied stimulations, foot trajectories, flexor muscle and foot speed are presented. (c) Bar plots show means and SEM of parameters that are modulated by stimulation. * $p < 0.05$, ** $p < 0.01$, paired t -test.

Chapter 6. Model-driven optimization of multipolar electrical stimulation of the lumbosacral posterior roots using transversal epidural implant



Supplementary Figure S6.5 – Long-term biocompatibility. (a) rats ($n = 6$ for transversal implant and 4 for sham) were sacrificed 8 weeks post implantation of a transversal spinal implant above S1 segment. (b) Representative scans of S1 spinal segment stained with GFAP to reveal neuro-inflammatory responses are shown for each group. (c) Digitalization and color-filtering by means of density was performed on each slide with constant threshold parameters. (d) Bar plot reporting mean and SEM values of computed GFAP density for each group. Non-parametric test does not show statistical significance.

Discussion & Outlook

Patients suffering a severe spinal cord injury such as classified ASIA-A or B do not have any volitional control over muscles below the lesion. Spontaneous recovery of locomotion with conventional rehabilitation protocols targeting locomotor system is highly unlikely. However, even if the interruption leads to complete paralysis, the majority of spinal cord lesions have spared neural tissue at the injury level. While a substantial set of fibers remains connected to the brain, those connections are not sufficient to activate lower circuits and leave them in a dormant state. EES is an embryonic and promising intervention to reactivate dormant neural network below the lesion and engage them into a rehabilitation process to restore locomotion after a SCI.

This thesis aimed to improve an empirical EES protocol into an optimized spatiotemporal neuromodulation paradigm to enhance the recovery of locomotion after a lesion of the spinal cord. Development of advance algorithm was necessary to trigger stimulation according to gait cycle and restore locomotion with spatiotemporal neuromodulation protocol in rats. NHP experiments confirm an easy translation of rodents success and open a perspective for patients with complete SCI to control their legs with brain-spinal interfaces. The critical need of spatial resolution promoted a new implant design, which allowed to play with multipolar stimulation paradigm

7.1 Spatiotemporal neuromodulation enhances locomotion

The therapeutic potential of EES demonstrated encouraging effects in animal models [31] [7], and also in paraplegic patients [68] [69]. Clinical trials to evaluate the recovery of motor control in SCI victims are imminent. However, incomplete understanding of the spinal neural networks responsible for locomotion resulted in basic stimulation protocols, mainly composed of single electrode usage and constant stimulation paradigms, thus neglecting spatial and temporal components of network activations in healthy conditions.

7.1.1 Spatiotemporal natural modulation

In the first part of this thesis, I proposed a novel strategy which derived from the natural activation patterns of motor neurons during a gait cycle. A stimulation protocol which respects the spatial and temporal conditions in order to optimally activate structures involved during locomotion. I thought that approach would help patient suffering from a SCI to recover more motor function and a better control if their spinal cord was activated as before. I extracted temporal structure of muscles involved in locomotion. As many studies suggested, global muscular activity is divisible into motor subgroups: muscle synergies [78] [87] [89]. They embed muscle co-activation during a gait cycle. A cut following synergy activities facilitate drastically the control algorithm by smartly reducing the degree of freedom. Thanks to the redundancy of multiple muscle activity, a smooth movement trajectory and control is conserved. I exploited this strategy to segment neuromodulation according to synergy spatiotemporal structures and sequences.

7.1.2 Key areas to control spinal cord

In rat, as well as in human [90], the walking pattern is divided in sequential phase that alternate between flexion and extension [38]. Involved neuronal circuits are spatially well distinct in specific areas along the spinal cord [93]. They integrate cortical and sensory informations to adjust with precision the temporal sequence of each muscle during the gait cycle [48]. Those key areas, also called hot spots, are formation centers that code for the synergy creation, which controls the leg movement[92]. In addition, the massive flux from afferent proprioceptive fibers in this area allowed local activity modulations. Indeed, the manipulation of proprioception circuit directly connected to primary motor synergy could anticipate the leg trajectory as it was done in frogs [97].

7.1.3 Selective movements

EES allows to generate movement from proprioceptive afferent fiber stimulation in many species [49] [45] including human [73]. Logically, a implant designed to activate hot spot through those fiber could control muscle synergies whose leg flexion and extension. I took advantage of the spinal cord somatotopy to tailor dedicated implant like tone specific cells and auditory afferent organization facilitated the development of cochlear implants [98]. In the same spirit, hot spots were used to reduce the electrode number needed and conserve the control of flexion and extension, which could be gradually modulated and independently controlled.

7.1.4 Superiority of spatiotemporal neuromodulation

I then characterized the effects of spatiotemporal neuromodulation on rats with complete lesion. Stimulations based on natural synergies allowed muscle recruitment closer to intact rats than continuous stimulation in middle and lateral positions. I emphasized here the importance of a temporal policy. Increasing the number of electrodes is not enough to improve walking. These lateral active sites have specific functions and must follow a strict temporal structure of their own to reinforce the gait cycle instead of destroying it.

7.1.5 Spatiotemporal neuromodulation for rehabilitation

The protocol was replicated on animals that suffered a spinal cord contusion to validate superior efficiency of spatiotemporal stimulations during rehabilitation. Where continuous stimulations were no longer efficient, spatiotemporal neuromodulation restored walking. Similar results were found between complete SCI and this clinically relevant injury model. I pointed out that this protocol significantly reduces fatigue. An activation with a discontinuous patterns must allow time for the muscles and neural circuits to rest. A subject that fatigues less leads to longer rehabilitation sessions and potentially more recovery related to this additional activity. rehabilitation sessions were run until rats did not need robotic support anymore, which underlined extensor muscle recovery. Flexor improvements were demonstrated with rat abilities to climb staircases.

7.1.6 Spatiotemporal features conserved through species

A huge gap in evolution split humans from rats, however this experiment animal model was valid since neural circuits were conserved through mammals, especially muscle synergies and proprioceptive afferent fibers. In addition, every concept used in the development of spatiotemporal stimulation in the rat is available or easily translatable to human. I proved it in the second chapter of this thesis, where NHP were involved.

Experimental framework for the NHP part is similar to the first part. Stimulation protocol is applied according to the natural activity of spinal cord. Regarding spatiotemporal map of motoneuron activations, the similarity between results in monkeys compared to finding in rats suggest a strong conservation through species and predict equivalent spatiotemporal map for human activity.

In the second part, the spinal cord spatiotemporal pattern was projected on the motor cortical activity processed in real-time. This ecological approach that link brain to spinal cord helped a smooth acceptance of stimulation pattern by neural circuit and allowed a modulation, with amplitude and frequency, of gait cycle in intact monkey. Finally, the brain-spinal interface restored gait cycles in a monkey suffering a thoracic lesion based on cortical activity.

I agree that those laboratory experimental conditions did not represent the full reality faced in clinic, such as the lesion severity, delay after injury and rehabilitation performance. Indeed, a complete bipedal locomotor rehabilitation for human may need the addition of monoaminergic drugs and robotic structure to apply a body weight support during the recovery training. Nevertheless, this novel spatiotemporal neuromodulation restored to an unprecedented level the locomotion in rodent and NHP model suffering a SCI.

7.2 Closed loop platform for temporal regulation

A severe injury on the spinal cord interrupts connexion between the brain and neuromotor circuits. EES studies permitted to know that segment below the injury are only in a dormant state and can be reactivated [7]. Lumbar segments are capable of generating locomotor activity in leg muscles and generating sufficient drive to those muscles to facilitate standing and stepping despite a complete transection of the spinal cord [56]. The concept of muscle synergy extracted from natural locomotion simplifies the control algorithm architecture. By extracting a short number of hot spots and therefore electrodes, I reduced existing combinations and the number of switches needed. Less operations to solve result in a latency reduction and a better system reaction to new events triggered.

7.2.1 Motion tracking for feedback

In the first chapter, I linked a infrared marker motion capture system with a high-speed stimulation processor. The goal of those markers is to mimic proprioceptive feedback afferents to deliver EES at the same time on spinal cord and reinforce their locomotion control power. The information embeds in cyclic foot trajectory can be correlated with muscle synergy temporal structure. In the end, I can control stepping with a unique parameter, the angle of gait cycle. Tracking becomes easier and more reliable, and triggering events that adjust stimulations more precise.

This technology requires an original movement either the backward leg motion im-

posed by a treadmill or volitional muscle contractions to elicit a small movement. Such requirements are fulfilled by normal rehabilitation protocol with incomplete patient, which will naturally recover some voluntary control. However, a patient with an anatomically complete lesion does not have this possibility and will require to pass through the gap with an artificial connection like a brain-spinal interface.

7.2.2 The Brain to control legs

In the second chapter, a link between an intra-cortical arrays to read motor cortex activity, wireless modules to bypass the gap and a pulse generator to activate the spinal cord was built. This work demonstrated that NHP could trigger detection algorithm based on brain activity to restore movement of their own legs. Information come directly from the brain. Cortical implantation are already commonly performed in tetrapelgic patients, mainly to control external computer or robotic arms [62]. This additional procedure is the cost to allow patients suffering any kind of paraplegia to recover control of his own legs.

7.2.3 Software modularity

In this thesis, I first recorded the cyclic foot trajectory with reflecting markers in a controlled environment. The algorithm was built in a modular way that allow easily any upgrade, add or remove input source and output stimulations. I demonstrated it by replacing markers tracking with brain activity in the nonhuman primate experiments. Walking is a cyclic task and the algorithm can perform with any correlated cyclic informations from reflecting markers, brain electrodes or others. In this continuity, for human applications, companies providing wireless sensors to track and follow steps in real-time already exist. The software adaptation should not be a limitation to any outcomes or medical validations. With this potential adaptation, I anticipated success that will bring patients outdoor.

This thesis focused on rehabilitation protocol for severely injured patients. However small lesion victims do not suffer heavy paralysis and could take advantage of peripheral nerve stimulations (PNS). This kind of modulation which is restricted to one articulation is very efficient for local activation. Activated muscle have to be synchronized with the gait cycle in order to improve locomotion. PNS delivered in closed-loop and in real-time could provide precise benefit to patient with small handicap.

7.3 Biocompatibility enhanced with soft spinal implant

In the field of neuroprosthetics, there are multiple applications that fail or are forgotten because the used implants were unadapted for long term stimulations or recordings. This fact often comes from the mismatch between neural tissue softness and the implant stiffness.

7.3.1 No physical constraints

In this thesis, I presented a novel soft implant, named: E-dura. Being PDMS-based, the mechanical properties of this implant are magnitudes closer to neural tissue than previous standard multi-electrode arrays. The implants' conductivity is warranted by gold line and platinum coating, both especially made to provide a stretchability.

The implants did not impose mechanical stress onto the spinal cord. In addition, bending, stretching and torsion did not significantly alter the electrical properties of the implant. Results were predicted by mechanical simulations made ex-vivo, then were further confirmed with histological analyses of the spinal cord tissue that evidenced no signs of deformation after a long term implantation.

7.3.2 No foreign body reactions

Similarly, inflammatory response resulting from a long term implantation reaction linked with their presence even implanted subdurally was not observed. The arrays did not generate foreign body responses which announced a good and longer lifetime regarding active site efficacy and scar tissue formation reduction. The absence of immune system reaction against implants avoid also many biological internal spinal cord degradation, such as scar formation and demyelination of residual neurons [159].

7.3.3 Microfluidic advantages

In addition of its property to embed conductive electric tracks, E-dura implants integrated also a microfluidic channel. Made in PDMS, the pipe follows same physical properties as the whole implant. A path was opened to directly deliver drugs on a targeted area. This intrathecal injection reduced many side effects that have been observed when systemically delivering serotonin agonists to increase the excitability of the neural networks below the injury. This capacity combined with stimulations delivered at the same time allowed precise electrochemical modulation. Neurons are sensitive to electrical and chemical stimulations, so neural implants incorporating

both aspects in one device open unprecedented possibilities.

7.3.4 Usable for spinal neuromodulation

In this thesis, I focused on spinal cord applications. The impressive synergistic effect of monoamine drugs and EES was already underlined with systemic injections [23]. Results reported that drug quantities could be drastically reduced by using intrathecal injections while primary effects such as the increased excitability continued to be effective. Monoaminergic compound injections directly on the spinal cord reduced drug side effects on rodents. Such devices scaled for human size combined with implantable micro pumps for drug delivery could be a viable solution for commercial application once a proper human drugs would be validated for clinical trial.

7.4 Multipolar strategies to fine tune stimulations

Spatiotemporal neuromodulation improved locomotion and mediated superior leg recovery after rehabilitation in rats compared to conventional monotonic stimulations. This new protocol is a candidate to replace current clinical process after its demonstration of gait restoration in NHP. However, the complete strategy could be ruined if one active site of the implant does not fulfill its role. This dependency to electrode specificity could be a brake to translational validation, unless optimized protocols refine stimulations.

7.4.1 Multipolarity to increase specificity

ESS generates movements by electrically recruiting dorsal root fibers. Main muscles involved in locomotion is located between the L2 and L6 segments of the spinal cord. Computational models showed the possibility of recruiting all roots coming from these areas by accessing only S1 segment. I confirmed these results by in-vivo experiments. Indeed, a grouping of electrodes in sacral area allowed roots activation with specificity, especially L2 roots which recruit flexor muscles.

I took advantage of the digital model and electrode proximity to seek a better specificity, thanks to a multipolar protocol. Numerical models combined with a genetic algorithm allowed to virtually test thousands of stimulation patterns and select them according to their specificity. Results have also validated these predictions of improved selectivity with multipolar stimulations, but also underline that a well-placed electrode can already be sufficiently with monopolar activity. Multipolar stimulations

offer the freedom to be optimized post implantation to answer any contingency.

7.4.2 Personalized stimulation

This protocol revolutionized electrode positioning and stimulation parameters, and preserved the ability to integrate other control protocols such as closed-loop stimulations and amplitude modulations. Application of this method on rat who received a severe spinal cord injury demonstrated that their combined effects were able to restore locomotion. Such a protocol should be applicable to humans and improve the specificity of future EES protocols. Trivial adaptations of computational models for humans should easily predict the electrode configurations needed for the next implant generation implants.

7.5 Ready for clinical trials

7.5.1 Spatiotemporal stimulations for patients

Based on works done in this thesis, a group of my laboratory runs a clinical feasibility study investigating the potential of EES in individuals with sensory and motor incomplete SCI classified as C or D according to the ASIA impairment scale in collaboration with the Centre Hospitalier Universitaire Vaudois (CHUV) in Lausanne. The protocol facilitated overground stepping and recovery of voluntary control. Their results will demonstrate precise involvement of this new stimulation protocol in the framework of a rehabilitation therapy for humans, which might be the next standard [160].

7.5.2 Soft implants in validation

E-dura implants required for Multipolar protocol are still far from clinical acceptance, since non-human primate validation is still ongoing. However, preliminary tests performed with existing MEA are promoting multipolar stimulations. Even with a non-optimized implant, they observed small enhancements in specificity. Such results are encouraging and will push the validation effort for a human transversal spinal implant.

7.5.3 Promising future

Spatiotemporal neuromodulation is at the dawn of passing clinical trials and promises encouraging results in humans. Innovative solutions supported by advanced technologies are passing through translational steps to reach clinical validation for future generation. Next decades announce a revolution in spinal cord injury field and strong hopes for patients to one day walk again.

List of Figures

3.1	Spatiotemporal dynamics of hindlimb motoneuron activation during locomotion	24
3.2	Design, fabrication and validation of spatially selective spinal implants . . .	25
3.3	Software to adjust spatiotemporal neuromodulation in real-time during locomotion	27
3.4	Spatiotemporal neuromodulation reproduces the natural pattern of motoneuron activation	29
3.5	Selective and gradual modulation of extension and flexion components . . .	31
3.6	Spatiotemporal neuromodulation improves motor control after clinically relevant SCI	33
4.1	Conceptual and technological design of the brain–spinal interface	68
4.2	Development and validation of selective spinal cord stimulation protocols .	70
4.3	Brain-controlled stimulation modulates the extension and flexion of the leg during locomotion in intact monkeys	71
4.4	The brain-spinal interface alleviates gait deficits after spinal cord injury . . .	73
5.1	Electronic dura mater, “e-dura,” tailored for the spinal cord	107
5.2	E-dura biointegration	108
5.3	Properties of e-dura electrodes	111
5.4	Recordings and stimulation with e-dura	112
6.1	Precise spinal cord anatomy.	154
6.2	Computational Model	155
6.3	A soft transversal electrode array	157
6.4	Transversal implant integration and stimulation on spinal cord.	158
6.5	Optimizing spinal selectivity.	159
6.6	In-vivo validation multipolar recruitment.	160
6.7	Long-term multipolar neuromodulation.	162

List of Supplementary Figures

S3.1	Spatial distribution of hindlimb motoneurons and 3D reconstruction of vertebrae, spinal cord and dorsal roots in Lewis rats	51
S3.2	Spatiotemporal maps of motoneuron activation	52
S3.3	Computer simulations to identify optimal electrode locations to target extensor versus flexor hotspots	53
S3.4	Design, fabrication and surgical procedures of spatially selective spinal implants	55
S3.5	Long-term functionality and bio-integration of epidural spinal implants . .	56
S3.6	Experiments to identify optimal temporal structure	57
S3.7	Changes in hindlimb muscle activity across conditions of neuromodulation	58
S3.8	Quantification of gait patterns in rats with complete SCI	59
S3.9	Modulation of motor responses during increase in stimulation amplitude . .	60
S3.10	Quantification of spared tissue in rats with contusion SCI.	61
S3.11	Quantification of locomotor performance during quadrupedal locomotion.	62
S3.12	Computed kinematic, kinetic, and muscle activity parameters	63
S4.1	Design and fabrication of the spatially selective spinal implant	86
S4.2	Protocols and technology of the spinal cord stimulation system	87
S4.3	Anatomical, computational, and functional experiments allowed the identification of stimulation protocols to access flexion and extension hotspots . .	89
S4.4	Procedure to calibrate the decoders for real-time detection of motor states .	90
S4.5	The real-time decoder accurately detected the motor states and triggered stimulation protocols during locomotion and when initiating and terminating it in intact monkeys	92
S4.6	Modulation of leg locomotor movements during brain-controlled stimulation in intact monkeys	93
S4.7	Quantification and reconstruction of the spinal cord lesions and quantification of gait deficits and spontaneous recovery after the spinal cord lesion . .	95
S4.8	Restoration of leg locomotor movements during overground locomotion after the spinal cord lesion	96
S4.9	Quantification of gait improvements and decoding accuracy during brain-controlled stimulation after the spinal cord lesion	98

List of Supplementary Figures

S4.10 The temporal structure and features of stimulation determine the quantity and quality of steps	99
S4.11 Experimental procedures conducted on the animals.	100
S4.12 Behavioral experiments conducted with each animal.	100
S4.13 Computed kinematic parameters.	101
S5.1 Tensile response of natural dura mater, silicone and e-dura implant.	132
S5.2 Soft neurotechnology for e-dura implants.	133
S5.3 Mechanical characterization of the platinum-silicone composite.	134
S5.4 E-dura chemotrode: compliant fluidic microchannel.	134
S5.5 Orthoses and surgical procedures for chronic e-dura implantation.	135
S5.6 Kinematic analysis of gait patterns during basic overground locomotion. . .	136
S5.7 Damage of spinal tissues after chronic implantation of stiff, but not soft, implants.	137
S5.8 Significant neuro-inflammatory responses after chronic implantation of stiff, but not soft, implants.	138
S5.9 Model of spinal cord and experimental quantification of vertebral column curvatures in freely behaving rats.	139
S5.10 Mechanical effects of implants on the model of spinal cord.	140
S5.11 Effect of tensile deformations on the implants and on the model of spinal cord.	141
S5.12 Determination of charge injection capacity of electrodes with platinum-silicone coating.	142
S5.13 Impedance spectroscopy of the soft electrodes under cyclic stretching to 20% strain.	143
S5.14 In-situ scanning electron micrographs of platinum-silicone coatings.	144
S5.15 Motor cortex electrocorticograms reflect motor states in freely moving rats. .	145
S5.16 Recordings of electrospinograms following peripheral nerve and brain stimulation.	146
S5.17 Drug delivery through the chemotrode annihilates side effects.	147
S5.18 The electrochemical neuroprosthesis e-dura mediates specific adjustments of locomotion.	149
S5.19 Computed kinematic, ground reaction force, and muscle activity variables. .	150
S6.1 Transversal spinal electrode array microfabrication.	174
S6.2 Quantification of spared tissue left by contusion SCI in rats.	175
S6.3 Real-time control platform.	176
S6.4 Multipolar modulation.	177
S6.5 Long-term biocompatibility.	178

Publication and contributions

- **Configuration of electrical spinal cord stimulation through real-time processing of gait kinematics.** Capogrosso M*, Wagner FB*, Gandar J, Moraud EM, Wenger N, Milekovic T, Shkorbatova P, Pavlova N, Musienko P, Bezard E, Bloch J, Courtine G. Nature Protocols (2018). *These authors contributed equally to this work
- **Advantages of soft subdural implants for the delivery of electrochemical neuromodulation therapies to the spinal cord.** Capogrosso M*, Gandar J*, Greiner N, Moraud EM, Wenger N, Shkorbatova P, Musienko P, Minev I, Lacour S, Courtine G., Journal of Neural Engineering (2018). *These authors contributed equally to this work
- **Long-term usability and bio-integration of polyimide-based intra-neural stimulating electrodes.** Wurth S, Capogrosso M, Raspopovic S, Gandar J, Federici G, Kinany N, Cutrone A, Piersigilli A, Pavlova N, Guiet R, Taverni G, Rigosa J, Shkorbatova P, Navarro X, Barraud Q, Courtine G, Micera S. Biomaterials (2017).
- **A brain-spine interface alleviating gait deficits after spinal cord injury in primates.** Capogrosso M*, Milekovic T*, Borton D*, Wagner F, Moraud EM, Mignardot JB, Buse N, Gandar J, Barraud Q, Xing D, Rey E, Duis S, Jianzhong Y, Ko WK, Li Q, Detemple P, Denison T, Micera S, Bezard E, Bloch J, Courtine G. Nature (2016). *These authors contributed equally to this work
- **Spatiotemporal neuromodulation therapies engaging muscle synergies improve motor control after spinal cord injury.** Wenger N*, Moraud EM*, Gandar J*, Musienko P, Capogrosso M, Baud L, Le Goff CG, Barraud Q, Pavlova N, Dominici N, Minev IR, Asboth L, Hirsch A, Duis S, Kreider J, Mortera A, Haverbeck O, Kraus S, Schmitz F, DiGiovanna J, van den Brand R, Bloch J, Detemple P, Lacour SP, Bézard E, Micera S, Courtine G. Nat Med (2016). *These authors contributed equally to this work
- **Biomaterials. Electronic dura mater for long-term multimodal neural interfaces.** Minev IR*, Musienko P*, Hirsch A, Barraud Q, Wenger N, Moraud EM, Gandar J, Capogrosso M, Milekovic T, Asboth L, Torres RF, Vachicouras N, Liu Q, Pavlova N, Duis S, Larmagnac A, Vörös J, Micera S, Suo Z, Courtine G, Lacour SP. Science (2015). *These authors contributed equally to this work

List of Abbreviation

ASIA	American Spinal Injury Association
BCI	Brain-Computer Interface
BF	Biceps Femoris
BSI	Brain-Spine Interface
BWS	Body Weight Support
CTscan	Computed Tomography Scan
EES	Epidural Electrical Stimulation
EDL	Extensor Digitorum Longus
EMG	Electromyography
FEM	Finite-element Method
FHL	Flexor Hallucis Longus
GA	Genetic Algorithm
GFAP	Glial Fibrillary Acidic Protein
GLu	Gluteus Medius
GM or MG	Gastrocnemius Medialis
IL or IPS	Iliopsoas
LG	Gastrocnemius Lateralis
MEA	Multi-Electrode Array
MEP	Motor Evoked Potential
MTP	Metatarsophalange
NHP	Non-Human Primate
PC	Princial Component
PNS	Peripheral Nerve Stimulation
RF	Rectus Femoris
SCI	Spinal Cord Injury
ST	Semitendinosus
TA	Tibilis Anterior
SEM	Standard Error Mean
VL	Vastus Lateralis
5HT	Serotonin

Bibliography

- [1] C. B. Jerome Bickenbach, "International perspectives on spinal cord injury," annual report, World Health Organization, WHO Press, World Health Organization, 20 Avenue Appia, 1211 Geneva 27, Switzerland, 2013.
- [2] "National spinal cord injury statistical center, facts and figures at a glance.," tech. rep., Birmingham, AL, University of Alabama at Birmingham, 2018.
- [3] V. Dietz and G. Colombo, "Recovery from spinal cord injury—underlying mechanisms and efficacy of rehabilitation," *Acta Neurochir Suppl*, vol. 89, pp. 95–100, 2004.
- [4] J. W. Fawcett, A. Curt, J. D. Steeves, W. P. Coleman, M. H. Tuszynski, D. Lamertse, P. F. Bartlett, A. R. Blight, V. Dietz, J. Ditunno, B. H. Dobkin, L. A. Havton, P. H. Ellaway, M. G. Fehlings, A. Privat, R. Grossman, J. D. Guest, N. Kleitman, M. Nakamura, M. Gaviria, and D. Short, "Guidelines for the conduct of clinical trials for spinal cord injury as developed by the iccp panel: spontaneous recovery after spinal cord injury and statistical power needed for therapeutic clinical trials," *Spinal Cord*, vol. 45, pp. 190–205, Mar 2007.
- [5] J. F. Ditunno, Jr, M. E. Cohen, W. W. Hauck, A. B. Jackson, and M. L. Sipski, "Recovery of upper-extremity strength in complete and incomplete tetraplegia: a multicenter study," *Arch Phys Med Rehabil*, vol. 81, pp. 389–93, Apr 2000.
- [6] C. S. Sherrington, "Flexion-reflex of the limb, crossed extension-reflex, and reflex stepping and standing," *The Journal of physiology*, vol. 40, no. 1-2, pp. 28–121, 1910.
- [7] G. Courtine, Y. Gerasimenko, R. van den Brand, A. Yew, P. Musienko, H. Zhong, B. Song, Y. Ao, R. M. Ichiyama, I. Lavrov, R. R. Roy, M. V. Sofroniew, and V. R. Edgerton, "Transformation of nonfunctional spinal circuits into functional states after the loss of brain input," *Nat Neurosci*, vol. 12, pp. 1333–42, Oct 2009.
- [8] E. R. Kandel, *Principles of Neural Science, Fifth Edition*. Cenveo, mcgraw-hill companies ed., 2013.
- [9] H. Barbeau and S. Rossignol, "Recovery of locomotion after chronic spinalization in the adult cat," *Brain Res*, vol. 412, pp. 84–95, May 1987.

Bibliography

- [10] R. G. Lovely, R. J. Gregor, R. R. Roy, and V. R. Edgerton, "Effects of training on the recovery of full-weight-bearing stepping in the adult spinal cat," *Exp Neurol*, vol. 92, pp. 421–35, May 1986.
- [11] C. A. Pratt, J. Fung, and J. M. Macpherson, "Stance control in the chronic spinal cat," *J Neurophysiol*, vol. 71, pp. 1981–5, May 1994.
- [12] A. Wernig, S. Müller, A. Nanassy, and E. Cagol, "Laufband therapy based on 'rules of spinal locomotion' is effective in spinal cord injured persons," *Eur J Neurosci*, vol. 7, pp. 823–9, Apr 1995.
- [13] V. Dietz and K. Fouad, "Restoration of sensorimotor functions after spinal cord injury," *Brain*, vol. 137, pp. 654–67, Mar 2014.
- [14] A. L. Behrman and S. J. Harkema, "Physical rehabilitation as an agent for recovery after spinal cord injury," *Phys Med Rehabil Clin N Am*, vol. 18, pp. 183–202, v, May 2007.
- [15] B. A. Kakulas, "A review of the neuropathology of human spinal cord injury with emphasis on special features," *J Spinal Cord Med*, vol. 22, no. 2, pp. 119–24, 1999.
- [16] A. Mailis-Gagnon, A. D. Furlan, J. A. Sandoval, and R. Taylor, "Spinal cord stimulation for chronic pain," *Cochrane Database Syst Rev*, vol. 3, no. 3, 2004.
- [17] C. C. McIntyre and T. J. Foutz, "Computational modeling of deep brain stimulation," *Handb Clin Neurol*, vol. 116, pp. 55–61, 2013.
- [18] P. A. Tass, L. Qin, C. Hauptmann, S. Dovero, E. Bezard, T. Boraud, and W. G. Meissner, "Coordinated reset has sustained aftereffects in parkinsonian monkeys," *Ann Neurol*, vol. 72, pp. 816–20, Nov 2012.
- [19] D. Borton, S. Micera, J. d. R. Millán, and G. Courtine, "Personalized neuroprosthetics," *Sci Transl Med*, vol. 5, p. 210rv2, Nov 2013.
- [20] S. J. Harkema, "Plasticity of interneuronal networks of the functionally isolated human spinal cord," *Brain Res Rev*, vol. 57, pp. 255–64, Jan 2008.
- [21] S. Harkema, Y. Gerasimenko, J. Hodes, J. Burdick, C. Angeli, Y. Chen, C. Ferreira, A. Willhite, E. Rejc, R. G. Grossman, and V. R. Edgerton, "Effect of epidural stimulation of the lumbosacral spinal cord on voluntary movement, standing, and assisted stepping after motor complete paraplegia: a case study," *Lancet*, vol. 377, pp. 1938–47, Jun 2011.

- [22] J. A. Beres-Jones and S. J. Harkema, "The human spinal cord interprets velocity-dependent afferent input during stepping," *Brain*, vol. 127, pp. 2232–46, Oct 2004.
- [23] P. Musienko, J. Heutschi, L. Friedli, R. van den Brand, and G. Courtine, "Multi-system neurorehabilitative strategies to restore motor functions following severe spinal cord injury," *Exp Neurol*, vol. 235, pp. 100–9, May 2012.
- [24] M. R. Dimitrijevic, Y. Gerasimenko, and M. M. Pinter, "Evidence for a spinal central pattern generator in humans," *Ann N Y Acad Sci*, vol. 860, pp. 360–76, Nov 1998.
- [25] P. E. Musienko, P. V. Zelenin, G. N. Orlovsky, and T. G. Deliagina, "Facilitation of postural limb reflexes with epidural stimulation in spinal rabbits," *J Neurophysiol*, vol. 103, pp. 1080–92, Feb 2010.
- [26] Y. Gerasimenko, R. R. Roy, and V. R. Edgerton, "Epidural stimulation: comparison of the spinal circuits that generate and control locomotion in rats, cats and humans," *Exp Neurol*, vol. 209, pp. 417–25, Feb 2008.
- [27] P. Musienko, R. van den Brand, O. Maerzendorfer, A. Larmagnac, and G. Courtine, "Combinatory electrical and pharmacological neuroprosthetic interfaces to regain motor function after spinal cord injury," *IEEE Trans Biomed Eng*, vol. 56, pp. 2707–11, Nov 2009.
- [28] B. Jilge, K. Minassian, F. Rattay, M. M. Pinter, F. Gerstenbrand, H. Binder, and M. R. Dimitrijevic, "Initiating extension of the lower limbs in subjects with complete spinal cord injury by epidural lumbar cord stimulation," *Exp Brain Res*, vol. 154, pp. 308–26, Feb 2004.
- [29] K. Minassian, I. Persy, F. Rattay, M. M. Pinter, H. Kern, and M. R. Dimitrijevic, "Human lumbar cord circuitries can be activated by extrinsic tonic input to generate locomotor-like activity," *Hum Mov Sci*, vol. 26, pp. 275–95, Apr 2007.
- [30] V. R. Edgerton and S. Harkema, "Epidural stimulation of the spinal cord in spinal cord injury: current status and future challenges," *Expert Rev Neurother*, vol. 11, pp. 1351–3, Oct 2011.
- [31] R. van den Brand, J. Heutschi, Q. Barraud, J. DiGiovanna, K. Bartholdi, M. Hurlimann, L. Friedli, I. Vollenweider, E. M. Moraud, S. Duis, N. Dominici, S. Micera, P. Musienko, and G. Courtine, "Restoring voluntary control of locomotion after paralyzing spinal cord injury," *Science*, vol. 336, pp. 1182–5, Jun 2012.

Bibliography

- [32] V. R. Edgerton, G. Courtine, Y. P. Gerasimenko, I. Lavrov, R. M. Ichiyama, A. J. Fong, L. L. Cai, C. K. Otsoshi, N. J. Tillakaratne, J. W. Burdick, *et al.*, “Training locomotor networks,” *Brain research reviews*, vol. 57, no. 1, pp. 241–254, 2008.
- [33] K. Minassian, B. Jilge, F. Rattay, M. M. Pinter, H. Binder, F. Gerstenbrand, and M. R. Dimitrijevic, “Stepping-like movements in humans with complete spinal cord injury induced by epidural stimulation of the lumbar cord: electromyographic study of compound muscle action potentials,” *Spinal Cord*, vol. 42, pp. 401–16, Jul 2004.
- [34] V. F. Lyalka, L.-J. Hsu, A. Karayannidou, P. V. Zelenin, G. N. Orlovsky, and T. G. Deliagina, “Facilitation of postural limb reflexes in spinal rabbits by serotonergic agonist administration, epidural electrical stimulation, and postural training,” *J Neurophysiol*, vol. 106, pp. 1341–54, Sep 2011.
- [35] D. T. Brocker, B. D. Swan, D. A. Turner, R. E. Gross, S. B. Tatter, M. M. Koop, H. Bronte-Stewart, and W. M. Grill, “Improved efficacy of temporally non-regular deep brain stimulation in parkinson’s disease,” *Exp Neurol*, vol. 239, pp. 60–7, Jan 2013.
- [36] B. Rosin, M. Slovik, R. Mitelman, M. Rivlin-Etzion, S. N. Haber, Z. Israel, E. Vaa-dia, and H. Bergman, “Closed-loop deep brain stimulation is superior in ame-liorating parkinsonism,” *Neuron*, vol. 72, pp. 370–84, Oct 2011.
- [37] J. T. Paz, T. J. Davidson, E. S. Frechette, B. Delord, I. Parada, K. Peng, K. Deis-seroth, and J. R. Huguenard, “Closed-loop optogenetic control of thalamus as a tool for interrupting seizures after cortical injury,” *Nat Neurosci*, vol. 16, pp. 64–70, Jan 2013.
- [38] S. Yakovenko, V. Mushahwar, V. VanderHorst, G. Holstege, and A. Prochazka, “Spatiotemporal activation of lumbosacral motoneurons in the locomotor step cycle,” *J Neurophysiol*, vol. 87, pp. 1542–53, Mar 2002.
- [39] G. Cappellini, Y. P. Ivanenko, N. Dominici, R. E. Poppele, and F. Lacquaniti, “Migration of motor pool activity in the spinal cord reflects body mechanics in human locomotion,” *Journal of neurophysiology*, vol. 104, no. 6, pp. 3064–3073, 2010.
- [40] Y. P. Ivanenko, R. Grasso, M. Zago, M. Molinari, G. Scivoletto, V. Castellano, V. Macellari, and F. Lacquaniti, “Temporal components of the motor patterns expressed by the human spinal cord reflect foot kinematics,” *J Neurophysiol*, vol. 90, pp. 3555–65, Nov 2003.

-
- [41] N. Dominici, U. Keller, H. Vallery, L. Friedli, R. van den Brand, M. L. Starkey, P. Musienko, R. Riener, and G. Courtine, "Versatile robotic interface to evaluate, enable and train locomotion and balance after neuromotor disorders," *Nat Med*, vol. 18, pp. 1142–7, Jul 2012.
- [42] S. Grillner, "Biological pattern generation: the cellular and computational logic of networks in motion," *Neuron*, vol. 52, pp. 751–66, Dec 2006.
- [43] F. Rattay, K. Minassian, and M. Dimitrijevic, "Epidural electrical stimulation of posterior structures of the human lumbosacral cord: 2. quantitative analysis by computer modeling," *Spinal cord*, vol. 38, no. 8, pp. 473–489, 2000.
- [44] J. Ladenbauer, K. Minassian, U. S. Hofstoetter, M. R. Dimitrijevic, and F. Rattay, "Stimulation of the human lumbar spinal cord with implanted and surface electrodes: a computer simulation study," *IEEE Trans Neural Syst Rehabil Eng*, vol. 18, pp. 637–45, Dec 2010.
- [45] I. Lavrov, C. J. Dy, A. J. Fong, Y. Gerasimenko, G. Courtine, H. Zhong, R. R. Roy, and V. R. Edgerton, "Epidural stimulation induced modulation of spinal locomotor networks in adult spinal rats," *J Neurosci*, vol. 28, pp. 6022–9, Jun 2008.
- [46] M. Capogrosso, N. Wenger, S. Raspopovic, P. Musienko, J. Beauparlant, L. Bassi Luciani, G. Courtine, and S. Micera, "A computational model for epidural electrical stimulation of spinal sensorimotor circuits," *J Neurosci*, vol. 33, pp. 19326–40, Dec 2013.
- [47] P. Gad, J. Choe, M. S. Nandra, H. Zhong, R. R. Roy, Y.-C. Tai, and V. R. Edgerton, "Development of a multi-electrode array for spinal cord epidural stimulation to facilitate stepping and standing after a complete spinal cord injury in adult rats," *J Neuroeng Rehabil*, vol. 10, p. 2, 2013.
- [48] S. Arber, "Motor circuits in action: specification, connectivity, and function," *Neuron*, vol. 74, no. 6, pp. 975–989, 2012.
- [49] Y. P. Gerasimenko, I. A. Lavrov, G. Courtine, R. M. Ichiyama, C. J. Dy, H. Zhong, R. R. Roy, and V. R. Edgerton, "Spinal cord reflexes induced by epidural spinal cord stimulation in normal awake rats," *Journal of neuroscience methods*, vol. 157, no. 2, pp. 253–263, 2006.
- [50] P. Moshayedi, G. Ng, J. C. F. Kwok, G. S. H. Yeo, C. E. Bryant, J. W. Fawcett, K. Franze, and J. Guck, "The relationship between glial cell mechanosensitivity and foreign body reactions in the central nervous system," *Biomaterials*, vol. 35, pp. 3919–25, Apr 2014.

Bibliography

- [51] K. A. Potter, M. Jorfi, K. T. Householder, E. J. Foster, C. Weder, and J. R. Capadona, "Curcumin-releasing mechanically adaptive intracortical implants improve the proximal neuronal density and blood-brain barrier stability," *Acta Biomater*, vol. 10, pp. 2209–22, May 2014.
- [52] T. Stieglitz and J. U. Meyer, "Implantable microsystems. polyimide-based neuro-prostheses for interfacing nerves," *Med Device Technol*, vol. 10, no. 6, pp. 28–30, 1999.
- [53]
- [54] S. P. Lacour, D. Chan, S. Wagner, T. Li, and Z. Suo, "Mechanisms of reversible stretchability of thin metal films on elastomeric substrates," *Applied Physics Letters*, vol. 88, no. 20, p. 204103, 2006.
- [55] J. C. Barrese, N. Rao, K. Paroo, C. Triebwasser, C. Vargas-Irwin, L. Franquemont, and J. P. Donoghue, "Failure mode analysis of silicon-based intracortical micro-electrode arrays in non-human primates," *J Neural Eng*, vol. 10, p. 066014, Dec 2013.
- [56] N. Wenger, E. M. Moraud, S. Raspopovic, M. Bonizzato, J. DiGiovanna, P. Musienko, M. Morari, S. Micera, and G. Courtine, "Closed-loop neuromodulation of spinal sensorimotor circuits controls refined locomotion after complete spinal cord injury," *Science translational medicine*, vol. 6, no. 255, pp. 255ra133–255ra133, 2014.
- [57] G. Courtine, M. B. Bunge, J. W. Fawcett, R. G. Grossman, J. H. Kaas, R. Lemon, I. Maier, J. Martin, R. J. Nudo, A. Ramon-Cueto, E. M. Rouiller, L. Schnell, T. Wanner, M. E. Schwab, and V. R. Edgerton, "Can experiments in nonhuman primates expedite the translation of treatments for spinal cord injury in humans?," *Nat Med*, vol. 13, pp. 561–6, May 2007.
- [58] B. K. Kwon, J. Hillyer, and W. Tetzlaff, "Translational research in spinal cord injury: a survey of opinion from the sci community," *J Neurotrauma*, vol. 27, pp. 21–33, Jan 2010.
- [59] L. Friedli, E. S. Rosenzweig, Q. Barraud, M. Schubert, N. Dominici, L. Awai, J. L. Nielson, P. Musienko, Y. Nout-Lomas, H. Zhong, S. Zdunowski, R. R. Roy, S. C. Strand, R. van den Brand, L. A. Havton, M. S. Beattie, J. C. Bresnahan, E. Bézard, J. Bloch, V. R. Edgerton, A. R. Ferguson, A. Curt, M. H. Tuszynski, and G. Courtine, "Pronounced species divergence in corticospinal tract reorganization and functional recovery after lateralized spinal cord injury favors primates," *Sci Transl Med*, vol. 7, p. 302ra134, Aug 2015.

- [60] R. N. Lemon, "Descending pathways in motor control," *Annu Rev Neurosci*, vol. 31, pp. 195–218, 2008.
- [61] J. L. Collinger, B. Wodlinger, J. E. Downey, W. Wang, E. C. Tyler-Kabara, D. J. Weber, A. J. C. McMorland, M. Velliste, M. L. Boninger, and A. B. Schwartz, "High-performance neuroprosthetic control by an individual with tetraplegia," *Lancet*, vol. 381, pp. 557–64, Feb 2013.
- [62] L. R. Hochberg, D. Bacher, B. Jarosiewicz, N. Y. Masse, J. D. Simeral, J. Vogel, S. Haddadin, J. Liu, S. S. Cash, P. van der Smagt, and J. P. Donoghue, "Reach and grasp by people with tetraplegia using a neurally controlled robotic arm," *Nature*, vol. 485, pp. 372–5, May 2012.
- [63] M. M. Shanechi, R. C. Hu, and Z. M. Williams, "A cortical-spinal prosthesis for targeted limb movement in paralysed primate avatars," *Nat Commun*, vol. 5, p. 3237, 2014.
- [64] M. Yin, D. A. Borton, J. Komar, N. Agha, Y. Lu, H. Li, J. Laurens, Y. Lang, Q. Li, C. Bull, L. Larson, D. Rosler, E. Bezard, G. Courtine, and A. V. Nurmikko, "Wireless neurosensor for full-spectrum electrophysiology recordings during free behavior," *Neuron*, vol. 84, pp. 1170–82, Dec 2014.
- [65] A. M. Lozano and N. Lipsman, "Probing and regulating dysfunctional circuits using deep brain stimulation," *Neuron*, vol. 77, no. 3, pp. 406–424, 2013.
- [66] D. Barthélemy, H. Leblond, and S. Rossignol, "Characteristics and mechanisms of locomotion induced by intraspinal microstimulation and dorsal root stimulation in spinal cats," *Journal of neurophysiology*, vol. 97, no. 3, pp. 1986–2000, 2007.
- [67] B. Holinski, D. Everaert, V. Mushahwar, and R. Stein, "Real-time control of walking using recordings from dorsal root ganglia," *Journal of neural engineering*, vol. 10, no. 5, p. 056008, 2013.
- [68] M. R. Carhart, J. He, R. Herman, S. D'luzansky, and W. T. Willis, "Epidural spinal-cord stimulation facilitates recovery of functional walking following incomplete spinal-cord injury," *IEEE Transactions on neural systems and rehabilitation engineering*, vol. 12, no. 1, pp. 32–42, 2004.
- [69] C. A. Angeli, V. R. Edgerton, Y. P. Gerasimenko, and S. J. Harkema, "Altering spinal cord excitability enables voluntary movements after chronic complete paralysis in humans," *Brain*, vol. 137, no. 5, pp. 1394–1409, 2014.

Bibliography

- [70] Y. P. Gerasimenko, D. C. Lu, M. Modaber, S. Zdunowski, P. Gad, D. G. Sayenko, E. Morikawa, P. Haakana, A. R. Ferguson, R. R. Roy, *et al.*, “Noninvasive reactivation of motor descending control after paralysis,” *Journal of neurotrauma*, vol. 32, no. 24, pp. 1968–1980, 2015.
- [71] R. Herman, J. He, S. D’luzansky, W. Willis, and S. Dilli, “Spinal cord stimulation facilitates functional walking in a chronic, incomplete spinal cord injured,” *Spinal cord*, vol. 40, no. 2, pp. 65–68, 2002.
- [72] U. S. Hofstoetter, S. M. Danner, B. Freundl, H. Binder, W. Mayr, F. Rattay, and K. Minassian, “Periodic modulation of repetitively elicited monosynaptic reflexes of the human lumbosacral spinal cord,” *Journal of neurophysiology*, vol. 114, no. 1, pp. 400–410, 2015.
- [73] D. G. Sayenko, C. Angeli, S. J. Harkema, V. R. Edgerton, and Y. P. Gerasimenko, “Neuromodulation of evoked muscle potentials induced by epidural spinal-cord stimulation in paralyzed individuals,” *Journal of neurophysiology*, vol. 111, no. 5, pp. 1088–1099, 2013.
- [74] S. M. Danner, U. S. Hofstoetter, B. Freundl, H. Binder, W. Mayr, F. Rattay, and K. Minassian, “Human spinal locomotor control is based on flexibly organized burst generators,” *Brain*, vol. 138, no. 3, pp. 577–588, 2015.
- [75] E. Rejc, C. Angeli, and S. Harkema, “Effects of lumbosacral spinal cord epidural stimulation for standing after chronic complete paralysis in humans,” *PloS one*, vol. 10, no. 7, p. e0133998, 2015.
- [76] S. Yakovenko, V. Mushahwar, V. VanderHorst, G. Holstege, and A. Prochazka, “Spatiotemporal activation of lumbosacral motoneurons in the locomotor step cycle,” *Journal of neurophysiology*, vol. 87, no. 3, pp. 1542–1553, 2002.
- [77] Y. P. Ivanenko, R. Grasso, M. Zago, M. Molinari, G. Scivoletto, V. Castellano, V. Macellari, and F. Lacquaniti, “Temporal components of the motor patterns expressed by the human spinal cord reflect foot kinematics,” *Journal of neurophysiology*, vol. 90, no. 5, pp. 3555–3565, 2003.
- [78] N. Dominici, Y. P. Ivanenko, G. Cappellini, A. d’Avella, V. Mondì, M. Cicchese, A. Fabiano, T. Silei, A. Di Paolo, C. Giannini, *et al.*, “Locomotor primitives in newborn babies and their development,” *Science*, vol. 334, no. 6058, pp. 997–999, 2011.
- [79] O. Kiehn, “Locomotor circuits in the mammalian spinal cord,” *Annu. Rev. Neurosci.*, vol. 29, pp. 279–306, 2006.

-
- [80] M. Berniker, A. Jarc, E. Bizzi, and M. C. Tresch, "Simplified and effective motor control based on muscle synergies to exploit musculoskeletal dynamics," *Proceedings of the National Academy of Sciences*, vol. 106, no. 18, pp. 7601–7606, 2009.
- [81] D. D. Lee and H. S. Seung, "Learning the parts of objects by non-negative matrix factorization," *Nature*, vol. 401, no. 6755, pp. 788–791, 1999.
- [82] R. A. Gaunt, A. Prochazka, V. K. Mushahwar, L. Guevremont, and P. H. Ellaway, "Intraspinal microstimulation excites multisegmental sensory afferents at lower stimulus levels than local α -motoneuron responses," *Journal of neurophysiology*, vol. 96, no. 6, pp. 2995–3005, 2006.
- [83] R. M. Ichiyama, G. Courtine, Y. P. Gerasimenko, G. J. Yang, R. van den Brand, I. A. Lavrov, H. Zhong, R. R. Roy, and V. R. Edgerton, "Step training reinforces specific spinal locomotor circuitry in adult spinal rats," *Journal of Neuroscience*, vol. 28, no. 29, pp. 7370–7375, 2008.
- [84] P. Gad, J. Woodbridge, I. Lavrov, H. Zhong, R. R. Roy, M. Sarrafzadeh, and V. R. Edgerton, "Forelimb emg-based trigger to control an electronic spinal bridge to enable hindlimb stepping after a complete spinal cord lesion in rats," *Journal of neuroengineering and rehabilitation*, vol. 9, no. 1, p. 38, 2012.
- [85] R. I. Pettigrew, W. J. Heetderks, C. A. Kelley, G. C. Peng, S. H. Krosnick, L. B. Jakeman, K. D. Egan, and M. Marge, "Epidural spinal stimulation to improve bladder, bowel, and sexual function in individuals with spinal cord injuries: A framework for clinical research," *IEEE Transactions on Biomedical Engineering*, vol. 64, no. 2, pp. 253–262, 2017.
- [86] E. Bizzi, M. C. Tresch, P. Saltiel, and A. d'Avella, "New perspectives on spinal motor systems," *Nature Reviews Neuroscience*, vol. 1, no. 2, pp. 101–108, 2000.
- [87] N. Bernstein, "The co-ordination and regulation of movements. pergamonpress ltd., headington hill hall," 1967.
- [88] S. F. Giszter, "Motor primitives—new data and future questions," *Curr Opin Neurobiol*, vol. 33, pp. 156–65, Aug 2015.
- [89] S. F. Giszter, "Motor primitives—new data and future questions," *Current opinion in neurobiology*, vol. 33, pp. 156–165, 2015.
- [90] V. La Scaleia, Y. P. Ivanenko, K. E. Zelik, and F. Lacquaniti, "Spinal motor outputs during step-to-step transitions of diverse human gaits," *Frontiers in human neuroscience*, vol. 8, 2014.

Bibliography

- [91] M. Hägglund, K. J. Dougherty, L. Borgius, S. Itohara, T. Iwasato, and O. Kiehn, "Optogenetic dissection reveals multiple rhythmogenic modules underlying locomotion," *Proceedings of the National Academy of Sciences*, vol. 110, no. 28, pp. 11589–11594, 2013.
- [92] A. J. Levine, C. A. Hinckley, K. L. Hilde, S. P. Driscoll, T. H. Poon, J. M. Montgomery, and S. L. Pfaff, "Identification of a cellular node for motor control pathways," *Nature neuroscience*, vol. 17, no. 4, pp. 586–593, 2014.
- [93] M. Tripodi, A. E. Stepien, and S. Arber, "Motor antagonism exposed by spatial segregation and timing of neurogenesis," *Nature*, vol. 479, no. 7371, pp. 61–66, 2011.
- [94] S. Grillner and T. M. Jessell, "Measured motion: searching for simplicity in spinal locomotor networks," *Current opinion in neurobiology*, vol. 19, no. 6, pp. 572–586, 2009.
- [95] S. Bourane, K. S. Grossmann, O. Britz, A. Dalet, M. G. Del Barrio, F. J. Stam, L. Garcia-Campmany, S. Koch, and M. Goulding, "Identification of a spinal circuit for light touch and fine motor control," *Cell*, vol. 160, no. 3, pp. 503–515, 2015.
- [96] C. B. Hart and S. F. Giszter, "A neural basis for motor primitives in the spinal cord," *Journal of Neuroscience*, vol. 30, no. 4, pp. 1322–1336, 2010.
- [97] W. J. Kargo, A. Ramakrishnan, C. B. Hart, L. C. Rome, and S. F. Giszter, "A simple experimentally based model using proprioceptive regulation of motor primitives captures adjusted trajectory formation in spinal frogs," *Journal of neurophysiology*, vol. 103, no. 1, pp. 573–590, 2010.
- [98] F.-G. Zeng, S. Rebscher, W. Harrison, X. Sun, and H. Feng, "Cochlear implants: system design, integration, and evaluation," *IEEE reviews in biomedical engineering*, vol. 1, pp. 115–142, 2008.
- [99] C. Capaday, "The special nature of human walking and its neural control," *TRENDS in Neurosciences*, vol. 25, no. 7, pp. 370–376, 2002.
- [100] F. Clarac, D. Cattaert, and D. Le Ray, "Central control components of a 'simple' stretch reflex," *Trends in neurosciences*, vol. 23, no. 5, pp. 199–208, 2000.
- [101] S. Canbay, B. Gürer, M. Bozkurt, A. Comert, Y. Izci, and M. K. Başkaya, "Anatomical relationship and positions of the lumbar and sacral segments of the spinal cord according to the vertebral bodies and the spinal roots," *Clinical anatomy*, vol. 27, no. 2, pp. 227–233, 2014.

-
- [102] B. Mariani, M. C. Jiménez, F. J. Vingerhoets, and K. Aminian, "On-shoe wearable sensors for gait and turning assessment of patients with parkinson's disease," *IEEE transactions on biomedical engineering*, vol. 60, no. 1, pp. 155–158, 2013.
- [103] P. Afshar, A. Khambhati, S. Stanslaski, D. Carlson, R. Jensen, S. Dani, M. Lazarewicz, J. Giftakis, P. Stypulkowski, and T. Denison, "A translational platform for prototyping closed-loop neuromodulation systems," *Frontiers in neural circuits*, vol. 6, p. 117, 2013.
- [104] I. R. Minev, P. Musienko, A. Hirsch, Q. Barraud, N. Wenger, E. M. Moraud, J. Gandar, M. Capogrosso, T. Milekovic, L. Asboth, R. F. Torres, N. Vachicouras, Q. Liu, N. Pavlova, S. Duis, A. Larmagnac, J. Vörös, S. Micera, Z. Suo, G. Courtine, and S. P. Lacour, "Biomaterials. electronic dura mater for long-term multimodal neural interfaces," *Science*, vol. 347, pp. 159–63, Jan 2015.
- [105] C. Ethier, E. R. Oby, M. J. Bauman, and L. E. Miller, "Restoration of grasp following paralysis through brain-controlled stimulation of muscles," *Nature*, vol. 485, pp. 368–71, May 2012.
- [106] C. E. Bouton, A. Shaikhouni, N. V. Annetta, M. A. Bockbrader, D. A. Friedenberg, D. M. Nielson, G. Sharma, P. B. Sederberg, B. C. Glenn, W. J. Mysiw, A. G. Morgan, M. Deogaonkar, and A. R. Rezai, "Restoring cortical control of functional movement in a human with quadriplegia," *Nature*, vol. 533, pp. 247–50, 05 2016.
- [107] V. K. Mushahwar, L. Guevremont, and R. Saigal, "Could cortical signals control intraspinal stimulators? a theoretical evaluation," *IEEE Trans Neural Syst Rehabil Eng*, vol. 14, pp. 198–201, Jun 2006.
- [108] C. H. Ho, R. J. Triolo, A. L. Elias, K. L. Kilgore, A. F. DiMarco, K. Bogie, A. H. Vette, M. L. Audu, R. Kobetic, S. R. Chang, *et al.*, "Functional electrical stimulation and spinal cord injury," *Physical Medicine and Rehabilitation Clinics*, vol. 25, no. 3, pp. 631–654, 2014.
- [109] N. Kapadia, K. Masani, B. Catharine Craven, L. M. Giangregorio, S. L. Hitzig, K. Richards, and M. R. Popovic, "A randomized trial of functional electrical stimulation for walking in incomplete spinal cord injury: Effects on walking competency," *J Spinal Cord Med*, vol. 37, pp. 511–24, Sep 2014.
- [110] N. Wenger, E. M. Moraud, J. Gandar, P. Musienko, M. Capogrosso, L. Baud, C. G. Le Goff, Q. Barraud, N. Pavlova, N. Dominici, I. R. Minev, L. Asboth, A. Hirsch, S. Duis, J. Kreider, A. Mortera, O. Haverbeck, S. Kraus, F. Schmitz, J. DiGiovanna, R. van den Brand, J. Bloch, P. Detemple, S. P. Lacour, E. Bézard, S. Micera, and G. Courtine, "Spatiotemporal neuromodulation therapies engaging muscle

Bibliography

- synergies improve motor control after spinal cord injury,” *Nat Med*, vol. 22, pp. 138–45, Feb 2016.
- [111] E. M. Moraud, M. Capogrosso, E. Formento, N. Wenger, J. DiGiovanna, G. Courtine, and S. Micera, “Mechanisms underlying the neuromodulation of spinal circuits for correcting gait and balance deficits after spinal cord injury,” *Neuron*, vol. 89, pp. 814–28, Feb 2016.
- [112] O. Kiehn, “Decoding the organization of spinal circuits that control locomotion,” *Nat Rev Neurosci*, vol. 17, pp. 224–38, Apr 2016.
- [113] K. V. Shenoy and J. M. Carmena, “Combining decoder design and neural adaptation in brain-machine interfaces,” *Neuron*, vol. 84, pp. 665–80, Nov 2014.
- [114] J. B. Zimmermann and A. Jackson, “Closed-loop control of spinal cord stimulation to restore hand function after paralysis,” *Front Neurosci*, vol. 8, p. 87, 2014.
- [115] Y. Nishimura, S. I. Perlmuter, R. W. Eaton, and E. E. Fetz, “Spike-timing-dependent plasticity in primate corticospinal connections induced during free behavior,” *Neuron*, vol. 80, pp. 1301–9, Dec 2013.
- [116] G. Courtine and J. Bloch, “Defining ecological strategies in neuroprosthetics,” *Neuron*, vol. 86, pp. 29–33, Apr 2015.
- [117] S. Shoham, E. Halgren, E. M. Maynard, and R. A. Normann, “Motor-cortical activity in tetraplegics,” *Nature*, vol. 413, p. 793, Oct 2001.
- [118] G. Courtine, R. R. Roy, J. Hodgson, H. McKay, J. Raven, H. Zhong, H. Yang, M. H. Tuszynski, and V. R. Edgerton, “Kinematic and emg determinants in quadrupedal locomotion of a non-human primate (rhesus),” *J Neurophysiol*, vol. 93, pp. 3127–45, Jun 2005.
- [119] G. W. Fraser, S. M. Chase, A. Whitford, and A. B. Schwartz, “Control of a brain-computer interface without spike sorting,” *J Neural Eng*, vol. 6, p. 055004, Oct 2009.
- [120] V. Gilja, C. Pandarinath, C. H. Blabe, P. Nuyujukian, J. D. Simeral, A. A. Sarma, B. L. Sorice, J. A. Perge, B. Jarosiewicz, L. R. Hochberg, K. V. Shenoy, and J. M. Henderson, “Clinical translation of a high-performance neural prosthesis,” *Nat Med*, vol. 21, pp. 1142–5, Oct 2015.

-
- [121] T. Aflalo, S. Kellis, C. Klaes, B. Lee, Y. Shi, K. Pejsa, K. Shanfield, S. Hayes-Jackson, M. Aisen, C. Heck, C. Liu, and R. A. Andersen, "Neurophysiology. decoding motor imagery from the posterior parietal cortex of a tetraplegic human," *Science*, vol. 348, pp. 906–10, May 2015.
- [122] T. Milekovic, T. Ball, A. Schulze-Bonhage, A. Aertsen, and C. Mehring, "Detection of error related neuronal responses recorded by electrocorticography in humans during continuous movements," *PLoS One*, vol. 8, no. 2, p. e55235, 2013.
- [123] E. Marieb, *Human Anatomy and Physiology*. Pearson Education, 6th ed., 2003.
- [124] H. G. J. M. Kuypers, *In Comprehensive Physiology*. No. ch3, John Wiley and Sons, 2011.
- [125] D.-H. Kim, J. Viventi, J. J. Amsden, J. Xiao, L. Vigeland, Y.-S. Kim, J. A. Blanco, B. Panilaitis, E. S. Frechette, D. Contreras, *et al.*, "Dissolvable films of silk fibroin for ultrathin conformal bio-integrated electronics," *Nature materials*, vol. 9, no. 6, pp. 511–517, 2010.
- [126] P. Fattahi, G. Yang, G. Kim, and M. R. Abidian, "A review of organic and inorganic biomaterials for neural interfaces," *Advanced materials*, vol. 26, no. 12, pp. 1846–1885, 2014.
- [127] D.-W. Park, A. A. Schendel, S. Mikael, S. K. Brodnick, T. J. Richner, J. P. Ness, M. R. Hayat, F. Atry, S. T. Frye, R. Pashaie, *et al.*, "Graphene-based carbon-layered electrode array technology for neural imaging and optogenetic applications," *Nature communications*, vol. 5, 2014.
- [128] J. C. Barrese, N. Rao, K. Paroo, C. Triebwasser, C. Vargas-Irwin, L. Franquemont, and J. P. Donoghue, "Failure mode analysis of silicon-based intracortical micro-electrode arrays in non-human primates," *Journal of neural engineering*, vol. 10, no. 6, p. 066014, 2013.
- [129] P. Moshayedi, G. Ng, J. C. Kwok, G. S. Yeo, C. E. Bryant, J. W. Fawcett, K. Franze, and J. Guck, "The relationship between glial cell mechanosensitivity and foreign body reactions in the central nervous system," *Biomaterials*, vol. 35, no. 13, pp. 3919–3925, 2014.
- [130] K. A. Potter, M. Jorfi, K. T. Householder, E. J. Foster, C. Weder, and J. R. Capadona, "Curcumin-releasing mechanically adaptive intracortical implants improve the proximal neuronal density and blood–brain barrier stability," *Acta biomaterialia*, vol. 10, no. 5, pp. 2209–2222, 2014.

Bibliography

- [131] Y.-B. Lu, K. Franze, G. Seifert, C. Steinhäuser, F. Kirchhoff, H. Wolburg, J. Guck, P. Janmey, E.-Q. Wei, J. Käs, and A. Reichenbach, “Viscoelastic properties of individual glial cells and neurons in the cns,” *Proc Natl Acad Sci U S A*, vol. 103, pp. 17759–64, Nov 2006.
- [132] B. S. Elkin, A. I. Ilankovan, and B. Morrison III, “A detailed viscoelastic characterization of the p17 and adult rat brain,” *Journal of neurotrauma*, vol. 28, no. 11, pp. 2235–2244, 2011.
- [133] A. F. Christ, K. Franze, H. Gautier, P. Moshayedi, J. Fawcett, R. J. Franklin, R. T. Karadottir, and J. Guck, “Mechanical difference between white and gray matter in the rat cerebellum measured by scanning force microscopy,” *Journal of biomechanics*, vol. 43, no. 15, pp. 2986–2992, 2010.
- [134] B. S. Elkin, E. U. Azeloglu, K. D. Costa, and B. Morrison Iii, “Mechanical heterogeneity of the rat hippocampus measured by atomic force microscope indentation,” *Journal of neurotrauma*, vol. 24, no. 5, pp. 812–822, 2007.
- [135] D. Enzmann and N. Pelc, “Brain motion: measurement with phase-contrast mr imaging,” *Radiology*, vol. 185, no. 3, pp. 653–660, 1992.
- [136] D. E. Harrison, R. Cailliet, D. D. Harrison, S. J. Troyanovich, and S. O. Harrison, “A review of biomechanics of the central nervous system—part i: Spinal canal deformations resulting from changes in posture,” *Journal of manipulative and physiological therapeutics*, vol. 22, no. 4, pp. 227–234, 1999.
- [137] P. Konrad and T. Shanks, “Implantable brain computer interface: Challenges to neurotechnology translation,” *Neurobiology of disease*, vol. 38, no. 3, pp. 369–375, 2010.
- [138] C. F. Guo, T. Sun, Q. Liu, Z. Suo, and Z. Ren, “Highly stretchable and transparent nanomesh electrodes made by grain boundary lithography,” *Nature communications*, vol. 5, p. 3121, 2014.
- [139] J. A. Fan, W.-H. Yeo, Y. Su, Y. Hattori, W. Lee, S.-Y. Jung, Y. Zhang, Z. Liu, H. Cheng, L. Falgout, *et al.*, “Fractal design concepts for stretchable electronics,” *Nature communications*, vol. 5, p. 3266, 2014.
- [140] J. Vanfleteren, I. Chtioui, B. Plovie, Y. Yang, F. Bossuyt, T. Vervust, S. Dunphy, and B. Vandecasteele, “Arbitrarily shaped 2.5 d circuits using stretchable interconnections and embedding in thermoplastic polymers,” *Procedia Technology*, vol. 15, pp. 208–215, 2014.

-
- [141] D.-H. Kim, R. Ghaffari, N. Lu, S. Wang, S. P. Lee, H. Keum, R. D'Angelo, L. Klinker, Y. Su, C. Lu, *et al.*, "Electronic sensor and actuator webs for large-area complex geometry cardiac mapping and therapy," *Proceedings of the National Academy of Sciences*, vol. 109, no. 49, pp. 19910–19915, 2012.
- [142] S. F. Cogan, "Neural stimulation and recording electrodes," *Annu. Rev. Biomed. Eng.*, vol. 10, pp. 275–309, 2008.
- [143] U. A. Aregueta-Robles, A. J. Woolley, L. A. Poole-Warren, N. H. Lovell, and R. A. Green, "Organic electrode coatings for next-generation neural interfaces," *Frontiers in neuroengineering*, vol. 7, 2014.
- [144] T. Pistohl, A. Schulze-Bonhage, A. Aertsen, C. Mehring, and T. Ball, "Decoding natural grasp types from human ecog," *Neuroimage*, vol. 59, no. 1, pp. 248–260, 2012.
- [145] P. Musienko, R. van den Brand, O. Märzendorfer, R. R. Roy, Y. Gerasimenko, V. R. Edgerton, and G. Courtine, "Controlling specific locomotor behaviors through multidimensional monoaminergic modulation of spinal circuitries," *J Neurosci*, vol. 31, pp. 9264–78, Jun 2011.
- [146] S. Cheng, E. C. Clarke, and L. E. Bilston, "Rheological properties of the tissues of the central nervous system: a review," *Med Eng Phys*, vol. 30, pp. 1318–37, Dec 2008.
- [147] L. E. Bilston and L. E. Thibault, "The mechanical properties of the human cervical spinal cord in vitro," *Ann Biomed Eng*, vol. 24, no. 1, pp. 67–74, 1996.
- [148] T. Saxena, J. L. Gilbert, and J. M. Hasenwinkel, "A versatile mesoindentation system to evaluate the micromechanical properties of soft, hydrated substrates on a cellular scale," *J Biomed Mater Res A*, vol. 90, pp. 1206–17, Sep 2009.
- [149] M. Capogrosso, T. Milekovic, D. Borton, F. Wagner, E. M. Moraud, J.-B. Mignardot, N. Buse, J. Gandar, Q. Barraud, D. Xing, E. Rey, S. Duis, Y. Jianzhong, W. K. D. Ko, Q. Li, P. Detemple, T. Denison, S. Micera, E. Bezard, J. Bloch, and G. Courtine, "A brain-spine interface alleviating gait deficits after spinal cord injury in primates," *Nature*, vol. 539, pp. 284–288, 11 2016.
- [150] M. Capogrosso, J. Gandar, N. Greiner, E. M. Moraud, N. Wenger, P. Shkorbatova, P. Musienko, I. Minev, S. Lacour, and G. Courtine, "Advantages of soft subdural implants for the delivery of electrochemical neuromodulation therapies to the spinal cord," *J Neural Eng*, vol. 15, p. 026024, Apr 2018.

Bibliography

- [151] J. P. Slopsema, E. Peña, R. Patriat, L. J. Lehto, O. Gröhn, S. Mangia, N. Harel, S. Michaeli, and M. D. Johnson, “Clinical deep brain stimulation strategies for orientation-selective pathway activation,” *J Neural Eng*, vol. 15, p. 056029, Oct 2018.
- [152] C. A. Bossetti, M. J. Birdno, and W. M. Grill, “Analysis of the quasi-static approximation for calculating potentials generated by neural stimulation,” *J Neural Eng*, vol. 5, pp. 44–53, Mar 2008.
- [153] S. Raspopovic, M. Capogrosso, and S. Micera, “A computational model for the stimulation of rat sciatic nerve using a transverse intrafascicular multichannel electrode,” *IEEE Trans Neural Syst Rehabil Eng*, vol. 19, pp. 333–44, Aug 2011.
- [154] S. F. Lempka, C. C. McIntyre, K. L. Kilgore, and A. G. Machado, “Computational analysis of kilohertz frequency spinal cord stimulation for chronic pain management,” *Anesthesiology*, vol. 122, pp. 1362–76, Jun 2015.
- [155] J. W. Ashford, K. L. Coburn, and J. M. Fuster, “The elgiloy microelectrode: fabrication techniques and characteristics,” *J Neurosci Methods*, vol. 14, pp. 247–52, Sep 1985.
- [156] C. C. McIntyre, A. G. Richardson, and W. M. Grill, “Modeling the excitability of mammalian nerve fibers: influence of afterpotentials on the recovery cycle,” *J Neurophysiol*, vol. 87, pp. 995–1006, Feb 2002.
- [157] C. L. A. M. Vleggeert-Lankamp, R. J. van den Berg, H. K. P. Feirabend, E. A. J. F. Lakke, M. J. A. Malessy, and R. T. W. M. Thomeer, “Electrophysiology and morphometry of the alpha- and beta-fiber populations in the normal and regenerating rat sciatic nerve,” *Exp Neurol*, vol. 187, pp. 337–49, Jun 2004.
- [158] Y. Sweeney, J. Hellgren Kotaleski, and M. H. Hennig, “A diffusive homeostatic signal maintains neural heterogeneity and responsiveness in cortical networks,” *PLoS Comput Biol*, vol. 11, p. e1004389, Jul 2015.
- [159] T. Hagg and M. Oudega, “Degenerative and spontaneous regenerative processes after spinal cord injury,” *J Neurotrauma*, vol. 23, no. 3-4, pp. 264–80, 2006.
- [160] F. B. Wagner, J.-B. Mignardot, C. G. Le Goff-Mignardot, R. Demesmaeker, S. Komi, M. Capogrosso, A. Rowald, I. Seáñez, M. Caban, E. Pirondini, M. Vat, L. A. McCracken, R. Heimgartner, I. Fodor, A. Watrin, P. Seguin, E. Paoles, K. Van Den Keybus, G. Eberle, B. Schurch, E. Pralong, F. Becce, J. Prior, N. Buse, R. Buschman,

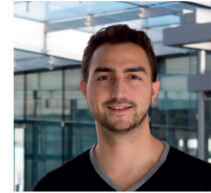
E. Neufeld, N. Kuster, S. Carda, J. von Zitzewitz, V. Delattre, T. Denison, H. Lambert, K. Minassian, J. Bloch, and G. Courtine, “Targeted neurotechnology restores walking in humans with spinal cord injury,” *Nature*, vol. 563, pp. 65–71, 11 2018.

CURRICULUM VITAE

Mr. Jérôme Gandar

Engineer in
Bioengineering
EPFL
(Swiss Federal Institute of Technology)

Ch. de la Butte, 30
1228 Plan-Les-ouates
Geneva, Switzerland
Phone: +41 (0)78 816 36 77
Mail: jerome.gandar@gmail.com



PERSONAL INFORMATION

Nationality	Swiss	Languages	French (mother tongue) English (fluent) German (Basic)
Date of birth	02.10.1988		

EDUCATION

2013-present	Ecole Polytechnique Fédérale de Lausanne, Switzerland PhD in Neuroscience at the Chair in Spinal Cord Repair
2007-2013	Ecole Polytechnique Fédérale de Lausanne, Switzerland Master in Bioengineering and Minor in Biomedical technologies Bachelor in Life Sciences and Technology
2003-2007	Swiss Maturity, at "Collège Madame de Staël", Geneva

PROFESSIONAL EXPERIENCES

2013-present	Doctoral research associate in Neuroscience, Campus Biotech, Geneva, Switzerland <ul style="list-style-type: none">- Design of a neuroscience project to optimize stimulations on spinal cord to restore locomotor functions after a spinal cord injury- Write scientific publications- Lead project composed of people with different status (master level, research assistants, post-docs and PhDs)- Teaching assistance for graduate students. Designing small projects and providing individual support- Coordination of international projects with large interdisciplinary skill
2009-2012	Teaching Assistant (Computer Science & Life Science) <ul style="list-style-type: none">- Assisted bachelor students in their computer science project (C++ programming)- Supervised exercise classes in computer programming- Monitor for student laboratory courses in the field of life science physiology- Exam marker and corrector
2008-2011	Coach for the Life Science Section <ul style="list-style-type: none">- Facilitated the campus integration of the 1 year students- Advised students in the section of their study options
2009-2010	Student Association President <ul style="list-style-type: none">- Organized a 15-day study trip in Japan for 70 students- Raised funds through sponsoring- Dealt with Japan universities- Setup visits with Japan enterprises in the field of Life Science
2008-2009	Class representative <ul style="list-style-type: none">- Represented student interests within the life science faculty organization- Kept students informed
2007-2012	Chief of holiday camp <ul style="list-style-type: none">- Organized summer and winter camps for groups of 10 to 20 kids- Submitted budget and planning to the Geneva State- Organized and prepared all teenagers activities- Managed the animators team

SKILLS

Technical	<p>Development of a closed-loop real-time platform for research studies</p> <p>Laboratory skills (surgical procedures with animals, tissue preparation, immunostainings...)</p> <p>Advance signal processing with MATLAB</p> <p>Responsible for resolving technical issues with electronic devices in the laboratory</p>
Management	<p>Direct supervision of a total of 5 students (2 Bachelor, 1 Technical, 2 Master students)</p> <p>Management of a team of people with different backgrounds and education levels</p> <p>Strong time-management skills developed in a high-pressure environment</p>
Software	<p>Advance knowledge in programming languages (MATLAB, C++/C)</p> <p>Proficient in Microsoft Office (PowerPoint, Excel, Word) for PC and Mac</p> <p>Experienced user of biomedical analysis programs (VICON, MeshLab, EEGLab, ANSYS fluent)</p> <p>Good knowledge of illustration and video editing programs (Adobe Illustrator and Premiere Pro)</p>
IT	<p>Administration of local lab and EPFL lab server (Synology, NAS)</p> <p>Order validator to laboratory IT hightech devices</p> <p>Checking server backups, safety of transferred data and server migration</p>

PUBLICATIONS

Configuration of electrical spinal cord stimulation through real-time processing of gait kinematics. Capogrosso M*, Wagner FB*, **Gandar J**, Moraud EM, Wenger N, Milekovic T, Shkorbatova P, Pavlova N, Musienko P, Bezard E, Bloch J, Courtine G. Nature Protocols (2018).

*These authors contributed equally to this work

Advantages of soft subdural implants for the delivery of electrochemicalv neuromodulation therapies to the spinal cord. Capogrosso M*, **Gandar J***, Greiner N, Moraud EM, Wenger N, Shkorbatova P, Musienko P, Minev I, Lacour S, Cour- tine G., Journal of Neural Engineering (2018).

*These authors contributed equally to this work

Long-term usability and bio-integration of polyimide-based intra-neural stimulating electrodes. Wurth S, Capogrosso M, Raspopovic S, **Gandar J**, Federici G, Kinany N, Cutrone A, Piersigilli A, Pavlova N, Guet R, Tavernier G, Rigosa J, Shkorbatova P, Navarro X, Barraud Q, Courtine G, Micera S. Biomaterials (2017).

A brain-spine interface alleviating gait deficits after spinal cord injury inprimates. Capogrosso M*, Milekovic T*, Borton D*, Wagner F, Moraud EM, Mignar- dot JB, Buse N,**Gandar J**, Barraud Q, Xing D, Rey E, Duis S, Jianzhong Y, Ko WK, Li Q, Detemple P, Denison T, Micera S, Bezard E, Bloch J, Courtine G. Nature (2016).

*These authors contributed equally to this work

Spatiotemporal neuromodulation therapies engaging muscle synergies improve motor control after spinal cord injury. Wenger N*, Moraud EM*, **Gandar J***, Musienko P, Capogrosso M, Baud L, Le Goff CG, Barraud Q, Pavlova N, Dominici N, Minev IR, Asboth L, Hirsch A, Duis S, Kreider J, Mortera A, Haverbeck O, Kraus S, Schmitz F, DiGiovanna J, van den Brand R, Bloch J, Detemple P, Lacour SP, Bézard E, Micera S, Courtine G. Nat Med (2016).

*These authors contributed equally to this work

Biomaterials. Electronic duramater for long-term multimodal neural interfaces. Minev IR*, Musienko P*, Hirsch A, Barraud Q, Wenger N, Moraud EM, **Gandar J**, Capogrosso M, Milekovic T, Asboth L, Torres RF, Vachicouras N, Liu Q, Pavlova N, Duis S, Larmagnac A, Vörös J, Micera S, Suo Z, Courtine G, Lacour SP. Science (2015).

*These authors contributed equally to this work

EXTRA-PROFESSIONAL ACTIVITIES

Hobbies Skiing, Trekking, climbing, theater and boardgames

